UNIVERSIDAD PÚBLICA DE NAVARRA
Departamento de Ingeniería Eléctrica y Electrónica

PUBLIC UNIVERSITY OF NAVARRE
Electrical and Electronic Engineering Department

FREQUENCY RESPONSES AND SYNTHESIS METHODS FOR ADVANCED MICROWAVE APPLICATIONS

RESPUESTAS EN FRECUENCIA Y MÉTODOS DE SÍNTESIS PARA APLICACIONES DE MICROONDAS AVANZADAS

Doctoral Thesis by / Tesis doctoral realizada por

Aintzane Lujambio Genua

Supervised by / Dirigida por

Dr. José María Lopetegui Beregaña

Dr. Miguel Ángel Gómez Laso

Pamplona, February 2014

upna

Universidad Pública de Navarra
Nafarroako Unibertsitate Publikoa

Acknowledgements

Now that the elaboration of this Thesis is coming to an end, I would like to acknowledge all the people that has made this possible. First of all, I would like to show my deepest gratitude to my supervisors Dr. Miguel A. G. Laso and Dr. Txema Lopetegi for making this research possible. All their guidance, support and advice during these years have been essential to accomplish this work. Moreover, I am very grateful to Israel Arnedo, Iván Arregui, Magda Chudzik, Fernando Teberio, Verónica Urrea and Esteban Menargues, all the members of my research group with whom I have shared my research activities. I would also like to thank all the people of the Electrical and Electronic Department that have been around my work in the last years and have provided me with their assistance in so many ways during the development of this Thesis.

I am indebted to Dr. Vicente E. Boria Esbert and Dr. Jorge Daniel Martínez Pérez, from the Universidad Politécnica de Valencia, for giving me access to the fabrication capability of the Laboratory of High Frequency LTCC Circuits, and for sparing no effort to offer me invaluable advice and guidelines for my research work.

I sincerely acknowledge Dr. Paco Medina Mena and his research group, from the Universidad de Sevilla, for giving me assistance to overcome the technical difficulties I encountered in the fabrication. A special mention deserves Dr. Armando Fernández Prieto who has coped with the challenging and hard work at the fabrication laboratories, always ready to help me in anything I required.

I gratefully acknowledge Dr. Leonardo Ranzani, from the University of Colorado at Boulder, and Dr. Mario Martinelli and Dr. Pierpaolo Boffi from the Politecnico di Milano, and their respective research groups, for their availability to scientific collaboration that has been a fruitful and enriching experience.

Last but not least, I would like to extend my warmest thanks to my family and friends that have been my support in each and every moment of my life.

upna

Universidad Pública de Navarra
Nafarroako Unibertsitate Publikoa

ABSTRACT

In this thesis, a new approximation procedure based on digital filter design techniques and a direct synthesis method based on inverse scattering are proposed to provide flexibility to the microwave filter design process. The combination of both methods has been used for the design, fabrication, and measurement of a multiband filter. Further modifications have been done in the design to improve its integration using the latest Low Temperature Cofired Ceramics (LTCC) multilayer technology.

Different type of rectangular waveguide filters with smooth profiles have been presented that provide wideband rejection, high power handling capability and higher order mode suppression, typical specifications of satellite communication systems. The analysis of the proposed devices makes special emphasis on multi-mode effects, which are analyzed using a home-made mode-matching program that allows to obtain the evolution of the modes and the coupling between them inside the structure.

Finally, dispersive delay lines (DDLs), the basic elements of analog signal processing systems, have been considered in detail. After a review of the state of the art, a new method to design chirped delay lines (CDLs) in coupled-lines is proposed and validated by the design, fabrication, and measurement of a device aimed for Ultra Wideband signal processing. In addition, several CDLs in coupled lines are designed to compensate the chromatic dispersion of optical communication systems obtaining very good results for relatively short optical links.

RESUMEN

En esta tesis, se han propuesto un método de aproximación basado en técnicas de diseño de filtros digitales y una técnica de síntesis directa basada en scattering inverso, para proporcionar flexibilidad al proceso de diseño de filtros de microondas. La combinación de ambos métodos ha sido utilizada en el diseño, fabricación y medida de un filtro multibanda. Se han realizado mejoras para una mayor integración del filtro utilizando la tecnologia multicapa Low Temperature Cofired Ceramics (LTCC).

Se han presentado diversos tipos de filtros en guía rectangulas con perfiles suaves que proporcionan grandes anchos de banda de rechazo, gran capacidad de manejo de potencia y supresión de modos de alto orden, especificaciones típicas de los sistemas de comunicaciones por satélite. El análisis de los dispositivos propuestos hace especial hincapié en los efectos multimodo, que han sido analizados utilizando un software propio de mode-matching que permite obtener la evolución de los modos y el acoplo entre los mismos a lo largo de la estructura.

Finalmente, se han considerado en detalle las líneas de retardo dispersivas (DDLs),

elementos básicos en sistemas de procesado analógico de señales. Tras realizar una revisión del estado del arte, se ha presentado un nuevo método para el diseño de líneas de retardo chirpeadas (CDLs) en líneas acopladas que ha sido validado mediante el diseño, la fabricación y medida de un dispositivo para el procesado de señales Ultra Wideband. Además, se han diseñado CDLs en líneas acopladas para compensar la dispersión cromática de los sistemas de comunicaciones ópticos obteniendo muy buenos resultados para enlaces de fibra óptica relativamente cortos.

Contents

upna

Universidad Pública de Navarra
Nafarroako Unibertsitate Publikoa

Chapter 1

Introduction

1.1. Motivation and target applications

A classical microwave filter is a two-port network used to control the frequency response at a certain point in a microwave system by providing transmission without attenuation at frequencies within the pass-band of the filter while others are rejected, constituting the stop-band of the filter. They can be sorted in many different ways, but common criteria approve five main groups such as low-pass, band-pass, band-reject, high-pass and all-pass filters. The properties of each group depend on the frequency band they allow to pass through, what perfectly matches with the classical definition given for a filter.

However, in this thesis, a microwave filter will be considered in a more generalized way, i.e., as a linear time-invariant, passive and causal N-port device that has the capital property of molding the flow of energy that goes to each port. This important property lies in an accurate control over the frequency response, i.e., the amplitude and the phase of the outgoing signal in relation to the incoming sinusoidal signal, for each frequency. The frequency response of the filter characterizes it univocally. This idea was partially introduced in [1]. As it is well-known, the Fourier transform brings the opportunity of the decomposition of any input signal in an integral of sinusoidal waves in order to know the output signal providing that the frequency response of the filter is given, based on linear systems theory [2]. Taking all this into account, a microwave filter can be considered as an analog signal processor in the sense that an incoming microwave signal is transformed by the device in an outgoing signal. Therefore, it will no longer be possible to sort out filters in such a narrow classification as the one mentioned before.

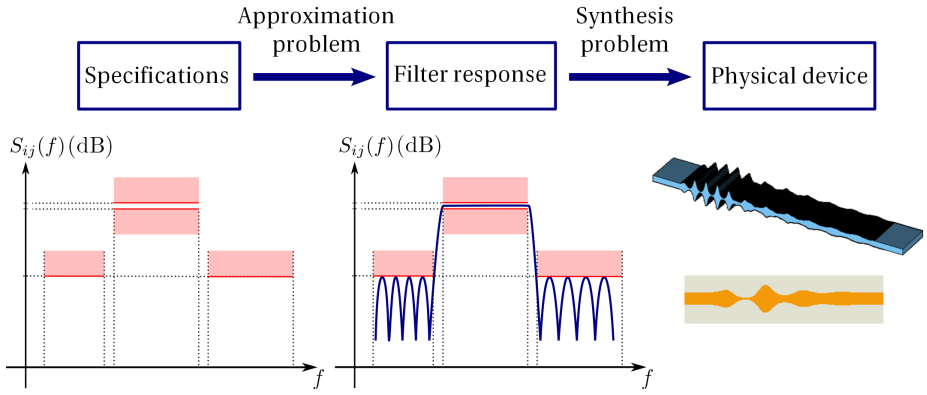

Figure 1.1: Schematic view of a filter design process.

In the same way as the microwave filters are generalized, design techniques have to be also modified to surpass the limitations of actual microwave design methods. The design process of a filter can be divided into two different parts, namely the approximation problem and the synthesis problem, as it is shown in Figure 1.1. The approximation problem consists in obtaining a filter response or transfer function that satisfies the given specifications. The limitations of the following steps of the design process should be also taken into account. The synthesis problem is that of finding the physical parameters of a device that performs the way it was defined by the previously obtained frequency or impulse response. Consequently, the main objective of this thesis is to provide more flexibility to both steps of the design process to satisfy the highly demanding requirements. The goal consists in providing the theoretical foundations as well as the necessary design tools for a novel microwave filter synthesis technique, which can find practical applications in the microwave industry.

Applications for the filters can be found in virtually any classical type of microwave communication, radar, or test and measurement system. Besides, the new emerging applications make even more interesting the development of new filter design techniques so as to satisfy non-conventional specifications. Thus, the general definition of microwave filter that has been proposed as a signal processor is a great challenge. The synthesized devices with the tools presented in this thesis will be characterized by smooth shapes. This feature will present new and interesting properties. Hence, it is expected that many devices will be improved with the techniques presented in this thesis.

Specially interesting and demanding applications will be considered to provide

specific solutions based on the new synthesis approach. One of those important applications involves space specifications for rectangular waveguide filters. In modern communication satellites, [3], more than 18 channels in Ku-band (12.4 to 18 GHz) are combined by the output multiplexer, with an individual power per channel of typically around 200 W. In addition, the stringent requirements impose a high rejection level up to the 3rd harmonic. The currently used standard filter types such as corrugated, waffle iron and ridge waveguide low-pass filters [4–8] can not satisfy both requirements at the same time due to multipactor effects [9, 10]. A channelized approach is usually employed including up to 18 low-pass filters despite the mass and volume drawbacks that this solution implies. With the smooth designs achieved through the novel design technique proposed in this work, the compromise between power and frequency behavior can be broken, to some extent, obtaining high power filters in rectangular waveguide for space applications. In addition, the multi-mode performance of these devices is also of particular interest and it will be considered during design.

Finally, analog signal processing (ASP) applications are new applications in which special heed should be paid [11–13]. The dispersive delay line (DDL) is the basic component in this group of applications. A pseudo-analytical technique in microstrip technology was proposed by Laso *et al.* [14], in order to manufacture devices called chirped delay lines. They are characterized by flat insertion losses and quadratic phase response with respect to the frequency inside the band of interest. Their applicability to the aforementioned ASP applications has been demonstrated with a great success in systems for real-time spectrum analysis [15], time magnification and compression of signals [16], continuously tunable delay lines [17], chromatic dispersion compensation in fiber optics communication systems [18] or sub-wavelength antenna arrays using time reversal technique [19]. More competitive structures will be attained in this thesis applying coupled-line technology.

In the following Section, the context of the filter design topic is introduced which is the background of the work developed in this thesis. A summarized review of the DDLs is also included.

1.2. Classical filter design methods: a brief overview

A wide variety of microwave filter design techniques are available in different technologies, using different basic microwave structures and topologies. A survey of the major classical techniques used in the design of microwave filters is presented in these well known review papers [20–22]. Additionally, many high quality books about this

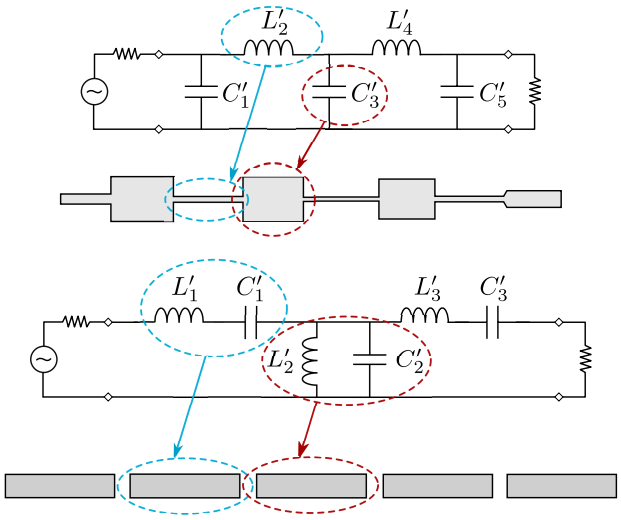

Figure 1.2: Distributed elements correspond to lumped ones to satisfy the model at the working frequency.

topic have been published during the last decades [1, 23–28]. However, the large majority of the design techniques used nowadays are based on the insertion loss method. This method relies on the use of the classical network synthesis theory [29], developed for lower frequencies, that allows us to systematically calculate the lumped-element network that satisfies a desired rational filtering function such as Butterworth, Chebyshev or Cauer. The microwave filter is then realized by implementing the lumped-elements with suitable microwave structures that have similar frequency behaviour over the frequency range of interest, see Figure 1.2. However, the equivalence between the microwave structures used and their lumped-element models will hold for a certain bandwidth but will quickly degrade as the frequency moves away from it. Consequently, microwave filters designed using this technique will provide the required behavior around the design frequency, but their out-of-band behavior will not be under control. Specifically, degradation in the frequency response is expected, often resulting in a loss of steepness in the transition bands and giving rise to new spurious pass/reject bands that can violate the out-of-band requirements of the filter [30]. These problems could be of little importance for narrowband applications, but they are undoubtedly becoming more troublesome during the last years with the emergence of demanding wideband applications.

A classical solution for the design of microwave filters with specifications defined over a wide frequency band is the use of the Richards transformation [31] (or other

similar transformations) and the so-called exact synthesis techniques [32]. Richards showed that microwave distributed networks, composed of commensurate (equal electrical length) transmission lines and lumped resistors, could be treated in analysis or synthesis as lumped-element networks, where together with the classical L, C, R elements the so-called unit element could be also employed. To do so, he proposed the use of a frequency transformation, known as the Richards transformation, that maps the frequency response of the microwave distributed network between $-f_0 \leq f \leq f_0$, into the frequency response of the equivalent lumped-element network in the whole frequency range, $-\infty \leq f \leq \infty$. The frequency f_0 is the frequency at which all the transmission lines of the distributed network feature an electrical length of 90º (i.e. $\lambda/4$). For higher frequencies, the frequency response of the distributed network will repeat periodically. Thus, the exact synthesis procedure will start by synthesizing the required frequency response using a lumped-element network that can include also unit elements. Then, by applying the Richards transformation, the lumped-elements will be implemented using commensurate transmission lines, and the resulting distributed network will feature the frequency response of the lumped-element network mapped between $-f_0 \leq f \leq f_0$, and repeated periodically for higher frequencies [32–36]. The commensurate transmission lines employed in the implementation could be quite complex, including coupled lines, combline and interdigital structures [37]. The technique can be also applied to the synthesis of waveguide filters [23–25, 38] or, by the introduction of approximations, even to mixed lumped/distributed networks [39, 40].

As it can be seen, the use of classical exact synthesis methods allows the designer to have a very good control over the frequency response of the microwave filter up to f_0 (frequency at which all the transmission lines feature a length of $\lambda/4$), but the response will always repeat periodically beyond that frequency.

In any case, conventional microwave filters (obtained by exact synthesis or directly by the insertion loss method), will be implemented by cascading suitable microwave structures as explained above, and will include sharp discontinuities at the connection junctions. These discontinuities can strongly influence the frequency response of the filter due to the fringing field effect [41], making necessary the use of complex models and/or a final electromagnetic optimization step in the design procedure to compensate for them. In any case, sharp discontinuities can be troublesome because they can give rise to the excitation of higher-order modes, or even radiation in open structures [42], and their sharp corners can limit the power handling capability in closed waveguides [1, 43].

To overcome all of these difficulties and limitations of the conventional microwave

filters, an alternative design strategy can be used. The microwave filter design problem can be formulated as a direct synthesis problem, where starting from the desired frequency response for the filter, the required filtering device is obtained by using a direct solution of the electromagnetic equations involved. This problem belongs to a much more general class of mathematical problems known as inverse scattering, where the unknown structure or geometry of an object is obtained from its scattered field. Actually, the inverse scattering techniques have been applied to many subjects such as quantum mechanics, acoustics, geophysics, optics and microwaves, among others [44]. The topic took off when it aroused the interest of researchers in quantum mechanics during the 50's [45, 46]. Later, it became of interest for the microwave community, where several mainly theoretical works were developed in the context of nonuniform transmission lines. Necessary and sufficient conditions for realizability in nonuniform transmission lines were stated, and the unique relationship between reflection coefficient and the shape of the line was established [47, 48]. Approximated synthesis methods were also studied during those early years, but with very difficult or no clear practical application [49]. The first demonstration of a microwave filter designed using inverse scattering was done in the 90's, and several different approaches have been proposed during the last years. Some authors have formulated the inverse scattering problem in terms of time domain reflectometry, using a discrete approach to build the synthesized circuit recursively layer by layer [50–52]. Other authors have managed to rewrite the synthesis problem as a system of Gel'fand-Levitan-Marchenko coupled integral equations [53, 54], or as an inverse classical Sturm-Liouville problem [55] using, afterwards, several complex numerical methods to obtain the solutions. Optimization methods have been also carefully designed and reported in the literature to solve the microwave synthesis problem [56–58]. However, it is important to note that all of these inverse scattering methods developed to synthesize microwave filters assume that the filter will be implemented using nonuniform transmission lines. Actually, microwave propagation along the device is modelled with the telegrapher equations, using distributed series inductance and shunt capacitance parameters, and a voltage and current model [30]. Therefore, the reported inverse scattering synthesis methods are valid to design filters in microwave planar technologies, like microstrip, stripline or coplanar, and in coaxial technology, but they can not be used to design filters in non-TEM waveguide technologies that can not be modeled as transmission lines.

The mentioned filter design techniques have been used for the classical definition of filter where the specifications were typically focused on the magnitude response. When considering dispersive delay lines (DDLs), the phase response has to be also

taken into account and this makes the DDLs a type of device which historically has not been considered as a filter. Several technologies have been used for DDLs with specific design techniques that differ from the filter design methods reviewed above.

A typical classification of DDLs is done based on their operation type: transmission operation or reflection operation. Among the transmission-type DDLs, surface acoustic wave (SAW) devices provide large delays while having a compact size, but their operation frequency is relative low and for a narrow bandwidth [59]. Magnetostatic wave (MSW) devices operate at relatively high operation frequencies and with relatively wide bandwidths, but their fabrication complexity and losses are very high [60]. Another transmission-type DDL design method, based on composite right/left handed (CRLH) transmission lines, has been reported for arbitrary operation frequencies and wide-band operation but its group-delay response is not exactly linear and it requires shielding to avoid radiation problems [61]. Recently, DDLs have been designed by cascading noncommensurate C-sections consisting of a pair of coupled lines shortcircuited at one end [62]. They provide an all-pass response with an arbitrary phase response but with a maximum variation that is limited by the coupling level achievable between the coupling lines. Hence, the design method is restricted to small group-delay slopes. This year, new closed-form synthesis methods to obtain arbitrary prescribed group-delays [63, 64] using the already described C-sections have been reported.

Effective transmission is obtained with DDLs based on cascading multi-section couplers that can operate at high frequencies and wide-band, but they require the use of high-temperature superconductors together to reduce losses to reasonable values [65, 66]. Finally, different reflection-type DDLs have been also published. Based on the Bragg reflection caused by a continuous and quasi-periodic impedance variation, wide-band operation for arbitrary frequencies is obtained by varying the strip width of a microstrip line [12, 14]. Newly, a method based in the same phenomenon was proposed where the impedance discontinuity is created in the substrate itself by alternating sections of an artificial dielectric substrate and a conventional dielectric substrate [67].

1.3. Overview of the thesis

As it has been mentioned before, the main goal of this thesis is to provide flexibility to the microwave filter design process depicted in Figure 1.1. Thus, Chapter 2 will be divided into two sections, each providing a new approach to the two steps of the design process: the approximation and the synthesis problems.

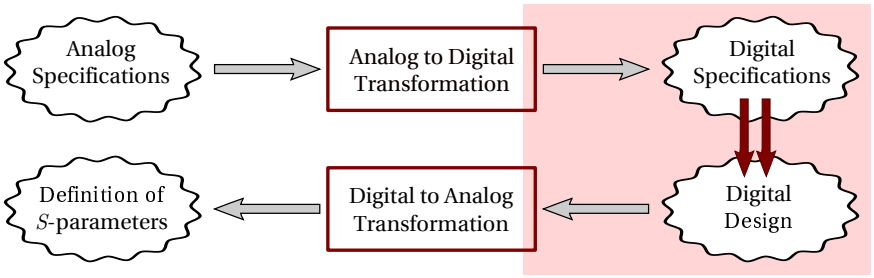

Figure 1.3: Scheme of the new strategy for the approximation problem.

The approximation problem is basically the problem devoted to obtain a filter response that satisfies the given specifications. Classical circuit theory has been employed typically to perform this step of the design, which results in the classical responses like Butterworth, Chebyshev, Cauer,... that are obtained using several well established procedures [1, 68–70]. In this thesis, a new approximation procedure is proposed using the well-established and readily available techniques for the design of digital filters, see Figure 1.3. The proposed methodology relies on the proper translation of the analog target specifications to the digital domain that allows the microwave designer to take advantage of the sophisticated and continuously developing digital filter design techniques without requiring a deep understanding of the complex mathematics involved. The resulting digital filter is then translated back into the analog domain obtaining the desired response.

The synthesis problem is that of finding a physical implementation for a given filter response. A new direct synthesis technique, based on inverse scattering, will be proposed and it is sketched in Figure 1.4. Microwave propagation along the device will be modeled using the coupled-mode theory and a mathematical method will be used to solve the inverse scattering problem. The method is valid when the target frequency response can be expressed as a rational function, and it will allow us to obtain an exact solution for the synthesis problem by means of an analytical closed-form expression. The novel microwave filter synthesis technique proposed will have some remarkable features, shared by all the inverse scattering techniques. Specifically, the synthesis technique is direct and it does not require the use of intermediate lumped-element networks and lumped-element models to design the filter. Moreover, it is exact for all the frequency range of interest, and consequently there is no loss of steepness in the transition bands and no spurious pass/reject bands that can violate the out-of-band requirements of the filter. The synthesis technique produces filters with continuously varying smooth profiles, avoiding the presence of sharp discontinuities and

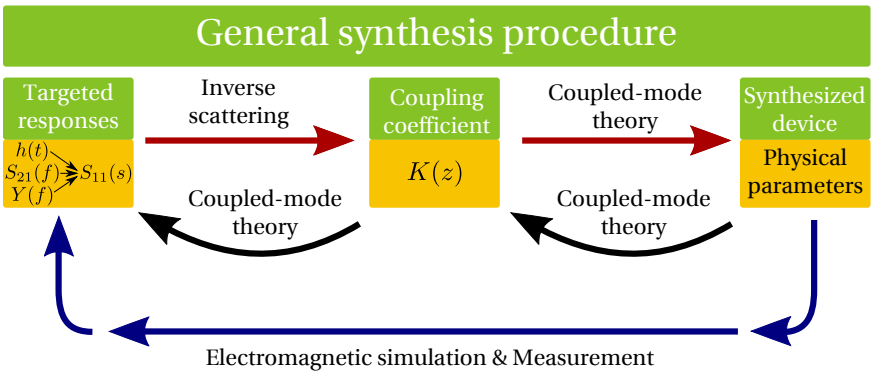

Figure 1.4: Diagram of the general synthesis procedure.

their detrimental effects. Finally, the synthesis technique is very flexible, and is valid for causal, passive and stable frequency responses that must be expressed as rational functions.

The validity of the two novel procedures proposed above for the approximation and for the synthesis problem has been demonstrated by the design, fabrication and measurement of two prototypes of multiband filters. Those filters satisfy specifications which are difficult to achieve using classical filter design techniques, and are found to be interesting applications for the newly proposed design scheme. Additionally, specific solutions are provided for two demanding applications, which are rectangular waveguide filters for space communication systems and dispersive delay lines.

In Chapter 3, three different techniques for the design of low-pass filters in rectangular waveguide are presented: a device designed using the synthesis technique presented in Chapter 2, a high power low-pass filter based on Bragg-reflectors, and a compact high-power low-pass filter. All three devices satisfy typical specifications of low-pass filters for satellite communication systems in Ku-band. Due to the requirements of the design technique or the target specifications of the filter, in all the presented devices the analysis of higher order modes becomes important. Actual simulation software such as Microwave CST Studio provides tools for this purpose. However, the well-known mode-matching technique can be also used. This technique will be implemented for rectangular waveguide in a home-made Matlab program to have a deeper insight of the operation of these devices obtaining information about the evolution and coupling of the modes along the filter structure. After a brief explanation of the mode-matching technique, the designed devices will be presented, making special emphasis on the information obtained with the multi-mode analysis performed

using the mentioned home-made tool.

Finally, in Chapter 4 dispersive delay lines (DDLs) will be considered which have become a very interesting field due to the recent interest on analog signal processing applications. A historical review of different DDL technologies is provided to introduce the topic. Chirped delay lines (CDLs) are one of the proposed solutions which have been demonstrated to be feasible for many applications. However, their operation in reflection requires the use of a wideband circulator to separate the input and output signals, which increases the cost and complexity of the systems. In this chapter, the use of coupled-lines for CDLs is proposed which provides much more competitive devices with effective transmission-type operation. The design method has been validated by the design, fabrication and characterization of a wideband device aimed for Ultra Wideband signal processing. In addition, several prototypes have been designed for a very interesting application which is the compensation of chromatic dispersion, one of the most limiting factors in actual optical communication systems.

References

[1] G. Matthaei, L. Young, and E. M. T. Jones, *Microwave filters, impedance-matching networks, and coupling structures*. Artech House, Inc., 1980.

[2] A. Papoulis, *The Fourier Integral and its applications*. New York: McGraw-Hill Electronic Science Series, 1962.

[3] P. Fortescue and J. Stark, *Spacecraft system engineering*. Chichester, UK: Wiley, 1995.

[4] E. D. Sharp, "A high-power wide-band waffle-iron filter," *IEEE Transactions on Microwave Theory & Techniques*, vol. 11, no. 2, pp. 111–116, March 1963.

[5] L. Young, "Postcript to two papers on waffle-iron filters," *IEEE Transactions on Microwave Theory & Techniques*, vol. 11, no. 6, pp. 555–557, November 1963.

[6] J. Caputo and F. Bell, "Waffle-iron harmonic suppresion filter," *IEEE Transactions on Microwave Theory & Techniques*, vol. 13, no. 5, pp. 701–703, September 1965.

[7] A. M. K. Saad, "Novel lowpass harmonic filters for satellite application," in *Microwave Symposium Digest, 1984 IEEE MTT-S International*, California, CA, USA, June 1984, pp. 292–294.

[8] R. Bunger and F. Arndt, "GSM/moment-method CAD of waffle-iron-filters with round teeth," in *Microwave Symposium Digest, 1999 IEEE MTT-S International*, vol. 4, Anaheim, CA, USA, June 1999, pp. 1691–1694.

[9] J. R. M. Vaughan, "Multipactor," *Electron Devices, IEEE Transactions on*, vol. 35, no. 7, pp. 1172–1180, July 1988.

[10] A. J. Hatch and H. B. Wiliams, "The secondary electron resonance mechanism of low-pressure high-frequency gas breakdown," *Journal of Applied Physics*, vol. 25, no. 4, pp. 417–423, April 1954.

[11] M. A. Jack, P. M. Grant, and J. H. Collins, "The theory, design, and applications of surface acoustic wave Fourier-transform processors," *Proc. IEEE*, vol. 68, no. 4, pp. 450–468, April 1980.

[12] M. A. G. Laso, T. Lopetegi, M. J. Erro, D. Benito, M. J. Garde, M. A. Muriel, M. Sorolla, and M. Guglielmi, "Real-time spectrum analysis in microstrip technology," *IEEE Transactions on Microwave Theory & Techniques*, vol. 51, no. 3, pp. 705–717, March 2003.

[13] C. Caloz, S. Gupta, Q. Zhang, and B. Nikfal, "Analog signal processing: A possible alternative or complement to dominantly digital radio schemes," *Microwave Magazine*, vol. 14, no. 6, pp. 87–103, Sept.-Oct. 2013.

[14] M. A. G. Laso, T. Lopetegi, M. J. Erro, D. Benito, M. J. Garde, M. A. Muriel, M. Sorolla, and M. Guglielmi, "Chirped delay lines in microstrip technology," *IEEE Microwave and Wireless Components Letters*, vol. 11, no. 12, pp. 486–488, Dec. 2001.

[15] J. D. Schwartz, J. Azaña, and D. V. Plant, "Experimental demonstration of real-time spectrum analysis using dispersive microstrip," *IEEE Microwave and Wireless Components Letters*, vol. 16, no. 4, pp. 215–217, April 2006.

[16] ——, "A fully electronic system for the time magnification of ultra-wideband signals," *IEEE Transactions on Microwave Theory & Techniques*, vol. 55, no. 2, pp. 327–334, Feb. 2007.

[17] J. D. Schwartz, I. Arnedo, M. A. G. Laso, T. Lopetegi, J. Azaña, and D. V. Plant, "An electronic UWB continuously tunable time-delay system with nanosecond delays," *IEEE Microwave and Wireless Components Letters*, vol. 18, no. 2, pp. 103–105, Feb. 2008.

[18] L. Ranzani, P. Boffi, R. Siano, S. Rondineau, Z. Popovic, and M. Martinelli, "Microwave-domain analog predistortion based on chirped delay lines for dispersion compensation fo 10-Gb/s optical communication signals," *Journal Lightwave Technol.*, vol. 26, no. 15, pp. 2641–2646, August 2008.

[19] S. Ding, B.-Z. Wang, G. Ge, and D. Zhao, "Sub-wavelength array with embedded chirped delay lines based on time reversal technique," *IEEE Transactions on Microwave Theory & Techniques*, vol. 61, no. 5, pp. 2868–2873, May 2013.

[20] R. Levy and S. B. Cohn, "A history of microwave filter research, design, and development," *IEEE Transactions on Microwave Theory & Techniques*, vol. 32, pp. 1055–1067, September 1984.

[21] R. Levy, R. V. Snyder, and G. Matthaei, "Design of microwave filters," *IEEE Transactions on Microwave Theory & Techniques*, vol. 50, no. 3, pp. 783–793, March 2002.

[22] I. C. Hunter, L. Billonet, B. Jarry, and P. Guillon, "Microwave filters – applications and technology," *IEEE Transactions on Microwave Theory & Techniques*, vol. 50, no. 3, pp. 794–805, March 2002.

[23] I. Hunter, *Theory and Design of Microwave Filters*. London, UK: IEE Electromagnetic Waves Series, 2001, vol. 48.

[24] J. Uher, J. Bornemann, and U. Rosenberg, *Waveguide Components for Antenna Feed Systems: Theory and CAD*. Artech House, 1993.

[25] R. J. Cameron, C. M. Kudsia, and R. R. Mansour, *Microwave filters for communications systems*. New York, NY: John Wiley & Sons, Inc., 2007.

[26] J. Hong, *Microstrip Filters for RF/Microwave Applications*, 2nd ed. Wiley Series in Microwave and Optical Engineering, 2011.

[27] J. A. G. Malherbe, *Microwave Transmission Line Filters*. Dedham, MA: Artech House, Inc., 1979.

[28] R. W. Rhea, *HF Filter Design and Computer Simulations*. Tucker, GA: Noble, 1994.

[29] E. A. Guillemin, *Synthesis of Passive Networks*. New York, NY: Wiley, 1957.

[30] D. M. Pozar, *Microwave engineering*, 4th ed. Hoboken (NJ), USA: John Wiley & Sons, 2012.

[31] P. I. Richards, "Resistor-transmission-line circuits," *Proc. IRE*, vol. 36, no. 2, pp. 217–220, February 1948.

[32] B. J. Minnis, *Designing Microwave Circuits by Exact Synthesis*. Norwood, MA: Artech House, 1996.

[33] H. Ozaki and J. Ishii, "Synthesis of a class of strip-line filters," *IRE Trans. Circuti Theory*, vol. CT-5, no. 2, pp. 104–109, June 1958.

[34] R. J. Wenzel, "Exact design of TEM microwave networks using quarter-wave lines," *IEEE Transactions on Microwave Theory & Techniques*, vol. 12, no. 1, pp. 94–111, January 1964.

[35] M. C. Horton and R. J.Wenzel, "General theory and design of optimum quarter-wave TEM filters," *IEEE Transactions on Microwave Theory & Techniques*, vol. 13, no. 5, pp. 316–327, May 1965.

[36] R. Levy and I.Whiteley, "Synthesis of distributed elliptic-function filters from lumped-constant prototypes," *IEEE Transactions on Microwave Theory & Techniques*, vol. 14, no. 11, pp. 506–517, November 1966.

[37] R. J. Wenzel, "Synthesis of combline and capacitively loaded interdigital band-pass filters of arbitrary bandwidth," *IEEE Transactions on Microwave Theory & Techniques*, vol. 19, no. 8, pp. 678–686, August 1971.

[38] R. Levy, "Tapered corrugated waveguide low-pass filters," *IEEE Transactions on Microwave Theory & Techniques*, vol. 21, no. 8, pp. 526–532, August 1973.

[39] ——, "A new class of distributed prototype filters with application to mixed lumped/distributed component design," *IEEE Transactions on Microwave Theory & Techniques*, vol. 18, no. 12, pp. 1064–1071, December 1970.

[40] ——, "A generalized design technique for practical distributed reciprocal ladder networks," *IEEE Transactions on Microwave Theory & Techniques*, vol. 21, no. 8, pp. 519–526, August 1973.

[41] W. K. Gwarek, "Analysis of an arbitrarily-shaped planar circuit – a time domain approach," *IEEE Transactions on Microwave Theory & Techniques*, vol. 33, no. 10, pp. 1067–1072, October 1985.

[42] M. D. Abouzahra and L. Lewin, "Radiation from microstrip discontinuities," *IEEE Transactions on Microwave Theory & Techniques*, vol. 27, no. 8, pp. 722–723, August 1979.

[43] M. Yu, "Power-handling capability for RF filters," *Microwave Magazine*, vol. 8, pp. 88–97, October 2007.

[44] R. Pike and P. Sabatier, *Scattering – Scattering and Inverse Scattering in Pure and Applied Science*. San Diego, CA: Academic, 2002.

[45] I. M. Gel'fand and B. M. Levitan, "On the determination of a differential equation by its spectral function," *Amer. Math. SOC. Transl.*, vol. 1, pp. 253–304, 1955.

[46] V. A. Marchenko, "Reconstruction of the potential energy from the phase of scattered waves," *Dokl. Akad. Nauk. SSSR*, vol. 104, pp. 635–698, 1955.

[47] D. S. Heim and C. B. Sharpe, "The synthesis of nonuniform lines of finite length – Part I," *IEEE Transactions on Circuit Theory*, vol. CT-14, pp. 393–403, 1967.

[48] M. R. Wohlers, "A realizability theory for smooth lossless transmission lines," *IEEE Trans. Circuit Theory*, vol. 13, no. 4, pp. 356–363, December 1966.

[49] C. Sharpe, "An alternative derivation of Orlov's synthesis formula for nonuniform lines," *Proceedings of the IEE - Part C: Monographs*, vol. 109, no. 15, pp. 226–229, 1962.

[50] F. Huang, "Quasi-transversal synthesis of microwave chirped filters," *Electron. Lett.*, vol. 28, no. 11, pp. 1062–1064, May 1992.

[51] T. W. Pan, C. W. Hsue, and J. F. Huang, "Arbitrary filter design by using nonuniform transmission lines," *IEEE Microw. Guided Wave Lett.*, vol. 9, no. 2, pp. 60–62, February 1999.

[52] R. P.Moreira and L. R. A. X. Menezes, "Direct synthesis of microwave filters using inverse scattering transmission-line matrix method," *IEEE Transactions on Microwave Theory & Techniques*, vol. 48, no. 12, pp. 2271–2276, December 2000.

[53] P. P. Roberts and G. E. Town, "Design of microwave filters by inverse scattering," *IEEE Transactions on Microwave Theory & Techniques*, vol. 43, no. 4, pp. 739–743, April 1995.

[54] G. Xiao and K. Yashiro, "An efficient algorithm for solving Zakharov-Shabat inverse scattering problem," *IEEE Trans. Antennas Propag.*, vol. 50, no. 6, pp. 807–811, June 2002.

[55] G. Xiao, K. Yashiro, N. Guan, and S. Ohkawa, "A new numerical method for synthesis of arbitrarily terminated lossless nonuniform transmission lines," *IEEE*

Transactions on Microwave Theory & Techniques, vol. 49, no. 2, pp. 369–376, February 2001.

[56] M. Le Roy, A. Pérennec, S. Toutain, and L. C. Calvez, "The continuously varying transmission-line technique – Application to filter design," *IEEE Transactions on Microwave Theory & Techniques*, vol. 47, no. 9, pp. 1680–1687, September 1999.

[57] M. Norgren, "Chebyshev collocation and Newton-type optimization methods for the inverse problem on nonuniform transmission lines," *IEEE Transactions on Microwave Theory & Techniques*, vol. 53, no. 5, pp. 1561–1568, May 2005.

[58] P. Miazga, "A new method of computer aided design of non-uniform transmission line filters and impedance matching circuits," in *Proc. Asia-Pacific Microw. Conf.*, Yokohama, Japan, December 1998, pp. 181–183.

[59] V. S. Dolat and R. C. Williamson, "A continuously variable delay-line system," in *Proc. IEEE Ultrason. Symp.*, Annapolis, MD, Sep. 1976, pp. 419–423.

[60] W. Ishak, "Magnetostatic wave technology: A review," *Proceedings of IEEE*, vol. 76, no. 2, pp. 171–178, Sept. 1988.

[61] S. Abielmona, S. Gupta, and C. Caloz, "Compressive receiver using a CRLH-based dispersive delay line for analog signal processing," *IEEE Transactions on Microwave Theory & Techniques*, vol. 57, no. 11, pp. 2617–2626, Nov. 2009.

[62] S. Gupta, A. Parsa, E. Perret, R. V. Snyder, R. J. Wenzel, and C. Caloz, "Group-delay engineered noncommensurate transmission line all-pass network for analog signal processing," *IEEE Transactions on Microwave Theory & Techniques*, vol. 58, no. 9, pp. 2392–2407, September 2010.

[63] S. Gupta, D. L. Sounas, Q. Zhang, and C. Caloz, "All-pass dispersion synthesis using microwave C-sections," *Int. J. Circ. Theor. Appl.*, 2013.

[64] Q. Zhang, S. Gupta, and C. Caloz, "Synthesis of broadband dispersive delay structures by commensurate C- and D-sections," *Int. J. RF and Microwave Comp. Aid. Eng.*, 2013.

[65] R. S. Withers, A. C. Anderson, P. V. Wright, and S. A. Reible, "Superconductive tapped delay lines for microwave analog signal processing," *IEEE Transactions on Magnetics*, vol. 19, no. 3, pp. 480–484, May 1983.

[66] M. J. Lancaster, *Passive microwave device applications of high-temperature superconductors*, 1st ed. Cambridge, U.K: Cambridge Univ. Press, 2006.

[67] M. Coulombe and C. Caloz, "Reflection-type artificial dielectric substrate microstrip dispersive delay line (DDL) for analog signal processing," *IEEE Transactions on Microwave Theory & Techniques*, vol. 57, no. 7, pp. 1714–1723, July 2009.

[68] W.-K. Chen, *The circuits and filters handbook*. CRC Press, 1995.

[69] R. Schaumann and M. E. V. Valkenburg, *Design of analog filters*. New York, NY: Oxford University Press, 2001.

[70] C. Charalambous, "A unified review of optimization," *IEEE Transactions on Microwave Theory & Techniques*, vol. 22, no. 3, pp. 289–300, Mar. 1974.

Chapter 2

Flexible microwave filter design

The design process of a microwave filter can be divided into two different parts, namely the approximation problem and the synthesis problem, as it is shown in Figure 2.1. The approximation problem consists in obtaining a filter response, either frequency or impulse response, that satisfies the given specifications. The limitations of the following steps of the design process should be also taken into account. The synthesis problem is that of finding the physical parameters of a device that performs the way it was defined by the previously obtained frequency or impulse response.

In this chapter, a new flexible way to perform each of the steps in the design will be introduced. The first section will deal with the approximation problem, providing a new method to generate valid responses, based on the ready-to-use digital filter design

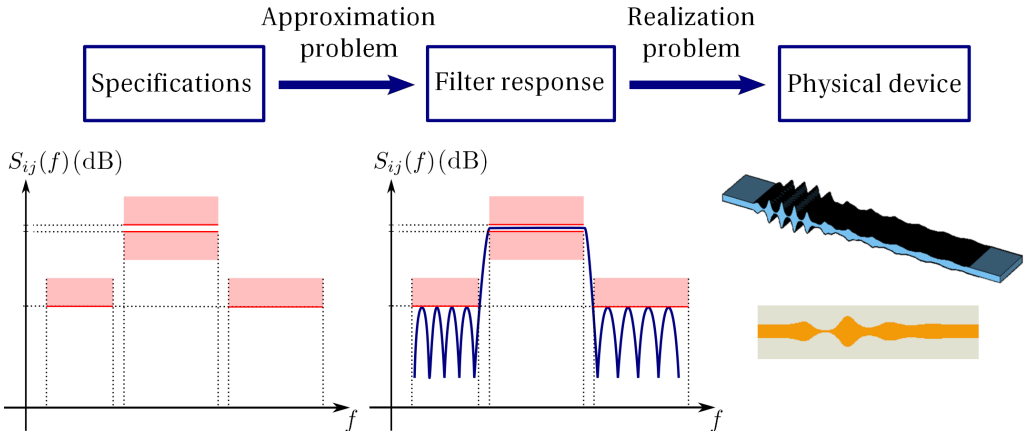

Figure 2.1: Schematic view of microwave filter design process.

techniques. The second section will present a new method that solves the synthesis problem for the case when the target response is a rational function, which is not a practical limitation since any response can be approximated by a rational function.

2.1. Digital filter design techniques for analog function generation

Scattering parameters (S-parameters) constitute the most usual way to present target specifications in microwave industry. Additionally, the microwave scientific community uses them to report the results. However, there is no restriction if for a particular application any other form of specification is used. Indeed, it will be possible to transform it univocally into S-parameters [1].

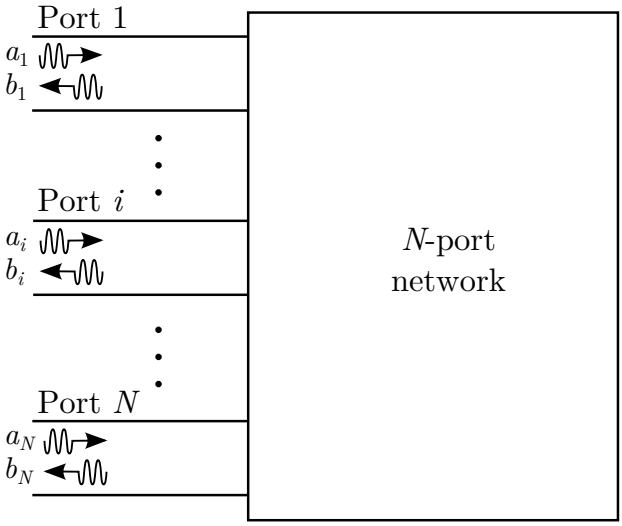

Figure 2.2: N-port network.

S-parameters for a N-port network as the one shown in Figure 2.2, are defined as

$$S_{ij} = \left.\frac{b_i}{a_j}\right|_{a_k=0\ \forall k\neq j} \tag{2.1}$$

where a_i and b_j represent the incident and reflected normalized voltage waves at the i-th port and j-th port respectively [1]. Thus, S_{ij} represents the ratio between the reflected wave at port i and the incident wave at port j when all other incident waves are null, i.e., all ports are connected to matched loads. This can be also expressed in

matrix form as

$$\begin{bmatrix} b_1 \\ b_2 \\ \dots \\ b_N \end{bmatrix} = \begin{bmatrix} S_{11} & S_{12} & \dots & S_{1N} \\ S_{21} & S_{22} & \dots & S_{2N} \\ \dots & \dots & \dots & \dots \\ S_{N1} & S_{N2} & \dots & S_{NN} \end{bmatrix} \begin{bmatrix} a_1 \\ a_2 \\ \dots \\ a_N \end{bmatrix} \quad \Rightarrow \quad \mathbf{b} = [S]\,\mathbf{a}. \tag{2.2}$$

obtaining the scattering matrix, $[S]$.

Steady-state sinusoidal excitation is supposed in the S parameters analysis [1]. Hence, the theoretical problem is solved for each frequency obtaining finally the S-parameters in the form of $S_{ij}(f)$.

Due to the fact that the S-parameters are complex functions of an independent real frequency variable, it is possible to represent them in two different ways. As any other complex number, the dependent variable can be separated into the real and the imaginary parts, (2.3a), or represented in the form of magnitude and phase, (2.3b).

$$S_{ij}(f) = \mathfrak{Re}\left\{S_{ij}(f)\right\} + j\,\mathfrak{Im}\left\{S_{ij}(f)\right\} \tag{2.3a}$$

$$S_{ij}(f) = \left|S_{ij}(f)\right| e^{j\theta_{ij}(f)} \tag{2.3b}$$

Time domain analysis is available being possible to obtain the S-parameters as a function of time [2, 3]. In fact, the relationship between the frequency and time dependent S-parameters can be stated in terms of the well-known Fourier Transform, abbreviated here as $\mathcal{F}$:

$$F_{ij}(t) = \mathcal{F}^{-1}\left\{S_{ij}(f)\right\} = \int_{-\infty}^{\infty} S_{ij}(f)\, e^{j2\pi f t} df \tag{2.4a}$$

$$S_{ij}(f) = \mathcal{F}\left\{F_{ij}(t)\right\} = \int_{-\infty}^{\infty} F_{ij}(t)\, e^{-j2\pi f t} dt \tag{2.4b}$$

The frequency dependency of the S-parameters can be represented through the phase constant variable, β. For this reason, it will be useful to define a new Fourier transform pair of the form

$$F_{ij}(\tau) = \mathcal{F}^{-1}\left\{S_{ij}(\beta)\right\} = \frac{1}{2\pi}\int_{-\infty}^{\infty} S_{ij}(\beta)\, e^{j\beta\tau} d\beta \tag{2.5a}$$

$$S_{ij}(\beta) = \mathcal{F}\left\{F_{ij}(\tau)\right\} = \int_{-\infty}^{\infty} F_{ij}(\tau)\, e^{-j\beta\tau} d\tau \tag{2.5b}$$

It is worth noting that variable τ, defined in spatial units, is related with the time domain through the phase velocity, v_p. Indeed, if the phase velocity is constant for all the bandwidth of interest, the following relationship can be written:

$$\tau = v_p\, t. \tag{2.6}$$

It is also necessary to introduce the unilateral Laplace transform, abbreviated as $\mathcal{L}$, which is also a very important tool for the analysis and design of classical circuits, and it is used in many synthesis methods of microwave filters. It is defined as

$$S_{ij}(s) = \mathcal{L}\left\{F_{ij}(\tau)\right\} = \int_0^\infty F_{ij}(\tau)\, e^{-s\tau} d\tau \tag{2.7}$$

where $s = \sigma + j\beta$ is a complex variable. The s-plane is commonly referred to as the s transformed Laplace domain. It should be observed that the Fourier transform can be obtained by evaluating the Laplace transform along the imaginary axis of the s-plane, i.e, $s = j\beta$.

All the mentioned characterizations are valid for an analog filter. However, the specifications for a filter are given typically in the frequency domain. They consist on the definition of the frequency ranges of the passbands and stopbands, and the required minimum attenuation for the stopbands and the accepted maximum loss in the passbands. Finding a response for the filter that satisfies these requirements is the goal of the approximation problem.

In this section, it is demonstrated that analog functions with especially demanding responses can be obtained by using the well-established and readily available techniques for the design of digital filters [4, 5]. The proposed methodology [6] relies on the proper translation of the analog target specifications to the digital domain. This allows the microwave designer to take advantage of the sophisticated and continuously developing digital filter design techniques without requiring a deep understanding of the complex mathematics involved. The resulting digital filter is then translated back into the analog domain obtaining the desired response.

The section is divided into four subsections. The first one will consider the limitations that apply to the frequency or impulse response of a microwave filter. The second subsection will summarize different transformation techniques between the digital and analog domains, which are essential for the presented generation technique. The third subsection will introduce a variety of digital filter design techniques, focusing on their main properties. And lastly, an example of the presented method will illustrate its validity.

2.1.1. Limits for achieving valid responses

This subsection deals with the unavoidable limits that exist in the impulse or frequency responses of the synthesized devices. The implications over the frequency response due to the kind of device and the selected implementation technology will be considered. And restrictions imposed on the achievable frequency response by the inviolable principles of nature will be also taken into account.

2.1.1.1. Limits due to the device implementation

For the kind of implementation used in this thesis, the properties presented in the following parts of the work will be assumed.

Linear and time-invariant devices

Time invariance implies that the performance of the device does not change with time. In fact the physical properties may vary, but much slower than the selected experimental time span. Linearity is presumed and nonlinear phenomena, such as electronic discharges due to the high power involved, are avoided. Thus, a robust theory can be used to calculate the output of the studied linear and time-invariant (LTI) system for any excitation [7]. In brief, in the system characterized by the frequency response $S_{ij}(f)$, the output signal spectrum, $Y(f)$, obtained for the incoming signal with spectrum $X(f)$, can be easily calculated as:

$$Y(f) = X(f)S_{ij}(f). \tag{2.8}$$

Equivalently, the time domain output signal, $y(t)$, of the system characterized by an impulse response, $F_{ij}(t)$, when the system is excited by the incoming time domain signal $x(t)$, can be expressed mathematically as a convolution:

$$y(t) = x(t) * F_{ij}(t) = \int_{-\infty}^{\infty} x(g)F_{ij}(g-t)dg. \tag{2.9}$$

Counterpart expressions to (2.8) and (2.9) can be attained in the β and τ domains, resulting as:

$$Y(\beta) = X(\beta)S_{ij}(\beta) \tag{2.10}$$

$$y(\tau) = x(\tau) * F_{ij}(\tau) = \int_{-\infty}^{\infty} x(g)F_{ij}(g-\tau)dg \tag{2.11}$$

Passive devices

The devices implemented in this thesis are passive. This can be represented mathematically as:

$$|S_{ij}| \leq 1, \tag{2.12}$$

where $|\ |$ stands for the absolute value.

Reciprocal devices

When a device is reciprocal (passive and without anisotropic elements such as ferrites or plasmas), the S-parameters satisfy the following relation written in a matrix form [8]:

$$[S] = [S]^t \tag{2.13a}$$

where $[\,]^t$ stands for the transposed matrix, and is equivalent to:

$$S_{ij} = S_{ji}. \tag{2.13b}$$

Reciprocal and lossless devices

Moreover, when the device is reciprocal and without losses, it holds:

$$[S]^t[S]^* = [I_n] \tag{2.14}$$

where * stands for the complex conjugate and $[I_n]$ is the unitary matrix of order n.

Concerning two-port devices only, the equation (2.13b) is transformed in

$$S_{12} = S_{21} \tag{2.15}$$

while equation (2.14) is expanded in four conditions expressed mathematically as

$$|S_{11}|^2 + |S_{21}|^2 = 1 \tag{2.16a}$$

$$S_{11}S_{12}^* + S_{21}S_{22}^* = 0 \tag{2.16b}$$

$$S_{12}S_{11}^* + S_{22}S_{21}^* = 0 \tag{2.16c}$$

$$|S_{22}|^2 + |S_{12}|^2 = 1 \tag{2.16d}$$

Rewriting the S-parameters in the magnitude and phase form, see (2.3b), equations (2.15) and (2.16) can be solved, which yields to:

$$S_{11} = |S_{11}|\, e^{j\theta_{11}} \tag{2.17a}$$

$$S_{22} = |S_{11}|\, e^{j\theta_{22}} \tag{2.17b}$$

$$S_{21} = S_{12} = \sqrt{1 - |S_{11}|^2}\, e^{j\theta_{12}} \tag{2.17c}$$

where phase variables are related as follows:

$$\theta_{12} = \frac{\theta_{11} + \theta_{22}}{2} + (1 \mp 2n)\frac{\pi}{2}, \quad n \in \mathbb{N}. \tag{2.17d}$$

It is important to emphasize that with only three free parameters, ($|S_{11}|$, θ_{11}, θ_{22}), all the S_{ij} of a two-port device (eight real parameters) are univocally determined as a result of equations (2.17).

If the device under considerations is reciprocal, lossless and end-to-end symmetrical, the freedom over the S-parameters is reduced once more, resulting in:

$$S_{11} = |S_{11}|\, e^{j\theta_{11}} \tag{2.18a}$$

$$S_{22} = S_{11} \tag{2.18b}$$

$$S_{21} = S_{12} = \sqrt{1-|S_{11}|^2}\, e^{j\left(\theta_{11}+(1\mp 2n)\frac{\pi}{2}\right)}, \quad n \in \mathbb{N}. \tag{2.18c}$$

Minimum-phase conditioned devices

It has been demonstrated, [9, 10], that for Bragg gratings imprinted in the core of an optical fiber, the transmitivity is always a minimum-phase function, after the linear phase associated with the pure propagation through the device is eliminated [11]. In two-port microwave devices, S_{12}- and S_{21}-parameters are minimum-phase functions (once the linear phase contribution in the β domain is subtracted) provided that the path of energy transmission between the input and output ports is defined unequivocally [12]. However, to the author's knowledge, a rigorous demonstration of this fact is still pending in the microwave domain although a demonstration intended for LTI systems was performed in [13]. Additionally, when the device is reciprocal, lossless, and end-to-end symmetrical, the relationship between the phases of the S-parameters, θ_{ij}, established previously in equation (2.18c) implies that S_{11} and S_{22} must be minimum-phase functions, since S_{21}-parameter is always a minimum-phase function.

Obviously, the system that is characterized by a minimum-phase function is called minimum-phase system. The three general properties that define these systems are [7, 14]:

a) Considering all the possible systems that have the same magnitude response and different phase response, the minimum-phase system will be the one which minimizes the quantity:

$$\tilde{\theta}_{ij}(f) = -\frac{\theta_{ij}}{2\pi f}. \tag{2.19}$$

This quantity corresponds to the physical magnitude called phase delay.

b) Under the same notation, the minimum-phase system minimizes the group delay as well, that is defined as:

$$\phi_{ij}(f) = -\frac{1}{2\pi}\cdot\frac{d\theta_{ij}(f)}{df}. \tag{2.20}$$

c) Finally, the time evolution of the energy in a system characterized by its impulse response, see equation (2.4a), can be mathematically defined as:

$$E_{ij}(t) = \int_0^t |F_{ij}(g)|^2 \, dg. \tag{2.21}$$

The evolution of $E_{ij}(t)$ can be understood as a delay of the energy. Thus, the minimum-phase system delivers the energy faster than any other system with the same magnitude frequency response (but different impulse response). In other words, the minimum-phase system minimizes the delay of the energy.

A case of particular interest is the one in which the S-parameters can be expressed as rational functions in the s transformed Laplace domain [15]. Under these circumstances, assuming that the transmission of energy between the input and output ports can take only one path and knowing that the devices will be reciprocal and lossless, the following properties can be underlined [12]

a) All the $S_{ij}(s)$-parameters have the same polynomial in the denominator and therefore, the same poles.

b) The $S_{12}(s) = S_{21}(s)$ have to be minimum-phase functions, which means that all of their zeros must lie in the left-hand side of the s-plane.

2.1.1.2. Physical devices principle

Another important property that must be satisfied is mathematically expressed as:

$$F_{ij}(t) \in \mathbb{R} \tag{2.22a}$$

$$S_{ij}(-f) = S_{ij}^*(f) \tag{2.22b}$$

where * stands for the complex conjugate and $F_{ij}(t)$ and $S_{ij}(f)$ are related trough equations (2.4). Thus, real devices must have real impulse responses as it can be seen in (2.22a). The property can be transposed to the frequency domain using (2.4b), resulting in (2.22b).

If the S-parameters can be written as rational functions in the transformed Laplace domain [15], the principle of physical devices implies that the poles and zeros can be real or complex, but if they are complex they must appear in complex conjugate pairs.

2.1.1.3. Stability principle

On the basis of energy conservation principle, a linear and time-invariant system is stable if for a bounded incoming signal, $x(t)$, the outgoing signal, $y(t)$, is also bounded. The signals $x(t)$ and $y(t)$ are considered bounded when they satisfy:

$$|x(t)| < M_1;\ |y(t)| < M_2; \tag{2.23}$$

being M_1 and M_2 constants with $M_1 < \infty$ and $M_2 < \infty$. Following the notation used in equation (2.9), a system characterized by $F_{ij}(t)$ is stable if and only if [7]:

$$\frac{M_2}{M_1} = \int_{-\infty}^{\infty} |F_{ij}(t)|\, dt < \infty \tag{2.24}$$

what guarantees the bounded considerations in (2.23). Although trivial, it is important to highlight that the ratio M_2/M_1 does not depend on the incoming signal.

If the S-parameters can be written as rational functions in the transformed Laplace domain [15], the principle of stability is satisfied if and only if all the poles are located on the left-hand side of the s-plane.

2.1.1.4. Causality principle

Causality principle connects cause and effect. In classical physics, the concept is defined by the fact that the effect will be preceded by the cause.

It will be useful for this subsection to introduce the definition of a new transform pair, the so-called Hilbert Transform, HT, [7]

$$R(f) = \mathrm{HT}\left(X(f)\right) = \frac{1}{\pi} C_{pv} \int_{-\infty}^{\infty} \frac{X(g)}{f-g} dg = X(f) * \frac{1}{j\pi f} \tag{2.25a}$$

$$X(f) = \mathrm{HT}^{-1}\left(R(f)\right) = -\frac{1}{\pi} C_{pv} \int_{-\infty}^{\infty} \frac{R(g)}{f-g} dg = -R(f) * \frac{1}{j\pi f} \tag{2.25b}$$

where C_{pv} stands for the Cauchy principal value of the integral and $*$ means convolutions. This symbol should not be mistaken with the superscript * that refers to complex conjugate.

In this subsection, the consequences of applying the causality principle over linear and time-invariant (LTI) systems will be shown. The key condition in order to guarantee causality in LTI devices is to impose that [7]

$$F_{ij}(t) = 0; \quad \forall t < 0. \tag{2.26}$$

Therefore, a real and causal impulse response can be written as follows, taking into account a possible discontinuity at the beginning of the impulse response:

$$F_{ij}(t) = F_{ij,e}(t) + F_{ij,o}(t) \tag{2.27}$$

being $F_{ij,e}(t)$ and $F_{ij,o}(t)$ the even and odd parts of the impulse response, which are defined by

$$F_{ij,e}(t) = \frac{F_{ij}(t) + F_{ij}(-t)}{2} + F_{ij,e0}\delta(t) \tag{2.28a}$$

$$F_{ij,o}(t) = \frac{F_{ij}(t) - F_{ij}(-t)}{2} \tag{2.28b}$$

The multiplying constant of the Dirac delta that appears in (2.28a), $F_{ij,e0}$, is univocally determined by:

$$F_{ij,e0} = \lim_{f\to\infty} \left(\mathfrak{Re}\{S_{ij}(f)\}\right) \tag{2.29}$$

for which a the mathematical proof is available in [7] for the interested reader.

Consequently, following the equations (2.28) as well as the definition of $\mathrm{sgn}(\,)$ function, i.e., $\mathrm{sgn}(t) = \dfrac{t}{|t|} = \begin{cases} 1 & t > 0 \\ -1 & t < 0 \end{cases}$, it can be derived that:

$$F_{ij,e}(t) = F_{ij,o}(t)\,\mathrm{sgn}(t) + F_{ij,e0}\,\delta(t) \tag{2.30}$$

It is well-known that the Fourier transform of an even function yields to a real function, while the Fourier transform of an odd function is imaginary. Thus, applying the Fourier transform defined in (2.4), the equation (2.27) is transformed in

$$S_{ij}(f) = \mathcal{F}\left\{F_{ij,e}(t)\right\} + \mathcal{F}\left\{F_{ij,o}(t)\right\} = \mathfrak{Re}\left\{S_{ij}(f)\right\} + j\,\mathfrak{Im}\left\{S_{ij}(f)\right\}. \tag{2.31}$$

As it can be seen, equation (2.31) coincides with (2.3a).

A straightforward relationship between the real and imaginary parts of a causal frequency response can be obtained. For doing so, the Fourier transform in equation (2.30) is applied, using the result of (2.31), and identifying the Hilbert transform defined in (2.25). Thus, the following equation is achieved:

$$\begin{aligned} \mathfrak{Re}\left\{S_{ij}(f)\right\} &= F_{ij,e0} + \mathrm{HT}\left(\mathfrak{Im}\left\{S_{ij}(f)\right\}\right) \\ &= F_{ij,e0} + C_{pv}\frac{1}{\pi}\int_{-\infty}^{\infty}\frac{\mathfrak{Im}\left\{S_{ij}(g)\right\}}{f-g}dg \end{aligned} \tag{2.32a}$$

Similarly, a second equation is generated by reversing the roles, giving:

$$\begin{aligned} \mathfrak{Im}\left\{S_{ij}(f)\right\} &= \mathrm{HT}^{-1}\left(\mathfrak{Re}\left\{S_{ij}(f)\right\}\right) = -\mathrm{HT}\left(\mathfrak{Re}\left\{S_{ij}(f)\right\}\right) \\ &= -C_{pv}\frac{1}{\pi}\int_{-\infty}^{\infty}\frac{\mathfrak{Re}\left\{S_{ij}(g)\right\}}{f-g}dg \end{aligned} \tag{2.32b}$$

Much more interesting for the industry and the scientific community is the relationship that can be established between the magnitude and phase of a causal frequency response. Taking the natural logarithm on both sides of equation (2.3b) yields

to:

$$\ln\left(S_{ij}(f)\right) = \underbrace{\ln\left(|S_{ij}(f)|\right)}_{\text{real part}} + j\underbrace{\theta_{ij}(f)}_{\text{imaginary part}}. \tag{2.33}$$

Causality has to be satisfied by the impulse response associated with this new function to obtain a Hilbert transform relation between the current real and imaginary parts. If and only if the $S_{ij}(f)$ is a minimum-phase function, then the new function, $\ln\left(S_{ij}(f)\right)$, will be causal [7]. Therefore, the relationship between the magnitude and phase contributions of a minimum-phase frequency response can be obtained as follows:

$$\ln\left(|S_{ij}(f)|\right) = S_{ij,e0} + \mathrm{HT}\left(\theta_{ij}(f)\right) = S_{ij,e0} + C_{pv}\frac{1}{\pi}\int_{-\infty}^{\infty}\frac{\theta_{ij}(g)}{f-g}dg \tag{2.34a}$$

$$\begin{aligned}\theta_{ij}(f) &= \mathrm{HT}^{-1}\left(\ln\left(|S_{ij}(f)|\right)\right) = -\mathrm{HT}\left(\ln\left(|S_{ij}(f)|\right)\right)\\ &= -C_{pv}\frac{1}{\pi}\int_{-\infty}^{\infty}\frac{\ln\left(|S_{ij}(f)|\right)}{f-g}dg\end{aligned} \tag{2.34b}$$

It is important to stress that by knowing $\theta_{ij}(f)$ only, the magnitude is not univocally determined, which is caused by the presence of a multiplicative constant that can be always included in $|S_{ij}(f)|$ for a given phase $\theta_{ij}(f)$. However, if the $|S_{ij}(f)|$ is known, the phase contribution is perfectly determined without ambiguity. Although several methods exist to calculate these troublesome integrals [7], a discrete algorithm detailed in [14] will be used along the thesis.

To finish this subsection it is important to highlight that if the S-parameters can be written as rational functions in the s transformed Laplace domain [15], the causality principle is guaranteed.

2.1.1.5. Uncertainty principle and duration of the impulse response

The duration of an impulse response and its relationship with the frequency response is an important matter of study. It is well-known that Fourier transform predicts short duration of impulse responses for wideband frequency responses and vice versa. An accurate definition for the duration of the impulse response will be given, although it has to be stressed that none of the definitions available is fully suitable [15]. Following Papoulis [7], $\int_{-\infty}^{\infty} t^2\left|F_{ij}(t)\right|^2 dt$ is often used in order to measure the persistence in time. Taking into account Parseval's theorem [7]:

$$\int_{-\infty}^{\infty}\left|F_{ij}(t)\right|^2 dt = \int_{-\infty}^{\infty}\left|S_{ij}(f)\right|^2 df, \tag{2.35}$$

and the general differentiation property of the Fourier transformed functions:

$$(-j2\pi t)^n F_{ij}(t) \xrightarrow{\mathcal{F}} \frac{d^n S_{ij}(f)}{df^n}, \tag{2.36}$$

a relationship between the time span of the impulse response, and the magnitude and phase components of the S-parameters can be given as [7]:

$$\int_{-\infty}^{\infty} t^2 \left|F_{ij}(t)\right|^2 dt = \frac{\displaystyle\int_{-\infty}^{\infty} \left(\left|S_{ij}(f)\right|^2 \left(\frac{d\theta_{ij}(f)}{df}\right)^2 + \left(\frac{d\left|S_{ij}(f)\right|}{df}\right)^2 \right) df}{4\pi^2} \tag{2.37}$$

This equation is of particular interest in the context of this thesis, because it links quantitatively the sharpness in the magnitude, as well as the ripple in the phase, with the time persistence. Actually, the group delay, defined in (2.20), can be identified in (2.37) stating its direct influence in the time duration. Going straightforward, the uncertainty principle postulates that if $F_{ij}(t)$ vanishes at infinity faster than $\sqrt{1/t}$, and for the sake of simplicity equation (2.35) equals 1, the following inequality can be stated:

$$\left(\int_{-\infty}^{\infty} t^2 \left|F_{ij}(t)\right|^2 dt\right) \cdot \left(\int_{-\infty}^{\infty} f^2 \left|S_{ij}(f)\right|^2 df\right) \geq \frac{1}{4\pi} \tag{2.38}$$

whereas equality holds for the Gaussian case [7]. This means that the product between the time duration and the frequency span (this is not exactly the bandwidth although both parameters are strongly related) is always bigger than $\frac{1}{4\pi}$. Moreover, it can be also concluded that for a fixed frequency span the shortest pulse will be the Gaussian pulse and, obviously, for a fixed pulse duration the shortest frequency span will follow a Gaussian shape. This fact makes Gaussian function especially interesting for communication applications.

2.1.2. Transformation techniques

The transformation techniques between the analog and digital domains are the cornerstone of the proposed design scheme. Therefore, the essential difference between analog and digital functions should be introduced first [14].

An analog function is the function evaluated in the continuous variable time. Both the variable time and the evaluated function are expressed as a real number which can take infinite values between two different ones. This can be expressed mathematically as a mapping $\mathbb{R} \rightarrow \mathbb{R}$. In contrast, if the time variable is discrete, which means it is quantized to a bunch of possible numbers, commonly integer numbers, the function evaluated over is called discrete-time function. Furthermore, if the resulting numbers

of the evaluation of the function are also quantized, the function is considered to be digital. In this case, it is expressed mathematically as $\mathbb{Z} \rightarrow \mathbb{Z}$. This is actually the case when computers are involved. Thus, strictly speaking, only digital functions can be assessed at the current computers as a result of the finite precision in the conventional binary code representation of numbers. However, actual implementations can provide very good approximations with a controlled accuracy. Although the reasoning about these differences has been carried out in the time domain, and so implicitly over the impulse response, it could have been done likewise in the frequency. Proper transformations exist to obtain frequency representations of the time domain information for the analog functions as well as for the digital ones.

As a discrete counterpart of the Laplace transform, when discrete time signals are considered, the z-transform is essential. It is mathematically defined as:

$$S_{ij}(z) = \mathcal{Z}\left\{F_{ij}[n]\right\} = \sum_{n=-\infty}^{\infty} F_{ij}[n]\, z^{-n} \tag{2.39a}$$

for all $z \in \mathbb{C}$ for which $S_{ij}(z)$ converges. The inverse z-transform is:

$$F_{ij}[n] = \mathcal{Z}^{-1}\left\{S_{ij}(z)\right\} = \frac{1}{2\pi j} \oint_{\Gamma} S_{ij}(z)\, z^{n-1} \tag{2.39b}$$

where Γ is a closed contour in the counterclockwise sense enclosing all the singularities of the integrand.

As it is depicted in Figure 2.3, the proposed design strategy relies in the proper transformation between the digital and the analog domains. The transformation techniques have to satisfy the following two prescriptions:

a) The analog filter should keep the essential properties of the digital filter. Thus, the unit circle $|z| = 1$ of the z-plane, must be transformed to the imaginary axis $s = j\beta$ of the s-plane.

b) Stability must be satisfied. Hence, the poles located in the inner of the unity circle $|z| < 1$ of the z-plane must be mapped to the left-hand side of the s-plane, $\mathfrak{Re}\{s\} < 0$.

Having this in mind, the three most important techniques to carry out a transformation between the analog and digital domains will be presented here. All the details of the techniques to go from the analog realm to the digital realm can be found in [4, 14, 16]. The novelty of this work rests on the fact that, once the digital filter is obtained, all of the three mentioned techniques can be used in a reverse manner, so as to get an analog function from a digital one. The following three sections will address these problems.

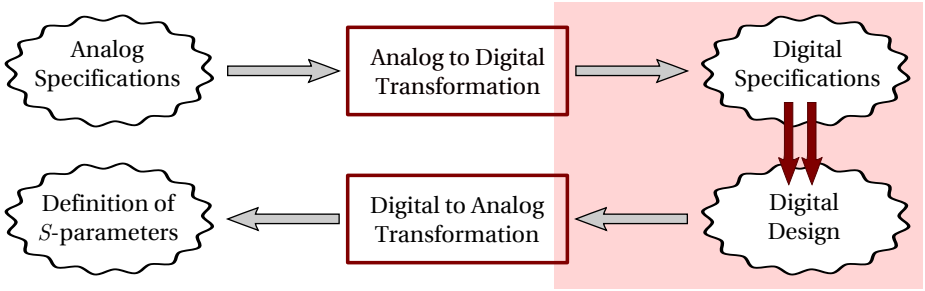

Figure 2.3: Scheme of the new strategy to solve the approximation problem.

2.1.2.1. Invariant impulse response method

A discrete time system obtained following this method, is defined by sampling an analog impulse response, fact from which it takes the name. Thus, the frequency response of the discrete system is determined by the frequency response of the analog system [14].

Analog to digital transformation

The digital system is defined taking equally distributed samples from the analog impulse response, mathematically:

$$h[n] = T_s\, h_c(nT_s) \tag{2.40}$$

where $h_c(\tau)$ is the impulse response of a system in continuous time, $h[n]$ is the impulse response in the discrete time and T_s is the sampling period, as it is shown in Figure 2.4.

Commonly, specifications are given as a frequency response. Thereby, it is interesting to know the relationship between the frequency response of the system in both, discrete and continuous time. From [14], the relationship can be expressed as[1]

$$H\left(e^{j\omega}\right) = \sum_{k=-\infty}^{\infty} H_c\left(j\frac{\omega}{T_s} + j\frac{2\pi}{T_s}k\right) \tag{2.41}$$

being ω the digital frequency. If the analog system is limited in bandwidth,

$$H_c(j\beta) = 0, \quad |\beta| \geq \pi/T_s \tag{2.42}$$

it can be stated that:

$$H\left(e^{j\omega}\right) = H_c\left(j\frac{\omega}{T_s}\right), \quad |\omega| \leq \pi \tag{2.43}$$

[1] Obviously, as a characteristic of the discrete time systems, the frequency response is periodic, with period equal to 2π.

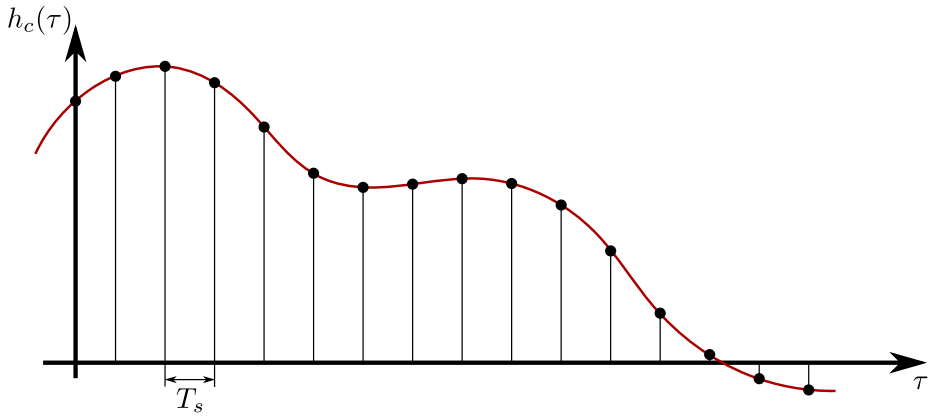

Figure 2.4: Impulse response $h[n]$ from $h_c(\tau)$.

where β, the phase constant, represents the analog frequency. It means that the frequency responses are related by a linear change in the frequency scale, specifically $\omega = \beta T_s$ for $|\omega| \leq \pi$. However, almost none of the practical frequency responses strictly satisfies the condition (2.42), having as a result interference between the periodic replicas of the spectrum, the so-called *aliasing* effect. Rapid decays of the frequency response at high frequencies provide better results due to the minimization of the aliasing.

When the analog frequency response can be expressed as a rational function and the denominator degree in $H_c(s)$ exceeds the numerator degree by at least 2, the basic assumption in (2.42) hold for a sufficiently high sampling frequency. If, in addition, the poles of $H_c(s)$ are simple, the locations of the digital and analog poles are related [14] as

$$H_c(s) = \sum_{i=1}^{N} \frac{A_i}{s - p_i} \tag{2.44}$$

$$H(z) = \sum_{i=1}^{N} \frac{T_s A_i}{1 - e^{p_i T_s} z^{-1}} \tag{2.45}$$

It is clear from equations (2.44) and (2.45) that the poles in the s-plane, p_i, are transformed in $z_i = e^{p_i T_s}$ of the z-plane. Besides, the coefficients of the partial fraction decomposition of the analog function have to be scaled by T_s. However, it is important to point out that there is no expression available for the mapping of the zeros. Indeed, their final positions will depend on the locations of the poles which constitutes a disadvantage of the method.

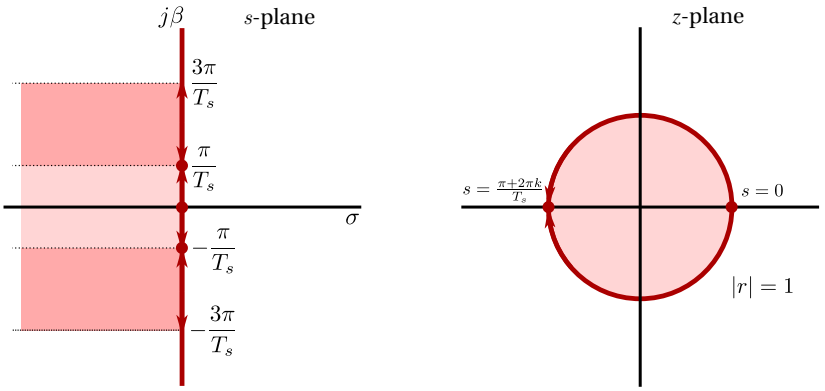

Figure 2.5: Mapping between the surfaces of the s-plane and the z-plane for the invariant-impulse-response method.

The aliasing effect can be observed in Figure 2.5, where different shaded regions of the analog domain collapse into the same area at the z-plane. The resulting effect is called *"mapping many-to-one"*. Therefore, the sampling frequency is a critical parameter to be determined. It is important to take into account that all the poles should be placed in the first light shaded area of the s-plane of Figure 2.5, the region determined by $\mathfrak{Re}\{s\} < 0$ and $-\pi/T_s < \mathfrak{Im}\{s\} < \pi/T_s$.

Three advantages can be highlighted for this technique. Firstly, the impulse response is preserved without modifications. Secondly, a stable system in one domain yields to a stable system in the other. Finally, the digital and analog frequencies are linearly related.

Digital to analog transformation

Two possible implementations come up for inverting the transformation from analog to digital: one in the transformed domain and the other in the τ domain.

Dealing with the technique in the transformed domain, the z-transform of the digital response has to be factorized using partial fraction decomposition

$$H(z) = \sum_{i=1}^{N} \frac{B_i}{1 - c_i z^{-1}} \tag{2.46}$$

which is possible if the denominator degree in $H(z)$ exceeds the numerator degree and the poles of $H(z)$ are simple.

Thus, the analog system is achieved by mapping the poles over the s-plane as follows:

$$p_i = \frac{1}{T_s}\ln(c_i) \tag{2.47}$$

and scaling the coefficients with the sampling period T_s:

$$A_i = \frac{B_i}{T_s} \tag{2.48}$$

resulting in the analog frequency response of equation (2.44).

The implementation in the transformed domain will be the most convenient strategy when the order of the considered filter is low and only if simple poles of multiplicity 1 are involved.

In other cases, the τ domain strategy should be used. It consists in the interpolation of the digital impulse response. However, due to the fact that the ideal interpolation is not possible an approximated method is applied. The only exact values of the analog impulse response are the ones that coincide with $\tau = nT_s$.

2.1.2.2. Bilinear transformation

The bilinear transformation is an algebraic transformation between the s- and z-planes expressed by

$$s = \frac{2}{T_s}\cdot\frac{z-1}{z+1} \tag{2.49a}$$

$$z = \frac{1+(T_s/2)s}{1-(T_s/2)s} \tag{2.49b}$$

for analog-to-digital conversion and digital-to-analog conversion, respectively, where T_s is the sampling period that will be chosen to satisfy Nyquist criterion [14].

Mathematically, the bilinear transformation is a conformal mapping [2] in the complex plane. Thus, expanding the complex variables $s = \sigma + j\beta$ and $z = |r|e^{j\omega}$, it can be seen that:

$$\begin{aligned} &\text{if} \quad \sigma > 0 && \text{then} \quad |r| > 1, \\ &\text{if} \quad \sigma = 0 && \text{then} \quad |r| = 1, \\ &\text{if} \quad \sigma < 0 && \text{then} \quad |r| < 1, \end{aligned}$$

where all the regions are depicted in Figure 2.6, for both planes.

[2] A conformal transformation is a one-to-one mapping between two planes that satisfies the property that intersecting curves in one plane map into intersecting curves into the other plane such that the angles between the intersecting curves keep unaltered in magnitude and sense.

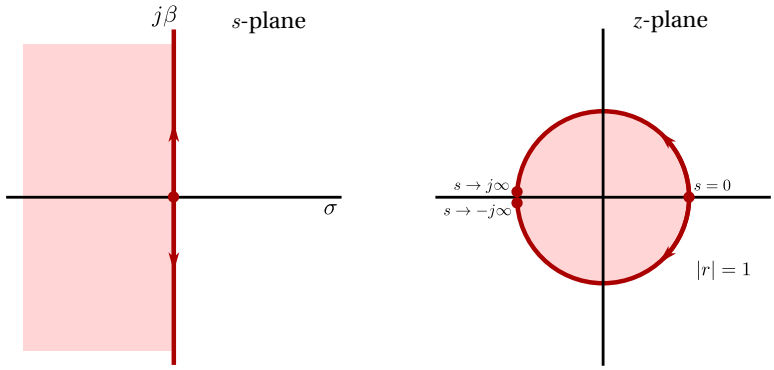

Figure 2.6: Mapping between the surfaces of the s-plane and the z-planes for the bilinear-transformation method.

Consequently, a causal and stable digital or analog system becomes causal and stable also in the other realm. Besides, if $\sigma = 0$, results that $s = j\beta$, $|r| = 1$, and we obtain a mapping between β, the phase constant that we use instead of the analog frequency, and the digital frequency, ω, of the form

$$\beta = \frac{2}{T_s} \tan\left(\frac{\omega}{2}\right) \tag{2.50}$$

Specifically:

$$\begin{aligned} &\text{if} \quad \omega = 0 && \text{then} \quad \beta = 0, \\ &\text{if} \quad \omega = -\pi && \text{then} \quad \beta = -\infty, \\ &\text{if} \quad \omega = +\pi && \text{then} \quad \beta = +\infty. \end{aligned}$$

Warping effect

Equation (2.50) establishes a non-linear relationship between the analog and the digital frequencies. For small values of ω, the $\tan(\omega/2)$ can be approximated by the first term of the Taylor series as $\omega/2$, and the relationship becomes linear $\beta \approx \omega/T_s$. However, the distortion increases with the rise of the frequency causing the so-called warping effect. The effect can be smoothed down employing an auxiliary frequency variable, called pre-warping frequency. The pre-warped form of the bilinear transformation is

$$z = \frac{\beta_p + s \tan\left(\frac{T_s}{2}\beta_p\right)}{\beta_p - s \tan\left(\frac{T_s}{2}\beta_p\right)} \tag{2.51}$$

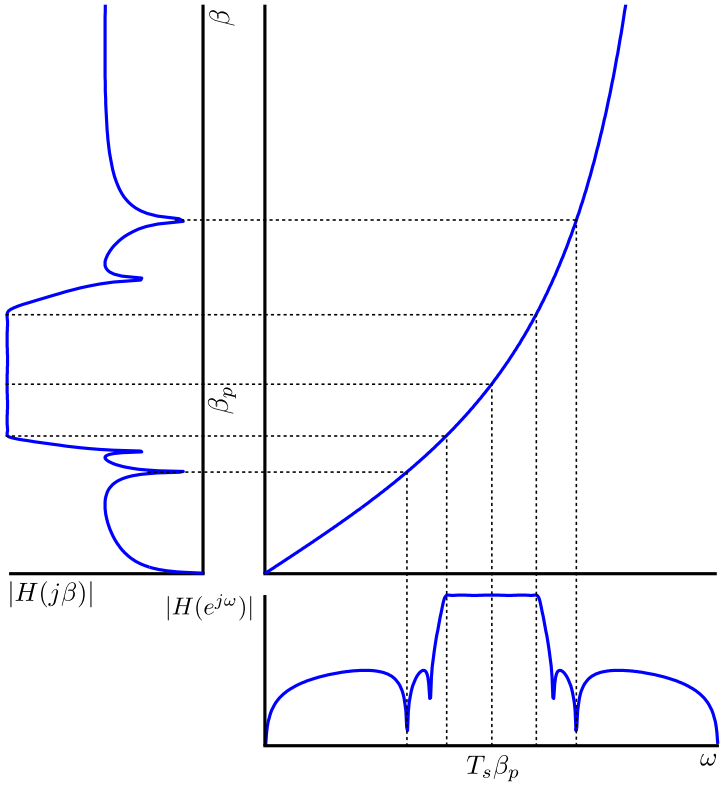

Figure 2.7: Representation of the effects of the bilinear transformation in the relationship between analog and digital frequency.

where the pre-warping frequency is noted as β_p and the inverse bilinear transformation can be expressed as:

$$s = \frac{\beta_p}{\tan\left(\frac{T_s}{2}\beta_p\right)} \cdot \frac{z-1}{z+1}. \tag{2.52}$$

After the modification a new relationship between the digital and analog frequencies is obtained

$$\beta = \frac{\beta_p}{\tan\left(\frac{T_s}{2}\beta_p\right)} \cdot \tan\left(\frac{\omega}{2}\right). \tag{2.53}$$

Using the pre-warped implementation of the transformation, the magnitude of the analog and digital responses are made equal for the pre-warping frequency. Then, only this exact frequency, β_p, matches linearly with its corresponding digital frequency,

$T_s\beta_p$. Moreover, a frequency compression occurs in the analog domain up to the pre-warping frequency, while from this frequency on, an expansion effect appears. The mentioned consequences are clearly represented in Figure 2.7.

2.1.2.3. Matched-z-transformation

The matched-z-transformation method is similar to a modified version of the invariant-impulse-response method [4]. The basic idea is to map the zeros in a similar fashion than the poles in the impulse invariant method. Thus, for an analog transfer function that can be expressed as follows:

$$H(s) = H_0 \frac{\prod_{i=1}^{M}(s - c_i)}{\prod_{i=1}^{N}(s - p_i)} \tag{2.54a}$$

the digital transfer function is obtained as:

$$H(z) = H_0' (z+1)^{L_a} \frac{\prod_{i=1}^{M}\left(z - e^{c_i T_s}\right)}{\prod_{i=1}^{N}\left(z - e^{p_i T_s}\right)} \tag{2.54b}$$

where L_a is an integer number that counts the amount of zeros of the analog starting transfer function, (2.54a), located in $|s| = \infty$.

It is important to highlight that this method does not control the level of the magnitude during the transformation from the analog to the digital realm. A constant H_0' has been added in order to cope with this inconvenience. Obviously, the calculus of the constant should be done in two steps. In first place, the maximum value of the digital frequency response, $M_{\max}$, should be found, i.e., the maximum of $H(z)/H_0'$ using (2.54b). In the second step the H_0' constant is calculated as $H_0' = H_0/M_{\max}$.

The matched-z-transformation method produces good results when the sampling frequency is much higher than the Nyquist frequency. However, the main drawback is the qualitatively high error that arises in the insertion losses of the passband, as it is explained in [4].

2.1.3. Digital filter design techniques

Many books are specifically devoted to the topic of this subsection [4, 5]. The aim of this part is to give a brief introduction and, above all, to show the maturity of the

design techniques of digital filters. Besides, the promising perspectives of future developments make this study extremely attractive.

The design techniques of digital filters are sorted in two main groups: IIR and FIR. The names arise directly from the characteristic impulse response of the produced filters: if its duration extends to infinity, IIR (Infinite Impulse Response), and if its duration is finite, FIR (Finite Impulse Response).

A recurrence equation (known also as difference equation) characterizes a discrete system in the same way as a differential equation does with an analog one. Thus, a digital system can be characterized by the recurrence equation and the transfer function [4]. Indeed, they are interrelated by the already defined z-transform, see (2.39), and written as

$$y[n] - \sum_{k=1}^{N} a_k y[n-k] = \sum_{k=0}^{M} b_k x[n-k] \tag{2.55a}$$

$$H(z) = \frac{Y(z)}{X(z)} = \frac{\sum_{k=0}^{M} b_k z^{-k}}{1 - \sum_{k=1}^{N} a_k z^{-k}} \tag{2.55b}$$

where M and N are natural numbers, $x[n]$ is the input sequence, and $y[n]$ is the output sequence with z-transforms $Y(z)$ and $X(z)$, respectively.

Analyzing carefully (2.55a) it can be seen that the output of the system depends on the current input sample, the previous input samples, and the previous output samples. Therefore, in general, the system is recursive what means that the output is infinitely long, as well as the impulse response (IIR). However, if $a_k = 0$ for $k = 1, 2, \ldots, N$ the expressions in (2.55) are simplified to:

$$y[n] = \sum_{k=0}^{M} b_k x[n-k] \tag{2.56a}$$

$$H(z) = \frac{Y(z)}{X(z)} = \sum_{k=0}^{M} b_k z^{-k} \tag{2.56b}$$

where the output of the system depends only on the current input sample and the previous input samples. Hence, the resulting system is not recursive. For this case, little mathematical modifications of equation (2.56a) are enough to prove that the impulse response is a finite sequence of length $M+1$, where M is the order of the filter:

$$y[n] = \sum_{k=0}^{M} b_k x[n-k] = x[n] * \sum_{k=0}^{M} b_k \delta[n-k] = x[n] * h[n]. \tag{2.57}$$

Once the notation and the nomenclature have been clarified, different design techniques of digital filters will be explored.

The first strategy to design digital filters relied into the well-known analog filter functions. It consists in transforming the classical analog filters, such as Butterworth, Chebyshev, Bessel or elliptic designs, into the digital domain. In fact, this is the reason why the analog-to-digital transformation methods described in Section 2.1.2 were developed [17]. Our goal is using the reverted form of this transformations to transform a digital filter into an analog response that satisfies the prescribed specifications. If the digital filter is obtained by this method, it already comes from an analog filter, so we would just revert the effect of the design method to get back to the very first and well-known solution. For this reason, this design method is of no interest for us, but digital-to-analog transformations will be used over pure digital design techniques.

Windowing techniques are in the middle between classical analog techniques and optimization methods. The procedures to find new windows are complex and need optimization tools as well as solid theoretical background. Nevertheless, the use of the ones already developed will need neither demanding computational cost nor deep theoretical background.

Finally, iterative techniques based on well-thought optimization strategies can be used for the design of digital filters. In other words, the issue of digital filter design can be treated as an approximation problem of the desired function. The difference between the desired and approximated functions is accounted by a particular error function which will be reduced iteratively to meet the given tolerances. Depending on the exact error function definition different optimization, or eventually minimization, algorithms will come up. The most extended criteria are:

a) Minimax. Under this criterion the maximum value of the error function is minimized:

$$E_{\text{minimax}} = \max_{\omega \in X} \left| W(\omega) \left[\left| H\left(e^{j\omega}\right) \right| - D\left(\omega\right) \right] \right| \tag{2.58a}$$

where particularly:

$$D(\omega) = \begin{cases} D_p(\omega) & \text{for} \quad \omega \in X_p \\ 0 & \text{for} \quad \omega \in X_s \end{cases} \tag{2.58b}$$

and

$$W(\omega) = \begin{cases} W_p(\omega) & \text{for} \quad \omega \in X_p \\ W_s(\omega) & \text{for} \quad \omega \in X_s \end{cases} \tag{2.58c}$$

being $D(\omega)$ the desired target function and $W(\omega)$ the weighting function. Subscripts p and s stand for passbands and stopbands, respectively. $X = X_p \cup X_s$

contains all the frequency bands of interest with the same meaning for both subscripts.

b) Least Squares. Although better known as a method of fitting data, this criterion is also applied in the optimization methods for the design of digital filters. The error function that needs to be minimized is defined as follows:

$$E_{\text{LeastSquares}} = \int_X \left(W(\omega)\left[\left|H\left(e^{j\omega}\right)\right| - D(\omega)\right]\right)^2 d\omega \tag{2.59}$$

c) p-Norm. This is a generalized version of the least squares criterion. Thus, the error function to be minimized corresponds to the following expression:

$$E_{p-\text{Norm}} = \int_X \left(W(\omega)\left[\left|H\left(e^{j\omega}\right)\right| - D(\omega)\right]\right)^p d\omega \tag{2.60}$$

where p is an integer number. Note that if $p = 2$, we get to the same error definition as in the least squares case. Moreover, it can be demonstrated that when $p \to \infty$, this criterion becomes equivalent to the aforementioned minimax rule [4].

2.1.3.1. IIR filters

Several techniques for the design of IIR filters are available in [4], [18], and [19], among others. The details of the methods are out of the scope of this thesis. Hence, only the names of the most relevant algorithms along with references to address the details are given here.

The Newton's method is an iterative procedure to find a minimum in a quadratic and convex function [4]. The so-called methods of quasi-Newton's type constitute more efficient implementations to find a minimum in this class of functions. These iterative procedures can be utilized in order to design IIR filters [19].

When the IIR design needs to be performed in a minimax sense, the most popular automatic procedure is the so-called least-p^{th} algorithm [19]. The p-norm minimization process is applied in a recursive manner, increasing in each step the value of p, usually following the series of the powers of 2.

If only magnitude requirements are involved in the specification, a particularly efficient computational procedure can be implemented. It is called Remez algorithm, [4, 18], and so obtained filters present and error function optimized in a minimax sense.

The last alternative presented here is the Yule-Walker method [19, 20]. The technique is of special interest because of a least squares algorithm that is applied in the time domain. This gives more flexibility in the design of IIR filters.

2.1.3.2. FIR filters

Two completely different strategies will be followed in order to design FIR filters. The first leads to a variety of impulse responses employing windowing techniques. The second provides iterative techniques without more limits than the computational cost of deriving the target function. The most important optimization algorithms will be surveyed to finish this part.

The windowing techniques are the most direct, simple and fast methods to attain FIR filters. Although they are equivalent to the direct windowing in the analog domain, [7], recent developments in the digital domain provide better performances [21]. Therefore, the ideal impulse response of the desired square-like[3] frequency response is computed through the discrete inverse Fourier transform. The sequence is truncated and smoothed down by a suitable window. Finally a linear phase term is added in order to satisfy the causality principle. The explained process is illustrated in Figure 2.8. Many types of windows already exist in a continually developing topic carried out by the signal processing community. All of them will be able to be utilized in order to satisfy the target specifications [4].

Different iterative methods for the design of FIR filters are available in the vast scientific literature [4, 5].

The most efficient algorithm to design optimum FIR filters is the well-known Remez algorithm. The Parks-McClellan implementation is also extensively used [4]. It can be applied to a broad collection of filters such as: low-pass, high-pass, band-pass, stop-band, multiband filters, Hilbert transformer, differentiators, and etcetera. The optimization is done in the minimax sense. As a result, the accomplished responses will be equi-ripple responses.

There exist cases where additional restrictions should be included in the frequency response or, directly, over the impulse response. Those cases are troublesome and exclude the usage of the Remez algorithm. However, after several mathematical treatments the linear programming techniques, [22], give good results.

In order to find FIR filters without equi-ripple frequency responses the least squares algorithm can be computed. A typical characteristic of this design is that the errors close to the transition bands are much more severe than in the middle of the pass- or reject-bands.

The design of digital filters is a widespread issue. As a consequence many specific

[3] Square-like word takes a broad meaning here. It means that there are non-differentiable points in the frequency response. The definition includes the conventional square functions but is not only restricted to them.

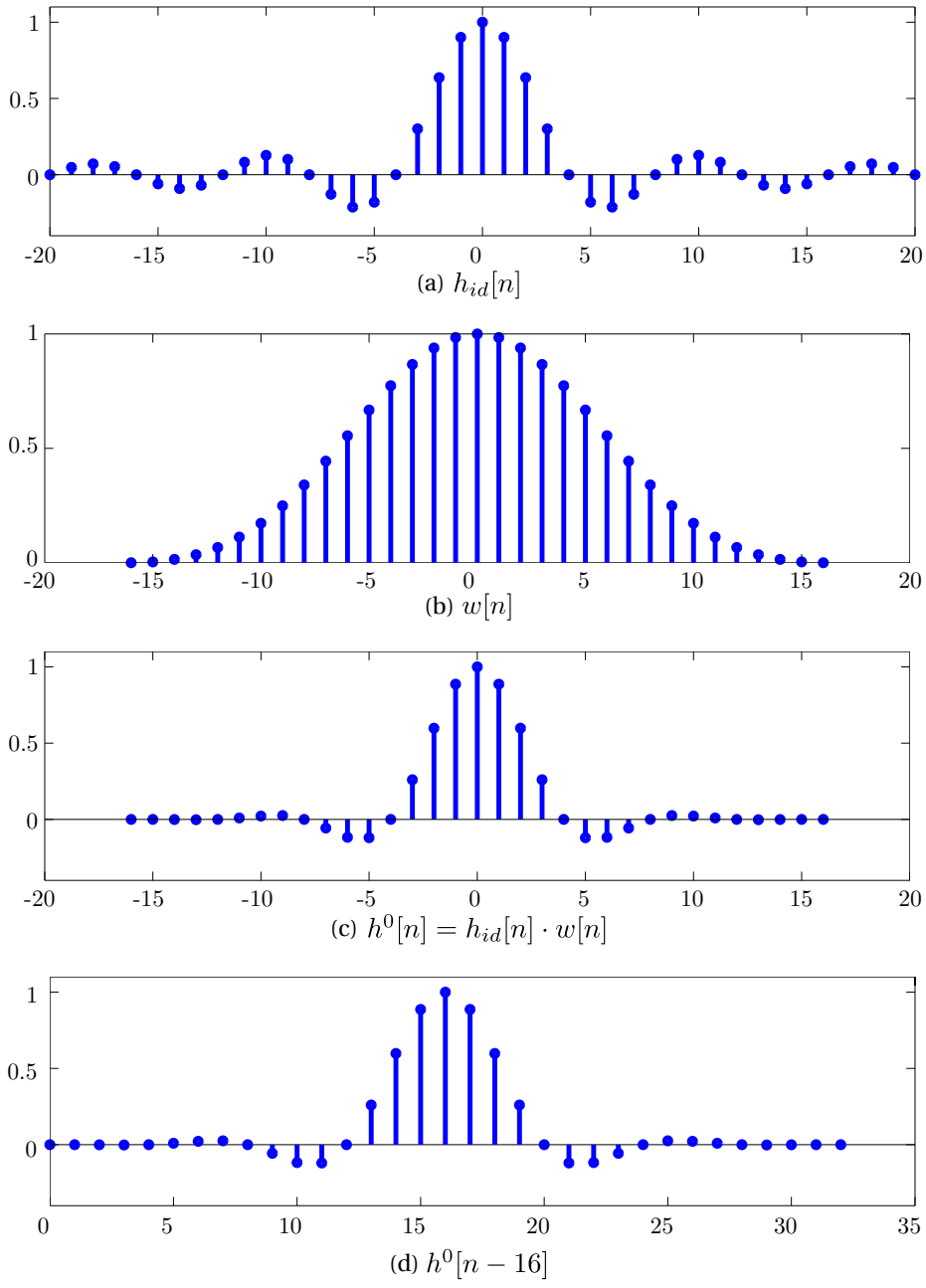

Figure 2.8: Windowing process: (a) Impulse response of an ideal low-pass filter. (b) Blackman window of length 33. (c) Result of the product between the ideal impulse response and the window. (d) Resulting causal impulse response.

problems have been already stated or even solved. Of particular interest is the problem of designing a family of impulse responses that satisfy orthogonal relationships between the members of the family while at the same time they fulfill specifications in their frequency response. This problem, was also studied for the analog functions [23], and has been fruitfully solved in the digital domain with many more degrees of freedom [24, 25].

2.1.4. Design of a multiband filter

In order to prove the validity of the proposed method [6], the design of a multiband filter has been accomplished. An analog response that satisfies the given specifications will be obtained using digital filter design methods as it has been previously described. The response will be later implemented as a stepped-impedance filter in microstrip technology deriving the associated ladder network of lumped elements.

2.1.4.1. Analog response

Analog specifications for a multiband filter with two passbands and two stopbands are chosen. Detailed specifications are given in Table 2.1.

Following the design scheme in Figure 2.3, analog specifications are first converted into digital specifications which have been included in Table 2.1. The selected transformation method has been the bilinear transformation, defined in (2.51). The sampling frequency is selected to be $f_s = 2f_{\max} = 2 \cdot 7 = 14$ GHz while the prewarping frequency, β_p, is chosen to match with $f_p = 2.4$ GHz to make the digital specifications more relaxed at the first stopband.

The digital filter design has been carried out using an iterative quasi-Newton type algorithm, implemented in the function `iirlpnorm.m` available in MATLAB [19]. This algorithm minimizes the error function defined as the p-norm of the weighted difference between the target filter frequency response and the designed one. The value

TABLE 2.1
ANALOG SPECIFICATIONS WITH THE CORRESPONDING DIGITAL SPECIFICATIONS FOR A MULTIBAND FILTER.

Passbands	DC to 0.8 GHz	Return loss > 15 dB	0 to 0.13π rad/s
	4 to 5.5 GHz		0.51π to 0.61π rad/s
Stopbands	2 to 3 GHz	Rejection > 10 dB	0.3π to 0.41π rad/s
	7 to 9 GHz	Rejection > 40 dB	0.67π to 0.74π rad/s

of p is increased from 2 to 128 iteratively by default, so that the final error function approaches the minimax error function.

Due to the restrictions imposed by the microwave implementation that it is aimed to use, the designed analog filter should be an all-pole filter. To satisfy this condition in the analog domain, we can take advantage of the mapping properties of the bilinear transformation. An interesting property is that a digital pole in $z = -1$ is mapped to $s \to \infty$. Thus, any digital zero introduced at this point will be mapped to infinity when transforming it to the analog domain. In our case, all the analog zeros should be at infinity, so we can set all the zeros of the digital filter to be $k_i = -1$ for $i = 1, \ldots, N$ being N the order of the filter. Their contribution to the overall filter will be of the form [14]:

$$H_{\text{zeros}}\left(z = e^{j\omega}\right) = \left(1 + e^{-j\omega}\right)^N . \tag{2.61}$$

The contribution of the manually introduced zeros has to be complemented with the contribution of the poles in order to satisfy the target digital specifications. Hence, the desired frequency response, H_{desired}, to be fulfilled with the contribution of the poles, needs to be be calculated by subtracting from the target specifications the contribution of the zeros, that is:

$$H_{\text{desired}}\left(z = e^{j\omega}\right) = \frac{H_{\text{target}}\left(z = e^{j\omega}\right)}{H_{\text{zeros}}\left(z = e^{j\omega}\right)} \tag{2.62}$$

being $H_{\text{target}}\left(z = e^{j\omega}\right)$ the target digital specifications. The algorithm will be used to find the position of the poles that approximates better this desired response. Thus, the input parameter of the function to define the numerator order is set to be 0, while the denominator order is chosen to be $N = 11$.

Finally, a weighting vector can be selected to define the weight of the error at a frequency point in the overall error function. For this specifications, the weighting vector is adjusted to be $W = [75000\,85000\,1500\,1500\,80000\,75000\,1\,1]$, each value corresponding to the edges of the specified frequency bands defined by the vector of normalized frequencies $F = [0\,0.13\,0.3\,0.41\,0.51\,0.61\,0.67\,0.74]$. As a result the poles and zeros of the digital filter are obtained which have been listed in Table 2.2 and depicted in Figure 2.9(a).

The frequency response of the resulting filter is calculated evaluating the contribution of each digital pole, p_i, and digital zero, k_i, following [14]:

$$20\log\left|H(z = e^{j\omega})\right| = 20\log(H_0) + \sum_{i=1}^{N} 20\log|1 - k_i e^{-j\omega}| - \sum_{i=1}^{N} 20\log|1 - p_i e^{-j\omega}| \tag{2.63}$$

and the result is depicted in Figure 2.10 together with the digital specifications.

TABLE 2.2
POLES AND ZEROS OF THE FILTER IN THE DIGITAL AND ANALOG DOMAINS.

p_i	k_i	p_n	k_n
0.6776	11 x -1	-24.81	No finite zeros
$0.7074 \pm 0.3772j$		$-15.08 \pm 31.85j$	
$0.0068 \pm 0.9094j$		$-12.14 \pm 127.57j$	
$-0.3299 \pm 0.9189j$		$-4.67 \pm 183.43j$	
$-0.2640 \pm 0.8918j$		$-13.04 \pm 172.23j$	
$-0.1501 \pm 0.8781j$		$-17.85 \pm 151.82j$	

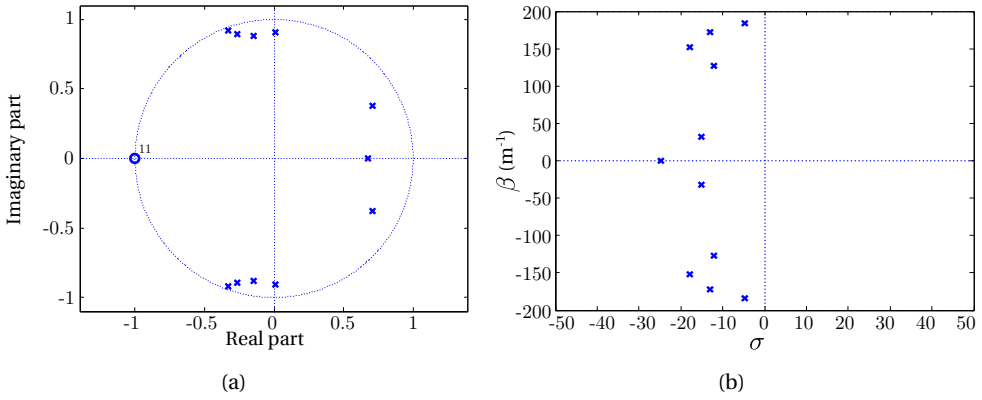

Figure 2.9: (a) Poles ('x') and zeros ('o') of the designed digital filter and (b) poles ('x') of the analog filter after the bilinear transformation.

The application of the bilinear transformation in the inverse direction, as defined in (2.52), to each pole and zero of the digital filter results in the poles and zeros of the analog response. While the zeros are mapped to infinity, the resulting poles are listed in Table 2.2 and also plotted in Figure 2.9(b). As it was done for the digital filter, the analytical frequency response, $S_{21}(f)$, of the microwave filter is obtained as the sum of the contributions of each analog pole, p_n, and analog zero, k_n, using [4]

$$20\log|H(s=j\beta)| = 20\log(H_0) + \sum_{n=1}^{N} 20\log|j\beta - k_n| - \sum_{n=1}^{N} 20\log|j\beta - p_n| \qquad (2.64)$$

being β univocally related with the frequency, f, by

$$\beta = \frac{2\pi f\sqrt{\varepsilon_e}}{c} \qquad (2.65)$$

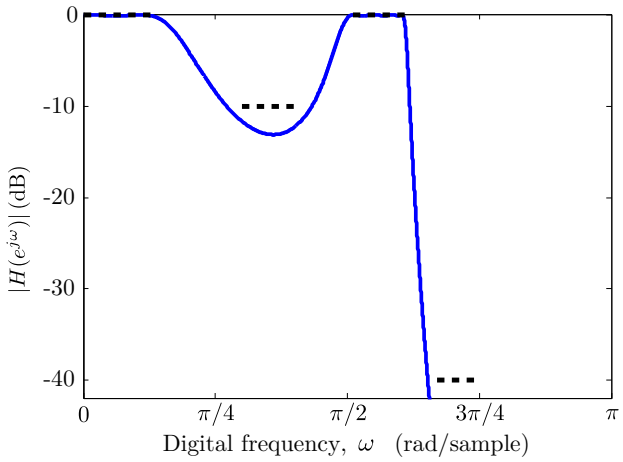

Figure 2.10: Frequency response of the digital filter (continuous blue line) together with the digital specifications (dashed black line).

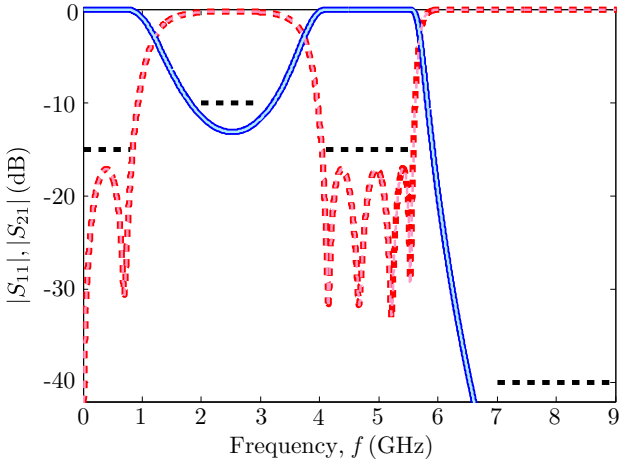

Figure 2.11: Analog specification (horizontal dashed black lines) together with the simulated $|S_{21}|$ (blue line) and $|S_{11}|$ (red line) parameters of the analytical analog filter (thick dark line) and the lumped-element ladder network (thin light line).

with ε_e is the effective permittivity of a microstrip line in the selected substrate, in our case CUCLAD-250 LX substrate ($\varepsilon_r = 2.43$, dielectric thickness $h = 0.49$ mm). Only the contribution of the poles will remain for this example, since the design has no finite zeros. The result is depicted in Figure 2.11 with the target analog specifications which are properly satisfied. Its corresponding $S_{11}(f)$ is also shown in the figure. From these data, different classical implementation procedures may be followed [26].

2.1.4.2. Microwave implementation

The microwave filter will be implemented as a stepped-impedance filter in microstrip technology after deriving the associated ladder network of lumped elements. The restrictions of this implementation technique were considered while deriving the required all-pole filter response by digital filer design techniques. However, it is important to stress that other technologies (even non-planar) and/or implementation schemes could be used [26].

The ladder network of lumped elements that implements the frequency response, $S_{21}(s)$, is shown in Figure 2.12. The values of the elements L_i, C_j can be easily obtained using the classical continuous fraction expansion method as explained in [27]. The capacitance and inductance values for our example are given in Table 2.3. The frequency response of this lumped-element network has been simulated using Agilent™ ADS and it is shown in Figure 2.11. As it can be seen, it matches perfectly with the desired analytical analog response.

TABLE 2.3
CAPACITANCE AND INDUCTANCE VALUES FOR THE LADDER NETWORK OF LUMPED ELEMENTS.

C_j (pF)	$C_1 = 1.45$	$C_3 = 2.39$	$C_5 = 0.69$	$C_7 = 0.71$	$C_9 = 2.28$	$C_{11} = 1.3$
L_i (nH)	$L_2 = 1.08$	$L_4 = 2.43$	$L_6 = 6.42$	$L_8 = 2.38$	$L_{10} = 1.15$	

The stepped-impedance technique allows us to implement the lumped-element ladder network in microstrip as a transmission line alternating high impedance (Z_{high}) and low impedance (Z_{low}) sections. The following design equations provide the required section lengths, l, in meters [26]:

$$l_{i,high} = \frac{v_p L_i}{Z_{high}} \quad ; \quad l_{j,low} = v_p C_j Z_{low} \tag{2.66}$$

where v_p is the phase velocity in the microstrip line. The discontinuities between the high- and low-impedance sections produce some fringing capacitances [26], whose parasitic effect can be compensated by means of a simple final optimization process

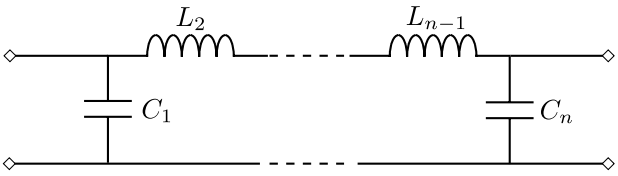

Figure 2.12: Ladder network of lumped elements.

TABLE 2.4
FINAL LENGTHS OF THE IMPLEMENTED HIGH- AND LOW-IMPEDANCE SECTIONS.

$l_{j,low}$ (mm)	$l_1 = 1.884$	$l_3 = 3.591$	$l_5 = 0.628$	$l_7 = 0.640$	$l_9 = 3.376$	$l_{11} = 1.626$
$l_{i,high}$ (mm)	$l_2 = 2.026$	$l_4 = 2.040$	$l_6 = 6.835$	$l_8 = 1.975$	$l_{10} = 2.201$	

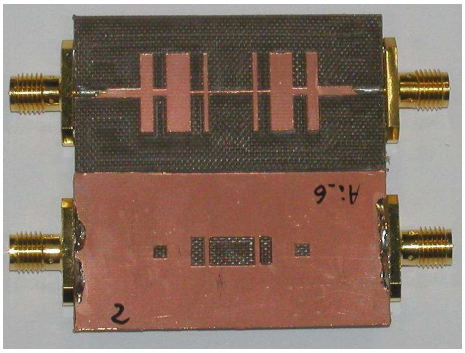

Figure 2.13: Photograph of the fabricated prototype.

in the section lengths.

The lumped-element ladder network is implemented using a CUCLAD-250 LX substrate ($\varepsilon_r = 2.43$, dielectric thickness $h = 0.49$ mm) with $50\ \Omega$ input and output ports. The low impedance sections are realized using a strip-width $W_{\max} = 12$ mm ($Z_{low} = 8.92\ \Omega$, $\varepsilon_{\text{eff}} = 2.32$). In order to ease the manufacturing process, the high impedance sections are implemented using two different width values and slots etched in the ground plane [28]: strip-width $W_{\min} = 2$ mm and slot width $S = 2$ mm ($Z_{high} = 97.02\ \Omega$, $\varepsilon_{\text{eff}} = 1.58$) for the first and the last section, and $W_{\min} = 0.2\,\text{mm}$ and $S = 4.5\,\text{mm}$ ($Z_{high} = 208.71\ \Omega$, $\varepsilon_{\text{eff}} = 1.43$) for the remaining sections. The required section lengths are calculated using (2.66) and optimized afterwards to compensate the effect of the mentioned fringing capacitances, to achieve the final lengths given in Table 2.4.

The microstrip filter has been fabricated using a numerical milling machine. A photograph of the fabricated prototype is shown in Figure 2.13. Its S_{11} and S_{21} parameters have been measured by means of an Agilent™ 8722ES Vector Network Analyzer and are depicted in Figure 2.14 together with the target analog response. A very good agreement is obtained between the target response and the measurements, confirming the very good performance of the proposed technique.

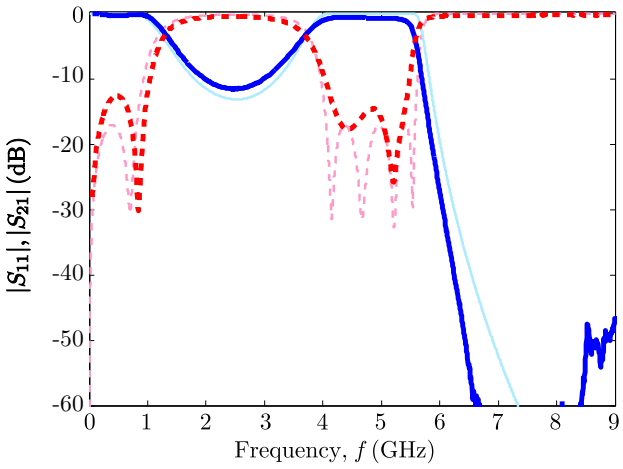

Figure 2.14: $|S_{21}|$ (continuous blue line) and $|S_{11}|$ (dashed red line) for the target analog response (thin light line) and for the measured microstrip filter (thick dark line).

2.2. Synthesis method using pole and zero decomposition (P&Z)

The main goal of Chapter 2 consists in improving the microwave filter design techniques to gain more flexibility. In the previous section a new method to obtain analog functions using digital filter design techniques has been presented. To take advantage of the flexibility provided by this solution, it is necessary to develop new synthesis techniques that can implement a physical device with the desired performance. In this section, such a technique will be presented which is valid for analog rational functions [29].

The scheme in Figure 2.15 describes the general synthesis procedure of the presented method. Starting from the target analog response, a coupling coefficient, $K(z)$, is obtained. This function relates the amount of energy that is transferred from a propagating mode to the same but counter propagating mode along a device. Afterwards, the coupling coefficient is implemented into a physical device using the selected technology which can be planar or non-planar.

As it can be seen in Figure 2.15, the coupled-mode theory is very important in the procedure. This theory connects in one side the coupling coefficient with the physical dimensions of the device, while in the other side, links the coupling coefficient to the target response. The cross-section method is used to formulate an accurate coupled-mode theory in the first subsection. Moreover, the step that takes us from

a given target response to the coupling coefficient, referred as the inverse scattering problem, can be solved by a new synthesis method that is introduced in the second subsection. Lastly, the validity of the method is demonstrated through the design and implementation of a multiband filter.

2.2.1. Coupled-mode theory in microwaves

2.2.1.1. General theory

In order to formulate an accurate coupled-mode theory suitable for microwave devices, the cross-section method will be employed. The basic idea of this method is that the electromagnetic fields at any cross-section of a nonuniform waveguide can be represented as a superposition of the different orthogonal modes (including their forward and backward traveling waves) corresponding to a uniform auxiliary waveguide that has the same cross-section with identical distribution of ε and μ [30, 31]. Steady-state sinusoidal time dependence of the fields will be assumed and their phasor representation in the frequency domain will be used. As it is well-known, this does not imply any restriction due to the possibility of expanding any signal as a sum of sinusoidals by the Fourier expansion. The classical discrete spectrum modes and the continuous spectrum modes must be considered to have a complete orthogonal system in general open waveguides [32–34]:

$$\hat{\vec{E}}(x,y,z) = \sum_i a_i(z)\,\vec{E}^i(x,y,z) + \sum_i \int_0^\infty a_i^c(k_t,z)\,\vec{E}^i(x,y,k_t,z)dk_t \tag{2.67a}$$

$$\hat{\vec{H}}(x,y,z) = \sum_i a_i(z)\,\vec{H}^i(x,y,z) + \sum_i \int_0^\infty a_i^c(k_t,z)\,\vec{H}^i(x,y,k_t,z)dk_t \tag{2.67b}$$

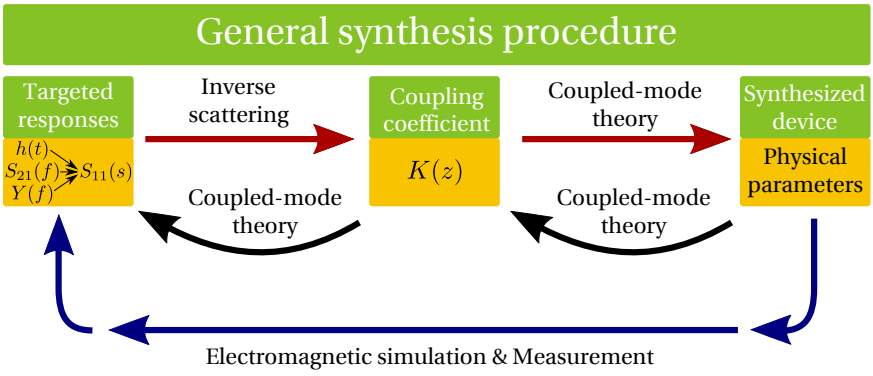

Figure 2.15: Diagram of the general synthesis procedure.

being $\hat{\vec{E}}$, $\hat{\vec{H}}$ the total electric and magnetic fields present in the structure; z the direction of propagation; $\vec{E}^i$, $\vec{H}^i$ the vector mode patterns (i.e. the (x, y) dependent parts of the electric and magnetic fields) of the i mode of the auxiliary uniform waveguide associated with the cross-section of interest. Besides, it is important to stress that the vector mode patterns depend on z, due to the variation of the cross-section (and hence the auxiliary uniform waveguide) along the z-axis. Finally, $a_i(z)$ is the complex amplitude of the i discrete spectrum mode and a_i^c is the complex amplitude of the i continuous spectrum mode along the nonuniform waveguide. It is interesting to note that unlike for the well-known discrete spectrum modes, the vector mode pattern of continuous spectrum modes depends also on the continuous variable k_t and their field contribution is always expressed as an integral in that variable k_t [32–34].

By substituting the expansion of the fields in terms of modes, see (2.67), into the Maxwell equations, and performing some mathematical manipulations, the so-called coupled-mode equations can be obtained [30–34]:

$$\frac{da_m}{dz} + j\beta_m a_m = \sum_i a_i\, C_{mi} + \sum_i \int_0^\infty a_i^c(k_t)\, C_{mi}^c(k_t) dk_t \tag{2.68a}$$

$$\frac{da_n^c(\widetilde{k}_t)}{dz} + j\beta_n^c(\widetilde{k}_t) a_n^c(\widetilde{k}_t) = \sum_i a_i\, C_{ni}^c(\widetilde{k}_t) + \sum_i \int_0^\infty a_i^{cc}(k_t)\, C_{ni}^{cc}(\widetilde{k}_t) dk_t \tag{2.68b}$$

where β_m and β_n^c are the phase constants of the m mode and the n mode, respectively, in the auxiliary uniform waveguide associated with the cross-section of interest (it might vary with z) and C_{mi} and C_{mi}^c are the coupling coefficients between the m and i modes while C_{ni}^c and C_{ni}^{cc} are between the n and i modes. Equation (2.68a) is valid for any m, i.e., for any mode of the discrete spectrum, and (2.68b) is valid for any n and $\widetilde{k}_t$, i.e., for any mode of the continuous spectrum. As it can be seen, the complex amplitudes of the modes, $a_m, a_n^c(\widetilde{k}_t)$, satisfy a set of first order linear ordinary differential equations, that turn into integro-differential equations for open waveguides. There exists one of the proposed equations for each mode. The modes, during propagation along the nonuniform waveguide, transfer power to each other as indicated by the coupled-mode equations. The coupling coefficients, C_{mi}, C_{mi}^c, C_{ni}^c, and C_{ni}^{cc}, relate the contribution of each mode amplitude in comparison with the variation of amplitude for another modes. The exact expressions to calculate the coupling coefficients depend on the kind of perturbation introduced in the nonuniform waveguide [30, 31]. For the case of nonuniform waveguides that include conductors with variable cross-section, which is of wide interest in microwave technologies, the coupling coefficients

can be calculated without any approximation as [32]:

$$C_{mi} = \frac{-1}{2N_m} \iint_{\breve{S}} \left(\vec{E}^m \times \frac{\partial \vec{H}^i}{\partial z} + \frac{\partial \vec{H}^m}{\partial z} \times \vec{E}^i \right) \hat{z}\, d\breve{S} - (\delta_{im} + \delta_{i,-m}) \frac{1}{2N_m} \cdot \frac{dN_i}{dz} \tag{2.69a}$$

$$C^c_{mi}(k_t) = \frac{-1}{2N_m} \iint_{\breve{S}} \left(\vec{E}^m \times \frac{\partial \vec{H}^i(k_t)}{\partial z} + \frac{\partial \vec{H}^m}{\partial z} \times \vec{E}^i(k_t) \right) \hat{z}\, d\breve{S} - (\delta_{im} + \delta_{i,-m}) \frac{1}{2N_m} \cdot \frac{dN_i(k_t)}{dz} \tag{2.69b}$$

$$C^c_{ni}(\widetilde{k}_t) = \frac{-1}{2N^c_n(\widetilde{k}_t)} \iint_{\breve{S}} \left(\vec{E}^n(\widetilde{k}_t) \times \frac{\partial \vec{H}^i}{\partial z} + \frac{\partial \vec{H}^n(\widetilde{k}_t)}{\partial z} \times \vec{E}^i \right) \hat{z}\, d\breve{S} - (\delta_{in} + \delta_{i,-n}) \frac{1}{2N^c_n(\widetilde{k}_t)} \cdot \frac{dN_i}{dz} \tag{2.69c}$$

$$C^{cc}_{ni}(\widetilde{k}_t, k_t) = \frac{-1}{2N^c_n(\widetilde{k}_t)} \iint_{\breve{S}} \left(\vec{E}^n(\widetilde{k}_t) \times \frac{\partial \vec{H}^i(k_t)}{\partial z} + \frac{\partial \vec{H}^n(\widetilde{k}_t)}{\partial z} \times \vec{E}^i(k_t) \right) \hat{z}\, d\breve{S} - (\delta_{in} + \delta_{i,-n}) \frac{1}{2N^c_n(\widetilde{k}_t)} \cdot \frac{dN^c_i(k_t)}{dz} \cdot \delta(k_t - \widetilde{k}_t) \tag{2.69d}$$

where $\breve{S}$ is the surface of the cross section except the conductors and the contour of intersection between the conductor-dielectric interfaces and the cross section, $\hat{z}$ is the unit vector in the z (propagation) direction, δ_{im} and δ_{in} are the Kronecker deltas, and N_i and N^c_i are the normalization factors of the i mode, defined as:

$$N_i = \iint_{\breve{S}} \left(\vec{E}^i \times \vec{H}^i \right) \hat{z}\, d\breve{S} \tag{2.70a}$$

$$N^c_i(k_t)\, \delta(k_t - \widetilde{k}_t) = \iint_{\breve{S}} \left(\vec{E}^i(k_t) \times \vec{H}^i(\widetilde{k}_t) \right) \hat{z}\, d\breve{S} \tag{2.70b}$$

It is assumed that the forward $(+)$ and backward $(-)$ traveling waves associated with the same i mode satisfy the following conditions [32]:

$$N_i = -N_{-i} \tag{2.71a}$$

$$N^c_i(k_t) = -N^c_{-i}(k_t) \tag{2.71b}$$

$$\beta_i = -\beta_{-i} \tag{2.71c}$$

$$\beta^c_i(\widetilde{k}_t) = -\beta^c_{-i}(\widetilde{k}_t) \tag{2.71d}$$

The (x, y) dependent parts of the fields of the forward and backward travelling waves associated with the i mode are chosen following [31] and result in:

$$E^{-i}_x = E^i_x \quad ; \quad E^{-i}_y = E^i_y \quad ; \quad E^{-i}_z = -E^i_z \tag{2.72a}$$

$$H_x^{-i} = -H_x^i \quad ; \quad H_y^{-i} = -H_y^i \quad ; \quad H_z^{-i} = H_z^i \tag{2.72b}$$

For the case of nonabsorbing waveguides (i.e. waveguides without dissipative losses) and propagating modes (i.e. real propagation constant), it is always possible to choose the vector mode patterns, $\vec{E}^i$ and $\vec{H}^i$, in such a way that the components in the transverse directions, E_x^i, E_y^i, H_x^i, and H_y^i, are real, and the components in the longitudinal direction, E_z^i and H_z^i, are imaginary. Thus, it is straightforward to demonstrate that, by using this convention, the coupling coefficient between the propagating modes will be always real. This assumption will be used through this thesis, because the total average power carried (in the increasing z direction) by the propagating modes will be easily calculated. The total average power can be found as the total time-averaged Poynting vector integrated over the cross-section:

$$P_{tot} = \frac{1}{2} \cdot \mathfrak{Re} \left(\iint_{\breve{S}} \hat{\vec{E}} \times \hat{\vec{H}}^* \right) \hat{z} \, d\breve{S}. \tag{2.73}$$

Taking into account the expansion of $\hat{\vec{E}}$ and $\hat{\vec{H}}$ as in equations (2.67), the choice of real transverse components of the field, the orthogonality, and normalization conditions, the total power simply results in:

$$P_{tot} = \sum_{i=-M}^{M} \frac{1}{2} |a_i|^2 N_i + \sum_{i=-Q}^{Q} \int_0^{k_0} \frac{1}{2} |a_i(k_t)|^2 N_i(k_t) dk_t = \sum_{i=-M}^{M} P_i + P_{rad} \tag{2.74}$$

where the summations are performed for all the propagation modes, including M discrete spectrum modes (or bounded modes) and Q continuous spectrum modes, with both signs. In order to calculate the power flow, the integral is performed over the range of $0 < k_t < k_0$, which accounts for the range corresponding to the propagating or radiative modes. The range of $k_0 < k_t < \infty$ is not included in the calculation, because it corresponds to the attenuating or evanescent modes, which do not propagate power.

Thus, the total power carried by the waveguide (in the increasing z direction) is equal to the power in all the forward propagating modes, subtracting the power in all the backward propagating modes (since the latter will have a normalization factor with negative sign, as it can be seen in (2.71a), and therefore the power carried by them will be negative, what physically means in the opposite sense).

Hence, the expression for the power carried by the i bound mode can be stated as:

$$P_i = \frac{1}{2} |a_i|^2 N_i \tag{2.75}$$

Although a single radiation mode is not physically meaningful, it constitutes a convenient block for mathematical description of the radiation. The total radiated power

can be obtained as a summation of individual radiation modes, which carry energy in parallel with the waveguide axis [32, 35]:

$$P_{rad} = \sum_{i=-Q}^{Q} \int_0^{k_0} \frac{1}{2} \left|a_i(k_t)\right|^2 N_i(k_t) dk_t. \tag{2.76}$$

Therefore, because of the interference between the fields of different radiation modes, the continuum of modes expressed by integral in (2.76) represents the expected behavior of the total radiation field, i.e., a flow of power away from the waveguide.

Equations (2.69) for the calculation of the coupling coefficients can be rewritten in a more simplified way. The detailed deductions are followed in [32], and lead to:

$$C_{mi} = \frac{-\pi f \oint \nu \left(\mu_0 H_z^i H_z^m - \mu_0 H_t^i H_t^m + \varepsilon E_n^i E_n^m\right) dt}{N_m(\beta_m - \beta_i)} \tag{2.77a}$$

$$C_{mi}^c(k_t) = \frac{-\pi f \oint \nu \left(\mu_0 H_z^i(k_t) H_z^m - \mu_0 H_t^i(k_t) H_t^m + \varepsilon E_n^i(k_t) E_n^m\right) dt}{N_m\left(\beta_m - \beta_i(k_t)\right)} \tag{2.77b}$$

$$C_{ni}^c\left(\widetilde{k}_t\right) = \frac{-\pi f \oint \nu \left(\mu_0 H_z^i H_z^n\left(\widetilde{k}_t\right) - \mu_0 H_t^i H_t^n\left(\widetilde{k}_t\right) + \varepsilon E_n^i E_n^n\left(\widetilde{k}_t\right)\right) dt}{N_n^c\left(\beta_n^c\left(\widetilde{k}_t\right) - \beta_i\right)} \tag{2.77c}$$

$$C_{ni}^{cc}\left(\widetilde{k}_t, k_t\right) = \frac{-\pi f \oint \nu \left(\mu_0 H_z^i(k_t) H_z^n\left(\widetilde{k}_t\right) - \mu_0 H_t^i(k_t) H_t^n\left(\widetilde{k}_t\right) + \varepsilon E_n^i(k_t) E_n^n\left(\widetilde{k}_t\right)\right) dt}{N_n^c\left(\beta_n^c\left(\widetilde{k}_t\right) - \beta_i^c(k_t)\right)} \tag{2.77d}$$

being f the frequency, $H_{z,t,n}^{i,m,n}$ and $E_{z,t,n}^{i,m,n}$ the magnetic and electric fields that belong to the uniform waveguide associated with the transverse cross-section, where z stands for the propagation direction, and subscript t (n) represents the tangential (normal) direction to the conducting contour in the cross-section. Indeed, the conducting contour of the cross-section is the path followed by the circular integrals that appear in equations (2.77). To remark the meaning of the coordinate system and the variables sketched in Figure 2.16, the following definitions will be established:

$\hat{z}$ is the unit vector of $\vec{z}$, which corresponds to the direction parallel to the propagation axis of the waveguide and the same sense as the forward waves.

$\hat{n}$ is the unit vector of $\vec{n}$, which corresponds to the direction contained in the transverse cross-section and perpendicular with the intersection between the conductor and the dielectric (normal direction). The sense points at the conductor.

$\hat{t}$ is the unit vector of $\vec{t}$, which corresponds to the direction contained in the transverse cross-section and tangential with the intersection between the conductor and

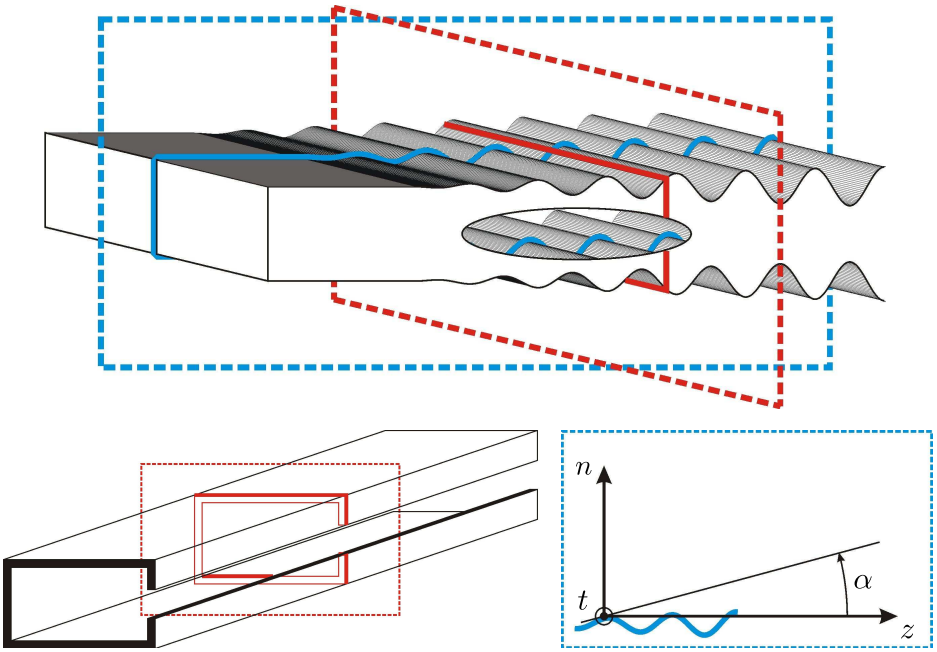

Figure 2.16: Scheme of a general nonuniform waveguide with detailed coordinate system.

the dielectric. The sense is chosen in order to achieve a right coordinate system, i.e.: $\hat{n} \times \hat{t} = \hat{z}$.

Superscripts i, m, and n represent the modes involved in the calculus, n for the continuous, m for the discrete spectrum, and i for both of them.

Moreover, N_i and N_i^c are the normalization factors, β_i and β_i^c the phase constants of the i mode and variable ν can be defined as:

$$\nu = \tan(\alpha) \tag{2.78}$$

being α, the angle between $\hat{z}$ and the tangent of the intersection between the conductor and the dielectric contained in the plane formed by $\hat{n}$ and $\hat{z}$. Obviously, $\hat{z}$ corresponds to $\alpha = 0^o$ and $\hat{n}$ with $\alpha = 90^o$, see Figure 2.16.

Finally, the coupling coefficients defined in (2.77) are valid for waveguides that include conductors with variable cross-section and satisfy the following properties [32]:

$$C_{mm} = \frac{-1}{2N_m} \cdot \frac{dN_m}{dz} \tag{2.79a}$$

$$C_{mm}^{cc}\left(\widetilde{k}_t, \widetilde{k}_t\right) = \frac{-1}{2N_m\left(\widetilde{k}_t\right)} \cdot \frac{dN_m\left(\widetilde{k}_t\right)}{dz} \cdot \delta(0) \tag{2.79b}$$

$$C_{mi}N_m = -C_{im}N_i \quad ; \quad m \neq i \tag{2.80a}$$

$$C_{mi} = -C_{-m,-i} \tag{2.80b}$$

Therefore, expressions (2.77) state a relationship between the coupling coefficients and the physical parameters. The relationship is implicit through the fields $H^{i,m,n}_{z,t,n}$ and $E^{i,m,n}_{z,t,n}$. These fields (which values vary with z) belong to the auxiliary infinite uniform waveguide with the same cross-section (therefore, different auxiliary infinite uniform waveguide has to be used for each z) and eventually will determine the physical dimensions of the cross-section for each z. Thereby, although the relationship between the coupling coefficients and the physical parameters is implicit in expressions (2.77), it is valid for many waveguide technologies and transmission line implementations. Furthermore, simplified expressions can be obtained for different technologies.

General coupled-mode theory is also used to link the target response of a device with its coupling coefficients. Taking into account the multimode decomposition, the two-port modal scattering matrix, which accounts for the S-parameters for each mode, can be defined as follows [36, 37]:

$$\begin{bmatrix} b_{11} \\ b_{12} \\ \dots \\ b_{1m} \\ \dots \\ b_{21} \\ b_{22} \\ \dots \\ b_{2m} \\ \dots \end{bmatrix} = \begin{bmatrix} S_{11,11} & S_{11,12} & \dots & S_{11,1i} & \dots & S_{12,11} & S_{12,12} & \dots & S_{12,1i} & \dots \\ S_{11,21} & S_{11,22} & \dots & S_{11,2i} & \dots & S_{12,21} & S_{12,22} & \dots & S_{12,2i} & \dots \\ \dots & \dots & \dots & \dots & \dots & \dots & \dots & \dots & \dots & \dots \\ S_{11,m1} & S_{11,m2} & \dots & S_{11,mi} & \dots & S_{12,m1} & S_{12,m2} & \dots & S_{12,mi} & \dots \\ \dots & \dots & \dots & \dots & \dots & \dots & \dots & \dots & \dots & \dots \\ S_{21,11} & S_{21,12} & \dots & S_{21,1i} & \dots & S_{22,11} & S_{22,12} & \dots & S_{12,1i} & \dots \\ S_{21,21} & S_{21,22} & \dots & S_{21,2i} & \dots & S_{22,21} & S_{22,22} & \dots & S_{12,2i} & \dots \\ \dots & \dots & \dots & \dots & \dots & \dots & \dots & \dots & \dots & \dots \\ S_{21,m1} & S_{21,m2} & \dots & S_{21,mi} & \dots & S_{22,m1} & S_{22,m2} & \dots & S_{22,mi} & \dots \\ \dots & \dots & \dots & \dots & \dots & \dots & \dots & \dots & \dots & \dots \end{bmatrix} \cdot \begin{bmatrix} a_{11} \\ a_{12} \\ \dots \\ a_{1m} \\ \dots \\ a_{21} \\ a_{22} \\ \dots \\ a_{2m} \\ \dots \end{bmatrix} = [S] \cdot \begin{bmatrix} a_{11} \\ a_{12} \\ \dots \\ a_{1m} \\ \dots \\ a_{21} \\ a_{22} \\ \dots \\ a_{2m} \\ \dots \end{bmatrix} \tag{2.81}$$

It is clear, that the first pair of subscripts of the S-parameters that form the S matrix stands for the numbers of the selected ports. Thus, the first digit of this first pair identifies the port acting as receiver and the second digit the port where the incident-wave excites the device. The second pair of subscripts stands for the modes that are taken into consideration, the first for the received mode and the second for the one with which the excitation is carried out. For these parameters it can be written that:

$$S_{11,mi} = \left.\frac{b_{1m}}{a_{1i}}\right|_{\substack{a_{1j}=0\ \forall j\neq i \\ a_{2j}=0\ \forall j}} = \left.\frac{\sqrt{N_m(z=0)}\cdot a^-_m(z=0)}{\sqrt{N_i(z=0)}\cdot a^+_i(z=0)}\right|_{\substack{a^+_j(z=0)=0\ \forall j\neq i \\ a^-_j(z=L)=0\ \forall j}} \tag{2.82a}$$

$$S_{12,mi} = \left.\frac{b_{1m}}{a_{2i}}\right|_{\substack{a_{1j}=0\ \forall j \\ a_{2j}=0\ \forall j\neq i}} = \left.\frac{\sqrt{N_m(z=0)}\cdot a^-_m(z=0)}{\sqrt{N_i(z=L)}\cdot a^-_i(z=L)}\right|_{\substack{a^+_j(z=0)=0\ \forall j \\ a^-_j(z=L)=0\ \forall j\neq i}} \tag{2.82b}$$

$$S_{21,mi} = \left.\frac{b_{2m}}{a_{1i}}\right|_{\substack{a_{1j}=0\ \forall j\neq i \\ a_{2j}=0\ \forall j}} = \left.\frac{\sqrt{N_m(z=L)}\cdot a_m^+(z=L)}{\sqrt{N_i(z=0)\cdot a_i^+(z=0)}}\right|_{\substack{a_j^+(z=0)=0\ \forall j\neq i \\ a_j^-(z=L)=0\ \forall j}} \tag{2.82c}$$

$$S_{22,mi} = \left.\frac{b_{2m}}{a_{2i}}\right|_{\substack{a_{1j}=0\ \forall j \\ a_{2j}=0\ \forall j\neq i}} = \left.\frac{\sqrt{N_m(z=L)}\cdot a_m^+(z=L)}{\sqrt{N_i(z=L)\cdot a_i^-(z=L)}}\right|_{\substack{a_j^+(z=0)=0\ \forall j \\ a_j^-(z=L)=0\ \forall j\neq i}} \tag{2.82d}$$

where extended multimode matching conditions are required in all the equations. Moreover, it is important to stress that in (2.81) and (2.82), both m and i are positive, and forward waves are labeled with superscript $+$, while backward with $-$. These modes are usually sorted by the cutoff frequency.

It is worth noting that the aforementioned equations are intended for two-port devices, however, this is not a restriction of the cross-section method. The ports will be located at the beginning and at the end (in the propagation direction) of the structure under study, e.g., at $z = 0$ and at $z = L$, being L the total length of the device. Therefore, a N-port device can be understood as a two-port device excited with different degenerated modes, i.e., modes with the same cutoff frequency. The components of the field for these modes will be null in all the ports located at the same z position except for one of them. This will provide the incident-wave in only one of the real ports.

In conclusion, the S-parameters, defined in (2.81) and (2.82), have been linked to the coupling coefficients trough the system in (2.68). It is important to note that, although the coupling coefficients have been defined in (2.69), during the design process they are unknowns that have to be calculated. The target response, given in terms of the S-parameters has to be used to solve the system in (2.68). This problem can be notably simplified by introducing several reasonable approximations that will lead to single-mode operation. The resulting simplified system, that is obtained in the following subsection, is the starting point of an analytical method to solve (2.68) that is presented in section 2.2.2.

2.2.1.2. Single-mode operation

The coupled-mode theory presented in the previous subsection allows us to study electromagnetic wave propagation along a nonuniform waveguide in a rigorous manner and with no approximations involved. However, it is important to note that in most of the cases in microwave design, the problem can be greatly simplified by introducing several reasonable approximations that will lead to single-mode operation.

In first place, we are going to neglect the coupling of energy to modes of the continuous spectrum. This can be usually done because the energy of these modes is primarily radiated, and since the devices we are interested in have very little radiation losses in the frequency band of interest (we exclude the antennas from this study), the error involved in the approximation will be small. Actually, in the case of closed waveguides, there will be no radiation losses and no continuous spectrum modes. This consideration reduces the expansion of the electric and magnetic fields of equation (2.67) to

$$\hat{\vec{E}}(x,y,z) = \sum_i a_i(z)\,\vec{E}^i(x,y,z) \tag{2.83a}$$

$$\hat{\vec{H}}(x,y,z) = \sum_i a_i(z)\,\vec{H}^i(x,y,z) \tag{2.83b}$$

and consequently, the coupled-mode equations of (2.68) result in

$$\frac{da_m}{dz} + j\beta_m a_m = \sum_i a_i\, C_{mi} \tag{2.84}$$

with

$$C_{mi} = \frac{-\pi f \oint \nu \left(\mu_0 H_z^i H_z^m - \mu_0 H_t^i H_t^m + \varepsilon E_n^i E_n^m\right) dt}{N_m(\beta_m - \beta_i)} \tag{2.85}$$

where the variables are defined as in (2.69).

Further assumptions will be stated regarding discrete spectrum modes. We will assume that for the frequency band of interest, either there is only one mode in propagation, while the rest are cutoff, or the geometry of the perturbation prevents the coupling between the working mode and the rest of the modes. These approximations lead us to assume single-mode operation in our study. Taking also advantage of the general property of the coupling coefficient (2.80a), and using (2.71a) and (2.71c), the coupled-mode equations can be thoroughly simplified to obtain:

$$\frac{da^+}{dz} = -j\beta a^+ + Ka^- \tag{2.86a}$$

$$\frac{da^-}{dz} = Ka^+ + j\beta a^- \tag{2.86b}$$

where

$$\hat{\vec{E}} = a^+\vec{E}^+ + a^-\vec{E}^- \tag{2.87a}$$

$$\hat{\vec{H}} = a^+\vec{H}^+ + a^-\vec{H}^- \tag{2.87b}$$

and

$$N^+ = \iint_S \left(\vec{E}^+ \times \vec{H}^+\right) d\vec{S} = -N^- = -\iint_S \left(\vec{E}^- \times \vec{H}^-\right) d\vec{S} \tag{2.88a}$$

$$\beta = \beta^+ = -\beta^- \tag{2.88b}$$

with $\hat{\vec{E}}$ and $\hat{\vec{H}}$ being the total electric and magnetic field present in the structure; $\vec{E}^+$, $\vec{H}^+$, $\vec{E}^-$, and $\vec{H}^-$ being the vector mode patterns of the forward $(+)$ and backward $(-)$ traveling waves corresponding to the mode of operation in the auxiliary uniform waveguide associated to the cross-section of interest; N^+ and N^- being the normalizations taken for the fields of the mode, assuming that they do not vary in the direction of propagation, z; β being the phase constant of the mode; a^+ and a^- being the complex amplitudes of the forward $(+)$ and backward $(-)$ traveling waves along the nonuniform waveguide; and K being the coupling coefficient between the forward and backward traveling waves, which from (2.85), and taking into account (2.72), can be calculated as:

$$K = \frac{-\pi f \oint \nu \left(\mu_0 \left(H_z^+ \right)^2 - \mu_0 \left(H_t^+ \right)^2 + \varepsilon \left(E_n^+ \right)^2 \right) dt}{2N^+\beta} \tag{2.89}$$

where f, $\nu = \tan(\alpha)$, μ_0, and ε are defined as in (2.77), and the local coordinate system with axes n, t, z is employed, also defined as in (2.77), and sketched in Figure 2.16.

The S-parameters of a two-port network relate the incident and reflected power wave amplitudes a_n, b_n in the following way [32]

$$\begin{bmatrix} b_1 \\ b_2 \end{bmatrix} = \begin{bmatrix} S_{11} & S_{12} \\ S_{21} & S_{22} \end{bmatrix} \cdot \begin{bmatrix} a_1 \\ a_2 \end{bmatrix} = [S] \cdot \begin{bmatrix} a_1 \\ a_2 \end{bmatrix} \tag{2.90}$$

From these equations it can be readily seen that:

$$S_{11} = \left.\frac{b_1}{a_1}\right|_{a_2=0} = \left.\frac{\sqrt{N^+(z=0)} \cdot a^-(z=0)}{\sqrt{N^+(z=0)} \cdot a^+(z=0)}\right|_{a^-(z=L)=0} = \left.\frac{a^-(z=0)}{a^+(z=0)}\right|_{a^-(z=L)=0} \tag{2.91a}$$

$$S_{12} = \left.\frac{b_1}{a_2}\right|_{a_1=0} = \left.\frac{\sqrt{N^+(z=0)} \cdot a^-(z=0)}{\sqrt{N^+(z=L)} \cdot a^-(z=L)}\right|_{a^+(z=0)=0} \tag{2.91b}$$

$$S_{21} = \left.\frac{b_2}{a_1}\right|_{a_2=0} = \left.\frac{\sqrt{N^+(z=L)} \cdot a^+(z=L)}{\sqrt{N^+(z=0)} \cdot a^+(z=0)}\right|_{a^-(z=L)=0} \tag{2.91c}$$

$$S_{22} = \left.\frac{b_2}{a_2}\right|_{a_1=0} = \left.\frac{\sqrt{N^+(z=L)} \cdot a^+(z=L)}{\sqrt{N^+(z=L)} \cdot a^-(z=L)}\right|_{a^+(z=0)=0} = \left.\frac{a^+(z=L)}{a^-(z=L)}\right|_{a^+(z=0)=0} \tag{2.91d}$$

It is worth noting that if the normalization of the fields is the same at the input and output ports of the device (because both ports are identical, or the normalization does not vary with z), the expressions for the S_{21} and S_{12} parameters can be simplified to:

$$S_{12} = \left.\frac{a^-(z=0)}{a^-(z=L)}\right|_{a^+(z=0)=0} \tag{2.92a}$$

$$S_{21} = \left.\frac{a^+(z=L)}{a^+(z=0)}\right|_{a^-(z=L)=0} \tag{2.92b}$$

This simplification is satisfied under single-mode operation, because the equation for the coupling coefficient (2.89) assumes that the normalization of the fields does not vary in the direction of propagation, z. It is important to highlight that in (2.91) and (2.92) matched ports are necessary in order to satisfy the conditions $a^-(z=L)=0$ and $a^+(z=0)=0$.

It is important to note that although the coupling coefficient has been already defined in (2.89), there is no direct connection with the frequency response, $S_{ij}(f)$, in that formula. Indeed, equation (2.89) relates the physical parameters with the coupling coefficient through the electric and magnetic fields involved. This result is valid for many waveguide technologies and transmission line implementations that satisfy the aforementioned assumed single-mode operation. In Section 2.2.3, ready to use formulas relating the physical parameters and the coupling coefficient will be obtained for the most interesting cases: rectangular waveguide, TEM or quasi-TEM transmission lines and side-by-side symmetrical coupled-lines.

The relationship between the frequency response and the coupling coefficient has been established for the single-mode case after several reasonable approximations. The system in (2.86) should be solved using the known S-parameters (equations (2.91a), (2.91d) and (2.92)). Due to the high complexity of the issue, Section 2.2.2 will be entirely devoted to this matter. Indeed, the output variable in the system of equations (2.86) will be the coupling coefficient, K, as a function of z provided that (2.91a) is known. The frequency dependent part of the system (2.86) is masked under phase constant. The dependence of the phase constant, β, on the propagation direction, z, will be of important relevance in Section 2.2.2. Indeed, no variation will be required, that is, β needs to be independent of z.

In practice, this independence condition is assumed to be satisfied and, when required, the effect of the actual dependence is compensated applying the algorithm presented here. Therefore, assuming that the auxiliary device, characterized univocally by $K(z)$, has a total length of L_{aux} and a phase constant independent of z, β_{aux}, the Algorithm 2.1 can be used to compensate the dependence of the phase constant on z, i.e., $\beta(z)$.

If the relationship between f and β is linear, the previous method is exact. However, for other cases, only approximated results are achieved. The problem is that a frequency dependence appears in the new propagation direction variable, z_n. This would force a dependence on the frequency for the coupling coefficient and eventually the electrical parameters and the physical dimensions. Therefore, one frequency

Inputs of the algorithm:

Definition of technology;

β_{aux};

$K(z) \quad \forall z \in [0, L_{\text{aux}}]$;

Outputs of the algoritm:

$K^{\text{out}}(z_n) \quad \forall z_n \in [0, L]$;

Algorithm:

Calculate the physical dimension associated with $K(z)$ $\forall z \in [0, L_{\text{aux}}]$ over the defined technology;

Calculate the $\beta(z) \quad \forall z \in [0, L_{\text{aux}}]$ associated with the physical dimension;

$$z_n = \int_0^z \frac{\beta_{\text{aux}}}{\beta(x)} dx;$$

Calculate the $K^{\text{out}}(z_n) \quad \forall z_n \in [0, L]$ associated with the physical dimension and the new propagation direction variable;

Algorithm 2.1: General compensation of the dependence of the phase constant on z.

needs to be selected before applying the algorithm in order to evaluate the phase constants. For doing so, it is recommended to use the central frequency of the defined specifications.

2.2.2. Analytical closed-form expression for the synthesis of microwave filters

In this section, an exact solution for the synthesis problem will be obtained by means of an analytical closed-form expression [29] that will allow us to calculate the coupling coefficient, $K(z)$, required for a microwave filter featuring a given target frequency response, see Figure 2.17.

The paper of Kay [38] is the first manuscript that deals with the problem of achieving an analytical solution for the coupling coefficient provided that the aimed frequency response is a rational function. The problem was covered in that paper in a rigorous manner from the mathematical point of view, resulting in the fundamentals

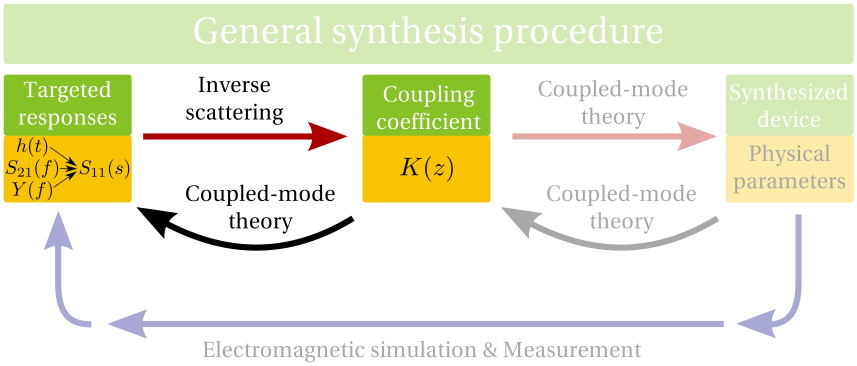

Figure 2.17: Scheme of the general synthesis procedure accordingly highlighted with the content of this section.

for the achievements presented in integrated optics by Song *et al.* [39]. It must be remarked that this article has become the basis of this subsection and many developments have been derived from there.

To obtain the sought closed-form expression for the coupling coefficient, we start from the simplified system of coupled-mode equations as given in (2.86), obtained assuming single-mode operation. Taking into account that $K(z)$ is a real function in our formulation, (2.86) can be rewritten as a Zakharov-Shabat system of quantum mechanics, obtaining [40]:

$$j \begin{bmatrix} \frac{d}{dz} & -K \\ K^* & -\frac{d}{dz} \end{bmatrix} \cdot \begin{bmatrix} a^+ \\ a^- \end{bmatrix} = \beta \begin{bmatrix} a^+ \\ a^- \end{bmatrix} \tag{2.93}$$

where * stands for complex conjugate.

A solution for the Zakharov-Shabat system (one of the so-called Jost functions) can be written as [40]:

$$\begin{bmatrix} \phi_1(z,\beta) \\ \phi_2(z,\beta) \end{bmatrix} = \begin{bmatrix} 1 \\ 0 \end{bmatrix} e^{-j\beta z} + \int_{-\infty}^{\infty} \begin{bmatrix} A_1(z,\tau) \\ A_2(z,\tau) \end{bmatrix} e^{-j\beta\tau}\, d\tau \tag{2.94}$$

It is important to note that β is the independent variable in the Zakharov-Shabat system, while frequency is the independent variable in the coupled-mode equations. Therefore, it is necessary to assume that variables β and frequency are univocally related in our device, and specifically that β does not vary with z for a given frequency. Actually, although the target device specifications are usually given as a function of frequency, the variable β will be used in our development in order to make the resulting

synthesis equations independent of the technology selected for the device implementation. An important consequence of the work with the β variable is that the presence of dispersion (phase velocity variable with frequency) in the implementation technology will not affect the synthesis method that will remain fully valid for those cases.

2.2.2.1. Laplace Transform Formulation

Since the exact solution for the synthesis problem will be obtained as a function of the poles and zeros of the target frequency response, it is convenient to extend analytically the solution (Jost function) in (2.94) to the complex Laplace plane by applying the well-known relationship $s = j\beta$, obtaining:

$$\begin{bmatrix} \phi_1(z,s) \\ \phi_2(z,s) \end{bmatrix} = \begin{bmatrix} 1 \\ 0 \end{bmatrix} e^{-sz} + \begin{bmatrix} a_1(z,s) \\ a_2(z,s) \end{bmatrix} \tag{2.95}$$

where the two-sided Laplace transform is defined as:

$$a_i(z,s) = \int_{-\infty}^{\infty} A_i(z,\tau)\, e^{-s\tau}\, d\tau \tag{2.96}$$

It is worth noting that since β plays the role of frequency in our derivation, variable τ has, strictly speaking, units of length and it is related with time, t, through the phase velocity, v_p. Actually, if v_p remains constant with frequency, then $\tau = v_p t$.

A linear combination of Jost functions of the kind shown below is also a solution for the Zakharov-Shabat system [40]:

$$\begin{bmatrix} u_1(z,s) \\ u_2(z,s) \end{bmatrix} = \begin{bmatrix} \phi_1(z,s) \\ \phi_2(z,s) \end{bmatrix} + S_{11} \begin{bmatrix} \phi_2^*(z,-s^*) \\ \phi_1^*(z,-s^*) \end{bmatrix} \tag{2.97}$$

being

$$S_{11}(s) = \rho(z=0,s) = \frac{a^-(z=0,s)}{a^+(z=0,s)} \tag{2.98}$$

where the solution $a^+(z,s) = u_1(z,s)$, $a^-(z,s) = u_2(z,s)$, as well as the variables $\rho(z = 0,s)$, $a^+(z = 0,s)$, $a^-(z = 0,s)$, correspond to the situation when the output port is matched and $S_{11}(s)$ is the well known scattering matrix parameter expressed as a function of the complex frequency s.

Let us define the following auxiliary functions, $y_1(z,s)$ and $y_2(z,s)$, as

$$\begin{bmatrix} y_1(z,s) \\ y_2(z,s) \end{bmatrix} = \begin{bmatrix} u_1(z,s) \\ u_2(z,s) \end{bmatrix} - \begin{bmatrix} 1 \\ 0 \end{bmatrix} e^{-sz}. \tag{2.99}$$

Using equations (2.97) and (2.95), they can be rewritten as:

$$\begin{bmatrix} y_1(z,s) \\ y_2(z,s) \end{bmatrix} = \begin{bmatrix} a_1(z,s) \\ a_2(z,s) \end{bmatrix} + S_{11}(s) \left\{ \begin{bmatrix} 0 \\ e^{sz} \end{bmatrix} + \begin{bmatrix} a_2^*(z,-s^*) \\ a_1^*(z,-s^*) \end{bmatrix} \right\} \tag{2.100}$$

As it is demonstrated in [40] the coupling coefficient can be calculated using these auxiliary functions as:

$$K(z) = -2 \cdot Y_2(z, \tau = z^+) \tag{2.101}$$

where $Y_2(z,\tau)$ is the inverse Laplace transform of $y_2(z,s)$.

It is important to note that to obtain (2.101) it was assumed that the coupling region (i.e. the designed device) begins at $z = 0$, and therefore $K(z) = 0$ for $z < 0$. From this condition, causality restrictions have been derived and applied. Additionally it was also assumed that $K(z)$ does not depend on β or, equivalently, on the frequency.

Obtaining the analytical solution for $y_2(z,s)$ from (2.100), and introducing it in (2.101) it can be seen that the coupling coefficient can be calculated as [39]:

$$K(z) = -2 \lim_{s \to -\infty} \left(e^{sz}\, s\, a_2(z,s) \right) \tag{2.102}$$

2.2.2.2. Closed-form expression for the case of rational functions

In this work we will assume that $S_{11}(s)$ is a rational function that can be expressed as a quotient of polynomials as:

$$S_{11}(s) = \frac{n(s)}{d(s)} = \frac{r_0 \prod_{n=1}^{M} (s - c_n)}{\prod_{n=1}^{N} (s - p_n)} \tag{2.103}$$

being c_n the zeros and p_n the poles of $S_{11}(s)$, M the number of zeros, and N the number of poles, where it is satisfied that $N \geq M + 1$ (to assure that $S_{11}(s = j\beta)$ is a band-limited function that tends to zero when frequency goes to infinity) and $\mathfrak{Re}\{p_n\} < 0$ (all the poles must lie in the left-half of the s-plane to be a stable system). Finally, r_0 is a constant that must be adjusted to satisfy that $|S_{11}(s = j\beta)| < 1$, to have a passive system.

It is important to highlight that although the frequency response has been expressed in terms of the S_{11} parameter, the S_{21} parameter of the device arises univocally from it for our case of interest of reciprocal and lossless two-port networks [41]. Specifically, the magnitude can be calculated for each frequency (or equivalently β) as [8]:

$$|S_{21}(s = j\beta)|^2 = 1 - |S_{11}(s = j\beta)|^2 \tag{2.104}$$

Taking into account that $S_{11}(s)$ is a rational function as given in (2.103), it follows from (2.104):

$$|S_{21}(s=j\beta)|^2 = \frac{d(s)\cdot d^*(-s^*) - n(s)\cdot n^*(-s^*)}{d(s)\cdot d^*(-s^*)} = \frac{\Delta(s)}{d(s)\cdot d^*(-s^*)} \tag{2.105}$$

The phase of the $S_{21}(s)$ can be retrieved using the Hilbert Transform as explained in [40, 42], or it can be also obtained by directly deducing $S_{21}(s)$ from (2.105) taking only the zeros and poles with negative real part [38]:

$$S_{21}(s) = \frac{\prod_{n=1}^{N}(s-k_n)}{\prod_{n=1}^{N}(s-p_n)} \tag{2.106}$$

being k_n the zeros and p_n the poles of $S_{21}(s)$, where $\mathfrak{Re}\{k_n\} < 0$ (all the zeros are in the left-half s plane because $S_{21}(s)$ is a minimum-phase function) and $\mathfrak{Re}\{p_n\} < 0$ (all the poles must be in the left-half s plane to be a stable system). It is interesting to note that $S_{21}(s)$ has the same poles as $S_{11}(s)$, but different zeros [38]. It is also worth noting that, strictly speaking, the $S_{21}(s=j\beta)$ parameter is a minimum-phase function of the form of (2.106) that additionally includes a linear phase term of the form $e^{-j\beta L}$ that accounts for the delay associated to the pure propagation along the device that features a total length L [9, 11].

Inspecting (2.102) it can be seen that the coupling coefficient, $K(z)$, necessary to implement a given frequency response can be calculated analytically by obtaining first an analytical solution for $a_2(z,s)$. To do it, we go back to (2.100), and taking into account that $S_{11}(s)$ can be expressed as a quotient of polynomials (2.103), it can be deduced that $d(s)\cdot y_1(z,s)$ and $d(s)\cdot y_2(z,s)$ are bounded entire functions of s that can be expressed as [39]:

$$d(s)\begin{bmatrix} y_1(z,s) \\ y_2(z,s) \end{bmatrix} = \begin{bmatrix} pol_1(z,s) \\ pol_2(z,s) \end{bmatrix} e^{-sz} \tag{2.107}$$

where $pol_1(z,s)$ and $pol_2(z,s)$ are polynomials in s of degree $N-1$ at most, whose coefficients are functions of z.

By introducing (2.103) in (2.100) and equating the result with (2.107), it is possible to get the required analytical solution for $a_2(z,s)$ as a function of the previously defined polynomials. Additionally, assuming that the N poles of $S_{11}(s)$ and $S_{21}(s)$, $p_1, p_2, \ldots, p_N$ are distinct, that the N zeros of $S_{21}(s)$, $k_1, k_2, \ldots, k_N$ are distinct, and that the M zeros of $S_{11}(s)$, $c_1, c_2, \ldots, c_M$, are different from the conjugated poles with opposite sign, $-p_1^*, -p_2^*, \ldots, -p_N^*$, then $a_1(z,s)$ and $a_2(z,s)$ can be expressed as a linear

combination of entire functions of the form [39]:

$$\begin{bmatrix} a_1(z,s) \\ a_2(z,s) \end{bmatrix} = 2 \cdot \sum_{n=1}^{N} \left\{ \begin{bmatrix} d_{1,n}(z) \\ d_{2,n}(z) \end{bmatrix} \frac{\sinh\left(z(s-k_n)\right)}{s-k_n} + \begin{bmatrix} g_{1,n}(z) \\ g_{2,n}(z) \end{bmatrix} \frac{\sinh\left(z(s+k_n^*)\right)}{s+k_n^*} \right\} \tag{2.108}$$

where the coefficients of the linear combination $d_{1,n}(z)$, $d_{2,n}(z)$, $g_{1,n}(z)$, $g_{2,n}(z)$ depend only on z and satisfy the following relationship [39]:

$$\frac{g_{1,n}(z)}{d_{2,n}^*(z)} = \frac{g_{2,n}(z)}{d_{1,n}^*(z)} = -S_{11}(-k_n^*). \tag{2.109}$$

Using (2.109), the coefficients $g_{1,n}(z), g_{2,n}(z)$ can be eliminated from (2.108). The remaining coefficients, $d_{1,n}(z), d_{2,n}(z)$ will be calculated introducing (2.108) and (2.103) into (2.100), and comparing the result with (2.107). By proceeding in that way it can be seen that only the terms containing the factor e^{-sz} must exist, while the rest of the terms containing the factor e^{sz} must vanish identically. To verify this condition the following pair of equations must be satisfied for each of the N poles $p_1, p_2, \ldots, p_i, \ldots, p_N$

Inputs of the algorithm:
- $S_{11}(s)$ in rational form: $S_{11}(s) = \dfrac{n(s)}{d(s)}$;
- $L \equiv$ Length of the device;

Outputs of the algoritm:
- $K(z)$;

Algorithm:
- Calculate p_n = poles of $S_{11}(s)$;
- Calculate $\Delta(s) = n(s)n^*(-s^*) - d(s)d^*(-s^*)$;
- Calculate k_n = zeros of $\Delta(s)$;
- Evaluate $S_{11kn^*} = S_{11}(-k_n^*)$;
- Evaluate $S_{11kn} = S_{11}(k_n)$;
- For $z_i \in [0, L]$;
- {
  - Obtain $d_{1,n}^*(z_i)$, $d_{2,n}(z_i)$ = solutions of linear system of $2N$ equations;
  - Calculate $K(z_i) = 2 \cdot \sum_{n=1}^{N} \left\{ d_{2,n}(z_i) \cdot e^{k_n \cdot z_i} - d_{1,n}^*(z_i) \cdot e^{-k_n^* \cdot z_i} \cdot S_{11kn^*} \right\}$;
- }

Algorithm 2.2: Pseudocode of the synthesis method based on the pole and zero decomposition.

[39]:

$$\sum_{n=1}^{N}\left\{\frac{1}{S_{11}(k_n)}\cdot\frac{e^{-k_n z}}{p_i-k_n}\cdot\begin{bmatrix}d_{1,n}(z)\\ d_{2,n}(z)\end{bmatrix}-\frac{e^{k_n^* z}}{p_i+k_n^*}\cdot\begin{bmatrix}d_{2,n}^*(z)\\ d_{1,n}^*(z)\end{bmatrix}\right\}=\begin{bmatrix}0\\ 1\end{bmatrix} \tag{2.110}$$

By solving the resulting linear system of $2N$ equations, the $2N$ unknowns, $d_{1,n}(z)$, $d_{2,n}(z)$, can be obtained and the analytical expression for $a_2(z,s)$ in (2.108) is fully determined with the aid of (2.109). Finally, introducing (2.108) in (2.102) and performing the limit, the sought analytical closed-form expression for the coupling coefficient, $K(z)$, of the microwave filter that satisfies the target frequency response is obtained [39]:

$$K(z)=2\sum_{n=1}^{N}\left\{d_{2,n}(z)\,e^{k_n z}-d_{1,n}^*(z)\,e^{-k_n^* z}S_{11}(-k_n^*)\right\} \tag{2.111}$$

where k_n are the zeros of $S_{21}(s)$ and $d_{1,n}(z), d_{2,n}(z)$ are the solutions of (2.110).

The proposed synthesis method can be performed following the pseudocode in Algorithm 2.2.

2.2.2.3. Discussion on the assumptions of the method and physical insight

As it has been explained in the previous sections, to obtain the analytical closed-form expression for the coupling coefficient (2.111) necessary to implement a given causal, passive and stable frequency response, it is assumed that it can be expressed as a rational function of the form of (2.103) and (2.106), where $|S_{11}(s=j\beta)|<1$, to have a passive system. This assumption does not limit significantly the validity of the synthesis technique in practical cases since the well known functions used for electronic or classical microwave filters (Butterworth, Chebyshev, Cauer,...) are always rational. Moreover, in any case, an arbitrary frequency specification can be always approximated by a rational function using several well established procedures [16, 26, 43, 44] or the method proposed in Section 2.1 based on digital filter design methods [6].

Additionally it has been assumed that the poles and zeros verify the following conditions:

a) $p_1, p_2, \ldots, p_N$ are the N poles of $S_{11}(s)$ and $S_{21}(s)$. They have to be distinct and with negative real part to guarantee the stability of the frequency response.

b) $k_1, k_2, \ldots, k_N$ are the N zeros of $S_{21}(s)$. They have to be distinct and with negative real part to satisfy the minimum-phase condition of the $S_{21}(s)$ parameter.

It is worth noting that the requirement of having distinct poles or zeros is not an actual limitation because the multiple roots can be always modified slightly so that they split up into simple roots.

c) $c_1, c_2, \ldots, c_M$ are the M zeros of $S_{11}(s)$. They have to be different from the conjugated poles with opposite sign, $-p_1^*, -p_2^*, \ldots, -p_N^*$. As a result, strictly speaking, it is not possible to implement poles-zeros groups constituting all-pass sections. However, this is not a real limitation because the poles-zeros groups can be always modified slightly and the all-pass original case can be considered as a limiting form of the actual implemented function.

d) $N \geq M+1$ and therefore the number of poles is larger than the number of zeros of $S_{11}(s)$, which physically implies that $S_{11}(s = j\beta)$ is a band-limited function that tends to zero when frequency goes to infinity. Again, this is not a real limitation for practical applications because the synthesized microwave device will cover all the frequency range of interest that in practice will be limited by the technology used and in any case will never extend to infinity.

Finally, it is worth noting that once a suitable rational frequency response is chosen, the only approximations introduced to obtain the synthesis solution of (2.111), are to consider single-mode operation, as well as to assume that the phase constant, β, does not vary with z for a given frequency along the device, and that $K(z)$ does not vary with frequency. These conditions are fully satisfied by transmission lines, like stripline and coaxial, that support a pure TEM mode, and by waveguides, like the rectangular waveguide operating with its fundamental TE_{10} mode and featuring E-plane perturbations, for example. These conditions can be also approximately satisfied by planar transmission lines, like microstrip and coplanar, that support a quasi-TEM mode, and by waveguides, like the ridge waveguide operating with its fundamental quasi-TE_{10} mode and featuring E-plane perturbations, for instance.

2.2.3. Relation between coupling coefficient, $K(z)$, and the physical parameters

In Section 2.2.2, an analytical closed-form expression has been provided to obtain the coupling coefficient of a device featuring as a given target response. However, the design process is not complete until the physical parameters of such a device are obtained. A relation between the coupling coefficient and the physical parameters is necessary, see Figure 2.18.

Assuming single-mode operation, the coupling coefficient for discrete spectrum modes in (2.69a) can be simplified to

$$C_{i,-i} = \frac{-1}{2N_i} \iint_{\breve{S}} \left(\vec{E}^i \times \frac{\partial \vec{H}^{-i}}{\partial z} + \frac{\partial \vec{H}^i}{\partial z} \times \vec{E}^{-i} \right) \hat{z}\, d\breve{S} - \frac{1}{2N_i} \cdot \frac{dN_{-i}}{dz} \tag{2.112}$$

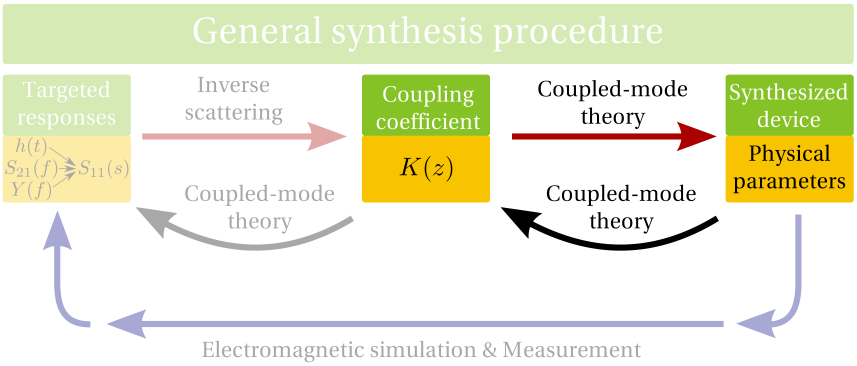

Figure 2.18: Scheme of the general synthesis procedure accordingly highlighted with the content of this section.

where subscripts i, $-i$ refer to the forward and backward traveling waves associated to the operation mode, respectively, and N_i, N_{-i} are the normalization factors defined as in (2.70a).

Equation (2.112) relates the physical dimensions of the device and the coupling coefficient, which obviously depends on the technology used. In this section specific relations will be given for the most usual technologies, such as rectangular waveguide, stripline and microstrip. Edge-coupled stripline and microstrip technologies will be also considered.

2.2.3.1. Rectangular waveguide

For the case of rectangular waveguide technology, it is convenient to use a simplified expression for the coupling coefficient that was already given in (2.89) and is rewritten here for completion

$$K = \frac{-\pi f \oint \nu \left(\mu_0 \left(H_z^+ \right)^2 - \mu_0 \left(H_t^+ \right)^2 + \varepsilon \left(E_n^+ \right)^2 \right) dt}{2N^+ \beta} \tag{2.113}$$

The expression in (2.113) can be evaluated for the fundamental TE_{10} mode, taking advantage of the analytical expressions available for the vector mode patterns of the

forward travelling wave of the mode:

$$\begin{aligned} E_x^+ &= 0 \\ E_y^+ &= \sqrt{\frac{4\pi\mu_0 f N^+}{ab\beta}} \cdot \sin\left(\frac{\pi}{a}x\right) \\ E_z^+ &= 0 \end{aligned} \tag{2.114a}$$

$$\begin{aligned} H_x^+ &= -\sqrt{\frac{N^+\beta}{ab\pi f\mu_0}} \cdot \sin\left(\frac{\pi}{a}x\right) \\ H_y^+ &= 0 \\ H_z^+ &= \frac{j}{a}\sqrt{\frac{\pi N^+}{ab\beta f\mu_0}} \cdot \cos\left(\frac{\pi}{a}x\right) \end{aligned} \tag{2.114b}$$

where a is the width and b is the height of the rectangular waveguide, N^+ is the normalization factor of the mode as defined in (2.88a), f is the frequency in Hz, μ_0 is the permeability of vacuum, β is the phase constant of the mode, and x, y, z is the coordinate system, see Figure 2.19(a).

Taking into account the geometrical relationship between the coordinate systems shown in Figure 2.19(a), and the definition for the perturbation angle, α, that allows for the proper calculation of the $\nu = \tan(\alpha)$ parameter at each wall of the rectangular waveguide, Figure 2.19(b), the coupling coefficient for the fundamental TE_{10} mode can be finally calculated from (2.113) as [30]:

$$K(z) = \frac{-1}{2b(z)} \cdot \frac{db(z)}{dz} + \frac{\pi^2}{2a(z)^3\beta^2} \cdot \frac{da(z)}{dz} \tag{2.115}$$

where the phase constant can be easily calculated for the fundamental TE_{10} mode, using the well-known expression [8]:

$$\beta = \beta_{\mathrm{TE}_{10}} = \sqrt{\varepsilon_r \left(\frac{2\pi f}{c}\right)^2 - \left(\frac{\pi}{a(z)}\right)^2} \tag{2.116}$$

being ε_r, the relative dielectric constant of the homogeneous medium that fills the waveguide and c, the speed of light in vacuum.

It should be noted that the expression obtained for $K(z)$ depends also on β and, therefore, on frequency. However, if only the height of the rectangular waveguide, b, is modified along the propagation axis while the width is kept constant, $a = a(z = 0) = a_0$, the coupling coefficient results in:

$$K(z) = \frac{-1}{2b(z)} \cdot \frac{db(z)}{dz} \tag{2.117}$$

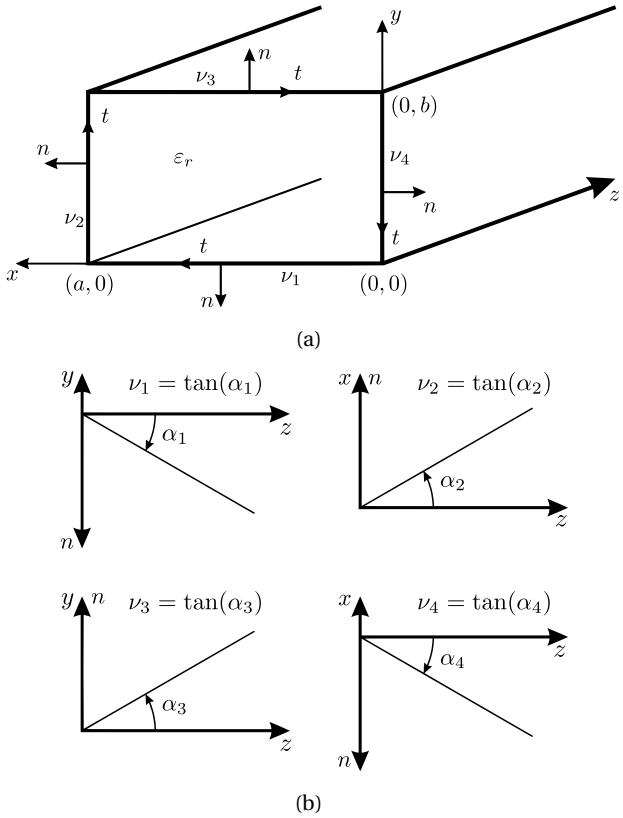

Figure 2.19: (a) Sketch of a rectangular waveguide. The coordinate system with axes x, y, z is included. The local coordinate system with axes n, t, z is also given. (b) Definition for the perturbation angle, α_i , at each of the four walls ($i = 1, 2, 3, 4$) of the rectangular waveguide.

This result is of particular interest because the coupling coefficient does not depend on the phase constant, and hence, it becomes independent of the frequency, as it is required by the synthesis method described in Section 2.2.2. Moreover, as it can be seen in (2.116), when $a = a(z = 0) = a_0$, the resulting phase constant does not depend on z, satisfying another assumption of our synthesis method.

Moreover, equation (2.117) can be analytically solved to obtain the varying height of the rectangular waveguide:

$$b(z) = b_0 \cdot e^{-2\int_0^z K(r)dr} \tag{2.118}$$

where b_0 is the height of the rectangular waveguide at the beginning of the device, $b(z = 0)$, and r is an auxiliary variable to calculate the integral.

2.2.3.2. TEM and quasi-TEM transmission lines

Any structure that consists of two lossless conductors that are placed in parallel in a homogeneous dielectric medium, supports a pure TEM mode of propagation. Common examples of these transmission lines structures are the stripline and the embedded differential line as it is shown in Figure 2.20. However, if a two-conductor transmission line is enclosed in an inhomogeneous dielectric medium, the fundamental mode of propagation is quasi-TEM. Several characteristic examples of these lines such as microstrip and coplanar waveguide are shown in Figure 2.20. Indeed, in general, if the separation between the conductors is very small in comparison with the wavelength (as a rule of thumb smaller than 1/20 of the wavelength in the medium), the quasi-TEM mode can be considered to be close to the TEM mode behavior.

When the mode of operation is TEM or quasi-TEM the expression for the coupling

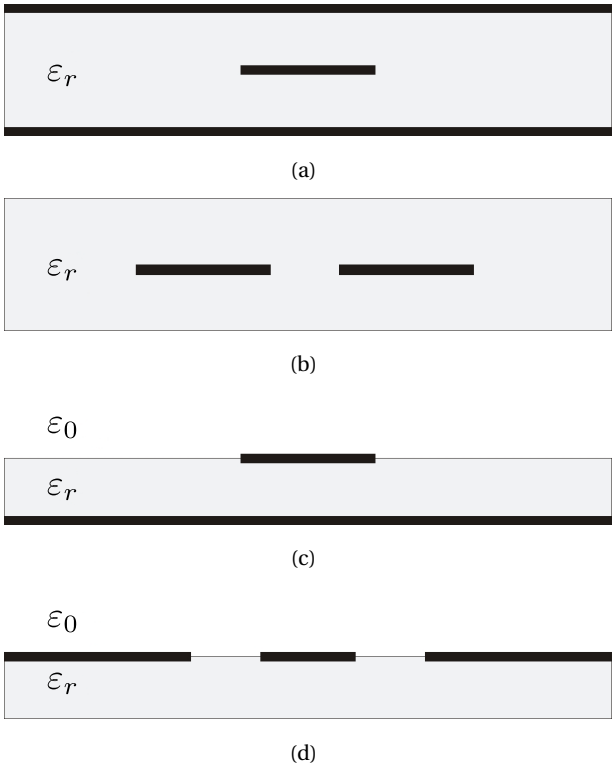

Figure 2.20: Transmission lines with fundamental TEM modes: (a) stripline and (b) embedded differential line; or quasi-TEM modes: (c) microstrip and (d) coplanar waveguide.

coefficient given in (2.112) can be reformulated with the introduction of the characteristic impedance of the mode, Z_{0i}. To do it, we are going to take advantage of the relation between the vector mode patterns of the forward and backward traveling waves associated to the operation mode that was already considered in (2.72):

$$E_x^{-i} = E_x^i \quad ; \quad E_y^{-i} = E_y^i \quad ; \quad E_z^{-i} = -E_z^i \tag{2.119a}$$

$$H_x^{-i} = -H_x^i \quad ; \quad H_y^{-i} = -H_y^i \quad ; \quad H_z^{-i} = H_z^i \tag{2.119b}$$

Using (2.119), and taking a normalization factor N_i, which does not vary with the cross section (i.e., constant with z), the coupling coefficient in (2.112) can be rewritten as

$$C_{i,-i} = \frac{-1}{N_i} \iint_{\breve{S}} \left(\vec{E}^i \times \frac{\partial \vec{H}^i}{\partial z} \right) \hat{z}\, d\breve{S} \tag{2.120}$$

Vector mode patterns can be expressed as a function of the characteristic impedance of the mode Z_{0i},

$$\vec{E}^i = \sqrt{Z_{0i}}\vec{e}^{\,i} \tag{2.121a}$$

$$\vec{H}^i = \frac{1}{\sqrt{Z_{0i}}}\vec{h}^i \tag{2.121b}$$

and introducing (2.121) in the coupling coefficient expression (2.120), it follows that

$$C_{i,-i} = \frac{-1}{2Z_{0i}} \cdot \frac{dZ_{0i}}{dz} + \frac{1}{N_i} \iint_{\breve{S}} \left(\vec{e}^{\,i} \times \frac{\partial \vec{h}^i}{\partial z} \right) \hat{z}\, d\breve{S}. \tag{2.122}$$

To complete this section the concept of characteristic impedance of the i mode, Z_{0i}, will be discusesed and the expressions for the stripline and microstrip technologies will be provided.

Under the assumption of TEM mode propagation, voltage V and current I can be defined in a unique way. In that case, the definition of the characteristic impedance of the mode is also unique and can be calculated as [1]:

$$Z_{0i} = Z_{0,\mathrm{TEM}} = \frac{V^+}{I^+} = -\frac{V^-}{I^-} \tag{2.123}$$

where $+$, $-$ superscripts refer to the forward and backward traveling waves, respectively. However, when a mode is not pure TEM, the definition of its characteristic impedance is no longer unique. In this case, a proper definition of Z_{0i} for the calculation of the coupling coefficient $C_{i,-i}$ should be given. The sought Z_{0i} has to feature the variations of the cross-section present in the transmission line. Besides, the most suitable characteristic impedance is the Z_{0i} that provides the same reflection coefficient as the one that is directly produced by the coupling coefficient between the forward

and backward waves of the i mode. Thus, under this definition, the part corresponding to the integral of the fields in expression (2.122) will be negligible. Consequently, the coupling coefficient will be accurately approximated for the discrete spectrum modes as:

$$C_{i,-i} \approx \frac{-1}{2Z_{0i}} \cdot \frac{dZ_{0i}}{dz}. \tag{2.124}$$

Due to the interest in planar transmission lines for the design of microwave devices, the following two parts will be devoted to stripline and microstrip technologies.

Stripline

A planar transmission line is a transmission line with conducting strips that lie entirely in parallel planes. The most common structure uses one or more parallel conducting strips placed on a dielectric substrate material adjacent to a conducting ground plane. The geometry of a stripline is shown in Figure 2.21. A thin conducting strip of width W_s is centered between two wide conducting ground planes with separation h_s, and the entire region between the ground planes is filled with a uniform dielectric. The stripline is easily constructed by etching the center conductor on a grounded substrate of height $h_s/2$, and then covering with another grounded substrate of the same thickness. An easy fabrication process causes that the stripline is the practical evolution of the coaxial line. This technology is often used in the design of high quality components for metrology or astronomy applications due to the ideal frequency behavior of the fabricated component. Since stripline has two conductors and a homogeneous dielectric, it can support a TEM mode, which is the fundamental operation mode. However, stripline can also support higher order TM and TE modes. In practice these modes are usually avoided choosing proper dimensions of the substrate (distance between the ground planes smaller than 1/4 of the wavelength in the

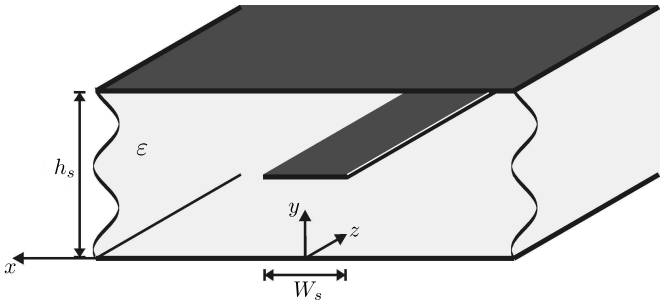

Figure 2.21: Sketch of stripline technology with defined physical parameters.

medium) and using sorting screws between the ground planes.

The phase constant of the fundamental TEM mode will depend only on the permittivity of the dielectric as it follows

$$\beta = \beta_s = \frac{2\pi f}{c}\sqrt{\varepsilon_r} \tag{2.125}$$

where, in accordance with Figure 2.21, the permittivity is: $\varepsilon = \varepsilon_0\varepsilon_r$.

Under single-mode operation, the coupling coefficient between the forward and backward waves of the fundamental TEM mode of the stripline can be written from (2.124) as:

$$K = \frac{-1}{2Z_0(z)} \cdot \frac{dZ_0(z)}{dz}. \tag{2.126}$$

This equation can be solved analytically. Thus, knowing the coupling coefficient between the forward and backward waves of the fundamental TEM mode an exact expression for the characteristic impedance of the stripline can be deduced as:

$$Z_0(z) = Z_0(0^+) \cdot e^{-2\int_0^z K(r)dr} \tag{2.127}$$

being $Z_0(0^+)$ the limit from the right side of the characteristic impedance at the beginning of the device ($z = 0$). In order to satisfy matching conditions, the value of the characteristic impedance at the excitation port will be taken equal to $Z_0(0^+)$ or vice versa. r is an auxiliary variable to calculate the integral.

The first approximation for the physical dimensions of the stripline as a function of its characteristic impedance can be found in [1] and is:

$$\frac{W_s}{h_s} = \begin{cases} \dfrac{30\pi}{Z_0\sqrt{\varepsilon_r}} - 0.441 & \text{for} \quad Z_0\sqrt{\varepsilon_r} < 120 \\ 0.85 - \sqrt{1.041 - \dfrac{30\pi}{Z_0\sqrt{\varepsilon_r}}} & \text{for} \quad 120 < Z_0\sqrt{\varepsilon_r} < 295 \end{cases} \tag{2.128}$$

More accurate expressions for the relationship between the physical dimensions and the characteristic impedance can be found in [8].

Due to the fact that there is no air-dielectric interface, the medium is essentially non-dispersive. Therefore, the aforementioned expressions are valid up to the highest frequency, at which a stripline operation remains single-mode. This tends to be limited by the onset of higher order modes such as the parallel plate waveguide modes. It is important to point out that parallel plate waveguides supports TE, TM and TEM modes, obviously the last one without cutoff frequency.

Moreover, it is well documented that if an air gap appears between substrate layers, the surface waves and the leaky modes can be easily excited [45] vitiating the frequency behavior of the designed device.

Microstrip

The microstrip line shown in Figure 2.22, is a widely used planar transmission line. It consists of a single conducting strip of width W_u placed on a dielectric substrate of thickness h_u and located on a ground plane. The microstrip transmission line can be fabricated using conventional printed circuit board techniques (without the need to attach a cover as it was necessary in stripline) favoring the mass production of low-cost components intended for wide market applications.

The dielectric air interface causes that the microstrip line can not support a pure TEM mode. Actually, the exact fields present in a microstrip line constitute a hybrid TM-TE mode. However, if the dielectric substrate is thin enough the quasi-TEM approximation will be accurate. Then the phase constant can be expressed as:

$$\beta = \beta_u = \frac{2\pi f}{c}\sqrt{\varepsilon_e} \tag{2.129}$$

where ε_e is the effective dielectric constant of the microstrip line and it can be calculated as a function of ε_r, W_u and h_u as, [1]

$$\varepsilon_e = \frac{\varepsilon_r + 1}{2} + \frac{\varepsilon_r - 1}{2} \cdot \frac{1}{\sqrt{1 + \dfrac{12h_u}{W_u}}} \tag{2.130}$$

where in accordance with Figure 2.22, the permittivity is: $\varepsilon = \varepsilon_0\varepsilon_r$.

For the devices under study, it will be assumed that there is no radiation, being possible to neglect continuous spectrum modes. Moreover, it will be also supposed that only the fundamental mode is excited and no coupling to higher order modes is allowed. Under these reasonable assumptions the coupling coefficient, K, between the forward and backward waves of the fundamental quasi-TEM mode of the microstrip line can be written from (2.124) as:

$$K \approx \frac{-1}{2Z_0(z)} \cdot \frac{dZ_0(z)}{dz}. \tag{2.131}$$

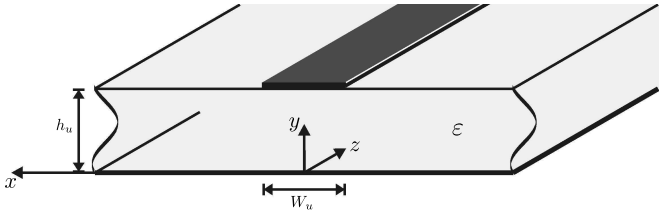

Figure 2.22: Sketch of microstrip technology with defined physical parameters.

provided that the characteristic impedance is properly implemented. Equation (2.131) can be easily solved analytically, resulting in:

$$Z_0(z) \approx Z_0(0^+) \cdot e^{-2\int_0^z K(r)dr} \tag{2.132}$$

where $Z_0(0^+)$ is the limit from the right side of the characteristic impedance at the beginning of the device ($z = 0$). In order to satisfy matching conditions, the value of the characteristic impedance at the excitation port will be taken equal to $Z_0(0^+)$. r is an auxiliary variable to perform the integral.

For the case of a fundamental TEM or quasi-TEM mode, the definition of the characteristic impedance, which features in the best way the variation of the cross-section in the microstrip line is as follows [8]

$$Z_0 = 2 \cdot \frac{P^+}{|I^+|^2} \tag{2.133}$$

being P^+ the power associated with the forward wave of the fundamental microstrip mode. Besides, the accuracy of (2.131) is guaranteed by the formulas available in the classical scientific literature [1]. Therefore, the relationship between the physical dimensions of the microstrip line and the coupling coefficient is successfully established by using equation (2.132) and the following expression from [1]

$$\frac{W_u}{h_u} = \begin{cases} \dfrac{8e^A}{e^{2A}-2} & \text{for} \quad \dfrac{W_u}{h_u} < 2 \\ \dfrac{2\left[B-1-\ln(2B-1)\right]}{\pi} + \dfrac{\varepsilon_r - 1}{\varepsilon_r \pi}\left(\ln(B-1)+0.39-\dfrac{0.61}{\varepsilon_r}\right) & \text{for} \quad \dfrac{W_u}{h_u} > 2 \end{cases} \tag{2.134}$$

with $B = \dfrac{311\pi}{2Z_0\sqrt{\varepsilon_r}}$ and $A = \dfrac{Z_0}{60}\sqrt{\dfrac{\varepsilon_r+1}{2}} + \dfrac{\varepsilon_r - 1}{\varepsilon_r + 1}\left(0.23 + \dfrac{0.11}{\varepsilon_r}\right)$.

More accurate expressions for the relationship between the physical parameters and the characteristic impedance can be found in [28].

In order to satisfy presumed single-mode operation, the substrate has to be carefully selected to avoid the coupling to higher order modes. Other propagating modes should be avoided, such as TM and TE surface waves that propagate in a grounded dielectric substrate. The lowest TM mode, TM_0 surface wave, propagates from DC (it has no cut off frequency) but studies have shown that the coupling between this mode and the fundamental quasi-TEM mode becomes significant above the frequency

$$f_{\substack{\mathrm{TM}_0 \\ \text{surface wave}}} = \frac{c\tan^{-1}(\varepsilon_r)}{\pi h_u \sqrt{2(\varepsilon_r - 1)}}. \tag{2.135}$$

when the phase velocities of both modes become close to each other [1, 46].

Coupling to TE_n surface wave modes can occur when the devices feature transverse discontinuities. In such a case, the cut-off frequency of the lowest order TE mode, TE_1, has to be considered [1]. Our synthesis technique results in continuously varying device profiles what prevents the coupling to these modes.

In addition, for wide microstrips a transverse resonant mode can be excited in the dielectric below the strip. This happens when the width of the strip is $\lambda/2$ in the dielectric. Due to the fringing fields, the effective width of the strip becomes a little larger. A rough approximation for the effective width W_{eff} is $W_u + 0.5h_u$ (also $W_u + 0.4h_u$ in other references [46]). Then, the frequency when this happens

$$f_{\substack{\mathrm{transverse}\\ \mathrm{resonance}}} = \frac{c}{2W_{\mathrm{eff}}\sqrt{\varepsilon_r}} = \frac{c}{\sqrt{\varepsilon_r}\,(2W_u + h_u)} \tag{2.136}$$

should be also considered as a limiting operation frequency that will depend not only on the substrate characteristic but also on the implemented microstrip widths, being the widest strip the most limiting.

When the separation between the strip and the ground plane approaches $\lambda/2$, a parallel-plate mode can be also propagated. An estimation for the threshold frequency (valid for wide microstrip) is

$$f_{\substack{\mathrm{parallel}\\ \mathrm{plate}}} = \frac{c}{2h_s\sqrt{\varepsilon_r}}. \tag{2.137}$$

For narrower microstrip lines, the fringing fields will increase the effective distance between the planes reducing the threshold frequency for the propagation of this mode.

In conclusion, the values for the frequency limits stated above need to be used as a first approximation in order to prevent unwanted behavior of the designed devices.

Another consideration refers to the dependence of the phase constant with z. For microstrip technology, this dependence exists since the effective dielectric constant, ε_e, depends on the geometry, which varies along the propagation direction. The Algorithm 2.1 presented in subsection 2.2.1.2 in order to compensate the dependence of the phase constant with z can be particularized for this technology achieving an exact compensation method, see Algorithm 2.3.

Finally, although all the expressions presented in this section are accurate enough, the precision for extreme values can not be always guaranteed. Hence, the LineCalc tool that belongs to the commercial electromagnetic software package Advanced Design System (ADS) of Agilent™ will be used for extreme values and eventually for the final prototypes [47].

Summarizing subsection 2.2.3.2, it must be added that other expressions that relate the characteristic impedance of the fundamental modes for several technologies, such as coaxial transmission line, two-wire transmission line, slotlines, etc., can be

Inputs of the algorithm:

Definition of the substrate for microstrip lines;

ε_{aux};

$K(z)\ \ \forall z \in [0, L_{\text{aux}}]$;

Outputs of the algoritm:

$K^{\text{out}}(z_n)\ \ \forall z_n \in [0, L]$;

Algorithm:

Calculate $Z_0(z)\ \forall z \in [0, L_{\text{aux}}]$ associated with $K(z)$ $\forall z \in [0, L_{\text{aux}}]$ using (2.132);

Calculate the physical dimensions associated with $Z_0(z)$ $\forall z \in [0, L_{\text{aux}}]$ using (2.134);

Calculate the $\varepsilon_e(z)\ \forall z \in [0, L_{\text{aux}}]$ associated with the physical dimension using (2.129) and (2.130);

$$z_n = \int_0^z \frac{\beta_{\text{aux}}}{\beta(x)} dx = \int_0^z \sqrt{\frac{\varepsilon_{\text{aux}}}{\varepsilon_e(x)}} dx;$$

Calculate the $K^{\text{out}}(z_n)\ \ \forall z_n \in [0, L]$ associated with the $Z_0(z_n)\ \forall z_n \in [0, L]$ using (2.131);

Algorithm 2.3: General compensation in microstrip lines of the dependence of the phase constant on z.

found in classical bibliography [1, 8]. For those technologies, similar studies as the ones provided for stripline and microstrip could be done, extending the scope of the thesis.

2.2.3.3. Coupled transmission lines

Although this part deals with multimode coupling, the aimed final result and the core foundations will be closer to single-mode considerations.

A wide variety of applications are covered by different configurations of couplers since the 50's [48–50]. Focusing henceforth on planar technology, the simplest form of directional coupler can be described. It consists of two parallel conducting strips situated close enough so as to assure a coupling of energy between the lines.

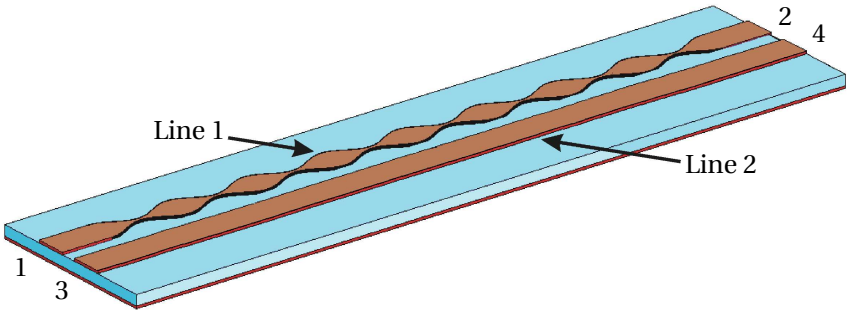

Figure 2.23: General sketch of a directional coupler in planar technology with labeled ports and constitutive lines.

A general description of the coupled transmission lines can be accomplished applying rigorously the cross-section method of the coupled-mode theory to the modes of each line. If only discrete spectrum modes are taken into account (what in a simplified manner means to avoid radiation) and the coupling to higher order modes is neglected, the following system of equations will characterize accurately the coupled transmission lines [51, 52]:

$$\begin{aligned}
\frac{da_1^+}{dz} &= -j\beta_1 a_1^+ + C_{1,-1}a_1^- + C_{1,2}a_2^+ + C_{1,-2}a_2^- \\
\frac{da_1^-}{dz} &= C_{-1,1}a_1^+ + j\beta_1 a_1^- + C_{-1,2}a_2^+ + C_{-1,-2}a_2^- \\
\frac{da_2^+}{dz} &= C_{2,1}a_1^+ + C_{2,-1}a_1^- - j\beta_2 a_2^+ + C_{2,-2}a_2^- \\
\frac{da_2^-}{dz} &= C_{-2,1}a_1^+ + C_{-2,-1}a_1^- + C_{-2,2}a_2^+ + j\beta_2 a_2^-
\end{aligned} \tag{2.138}$$

being a_1^+ and a_2^+ the complex amplitudes of the forward waves of the fundamental mode of each line numbered as 1 and 2, respectively, and labeled in Figure 2.23; a_1^- and a_2^- the complex amplitudes of the backward waves of the fundamental mode of each line; β_1 and β_2 the phase constants of the forward waves of the fundamental mode of each line; C_{mi} the coupling coefficients between m and i modes, i.e., between all the forward and backward waves of the fundamental modes for the lines 1 and 2.

The system of equations (2.138) has been studied by Adair et al. in [51] and Krage et al. in [52]. As a result, expressions for the previous parameters have been provided as functions of the distributed inductance and capacitance per unit length. However, in this thesis, such a general solution is not necessary, because side-by-side symmetry is desired [53].

In side-by-side symmetrical coupled lines, even and odd mode decomposition can

be used and both modes are taken as fundamental modes of the two coupled lines. By doing so, the target relationships between the S-parameters, the C_{mi}, and the physical dimensions in symmetrical coupled transmission lines can be obtained [54, 55]. Under this decomposition, coupled lines can be modeled and simply characterized by the even- and odd-mode characteristic impedances and the even- and odd-mode phase constants, as it will be seen in this subsection.

Considering side-by-side symmetry and only fundamental even and odd modes involved in the coupling process, the coupled-mode theory can be applied leading to

$$\begin{aligned}
\frac{da_e^+}{dz} &= -j\beta_e a_e^+ + C_{e,-e}a_e^- \\
\frac{da_e^-}{dz} &= C_{-e,e}a_e^+ + j\beta_e a_e^- \\
\frac{da_o^+}{dz} &= -j\beta_o a_o^+ + C_{o,-o}a_o^- \\
\frac{da_o^-}{dz} &= C_{-o,o}a_o^+ + j\beta_o a_o^-
\end{aligned} \tag{2.139}$$

where a_e^+, a_e^- are the complex amplitudes of the forward and backward waves of the even mode and a_o^+, a_o^- are the complex amplitudes of the forward and backward waves of the odd mode; β_e and β_o are the phase constants of the forward waves of the even and odd modes, respectively; $C_{\pm e,\mp e}$ and $C_{\pm o,\mp o}$ are the coupling coefficients between the forward and backward waves of the even and odd modes, respectively.

It can be seen that the system (2.139) can be actually split into two independent systems: the first one involves only even mode variables, while the second only odd mode variables. For the even mode it can be shown that:

$$\begin{aligned}
\frac{da_e^+}{dz} &= -j\beta_e a_e^+ + C_{e,-e}a_e^- \\
\frac{da_e^-}{dz} &= C_{-e,e}a_e^+ + j\beta_e a_e^-
\end{aligned} \tag{2.140}$$

where in order to relate the characteristic impedance with the coupling coefficient, equation (2.122) can be used, knowing also that $C_{e,-e} = C_{-e,e}$ as it can be readily obtained from (2.80a). For the odd mode a resembled system can be shown:

$$\begin{aligned}
\frac{da_o^+}{dz} &= -j\beta_o a_o^+ + C_{o,-o}a_o^- \\
\frac{da_o^-}{dz} &= C_{-o,o}a_o^+ + j\beta_o a_o^-
\end{aligned} \tag{2.141}$$

where equation (2.122) can be used once again, knowing also that $C_{o,-o} = C_{-o,o}$ as it can be deduced again from (2.80a). Moreover, both of them are formally identical to

each other and also to the one obtained in subsection 2.2.1.2 for single transmission lines or waveguides, and listed as (2.86).

Taking advantage of the even and odd mode decomposition, the most meaningful S-parameters can be calculated as [56]

$$S_{11} = \frac{\Gamma_e + \Gamma_o}{2} \tag{2.142a}$$

$$S_{21} = \frac{\mathrm{T}_e + \mathrm{T}_o}{2} \tag{2.142b}$$

$$S_{31} = \frac{\Gamma_e - \Gamma_o}{2} \tag{2.142c}$$

$$S_{41} = \frac{\mathrm{T}_e - \mathrm{T}_o}{2} \tag{2.142d}$$

where Γ_e, Γ_o are the reflection coefficients, T_e, T_o are the transmission coefficients of the even and odd modes, respectively, where the port numbers follow the convention of Figure 2.24. Indeed, these coefficients can be linked with the variables defined in the systems (2.140) and (2.141), resulting in:

$$\Gamma_e = \left.\frac{b_{1e}}{a_{1e}}\right|_{a_{2e}=0} = \left.\frac{\sqrt{N_e^+(z=0)}\cdot a_e^-(z=0)}{\sqrt{N_e^+(z=0)}\cdot a_e^+(z=0)}\right|_{a_e^-(z=L)=0} = \left.\frac{a_e^-(z=0)}{a_e^+(z=0)}\right|_{a_e^-(z=L)=0} \tag{2.143a}$$

$$\Gamma_o = \left.\frac{b_{1o}}{a_{1o}}\right|_{a_{2o}=0} = \left.\frac{\sqrt{N_o^+(z=0)}\cdot a_o^-(z=0)}{\sqrt{N_o^+(z=0)}\cdot a_o^+(z=0)}\right|_{a_o^-(z=L)=0} = \left.\frac{a_o^-(z=0)}{a_o^+(z=0)}\right|_{a_o^-(z=L)=0} \tag{2.143b}$$

$$\mathrm{T}_e = \left.\frac{b_{2e}}{a_{1e}}\right|_{a_{2e}=0} = \left.\frac{\sqrt{N_e^+(z=L)}\cdot a_e^+(z=L)}{\sqrt{N_e^+(z=0)}\cdot a_e^+(z=0)}\right|_{a_e^-(z=L)=0} \tag{2.143c}$$

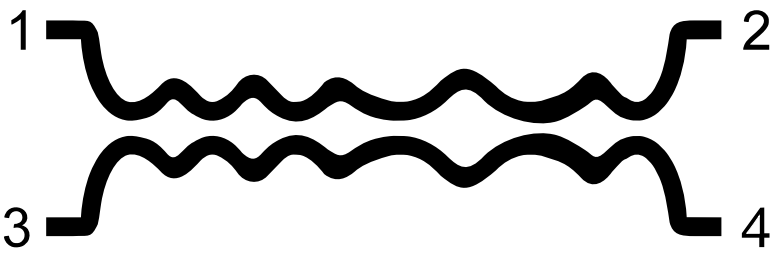

Figure 2.24: Sketch of side-by-side symmetrical coupled transmission lines. The ports are labeled according to the Figure 2.23.

$$\mathrm{T}_o = \left.\frac{b_{2o}}{a_{1o}}\right|_{a_{2o}=0} = \left.\frac{\sqrt{N_o^+(z=L)}\cdot a_o^+(z=L)}{\sqrt{N_o^+(z=0)}\cdot a_o^+(z=0)}\right|_{a_o^-(z=L)=0} \tag{2.143d}$$

It is worth noting that if all the involved ports are identical and/or the normalization does not vary with z, the expressions for the T_e and T_o parameters can be simplified and expressed as:

$$\mathrm{T}_e = \left.\frac{a_e^+(z=L)}{a_e^+(z=0)}\right|_{a_e^-(z=L)=0} \tag{2.144a}$$

$$\mathrm{T}_o = \left.\frac{a_o^+(z=L)}{a_o^+(z=0)}\right|_{a_o^-(z=L)=0} \tag{2.144b}$$

Considering (2.142a) and (2.142c), it is straightforward to show that if the design condition

$$\Gamma_e(f) = -\Gamma_o(f) \tag{2.145}$$

is satisfied, then $S_{11}(f) = 0$ and $S_{31}(f) = \Gamma_e(f)$, producing a device with the input port (#1) matched at all frequencies and with the reflected signal redirected to the coupled port (#3).

Once again, a link has been established between the frequency response, in terms of S-parameters, and both coupling coefficients, through systems (2.140) and (2.141). In order to obtain ready to use equations for the connection between physical parameters and the previously defined coupling coefficients, a particular technology has to be selected. This connection will be obtained below for symmetrical edge-coupled stripline and microstrip.

Symmetrical edge-coupled stripline

The edge-coupled stripline technology consists of two striplines placed side-by-side with the conducting strips close enough so as to have a transfer of energy between them. Forcing symmetry in order to apply the even and odd mode decomposition, this technology will be characterized by the width of the conducting strips, W_{cs}, and their separation, S_{cs}, see Figure 2.25. Moreover, the distance between the ground planes that embeds a homogeneous dielectric with relative permittivity, ε_r, will be fixed to h_{cs}. The distance between the conducting strips and the two ground planes must be equal, yielding to the configuration shown in Figure 2.25.

Even and odd mode decomposition will be fruitfully used if the coupling to higher order modes is prevented. The electric field distributions for the fundamental even and odd modes in edge-coupled stripline are depicted in Figure 2.26.

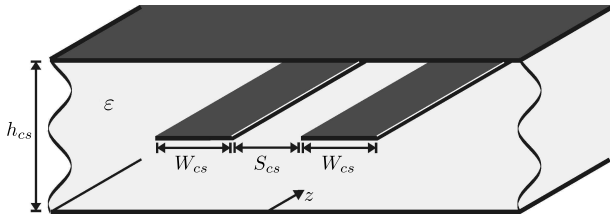

Figure 2.25: Sketch of symmetrical edge-coupled stripline technology with defined physical parameters.

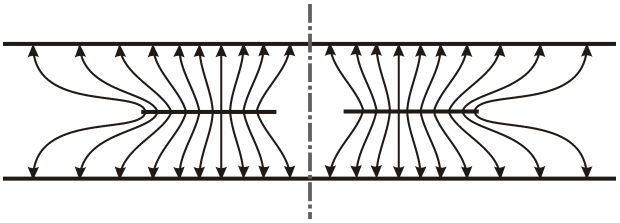

(a) Even mode

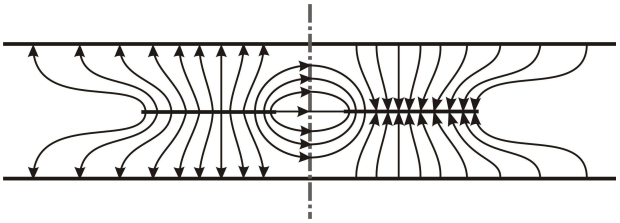

(b) Odd mode

Figure 2.26: Sketch of the E-field lines in symmetrical edge-coupled stripline technology for even and odd modes.

Due to the fact that the cross-section of the coupled striplines is filled by a single homogeneous dielectric medium, the phase constants for the even and odd modes, β_{cse} and β_{cso}, respectively, are equal and can be calculated as:

$$\beta = \beta_{cse} = \beta_{cso} = \frac{2\pi f}{c} \cdot \sqrt{\varepsilon_r} \tag{2.146}$$

Thus, system (2.140) can be rewritten in the following form:

$$\begin{aligned} \frac{da_e^+}{dz} &= -j\beta a_e^+ + K_e a_e^- \\ \frac{da_e^-}{dz} &= K_e a_e^+ + j\beta a_e^- \end{aligned} \tag{2.147}$$

being K_e the coupling coefficient between the forward and backward waves of the

even mode, which can be related with the even characteristic impedance, $Z_{0e}(z)$, from (2.124) as follows:

$$K_e = \frac{-1}{2Z_{0e}(z)} \cdot \frac{dZ_{0e}(z)}{dz}. \tag{2.148}$$

Likewise, (2.141) can be rewritten as:

$$\begin{aligned} \frac{da_o^+}{dz} &= -j\beta a_o^+ + K_o a_o^- \\ \frac{da_o^-}{dz} &= K_o a_o^+ + j\beta a_o^- \end{aligned} \tag{2.149}$$

being K_o the coupling coefficient between the forward and backward waves of the odd mode, which can be related with the odd characteristic impedance, $Z_{0o}(z)$, from (2.124) as follows:

$$K_o = \frac{-1}{2Z_{0o}(z)} \cdot \frac{dZ_{0o}(z)}{dz}. \tag{2.150}$$

In order to express in a closed form the relationship between the previously defined coupling coefficients and physical parameters, equations (2.148) and (2.150) can be solved analytically. Thus, knowing the coupling coefficients between the forward and backward waves of the even and odd modes, exact formulas for the even and odd characteristic impedances of the symmetric edge-coupled stripline can be deduced as:

$$Z_{0e}(z) = Z_{0e}(0^+)\, e^{-2\int_0^z K_e(r)dr} \tag{2.151}$$

$$Z_{0o}(z) = Z_{0o}(0^+)\, e^{-2\int_0^z K_o(r)dr} \tag{2.152}$$

being $Z_{0e}(0^+)$ and $Z_{0o}(0^+)$ the limits from the right side of the even and odd characteristic impedances, respectively, at the beginning of the device ($z = 0$) and r an auxiliary variable over which the integral is carried out.

Finally, the relationship between the physical dimensions and the even and odd characteristic impedances can be found in [8]:

$$\begin{aligned} Z_{0e} &= \frac{30\pi}{\sqrt{\varepsilon_r}} \cdot \frac{\mathrm{E}_1(\chi_e')}{\mathrm{E}_1(\chi_e)} \\ Z_{0o} &= \frac{30\pi}{\sqrt{\varepsilon_r}} \cdot \frac{\mathrm{E}_1(\chi_o')}{\mathrm{E}_1(\chi_o)} \end{aligned} \tag{2.153}$$

where

$$\mathrm{E}_1(\chi) = \int_0^{\pi/2} \frac{d\vartheta}{\sqrt{1 - \chi \sin^2(\vartheta)}} \tag{2.154}$$

$$\chi_e = \tanh\left(\frac{\pi}{2}\cdot\frac{W_{cs}}{h_{cs}}\right)\cdot\tanh\left(\frac{\pi}{2}\cdot\frac{W_{cs}+S_{cs}}{h_{cs}}\right) \tag{2.155}$$

$$\chi_o = \tanh\left(\frac{\pi}{2}\cdot\frac{W_{cs}}{h_{cs}}\right)\cdot\coth\left(\frac{\pi}{2}\cdot\frac{W_{cs}+S_{cs}}{h_{cs}}\right) \tag{2.156}$$

$$\chi'_e = \sqrt{1-\chi_e} \tag{2.157}$$

$$\chi'_o = \sqrt{1-\chi_o} \tag{2.158}$$

$\mathrm{E}_1(\chi)$ is the well-known complete elliptic integral of the first kind.

Conclusively, it must be said that for this technology the relation

$$Z_{0e} \geq Z_{0o} \tag{2.159}$$

between the even and odd impedances, will always hold and the equality will be possible only in the limit, when S_{cs} tends to infinite, and hence the striplines are decoupled [56].

If the even and odd modes feature the same phase constant, β, for a given frequency, as it happens for this technology, see (2.146), then, the design condition for devices with matched ports at all frequencies expressed in equation (2.145) can be rewritten as:

$$\Gamma_o(\beta) = -\Gamma_e(\beta). \tag{2.160}$$

If a change in sign in the reflection coefficient is introduced, see left hand side of (2.143a), the sign of the forward or the backward wave has to change, see right hand side of (2.143a). Hence, to keep the same solution in the coupled-mode system of equations (2.147), it is also necessary to take opposite sign in the coupling coefficient. Thus, the design condition can be finally rewritten as:

$$K_o(z) = -K_e(z) \tag{2.161}$$

This relationship is equivalent to:

$$Z_{0e}(z)\cdot Z_{0e}(z) = Z_{0e}(0^+)\cdot Z_{0e}(0^+) = Z_0^2 \tag{2.162}$$

where Z_0 is the characteristic impedance of the access lines that coincides with the one of the ports. The equivalence has been obtained just by substituting (2.161) in (2.152) and multiplying the result with equation (2.151). It has been supposed that the ports are decoupled (independent ports), where obviously, $Z_{0e}(0^+) = Z_{0o}(0^+) = Z_0$.

Symmetrical edge-coupled microstrip line

The edge-coupled microstrip line is achieved when two conducting strips over a grounded substrate are placed close enough so as to assure transfer of energy between them. Forcing symmetry in order to use the even and odd mode decomposition, this technology will be characterized by the width of the conducting strips, W_{cu}, their separation, S_{cu}, the height of the substrate h_{cu}, and its relative permittivity, ε_r. The geometry of the cross-section described is shown in Figure 2.27.

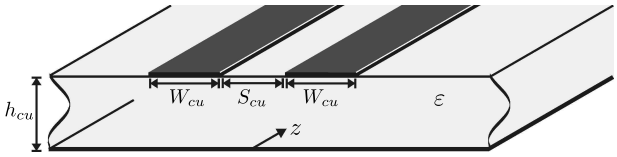

Figure 2.27: Sketch of symmetrical edge-coupled microstrip technology with defined physical parameters.

Even and odd mode decomposition will be fruitfully used if the coupling to higher order modes is avoided. The electric field distributions for the fundamental even and odd modes in edge-coupled microstrip lines are depicted in Figure 2.28.

Due to the fact that there is an air dielectric interface, the phase constants for the

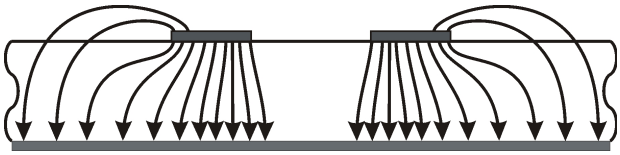

(a) Even mode

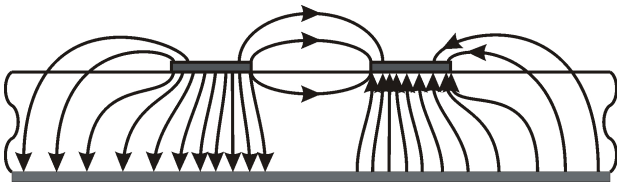

(b) Odd mode

Figure 2.28: Sketch of the E-field lines in symmetrical edge-coupled microstrip technology for even and odd modes.

even, β_{cue}, and the odd, β_{cuo}, modes are different and can be calculated as follows:

$$\begin{aligned}\beta_{cue} &= \frac{2\pi f}{c}\cdot\sqrt{\varepsilon_{ee}}\\ \beta_{cuo} &= \frac{2\pi f}{c}\cdot\sqrt{\varepsilon_{eo}}\end{aligned} \tag{2.163}$$

being ε_{ee} and ε_{eo} the effective relative permittivities for the even and odd modes, respectively, that can be calculated accurately from [1] and [57]:

$$\begin{aligned}\varepsilon_{ee} &= 0.5(\varepsilon_r+1)+0.5(\varepsilon_r-1)\left(1+\frac{10}{\nu}\right)^{-a_e(\nu)b_e(\varepsilon_r)}\\ \varepsilon_{eo} &= (0.5(\varepsilon_r+1)+a_o(u,\varepsilon_r)-\varepsilon_e)\ e^{-c_o g^{d_o}}+\varepsilon_e\end{aligned} \tag{2.164}$$

where

$$\begin{aligned}&\nu = \frac{u(20+g^2)}{10+g^2}+ge^{-g}\quad \text{being}\quad u=\frac{W_{cu}}{h_{cu}}; g=\frac{S_{cu}}{h_{cu}}\\ &a_e(\nu) = 1+\frac{1}{49}\ln\left(\frac{\nu^4+\left(\frac{\nu}{52}\right)^2}{\nu^4+0.432}\right)+\frac{1}{18.7}\ln\left(1+\left(\frac{\nu}{18.1}\right)^3\right)\\ &b_e(\varepsilon_r) = 0.564\left(\frac{\varepsilon_r-0.9}{\varepsilon_r+3}\right)^{0.053}\\ &a_o(u,\varepsilon_r) = 0.7287\left(\varepsilon_e-0.5(\varepsilon_r+)\right)\left(1+e^{-0.179u}\right)\\ &b_o(\varepsilon_r) = 0.7287\frac{\varepsilon_r}{0.15+\varepsilon_r}\\ &c_o = b_o(\varepsilon_r)-(b_o(\varepsilon_r)-0.207)\,e^{0.414u}\\ &d_o = 0.593+0.694e^{-0.562u}\end{aligned} \tag{2.165}$$

and ε_e denotes the effective dielectric constant of a single microstrip of width W_{cu}.

Thus, system (2.140) can be rewritten in the following form:

$$\begin{aligned}\frac{da_e^+}{dz} &= -j\beta_{cue}a_e^+ + K_e a_e^-\\ \frac{da_e^-}{dz} &= K_e a_e^+ + j\beta_{cue}a_e^-\end{aligned} \tag{2.166}$$

being K_e the coupling coefficient between the forward and backward waves of the even mode, which can be related with the even characteristic impedance, $Z_{0e}(z)$, from (2.124) as follows:

$$K_e \approx \frac{-1}{2Z_{0e}(z)}\cdot\frac{dZ_{0e}(z)}{dz}. \tag{2.167}$$

Correspondingly, (2.141) can be rewritten as:

$$\begin{aligned}\frac{da_o^+}{dz} &= -j\beta_{cuo}a_o^+ + K_o a_o^- \\ \frac{da_o^-}{dz} &= K_o a_o^+ + j\beta_{cuo}a_o^-\end{aligned} \tag{2.168}$$

being K_o the coupling coefficient between the forward and backward waves of the odd mode, which can be related with the odd characteristic impedance, $Z_{0o}(z)$, from (2.124) as follows:

$$K_o \approx \frac{-1}{2Z_{0o}(z)} \cdot \frac{dZ_{0o}(z)}{dz}. \tag{2.169}$$

In order to express in closed form the relationship between the previously defined coupling coefficients and physical parameters, equations (2.167) and (2.169) can be solved analytically. Thus, knowing the coupling coefficients between the forward and backward waves of the even and odd modes, approximate expressions for the even and odd characteristic impedances of the symmetrical edge-coupled microstrip can be extracted as:

$$Z_{0e}(z) \approx Z_{0e}(0^+)\, e^{-2\int_0^z K_e(r)dr} \tag{2.170}$$

$$Z_{0o}(z) \approx Z_{0o}(0^+)\, e^{-2\int_0^z K_o(r)dr} \tag{2.171}$$

being $Z_{0e}(0^+)$ and $Z_{0o}(0^+)$ the limits from the right side of the even and odd characteristic impedances, respectively, at the beginning of the device ($z = 0$) and r an auxiliary variable over which the integral is performed. It is important to take into account that the accuracy of (2.167), (2.169), (2.170), and (2.171) will depend on how well the characteristic impedance (and eventually the physical dimension) features the variation of the cross-section present in the microstrip coupled lines in terms of the reflection coefficient of the even and odd incident modes over the reflected ones.

Finally, the relationship between the physical dimensions and the even and odd characteristic impedances can be found in [57]:

$$\begin{aligned}Z_{0e} &= Z_0 \frac{\left(\frac{\varepsilon_e}{\varepsilon_{ee}}\right)^{0.5}}{1 - Q_4\left(\varepsilon_e\right)^{0.5}\left(\frac{Z_0}{377}\right)} \\ Z_{0o} &= Z_0 \frac{\left(\frac{\varepsilon_e}{\varepsilon_{eo}}\right)^{0.5}}{1 - Q_{10}\left(\varepsilon_e\right)^{0.5}\left(\frac{Z_0}{377}\right)}\end{aligned} \tag{2.172}$$

where

$$Q_1 = 0.8695u^{0.194} \tag{2.173a}$$

$$Q_2 = 1 + 0.7519g + 0.189g^{2.31} \tag{2.173b}$$

$$Q_3 = 0.1975 + \left(16.6 + \left(\frac{8.4}{g}\right)^6\right)^{-0.387} + \frac{1}{241}\ln\left(\frac{g^{10}}{1+\left(\frac{g}{3.4}\right)^{10}}\right) \tag{2.173c}$$

$$Q_4 = \frac{2Q_1}{Q_2}\cdot\frac{1}{e^{-g}u^{Q_3} + (2-e^{-g})u^{-Q_3}} \tag{2.173d}$$

$$Q_5 = 1.794 + 1.14\ln\left(1 + \frac{0.638}{g + 0.517g^{2.43}}\right) \tag{2.173e}$$

$$Q_6 = 0.2305 + \frac{1}{281.3}\ln\left(\frac{g^{10}}{1+\left(\frac{g}{5.8}\right)^{10}}\right) + \frac{1}{5.1}\ln\left(1 + 0.598g^{1.154}\right) \tag{2.173f}$$

$$Q_7 = \frac{10 + 190g^2}{1 + 82.3g^3} \tag{2.173g}$$

$$Q_8 = e^{-6.5-0.95\ln(g)-\left(\frac{g}{0.15}\right)^5} \tag{2.173h}$$

$$Q_9 = \ln(Q_7)\left(Q_8 + \frac{1}{16.5}\right) \tag{2.173i}$$

$$Q_{10} = \frac{Q_2Q_4 - Q_5e^{\ln(u)Q_6u^{-Q_9}}}{Q_2} \tag{2.173j}$$

$$Z_0 = \begin{cases} \dfrac{60}{\sqrt{\varepsilon_e}}\ln\left(\dfrac{8h_{cu}}{W_{cu}} + \dfrac{W_{cu}}{4h_{cu}}\right) & \text{for} \quad \dfrac{W_{cu}}{h_{cu}} \leq 1 \\ \dfrac{120\pi}{\sqrt{\varepsilon_e}\left(\dfrac{W_{cu}}{h_{cu}} + 1.393 + 0.667\ln\left(\dfrac{W_{cu}}{h_{cu}} + 1.444\right)\right)} & \text{for} \quad \dfrac{W_{cu}}{h_{cu}} \geq 1 \end{cases} \tag{2.173k}$$

and ε_e denotes the effective dielectric constant of a single microstrip of width W_{cu}.

After all, it must be asserted that for microstrip technology the relation

$$Z_{0e} \geq Z_{0o} \tag{2.174}$$

between the even and odd impedance will always hold and the equality will be only possible when S_{cu} is infinite [56].

It can also be stated that the following relationship between the effective relative permittivities involved in edge-coupled microstrip lines will be always satisfied:

$$\varepsilon_r > \varepsilon_{ee} > \varepsilon_{eo} \tag{2.175}$$

The design condition for devices with matched ports at all frequencies expressed in equation (2.160) can be rewritten taking into account (2.163) as:

$$\Gamma_o(\beta_{cuo}) = -\Gamma_e(\beta_{cue}) \tag{2.176}$$

which can be transformed to the following equation as it was explained for the coupled stripline case:

$$K_o(z_o) = -K_e(z_e) \tag{2.177}$$

However, the effective relative permittivities for the even and odd modes have a complicated dependence with the physical dimensions (2.164), forcing to a new strategy for the application of condition (2.145).

The idea is to obtain the even- and odd-mode characteristic impedances for an auxiliary device without taking into account the difference between the even and odd phase constants (like in the stripline case). Then, an algorithm for compensating the actual difference in the phase constants over symmetrical edge-coupled microstrip lines, once the substrate is selected, will be applied [58, 59]. Therefore, assuming that the auxiliary device has a total length of L_{aux} and relative permittivity of ε_{aux}, and using equations (2.146), (2.147), (2.151), (2.152), and (2.162), the even and odd mode characteristic impedances are achieved. Now, the algorithm which takes into account in each step the speed of propagation of each mode along the device has to be computed as described in Algorithm 2.4.

The effect of the algorithm can be explained intuitively as a redistribution of the even- and odd-mode characteristic impedances calculated for the case where both modes propagate at the same speed. The auxiliary impedances are redistributed along the propagation direction, z, in such a way that the even and odd modes propagating at different speeds are affected at each time instant by the same pair of even and odd impedances, as in the case of equal speed propagation. Due to the fact that (2.175) always holds, the process leads to a local compression for the even-mode characteristic impedance, and to a local expansion for the odd-mode characteristic impedance. For the same reason, it will be necessary to pad with enough values equal to $Z_{0e}(L_{\text{aux}})$ the even characteristic impedance $Z_{0e}(z)$, in order to have both characteristic impedances with the same length at the output of the algorithm. It is worth noting that in general, $Z_{0e}(L_{\text{aux}})$ will be similar to Z_0, the impedance of the ports and the access lines.

Although the expressions that relate the physical parameters to the characteristic impedances (for the different technologies presented in this section) are accurate enough in general, precision for extreme values will not be always guaranteed. Hence, the LineCalc tool that belongs to the electromagnetic commercial software package Advanced Design System (ADS) of Agilent™ will be used for the extreme values and eventually for the final prototypes [47].

Inputs of the algorithm:

ε_{aux};

$Z_{0e,\text{in}}(z), Z_{0o,\text{in}}(z) \;\; \forall z \in [0, L_{\text{aux}}]$;

Definition of the substrate for microstrip coupled-lines;

Outputs of the algoritm:

$Z_{0e}^{\text{out}}(z_n), Z_{0o}^{\text{out}}(z_n) \quad \forall z_n \in [0, L]$;

Algorithm:

For $z_n \in [0, L]$

{

$z_e = \int_0^{z_n} \sqrt{\varepsilon_{ee}(x)/\varepsilon_{\text{aux}}}dx$;

$z_o = \int_0^{z_n} \sqrt{\varepsilon_{eo}(x)/\varepsilon_{\text{aux}}}dx$;

$Z_{0e}(z_n) = Z_{0e,\text{in}}(z_e)$;

$Z_{0o}(z_n) = Z_{0o,\text{in}}(z_o)$;

Calculation of $\varepsilon_{ee}(z_n)$ and $\varepsilon_{eo}(z_n)$ for $Z_{0e}(z_n)$ and $Z_{0o}(z_n)$ in the microstrip substrate;

$\varepsilon_{ee}(z_{n+1}) = \varepsilon_{ee}(z_n)$;

$\varepsilon_{eo}(z_{n+1}) = \varepsilon_{eo}(z_n)$;

}

Algorithm 2.4: Compensation in coupled microstrip line of the different dependence of the even and odd phase constants on z.

2.2.4. Design of a filter with two independent passbands

The general synthesis technique presented in previous sections is not restricted to the classical function responses, i.e. Butterworth, Chebyshev, and Cauer. Hence, in order to demonstrate that microwave filters with arbitrary responses can be perfectly achieved with this synthesis method, a double bandpass filter will be designed. Although usually direct optimization methods have been applied for these cases [44], here the rational function that satisfies the intended specifications will be accomplished by means of the technique presented in Section 2.1. The proposed methodology rests on the translation of the target specifications from the analog to the digital domain, where the microwave designer can take immediate advantage of the sophisticated and continuously developing digital filter design techniques.

TABLE 2.5
ANALOG SPECIFICATIONS WITH THE CORRESPONDING DIGITAL SPECIFICATIONS FOR A FILTER WITH TWO INDEPENDENT PASSBANDS.

Passbands	DC to 4 GHz	Return loss > 20 dB	0 to 0.5π rad/s
	8.25 to .75 GHz		0.71π to 0.75π rad/s
Stopbands	6 to 7.5 GHz	Rejection > 20 dB	0.62π to 0.68π rad/s
	10.5 to 12 GHz		0.76π to 0.79π rad/s

The specifications that are aimed to satisfy are summarized in Table 2.5 which include two independent passbands and two stopbands. The digital specifications are obtained applying the bilinear transformation introduced in subsection 2.1.2.2 by means of (2.51) to the provided analog specifications. The two parameters involved in the bilinear transformation are the sampling frequency f_s and the pre-warping frequency β_p, as it was explained. The sampling frequency has been fixed to 30 GHz and the pre-warping frequency selected to match 6 GHz. The final digital specifications are included in Table 2.5.

An iterative quasi-Newton type algorithm has been used to design the digital filter satisfying the calculated digital specifications. An additional stopband above 0.83π, corresponding to 15 GHz, has been included to the digital specifications, so that it is assured that the frequency response tends to zero when the frequency goes to infinity, as it is required by the synthesis method. The quasi-Newton type algorithm, available in the MATLAB standard function called `iirlpnorm.m`, minimizes the error function defined as the p-norm of the weighted difference between the target and the obtained frequency response of the filter, see (2.60). The value of p is increased from 2 to 128

TABLE 2.6
POLES AND ZEROS OF THE DIGITAL FILTER AND THE ANALOG FILTER RESPONSES $S_{11}(s)$ AND $S_{21}(s)$.

p_i	c_i	p_n	c_n	k_n
$-0.6466 \pm 0.7174j$	$-0.4001 \pm 0.9163j$	$-37.889 \pm 809.83j$	$-0.1084 \pm 551.53j$	$-1.6481 \pm 779.31j$
$-0.5650 \pm 0.7380j$	$-0.5040 \pm 0.8635i$	$-66.923 \pm 726.01j$	$-0.0991 \pm 628.64j$	$-2.9487 \pm 732.98j$
$-0.5375 \pm 0.8137j$	$-0.4557 \pm 0.4378j$	$-20.1863 \pm 670.5940j$	$-444.31 \pm 647.72j$	$-1.1666 \pm 693.58j$
$-0.0280 \pm 0.9012j$	-2.3294	$-38.4387 \pm 370.3121j$	904.03	$-1.1901 \pm 486.60j$
$-0.3205 \pm 0.9085j$	-1.1801	$-20.1715 \pm 509.5601j$	4369.88	$-3.0464 \pm 447.26j$
$-0.2069 \pm 0.8424j$	-0.8634	$-66.7560 \pm 454.32j$	-4924.05	$-1.8589 \pm 400.88j$
	-0.3095		-684.64	
	-0.2245		-569.99	
	-0.2113		-554.38	

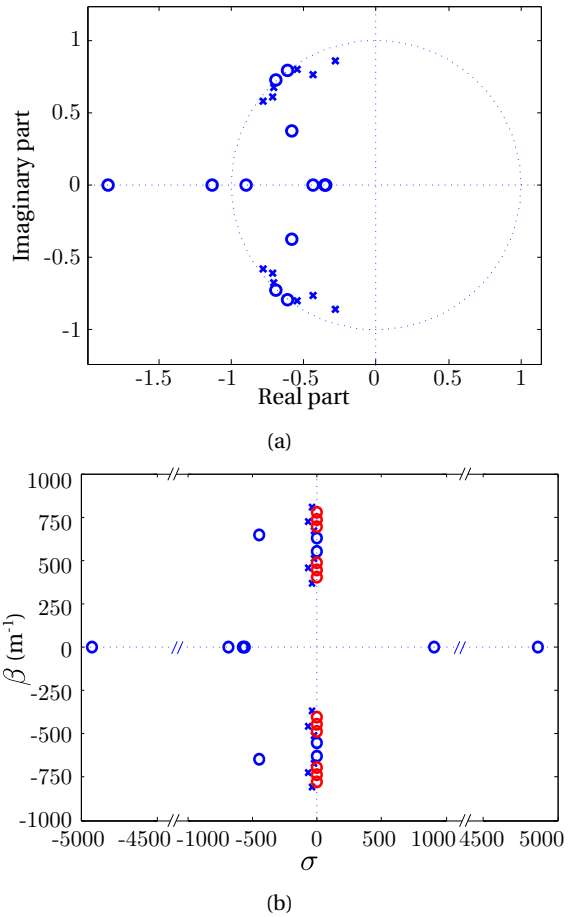

Figure 2.29: (a) Poles ('x') and zeros ('o') of the designed digital filter and (b) poles ('x') of the analog filter after the bilinear transformation.

iteratively by default, so that the final error function approaches the minimax error function. The order has been chosen to be $n = 12$. Furthermore, a weighting vector can be included in the input parameters of the function to increase the contribution of the error at a given frequency, so that the error at this point is reduced. In this case, the weighting vector is adjusted to be $W = [10\,10\,5000\,5000\,100\,100\,5000\,5000\,20\,20]$ each value corresponding to the edges of the specified frequency bands (including the additional stopband). As a result of the algorithm, the poles and zeros of the digital filter are found which have been depicted in Figure 2.29(a) and their values written in table Table 2.6.

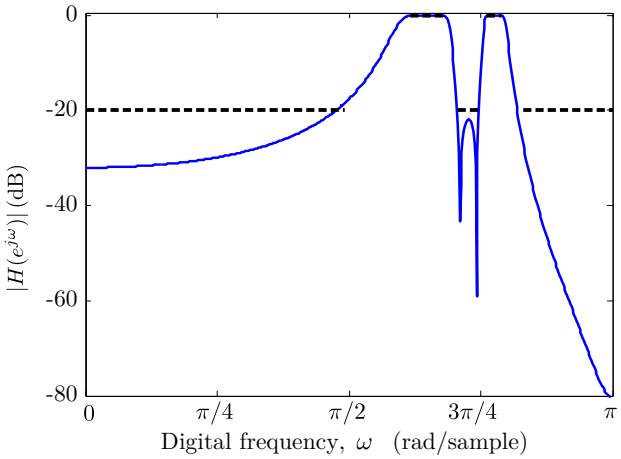

Figure 2.30: Frequency response of the digital filter (blue solid line) including the digital specifications (horizontal dashed black lines).

The frequency response of the resulting filter is calculated evaluating the contribution of each digital pole, p_i, and digital zero, c_i, following [14]

$$20\log\left|H(e^{j\omega})\right| = 20\log(H_0) + \sum_{i=1}^{N} 20\log|1 - c_i e^{-j\omega}| - \sum_{i=1}^{N} 20\log|1 - p_i e^{-j\omega}| \quad (2.178)$$

and the result is depicted in Figure 2.30 together with the digital specifications.

The pursued analog filter is obtained applying the inverse bilinear transformation as described in subsection 2.1.2.2. Indeed, applying (2.52) to each pole and zero of the digital filter, the analog poles and zeros are obtained. The resulting poles and zeros are listed in Table 2.6 and plotted in Figure 2.29(b). Moreover, the zeros of the corresponding $S_{21}(s)$ are included since they are required also in the synthesis method.

As it was done for the digital filter, the analytical frequency response, $S_{11}(s)$, of the microwave filter is obtained as the sum of the contributions of each analog pole, p_n, and analog zero, c_n, using [4]

$$20\log|H(j\beta)| = 20\log(H_0) + \sum_{n=1}^{N} 20\log|j\beta - c_n| - \sum_{n=1}^{N} 20\log|j\beta - p_n| \quad (2.179)$$

with β related to the frequency by the well-known expression

$$\beta = \frac{2\pi f\sqrt{\varepsilon_r}}{c} \quad (2.180)$$

being c the speed of light in vacuum and ε_r the relative permittivity of the stripline technology which is the one aimed to be used, in this case $\varepsilon_r = 9.8$. The resulting

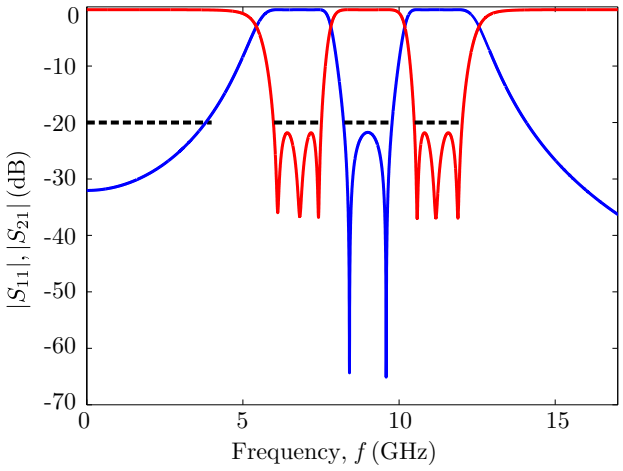

Figure 2.31: Analog specification (horizontal dashed lines) together with the simulated $|S_{21}|$-(red line) and $|S_{11}|$-parameters (blue line) of the analytical analog function.

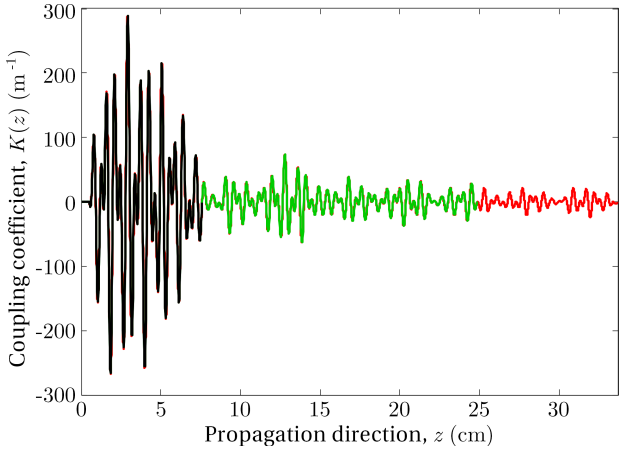

Figure 2.32: Coupling coefficient as a function of the distance for three different lengths: 71 mm (black line), 254 mm (green line), and 337 mm (red line).

frequency response is depicted in Figure 2.31 together with the target analog specifications which are properly satisfied. Its corresponding $S_{21}(s)$ is also included.

Starting from the analog poles and zeros found in the mapping process, the synthesis technique presented in the subsection 2.2.2 can be directly applied in order to accomplish the required coupling coefficient following the proposed Algorithm 2.2.

The analog poles and zeros yield to a coupling coefficient that extends along an infinite length. From the practical point of view, the coupling coefficient needs to be

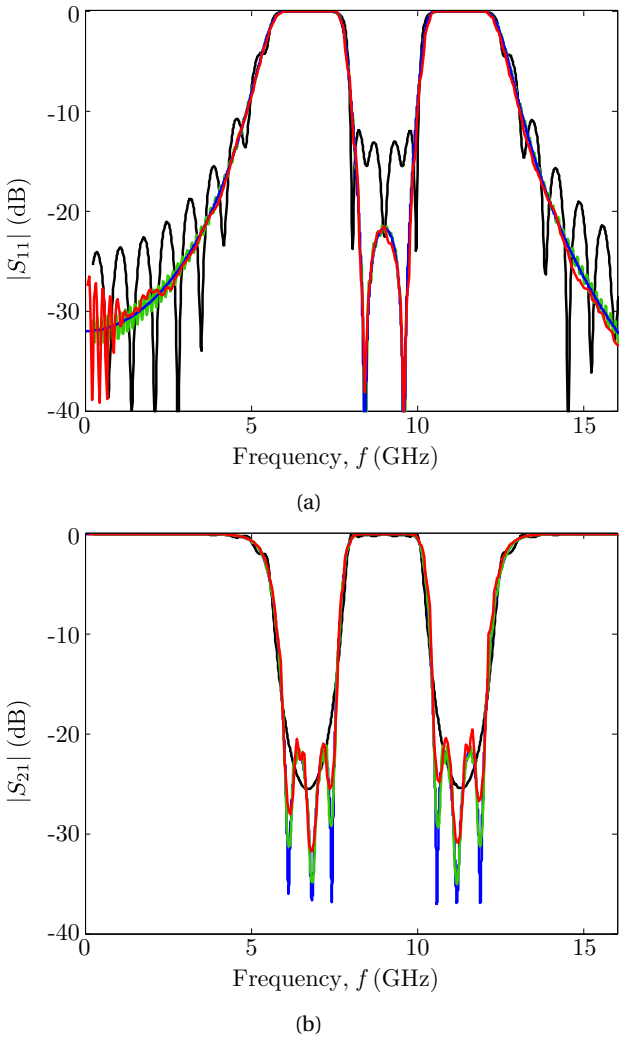

Figure 2.33: Target (blue line) and simulated (a) $|S_{11}|$- and (b) $|S_{21}|$-parameters of the analog filter with two-independent passbands for three different lengths of the coupling coefficient: 71 mm (black line), 254 mm (green line), and 337 mm (red line).

truncated. Three different lengths have been analyzed here in order to compare their performances. The truncated coupling coefficients are shown in Figure 2.32 and the corresponding Matlab simulations (using the coupled-mode theory and taking into account single-mode operation) are plotted in Figure 2.33. The 254-mm-long coupling coefficient is finally selected which provides a perfect agreement between the

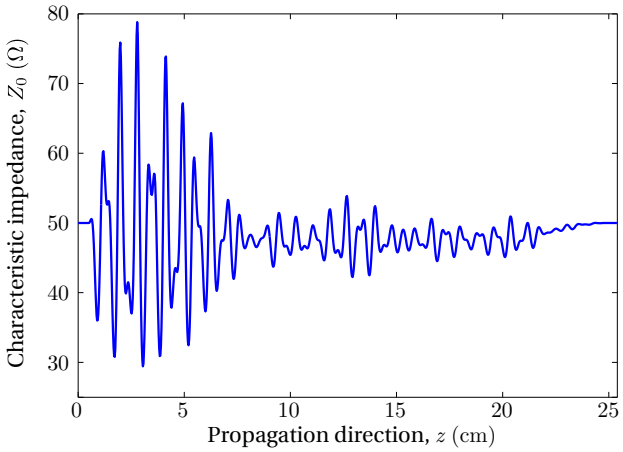

Figure 2.34: Characteristic impedance as a function of the distance.

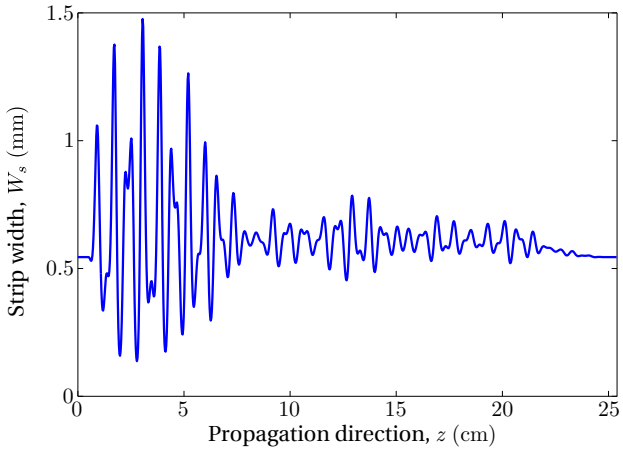

Figure 2.35: Strip width variation along the distance of the stripline implementation.

simulation and the target analog response. The longest one (337 mm) does not give almost any advantage in the obtained S-parameters while the shortest option (71 mm) does not fulfill the aimed specification. A Hanning windowing function is applied to the final part of the selected coupling coefficient in order to smooth the abrupt transition that appears when it is truncated.

The microwave filter is implemented in stripline technology using a Taconic CER10 substrate ($\varepsilon_r = 9.8$, dielectric thickness $h_s = 2.54$ mm) with $50\,\Omega$ input and output ports. The characteristic impedance along the distance is achieved following (2.127), see Figure 2.34. It will be eventually accomplished varying the width of the conducting

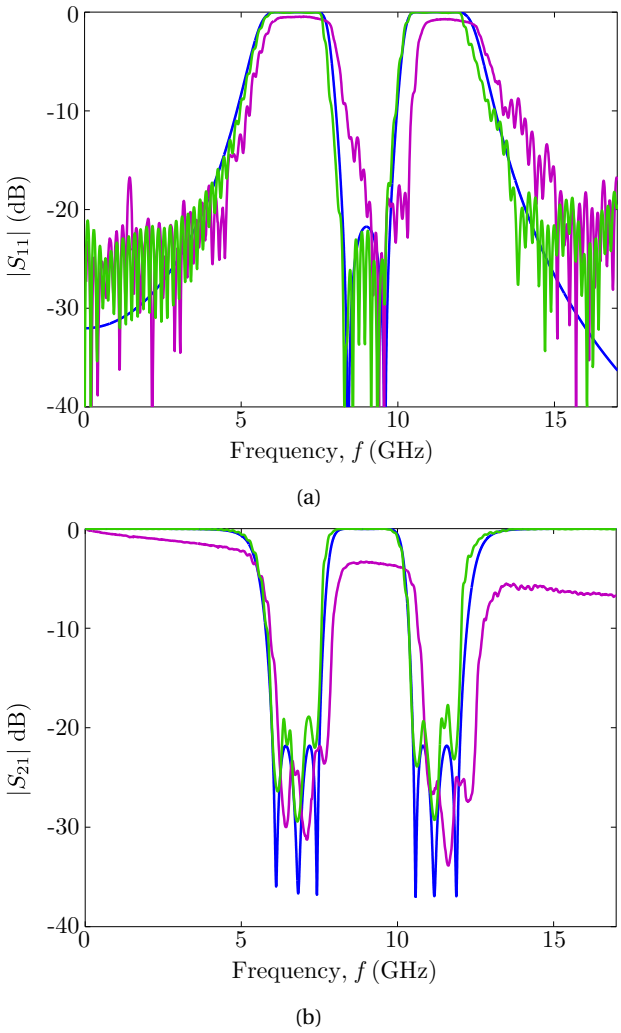

Figure 2.36: (a) $|S_{11}|$- and (b) $|S_{21}|$-parameters of the target frequency response (blue line), ADS Momentum simulation (green line), and measurements (purple line) of the two independent passband filter.

strip of the stripline, see Figure 2.35.

The stripline filter with a final total length of 254 mm has been fabricated and its S_{11}-and S_{21}-parameters have been measured by means of Agilent™ 8722ES Vector Network Analyzer and are depicted in Figure 2.36 together with the target analog response and the simulations performed with Agilent™ ADS Momentum.

A good agreement is obtained between the target responses, the simulations and

the measurements, confirming the good performance of the proposed technique. However, an appreciable frequency shift has occurred in the fabricated prototype due to the appearance of an air-gap between the substrate layers of the stripline. Moreover, the losses, which have not been taken into account during the design process, introduce circa 7 dB of attenuation at the highest frequencies (17 GHz). Superconducting materials over alumina substrates can strongly reduce the effect of losses, making the device more competitive from the performance point of view.

2.2.4.1. Compacting methods using multilayer technology

Observing the physical dimensions of the filter, it is clear that the presented synthesis technique produces electrically large devices. However, more compact devices can be obtained using multilayer technology. Low Temperature Cofired Ceramic (LTCC) will be used to demonstrate how the device can be integrated into a multilayer device.

In the following sections LTCC technology will be introduced, and afterwards, the design will be adapted to the new technology considering its practical limitations.

Low Temperature Cofired Ceramic (LTCC)

Low Temperature Cofired Ceramic (LTCC) is an advanced ceramic material that enables the creation of multilayer/3D circuits [60].

The origin of ceramic substrates goes back to the 1950s, when the basics of the current technology process where discovered. The necessary steps to obtain a monolithic ceramic substrate were described at that time. In the early 1980s, the first applications of the technology were already developed. A multilayer circuit board was created for IBM's mainframe computer made of a ceramic substrate using alumina as dielectric. This material required a firing temperature of 1600ºC, and conducting materials with very high melting points such as molybdenum (Mo) or tungsten (W) had to be used despite of not having high conductivity. This technology was named as High Temperature Cofired Ceramic (HTCC).

As the density of components and wiring on the circuit board increased, the electric resistance of the wiring also increased, requiring the use of conducting materials with lower electric resistance, as copper (Cu), gold (Au) or silver (Ag). However, the melting point of this metals is between 900 and 1000ºC, much lower than the required temperature for the firing of the alumina ceramics.

By the 1990s, research of many manufacturers gives as a result the first Low Temperature Cofired Ceramics (LTCC). In this case, glass and ceramic composites are used as insulating material, and metals with high conductivity as conducting materials.

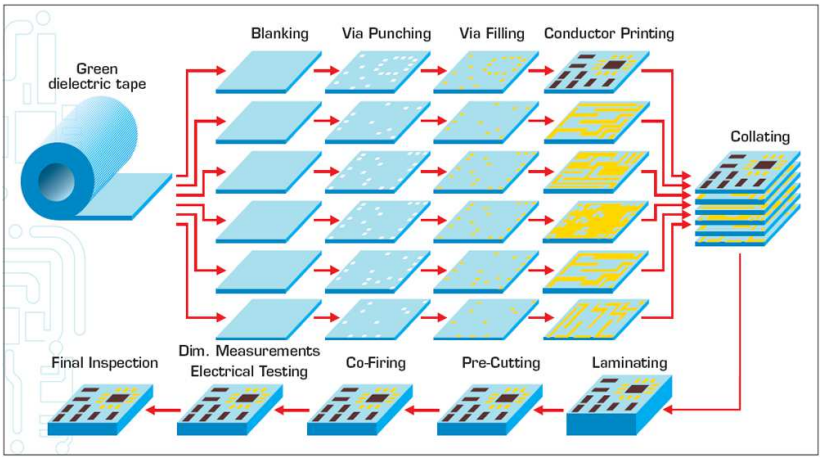

Figure 2.37: Typical manufacturing process of a multilayer ceramic substrate.
Source: http://www.imc-india.com

This ceramic composites require a firing temperature of approximately 850°C, below the melting point of the conductor materials.

Figure 2.37 describes the manufacturing process of a typical multilayer ceramic substrate. The "green dielectric tape" takes this name to describe that it is the raw or unprocessed ceramic material. It consists of a mixture of ceramic powders and an organic binder, that is cast creating the green sheet which is flexible before the firing. Each of the layers composing the substrate is processed separately and afterwards all of them are assembled together. During lamination the stacked layers are pressed under the proper temperature conditions indicated by the supplier. After cutting the remaining material, the co-firing process starts consisting in a heating and cooling process following the temperature and timing indicated by each supplier. During firing the binder acts as bonding between layers, creating a compact monolithic substrate.

The good electric properties of LTCC substrates makes them a good choice for high frequency applications. Dielectric permittivity of LTCC substrates are relatively high contributing to the reduction of the component size. Typical values go from 5 to 9.5 [61–63], but values up to 15.1 are available [64]. Moreover, the loss tangent is low compared to resins like FR4 and comparable to the high frequency substrates based on PTFE material. It varies between 0.001 to 0.0063, a quite wide range of values depending on the supplier and the material [65, 66].

In addition, probably the most appealing property of LTCC technology is its integration capability. Buried passive elements (R, L, C) can be implemented, antennas can be integrated in the same substrate, and surface mounted devices can be also

used. Actually, several front-end modules including the antenna and all the radio frequency circuitry have been already reported in the literature [67–69]. This integration is also possible with silicon based elements due to the low thermal expansion coefficient of LTCC substrates, which is close to that of the semiconductors producing a good matching between the components.

As a disadvantage, we can say that the technology is not mature yet and the manufacturing processes have to be optimized. Moreover, typical LTCC substrates suffer a shrinkage process during firing that has to be taken into account during design. However, the most recently commercialized products are new green tapes that use a zero shrinkage sintering process, which restricts the ceramic shrinkage to the z direction (thickness), such as Heralock™ tapes (Heraeus Inc. [62]) and LCF™ tapes (Murata Manufacturing Co., Ltd [64]). Another alternative is the Zero Shrinkage Technology (ZST™) that uses an alternative processing for the green tape manufacturing called the High Shear Compaction (HSC™) method [70]. This is the actual trend of the development of the green tapes, together with environmental friendly substrates, that means being lead and cadmium free.

Modified design for LTCC

Considering the advantages of the LTCC technology and having the possibility to use it thanks to our colleagues of the Universidad Politécnica de Valencia, we will modify the design obtained previously to implement it in LTCC technology.

First of all, the design has to be adapted to a new substrate selected between the *green tapes* of various suppliers. For this purpose it is not necessary to repeat all the process described before. The design can be easily adapted to the new substrate using the *scaling* property of the relationship $K(z) \longleftrightarrow S_{11}(\beta)$ reported in [40]. This property states that

$$\psi \cdot K(\psi \cdot z) \longleftrightarrow S_{11}\left(\frac{\beta}{\psi}\right) \tag{2.181}$$

where ψ is a real positive constant. Introducing this property into the relationship between $K(z)$ and $Z_0(z)$, (2.126), leads to a similar relationship between $Z_0(z) \longleftrightarrow S_{11}(\beta)$ that is

$$Z_0(\psi \cdot z) \longleftrightarrow S_{11}\left(\frac{\beta}{\psi}\right). \tag{2.182}$$

If the permittivity of the substrate changes from ε' to ε, the phase constant for a given frequency also changes from β' to β. Using the scaling property described above, we can keep the frequency response unchanged if

$$\beta' = \frac{\beta}{\psi}$$

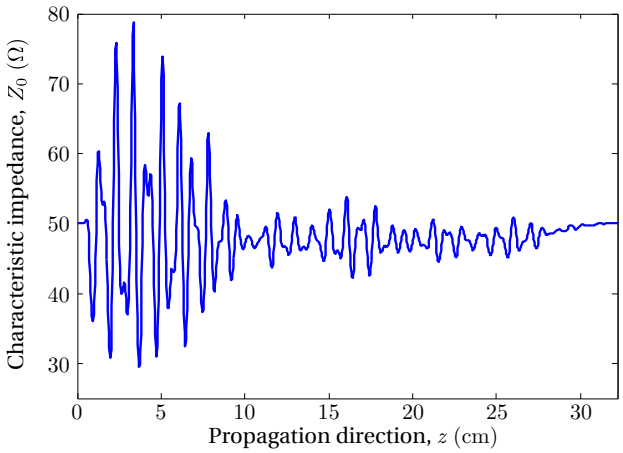

Figure 2.38: Characteristic impedance for the Ferro A6-S substrate of 8 layers of thickness.

which implies

$$\frac{2\pi f\sqrt{\varepsilon'}}{c} = \frac{2\pi f\sqrt{\varepsilon}}{c\cdot\psi} \Rightarrow \psi = \sqrt{\frac{\varepsilon}{\varepsilon'}}$$

giving the necessary scaling factor ψ so that the response, $S_{11}(\beta)$, is shifted to the values of β that correspond to the same frequency specifications in the new substrate.

For any selected substrate, the relation in (2.182) only modifies the scaling in the propagation direction, but does not change the impedance values which will vary from 30 to 80 Ω, see Figure 2.34. In this case, the selected substrate is Ferro A6-S with a relative permittivity of $\varepsilon_r = 5.9$. Hence, $\psi = \sqrt{5.9/9.8}$ has to be used to modify the impedance in Figure 2.34 into the new one, depicted in Figure 2.38. It can be seen that the total length of the device is now approximately 322 mm, longer than before, as it is expected due to the lower dielectric permittivity of the new substrate.

The obtained characteristic impedance will be implemented again varying the width of the conducting strip of the stripline that depends on the thickness of the substrate we want to implement. The selected substrate is provided in laminates of 0.254 mm of thickness (which result in 0.193 mm after firing). We will use 8 layers of Ferro A6-S substrate, with a total post-fired thickness of 1.544 mm, in order to be able to implement the impedances with a minimum strip width of 0.1 mm. The strip width to be implemented is calculated using Agilent™ LineCalc and it is shown in Figure 2.39, where it can be confirmed that the required minimum of 0.1 mm is satisfied.

The stripline with a varying strip width following the curve in Figure 2.39 has been simulated using Agilent™ ADS Momentum to confirm the correct performance of the

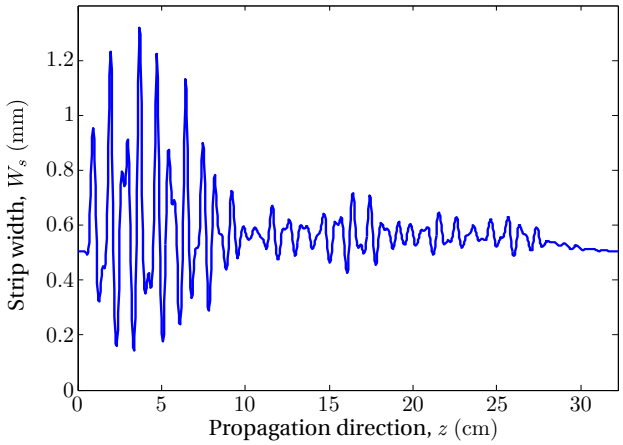

Figure 2.39: Strip width variation along the distance of the stripline implementation for the Ferro A6-S substrate.

design in the new substrate. The result of the simulation is shown in Figure 2.40 together with the target response, and a good agreement can be observed. However, the device is too long to fabricate as a single line in one direction. The maximum available area for the fabrication is a square area of 87.5 mm by 87.5 mm. In addition, the shrinkage of the material during co-firing will reduce the dimensions of the final device in a 15.3 %, which means that the size of the available area is 75 mm by 75 mm. Hence, the device will be meandered to fit into the maximum available area.

Several options have been considered to bend the device in a zigzag, such as curving the strip in a semicircular manner (Figure 2.41(a)) or using 90º bends with mitered corners (Figure 2.41(b)). However, the configuration in Figure 2.41(c) barely alters the performance of the original device implemented in line if the position of the bends is selected appropriately. Those points are selected where the coupling coefficient is close to zero, so that the influence of the bends in the response is minimized. Moreover, the 90º bends are implemented in two steps of 45º in order to have a smoother transition. In addition, the separation of the different sections has to be high enough so that there is no coupling between the lines. Considering all these, the device has been meandered to fit the maximum available area, resulting in the layout shown in Figure 2.42. The total occupied area is also indicated, which is 62.2 mm by 52.5 mm.

The final meandered device has been simulated using Agilent™ ADS Momentum, and the results are shown in Figure 2.43 where the simulation results of the not meandered device has been also included. A good agreement can be observed between

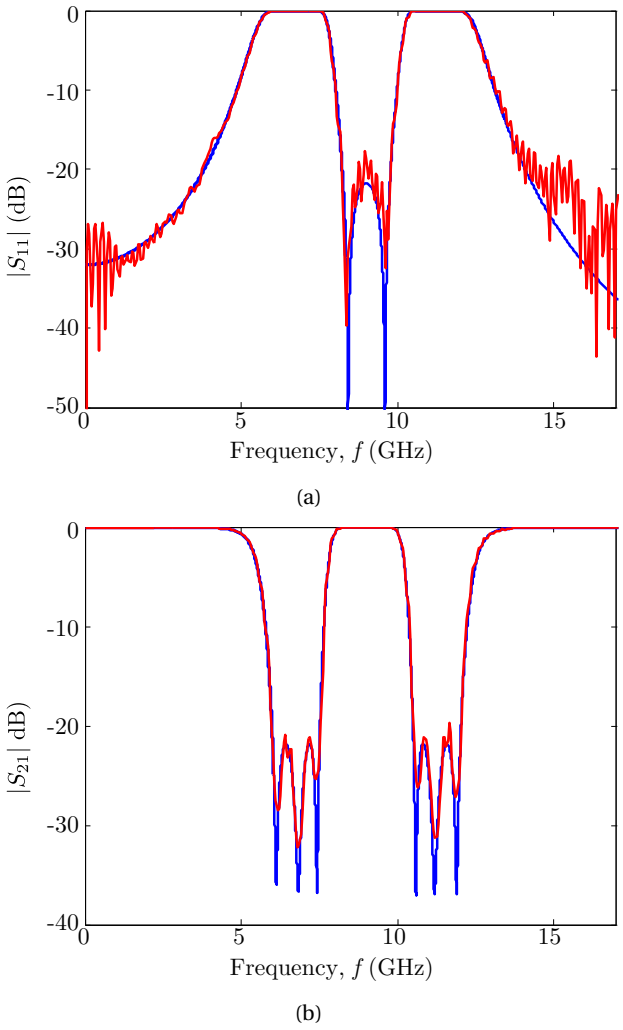

Figure 2.40: (a) $|S_{11}|$ and (b) $|S_{21}|$ of the target frequency response (blue line) and the simulation of the design adapted to the Ferro A6-S substrate (red line).

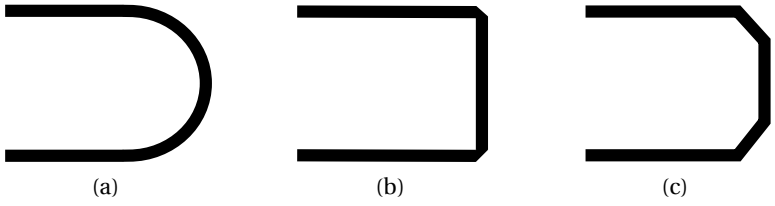

Figure 2.41: Different bend types: (a) semicircular, (b) mitered 90^o bend, and (c) 90^o bend in two steps of 45^o.

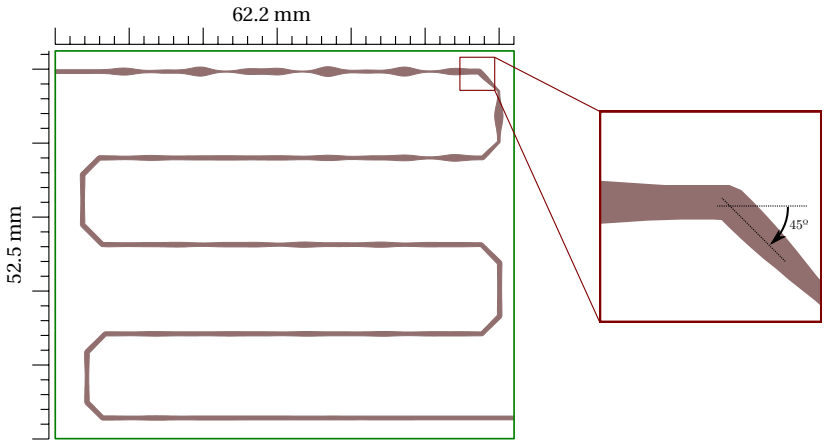

Figure 2.42: Layout of the meandered device with a detailed zoom of a bend. The size of the total occupied area is also indicated.

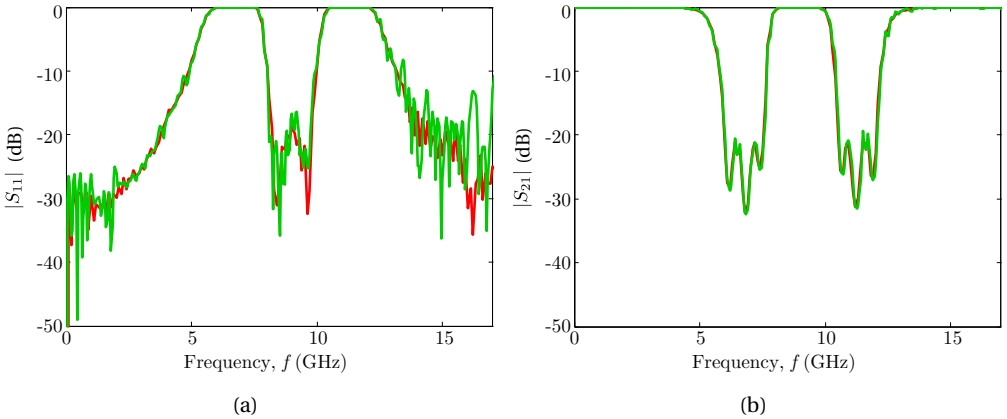

Figure 2.43: (a) $|S_{11}|$ and (b) $|S_{21}|$ of the target frequency response (blue line) and the simulation of the meandered design.

both responses, with a slightly worse matching of the meandered device at high frequencies.

Using stripline technology means that the device will be embedded into the LTCC substrate so, in practice, it is necessary to add transitions to the internal layers of the device. We have used a coplanar-to-stripline transition that can be implemented directly in the stripline substrate and that will allow us to measure the device using coplanar probes. Figure 2.44 shows a sketch of the transition. The coplanar waveguide is implemented on the metallic top plane of the stripline, and the transition is

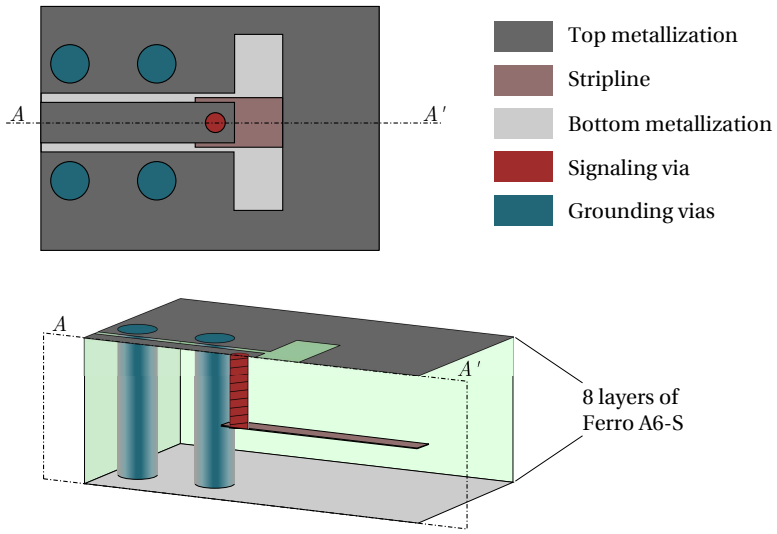

Figure 2.44: Sketch of the coplanar-to-stripline transition.

basically a metallic via connecting the signal line of the coplanar port to the signal line of the stripline. An aperture in the ground plane at the end of the coplanar waveguide is included to compensate for the inductance of the via. Other four vias are placed to short-circuit the ground planes in order to avoid the propagation of the slot-mode of the coplanar waveguide and the parallel-plate mode of the stripline. The diameter of the vias is of 0.2 mm for the signal line and 0.4 mm for the grounding. The width of the line and the separation are selected obviously to match the port impedance of 50 Ω. The size of the aperture has been optimized to get a good matching in the transition which is below -20 dB for the frequency band of interest.

The final device, including the coplanar ports, has been simulated using Agilent™ ADS Momentum giving the results in Figure 2.45. It can be observed that the simulation results follow satisfactorily the target response. The return loss is the most affected parameter since all the performed operations produce slight mismatch effects. However, the obtained results still meet the requirements.

At this point we can say that the design has been modified to adapt it to a new substrate and also to the requirements of the LTCC fabrication. However, the advantages of the LTCC technology have not been completely exploited yet. The key benefit of LTCC is the integration and compaction capability thanks to the possibility of implementing multiple layers. We have used 8 layers of substrate in our design, but they were used to implement a single stripline. The next step forward to improve the integration of our device (which is still quite large) is separating the device into two

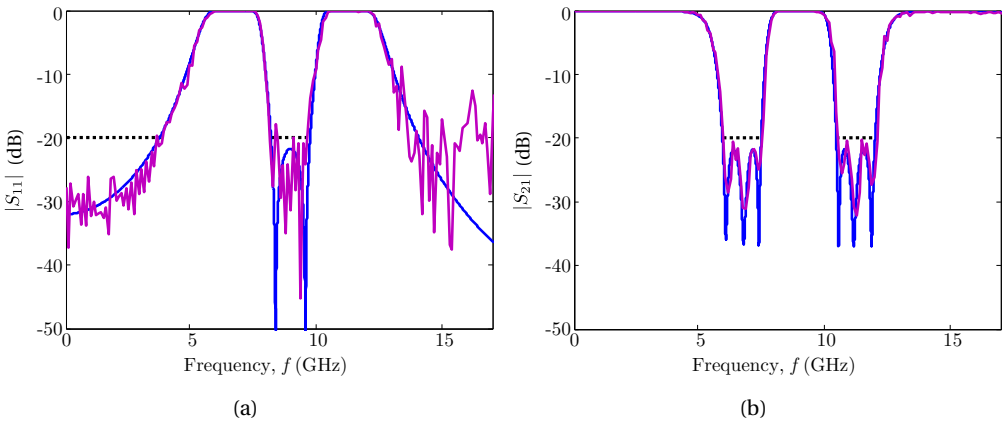

Figure 2.45: (a) $|S_{11}|$ and (b) $|S_{21}|$ of the simulation of the final design (purple line), meandered and with coplanar ports, and the target response (blue line). Initial specifications have been also included (dotted black lines).

striplines to implement them in two layers, one above the other, and sharing a common ground plane between them, as it is sketched in Figure 2.46. The device will have a total thickness of approximately 3 mm, composed by 16 layers of the same substrate used before.

In order to divide the design into two layers, it is important to keep the total length of the coupling coefficient unaltered. A shift of all the coupling coefficient would introduce a linear phase term in the frequency response, following the *space shifting* property of the $K(z) \longleftrightarrow S_{11}(\beta)$ relationship [40]. However, if only a part of the coupling coefficient is shifted, by introducing a shift in the middle of the coupling coefficient, the frequency response is altered in an uncontrolled manner. For this reason, it is preferable to nullify a section of the coupling coefficient of the same length of the transition, than shifting part of the coupling coefficient, to accommodate the transition in the middle of it. Obviously, the nullified section should be chosen in areas where the coupling coefficient is low to minimize the changes. Hence, a minimum coupling section around the middle of the device is searched for, to nullify a part equal in length to the length of the transition. In our case, the separation between the signal lines of the device is of 1.544 mm and thus, this is also the length of the transition. Each of the two parts of the device will be implemented in a different layer.

To connect both layers, a stripline-to-stripline transition will be implemented by a metallic via. In order to avoid the propagation of the parallel-plate mode of the stripline at the end and beginning of the lines, several vias are used to short-circuit the ground planes. They are placed in a pseudo-coaxial configuration surrounding

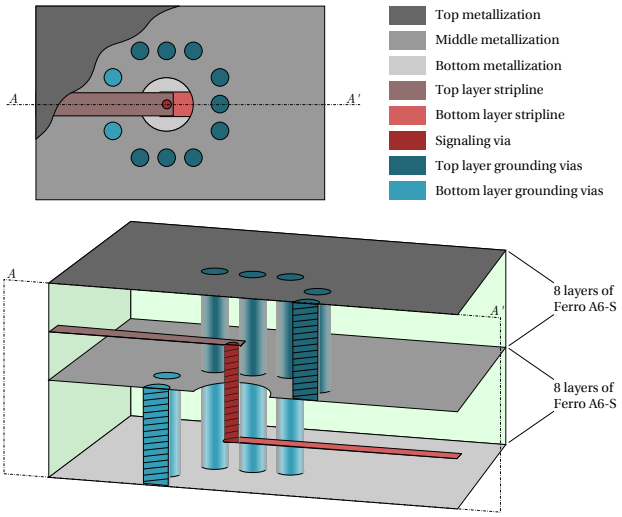

Figure 2.46: Sketch of the stripline-to-stripline transition.

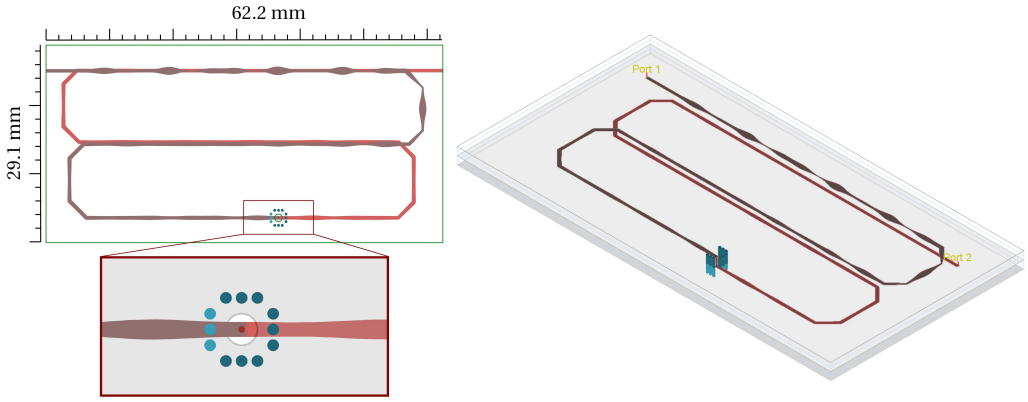

Figure 2.47: Layout and 3D view of the 2-layer device.

the via of the signal line, as it is shown in the sketch of Figure 2.46 [71]. On the top view, only a small section of the top metallization plane has been depicted in order to show all the structure elements, but it is obviously a solid ground plane that covers all the device.

According to this, the meandered layout (sketched in Figure 2.42) is divided into two parts and the stripline-to-stripline pseudo-coaxial transition is included. The layout of the 2-layer device is shown in Figure 2.47, where the metal strips of each layer are distinguished by different colors. A zoom of the stripline-to-stripline transition is included below the layout. As it can be seen, the necessary area has been reduced to

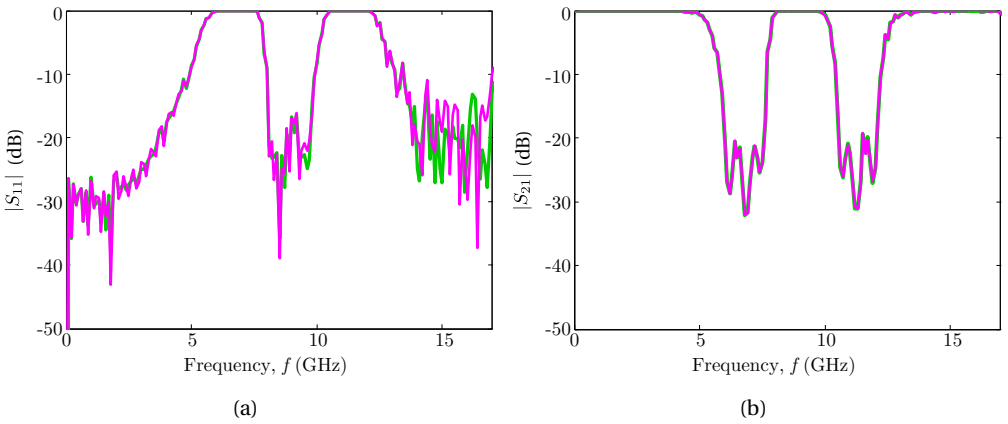

Figure 2.48: (a) $|S_{11}|$ and (b) $|S_{21}|$ of the simulation of the 2-layer design (magenta line) and the meandered device in one layer (green line).

62.2 mm by 29.1 mm. Figure 2.47 shows also a 3D view of the final device where the ground planes are made semi-transparent in order to view the general structure of the device. The 2-layer device has been simulated using Agilent™ ADS Momentum and very satisfactory results have been obtained, as depicted in Figure 2.48. The results of the 2-layer device and those of the meandered device implemented in one layer (Figure 2.43) are almost identical.

At this point, another requirement of the LTCC fabrication process has to be considered. As it has been already explained, the green tape of LTCC substrates includes a binder that acts as a *glue* between different layers, so the substrate layers have to touch each other. If we include big internal metallic planes, such as the ground plane we aim to create, there is a risk of delamination of the substrate. Therefore, gridded metallic layers are used instead of solid planes. The density of the grid is recommended to be between 30 % and 60 %. Moreover, the configurations shown in Figure 2.49 are recommended, following a mosaic configuration, or placing the regular grid in angle with the edges of the device. In our case, we will use the mosaic configuration, with a metallic density of 55 %, choosing $l_1 = 0.4$ mm and $l_2 = 0.27$ mm. It is important to point out that this grid can not be used in all the layer. An area below and/or above the metal strips will be a solid metallic plane to keep the stripline configuration. The width of this area is chosen to be 4 times the maximum width of the strip.

Finally, the embedded stripline has to be accessed from outside the device for measurement purposes and again, the coplanar-to-stripline transition is used at both

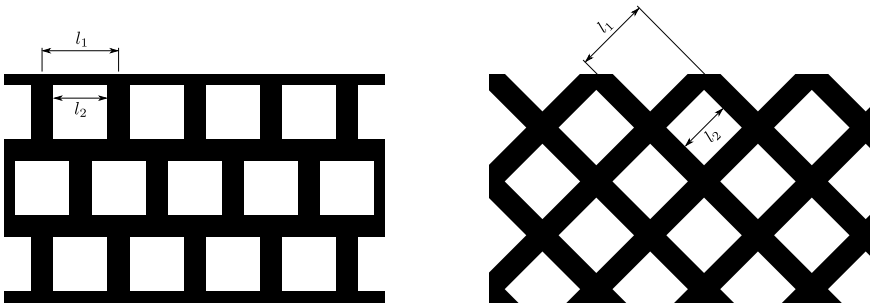

(a) (b)

Figure 2.49: Sketch of the gridded metallic planes in (a) mosaic form and (b) in angle respect to the edges.

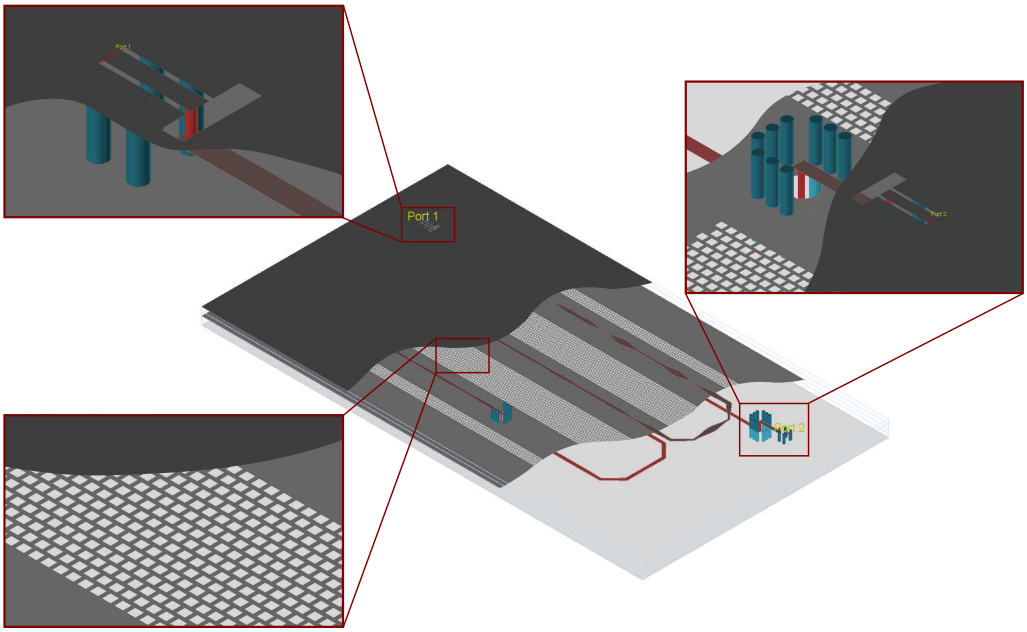

Figure 2.50: 3D view of the final device with details of the coplanar ports and the gridded intermediate ground plane.

ports to allow us to measure the device using coplanar probes. Moreover, the stripline-to-stripline transition is used also at the end of the device to place both ports on the top plane of the device.

A 3D view of the final design is shown in Figure 2.50. The metallization planes are partly hidden in order to display the structure. The final area, including the coplanar

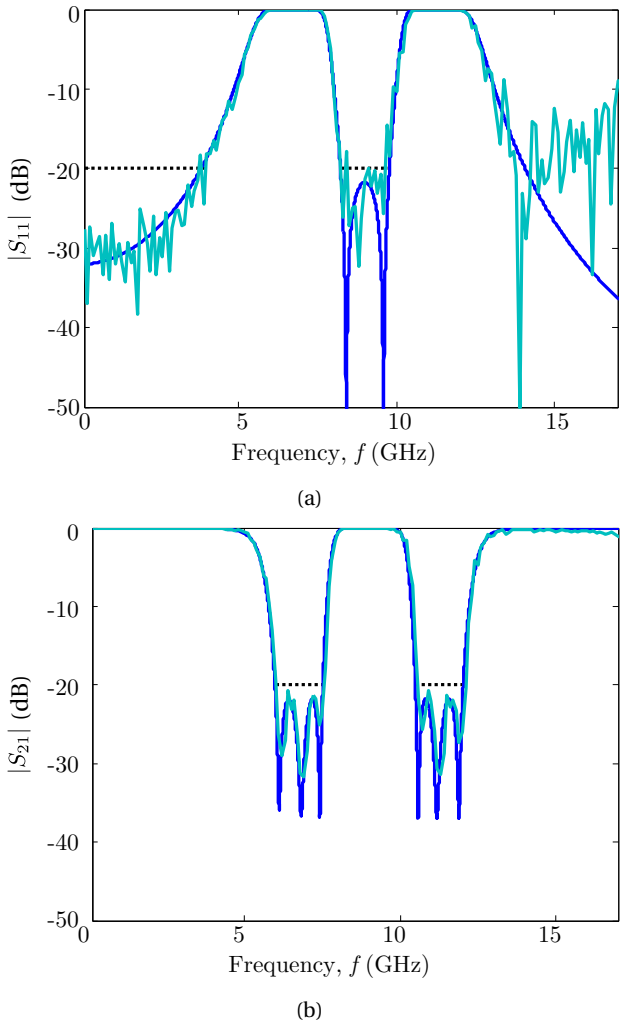

Figure 2.51: (a) $|S_{11}|$ and (b) $|S_{21}|$ of the simulation of the 2-layer final design (turquoise line), meandered and with coplanar ports, and the target response (blue line). Initial specifications have been also included (dotted black lines).

ports and all the necessary transitions, is 70.9 mm by 33.3 mm. The designed final device has been simulated using Agilent™ ADS Momentum, and the simulation results are depicted in Figure 2.51 together with the target response. The results follow the target response adequately, with slight differences in the return loss parameter. All the included transitions and bends affect the matching of the device, but not too badly, so that the final results still satisfy the initial requirements. Those differences are more

pronounced at high frequencies due to a worse performance of the transitions at these frequencies.

To conclude, we should point out that the design has been successfully modified to be implemented into the new LTCC multilayer technology and to fit in the maximum allowed area. The results provide a good example of the LTCC integration and compaction capability. In addition, they also demonstrate the possibility of compacting the devices designed using the proposed synthesis technique.

2.3. Conclusions

This Chapter aims to provide flexibility to the microwave filter design techniques. Classical design techniques divide the design process into two steps: the approximation problem and the synthesis problem. A new approach to each of these steps has been proposed in the two sections of this Chapter.

The approximation problem consists in obtaining a frequency response that satisfies the given specifications. Section 2.1 proposes a new method, based in digital filter design techniques, to accomplish this process. Several transformation methods have been presented, to allow the transformation of the analog specifications into digital specifications. Afterwards, the ready-to-use digital filter design techniques are employed to satisfy the transformed specifications obtaining a digital filter that is then transformed back into the analog domain. An example is presented at the end of the section where a multiband filter has been designed demonstrating the validity of the method.

The synthesis problem is that of finding the physical parameters of a device with a performance that satisfies the given filter response. Classical methods usually relay on equivalent circuits of lumped-elements, which are implemented with distributed components using transmission lines. In Section 2.2, a direct synthesis method based on inverse scattering has been presented which does not require an equivalent lumped-element network. It permits to calculate the coupling coefficient needed for the filter by means of a closed-form expression, that requires just to solve a linear system of equations. The method is exact for all the frequency range of interest and valid when the target frequency response can be expressed as a rational function. The restrictions in the positions allowed for the poles and zeros are due to fundamental physical considerations (like the requirement of stability for the frequency response) and can be easily avoided in practical applications. The resulting microwave filters feature a continuously varying smooth profile, avoiding the presence of sharp discontinuities and their detrimental effects. In order to validate the synthesis method, a multiband filter

has been designed, fabricated and measured. The synthesis method has been combined with the digital filter design techniques, providing great flexibility. To improve the integration of the device, a compaction process using Low Temperature Cofired Ceramics (LTCC) multilayer technology has been employed. A compact version of the filter has been designed which satisfies the required specifications.

References

[1] D. M. Pozar, *Microwave engineering*, 4th ed. Hoboken (NJ), USA: John Wiley & Sons, 2012.

[2] Hewlett-Packard, *Time domain reflectometry*. Palo Alto, CA: Application Note 62, 1964.

[3] C. L. Benett and G. F. Ross, "Time-domain electromagnetics and its applications," *Proceedings of IEEE*, vol. 66, pp. 299–318, March 1978.

[4] A. Antoniou, *Digital Signal Processing*. McGraw-Hill, 2005.

[5] T. W. Parks and C. S. Burrus, *Digital Filter Design*. New York: John Wiley & Sons, 1987.

[6] I. Arnedo, A. Lujambio, T. Lopetegi, and M. A. G. Laso, "Design of microwave filters with arbitrary frequency response based on digital methods," *IEEE Microwave and Wireless Components Letters*, vol. 17, no. 9, pp. 634–636, September 2007.

[7] A. Papoulis, *The Fourier Integral and its applications*. New York: McGraw-Hill Electronic Science Series, 1962.

[8] R. E. Collin, *Foundations for microwave engineering*, 2nd ed. New York, NY: McGraw Hill, 1992.

[9] L. Poladian, "Group-delay reconstruction for fiber bragg gratings in reflection and transmission," *Optics Letters*, vol. 22, no. 20, pp. 1571–1573, Oct. 1997.

[10] G. Lenz, B. J. Eggleton, C. R. Giles, C. K. Madsen, and R. E. Slusher, "Dispersive properties of optical filters for WDM systems," *IEEE Journal of Quantum Electronics*, vol. 34, no. 8, pp. 1390–1402, August 1998.

[11] E. Brinkmeyer, "Simple algorithm for reconstructing fiber gratings from reflectometric data," *Optics Letters*, vol. 20, no. 8, pp. 810–812, Apr. 1995.

[12] I. Hunter, *Theory and Design of Microwave Filters*. London, UK: IEE Electromagnetic Waves Series, 2001, vol. 48.

[13] J. S. Toll, "Causality and the dispersion relation: Logical foundations," *Phys. Rev.*, vol. 104, pp. 1760–1770, Dec. 1956.

[14] A. V. Oppenheim, R. W. Schafer, and J. R. Buck, *Discrete-Time Signal Processing*, 2nd ed. Upper Saddle River (NJ): Prentice-Hall Signal Processing Series, 1999.

[15] I. N. Bronshtein, K. A. Semendyayev, G. Musiol, and H. Muehlig, *Handbook of Mathematics*, 5th ed. Springer-Verlag, 2007.

[16] W.-K. Chen, *The circuits and filters handbook*. CRC Press, 1995.

[17] R. M. Golden, "Digital filter synthesis by sampled-data transformation," *IEEE Transactions on Audio and Electroacoustics*, vol. 16, no. 3, pp. 321–329, 1968.

[18] T. Saramäki, "An efficient Remez-type algorithm for the design of optimum IIR filters with arbitrary partially constrained specifications," in *Proc. of the 1992 International Symposium on Circuits and Systems*, May 1992, pp. 2577–2580.

[19] Matlab. [Online]. Available: http://www.mathworks.com

[20] B. Friedlander and B. Porat, "The modified Yule-Walker method of ARMA spectral estimation," *IEEE Transactions on Aerospace Electronic Systems*, vol. AES-20, no. 2, pp. 158–173, Mar. 1984.

[21] K. Avci and A. Nacaroglu, "High quality low order nonrecursive digital filters design using modified Kaiser window," in *Proc. of the 6th International Symposium on Communication Systems, Networks and Digital Signal Processing, CNSDSP*, Graz, Austria, 2008.

[22] D. G. Luenberger, *Introduction to linear and nonlinear programming*. Addison-Wesley, 1973.

[23] L. B. Michael, M. Ghavami, and R. Kohno, "Multiple pulse generator for ultra-wideband communication using hermite polynomial based orthogonal pulses," in *Proc. on the IEEE Conference on Ultra Wideband Systems and Technologies*, Baltimore, USA, May 2002.

[24] X. Luo, L. Yang, and G. Giannakis, "Designing optimal pulse-shapers for ultra-wideband radios," *Journal of Communications and Networks*, vol. 5, no. 4, pp. 344–353, 2003.

[25] X. Wu, Z. Tian, T. N. Davidson, and G. B. Giannakis, "Optimal waveform design for UWB radios," *IEEE Transactions on Signal Processing*, vol. 54, no. 6, pp. 2009–2021, June 2006.

[26] G. Matthaei, L. Young, and E. M. T. Jones, *Microwave filters, impedance-matching networks, and coupling structures*. Artech House, Inc., 1980.

[27] R. Schaumann, M. S. Ghausi, and K. R. Laker, *Design of analog filters: passive, active RC, and switched capacitor*. Prentice Hall, 1990.

[28] K. C. Gupta, R. Garg, I. Bahl, and P. Bhartia, *Microstrip lines and slotlines*, 2nd ed. Artech House, 1996.

[29] I. Arnedo, I. Arregui, A. Lujambio, M. Chudzik, M. A. Laso, and T. Lopetegi, "Synthesis of microwave filters by inverse scattering using a closed-form expression valid for rational frequency responses," *IEEE Transactions on Microwave Theory & Techniques*, vol. 60, no. 5, pp. 1244–1257, May 2012.

[30] B. Z. Katsenelenbaum, L. Mercader, M. Pereyaslavets, M. Sorolla, and M. Thumm, *Theory of nonuniform waveguides – The cross-section method*. London, UK: IEE Electromagnetic Waves Series, 1998, vol. 44.

[31] F. Sporleder and H. G. Unger, *Waveguide tapers, transitions and couplers*. London, UK: Peter Peregrinus Ltd., 1979.

[32] T. Lopetegi, "Photonic bandgap structure in microstrip technology: Study using the coupled mode formalism and applications," Ph.D. dissertation, Universidad Pública de Navarra, 2002.

[33] V. V. Shevchenko, *Continuous Transitions in Open Waveguides – Introduction to the Theory*. Boulder, CO: The Golem Press, 1971.

[34] T. Rozzi and M. Mongiardo, *Open Electromagnetic Waveguides*. London, UK: IEE Electromagnetic Waves Series, 1997, vol. 43.

[35] A. W. Snyder and J. D. Love, *Optical Waveguide Theory*. London, UK: Chapman & Hall, 1983.

[36] J. Uher, J. Bornemann, and U. Rosenberg, *Waveguide Components for Antenna Feed Systems: Theory and CAD*. Artech House, 1993.

[37] R. Savafi-Naini and R. H. MacPhie, "Scattering at rectangular-to-rectangular waveguide junctions," *IEEE Transactions on Microwave Theory & Techniques*, vol. MTT-30, no. 2, pp. 2060–2063, Nov. 1982.

[38] I. Kay, "The inverse scattering problem when the reflection coefficient is a rational function," *Communications on Pure and Applied Mathematics*, vol. 13, no. 3, pp. 371–393, 1960.

[39] G. H. Song and S. Y. Shin, "Design of corrugated waveguide filters by the Gel'fand-Levitan-Marchenko inverse-scattering method," *J. Opt. Soc. Amer. A*, vol. 2, no. 11, pp. 1905–1915, Nov. 1985.

[40] I. Arnedo, M. A. G. Laso, F. Falcone, D. Benito, and T. Lopetegi, "A series solution for the single-mode synthesis problem based on the coupled mode theory," *IEEE Transactions on Microwave Theory & Techniques*, vol. 56, no. 2, pp. 457–466, February 2008.

[41] D. S. Heim and C. B. Sharpe, "The synthesis of nonuniform lines of finite length – part I," *IEEE Transactions on Circuit Theory*, vol. CT-14, pp. 393–403, 1967.

[42] M. J. Erro, I. Arnedo, M. A. G. Laso, T. Lopetegi, and M. A. Muriel, "Phase-reconstruction in photonic crystals from S-parameter magnitude in microstrip technology," *Optical Quantum Electronics*, vol. 39, no. 4–6, pp. 321–331, Jun. 2007.

[43] R. Schaumann and M. E. V. Valkenburg, *Design of analog filters*. New York, NY: Oxford University Press, 2001.

[44] C. Charalambous, "A unified review of optimization," *IEEE Transactions on Microwave Theory & Techniques*, vol. 22, no. 3, pp. 289–300, Mar. 1974.

[45] F. J. Villegas, D. R. Jackson, J. T. Williams, and A. A. Oliner, "Leakage fields form planar semi-infinite transmission lines," *IEEE Transactions on Microwave Theory & Techniques*, vol. 47, no. 4, pp. 443–454, April 1999.

[46] J. Hong, *Microstrip Filters for RF/Microwave Applications*, 2nd ed. Wiley Series in Microwave and Optical Engineering, 2011.

[47] LineCalc, Agilent ADS. [Online]. Available: http://www.agilent.com

[48] W. W. Mumford, "Directional couplers," *Proc. IRE*, vol. 35, pp. 160–165, February 1947.

[49] F. Bolinder, "Approximate theory of the directional coupler," *Proc. IRE*, vol. 39, p. 291, March 1951.

[50] B. M. Oliver, "Directional electromagnetic couplers," *Proc. IRE*, vol. 42, pp. 1686–1692, November 1954.

[51] J. E. Adair and G. I. Haddad, "Coupled-mode analysis of nonuniform coupled transmission lines," *IEEE Transactions on Microwave Theory & Techniques*, vol. 17, no. 4, pp. 746–752, October 1969.

[52] M. K. Krage and G. I. Haddad, "Characteristics of coupled microstrip transmission lines-I: Coupled-mode formulation for inhomogeneous lines," *IEEE Transactions on Microwave Theory & Techniques*, vol. 18, no. 4, pp. 217–222, April 1970.

[53] C. B. Sharpe, "An equivalence principle for nonuniform transmission line directional couplers," *IEEE Transactions on Microwave Theory & Techniques*, vol. 15, no. 7, pp. 398–405, July 1967.

[54] J. Reed and G. J. Wheeler, "A method of analysis of symmetrical four-port networks," *IRE Trans. on Microwave Theory and Techniques*, vol. 4, no. 4, pp. 327–334, October 1956.

[55] E. M. T. Jones and J. T. Bolljahn, "Coupled-strip-transmission-line filters and directional couplers," *IRE Trans. on Microwave Theory and Techniques*, vol. 4, no. 2, pp. 75–81, April 1956.

[56] R. Mongia, I. Bahl, and P. Bhartia, *RF and microwave couple-line circuits*, 1st ed. London: Artech House, 1999.

[57] M. Kirschning and R. H. Jansen, "Accurate wide-range design equations for the frequency-dependent characteristic of parallel coupled microstrip lines," *IEEE Transactions on Microwave Theory & Techniques*, vol. 32, no. 1, pp. 83–90, January 1984.

[58] G. Xiao, K. Yashiro, N. Guan, and S. Ohkawa, "An effective method for designing nonuniformly coupled transmission-line filters," *IEEE Transactions on Microwave Theory & Techniques*, vol. 49, no. 6, pp. 1027–1031, June 2001.

[59] M. Chudzik, I. Arnedo, A. Lujambio, I. Arregui, I. Gardeta, F. Teberio, J. Azaña, D. Benito, M. A. G. Laso, and T. Lopetegi, "Design of transmission-type Nth-order differentiators in planar microwave technology," *IEEE Transactions on Microwave Theory & Techniques*, vol. 60, no. 11, pp. 3384–3394, November 2012.

[60] Y. Imanaka, *Multilayered Low Temperature Cofired Ceramics LTCC Technology*. Springer, 2006.

[61] DuPont. [Online]. Available: http://www.dupont.com/

[62] Heraeus, Inc. [Online]. Available: http://www.heraeus.com

[63] Ferro. [Online]. Available: http://www.ferro.com

[64] Murata Manufacturing Co., Ltd. [Online]. Available: http://www.murata.com

[65] L. Devlin, G. Pearson, J. Pittock, and B. Hunt, "RF and microwave component development in LTCC," in *IMAPS Nordic 38th Annu. conf.*, Sept. 2001.

[66] K. Kuang, F. Kim, and S. S. Cahill, *RF and Microwave Microelectronics Packaging*. Springer, 2009, ch. 9.

[67] T. Klein, M. Faassen, C. Rusch, and R. Kulke, "A 77 GHz radar frontend in LTCC for short range, high precision industrial applications," in *Proc. of the 42th European Microwave Conference (EuMC)*, Amsterdam, Oct. 28 - Nov. 2 2012, pp. 1285–1288.

[68] W. Simon, J. Kassner, O. Litschke, H. Fischer, and S. Holzwarth, "Highly integrated KA-Band Tx frontend module including 8x8 antenna array," in *Proc. of the Asia Pacific Microwave Conference (APMC)*, Singapore, December 7-10 2009, pp. 5–8.

[69] R. Kulke, C. Günner, S. Holzwarth, J. Kassner, A. Lauer, M. Rittweger, P. Uhlig, and P. Weigand, "24 GHz radar sensor integrates patch antenna and frontend module in single multilayer LTCC substrate," in *Proc. of the 15th European Microelectronics and Packaging Conference (IMAPS)*, Brugge, June 12-15 2005.

[70] Ragan Technologies, Inc. [Online]. Available: http://www.ragantech.com

[71] Q. Huang, S. Zhang, and W. Jiang, "A shielded microstrip-to-stripline vertical transition for multilayer printed circuit board," in *Microwave and Millimeter Wave Technology (ICMMT), 2012 International Conference on*, vol. 2, Shenzhen, China, May 3-5 2012, pp. 1–3.

Chapter 3

Smooth profile rectangular waveguide filters

Microwave filters are essential components used in any modern communication systems, such as radio/television broadcasting, mobile communications services or satellite communications. Their implementation in a specific microwave technology depends on the needs of a particular application, being the coaxial, planar or waveguide technologies the most commonly used. Each technology features different properties as for the mass/volume, loss, power-handling capability, cost, etc. (see Figure 3.1 [1]). For instance, in the payload of a communication satellite all of these technologies, among others, can coexist, being the rectangular waveguide technology the selected one when high power-handling capability is required.

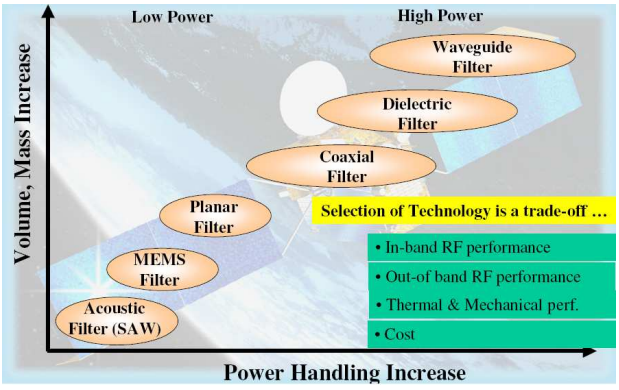

Figure 3.1: Microwave technologies used in satellite communications [1].

In spite of all the research performed in the last decades, the design of filters for microwave applications usually follows the procedure mentioned in [2]: 1) an equivalent circuit prototype based on lumped and/or distributed elements is synthesized [3], 2) the initial physical dimensions are obtained by relating the prototype elements to the components of a real filter structure [4, 5], and 3) a final optimization of the final dimensions is usually needed [6, 7].

In this chapter, microwave rectangular waveguide filters will be designed using a different perspective, giving rise to devices with smooth profiles. Several rectangular waveguide filters will be presented: a device designed using the synthesis technique presented in Section 2.2, a low-pass filter based on Bragg-reflectors, and a compact high-power low-pass filter.

Due to the requirements of the design technique or the target specifications of the filter, in all the presented devices the analysis of high order modes becomes important. Actual simulation software such as Microwave CST Studio provides tools for this purpose. However, the well-known mode-matching technique can be also used [8]. This method has been implemented for rectangular waveguide in a home-made Matlab program to have a deeper insight of the operation of these devices. Specifically, the program allows us to calculate the evolution of the electromagnetic fields of the different modes in the filter. Known the amplitude of the modes, the evolution of the power of each mode can be represented observing if coupling occurs from one mode to another inside the structure. After a brief explanation of the mode-matching technique, the designed devices will be presented, making special emphasis on the results of the multi-mode analysis performed using the mentioned home-made tool.

3.1. Multi-mode analysis by mode matching technique

It is well-known that electromagnetic waves can adopt several solutions inside any waveguide technology or transmission line. Those solutions, named as modes, can be propagating or in cut-off depending on the geometry and the operation frequency. Microwave devices are usually designed assuming that only one mode is propagating. However, higher-order modes can become troublesome as they can interfere with the fundamental mode, specially in applications where wideband operation is required.

Furthermore, higher order modes can be also excited when discontinuities are present in a device. For this reason, multi-mode analysis of discontinuities has been performed for several discontinuity types. Mode-matching technique is a well-known method that can be used for this purpose. Although the theory is valid for many waveguide technologies and transmission lines [8, 9], in this section we will focus only in

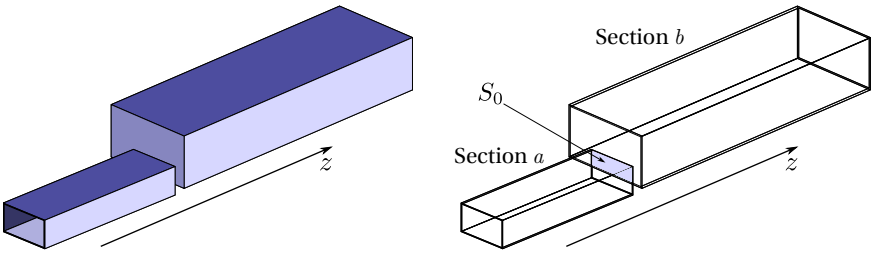

Figure 3.2: Sketch of a discontinuity in rectangular waveguide technology.

rectangular waveguide technology which is the chosen technology for the presented filters [10]. Specifically, we will consider a discontinuity of the type shown in Figure 3.2. The transversal section of the waveguides at the junction is assumed to be metallic except for the common aperture between both sections.

The total electric and magnetic fields, $\hat{\vec{E}}$ and $\hat{\vec{H}}$, present in a generic nonuniform waveguide structure can be expressed as follows [11]

$$\hat{\vec{E}}(x,y,z,f) = \sum_i a_i(z,f)\vec{E}^i(x,y,z,f) \tag{3.1a}$$

$$\hat{\vec{H}}(x,y,z,f) = \sum_i a_i(z,f)\vec{H}^i(x,y,z,f) \tag{3.1b}$$

being z the direction of propagation, f the operation frequency, $\vec{E}^i$ and $\vec{H}^i$ the vector mode patterns of the electric and magnetic fields respectively, i.e., the (x,y)-dependent part of the electric field of the i-mode in the auxiliary uniform waveguide associated to the cross-section of the nonuniform waveguide at z, and $a_i(z,f)$ the complex amplitude of the i-mode along the nonuniform waveguide.

This decomposition of the total electric and magnetic fields can be done at both sides of the discontinuity obtaining $\hat{\vec{E}}^a$, $\hat{\vec{H}}^a$ and $\hat{\vec{E}}^b$, $\hat{\vec{H}}^b$. Afterwards, boundary conditions at the discontinuity are applied to obtain the complex amplitudes of the modes, $a_i(z,f)$, for both sides of the discontinuity. The tangential components of the total electric and magnetic fields have to be equal at the discontinuity, i.e. in the area defined as S_0 in Figure 3.2

$$\hat{\vec{E}}_t^a(x,y,z,f) = \hat{\vec{E}}_t^b(x,y,z,f) \tag{3.2a}$$

$$\hat{\vec{H}}_t^a(x,y,z,f) = \hat{\vec{H}}_t^b(x,y,z,f) \tag{3.2b}$$

Applying these boundary conditions a set of equations is achieved. Known the complex amplitudes of the modes at one side, the set of equations can be solved to obtain the complex amplitudes of the modes for the other side. In other words, the

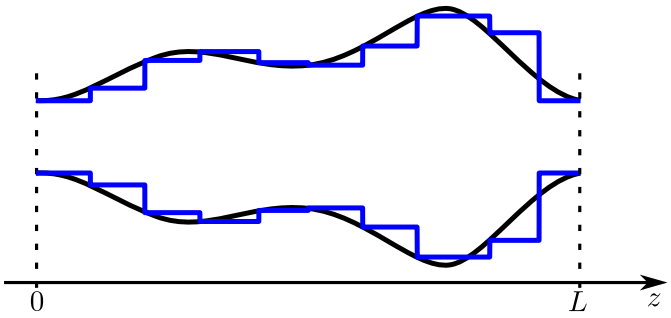

Figure 3.3: Device analysis: profile of a device (black line) and approximation to the device by cascaded rectangular waveguide sections (blue line).

total electric and magnetic fields are calculated through the complex amplitudes of the modes. This provides a deep understanding of the interaction between different modes and how they contribute to the total electric and magnetic field present inside the waveguide.

The modal analysis described here can be used to analyze not only a discontinuity, but a complete device. If the device is divided along the propagation direction, z, in various uniform rectangular waveguide sections, it can be analyzed as several cascaded discontinuities. This way, the profile of the device is approximated by uniform rectangular waveguide sections as it is shown in Figure 3.3. A coarse approximation has been done for illustrating purposes, but the section length can be reduced for a better approximation of the device profile. A known excitation pattern is applied to the input port of the device. Afterwards, analyzing each discontinuity and adding the phase change due to the propagation of the wave through the uniform sections between discontinuities, the complex amplitudes of the modes are calculated along the entire device, providing valuable information for the designer. This information is specially important when multi-mode effects need to be considered.

It is important to point out that only a finite number of modes can be considered in the summation of (3.1). Hence, the solution for the electric and magnetic fields is an approximation which can be very accurate if the number of considered modes is large enough. This number will be highly influenced by the geometry of the device. If the excitation of higher order modes is high inside the device, a larger number of modes will be required for an accurate analysis.

In order to analyze the excitation level of a given mode along the nonuniform waveguide the expression proposed in [12] can be used

$$P(z,f) = \frac{1}{2}\left|a^{+}(z,f)\right|^{2} + \frac{1}{2}\left|a^{-}(z,f)\right|^{2} \tag{3.3}$$

being $a^+(z,f)$ and $a^-(z,f)$ the complex amplitudes of the forward (+) and backward (−) traveling waves associated to the mode of interest at an arbitrary position, z, and frequency, f, see equation (3.1). $P(z,f)$ represents the addition (in modulus) of the power carried by the forward and backward traveling waves of the mode assuming that the vector mode patterns used are normalized to carry 1 W (for propagating modes) or $\pm j$ W (for cut-off modes). If a mode is in cut-off at a cross-section z, $P(z,f)$ is associated to the reactive energy stored by the cut-off mode, instead of the active power carried. Although this expression does not represent the actual power flow (which would be obtained by subtracting the power of the forward and backward waves), it provides the maximum contrast to show the excitation level of each mode along the waveguide through its graphical representation. This type of representations will be very useful in the following sections to understand the operation of the presented devices.

3.2. Synthesis based on pole and zero decomposition (P&Z)

In this section the synthesis method proposed in 2.2 is used to design a multiband filter in rectangular waveguide technology [13]. Single-mode operation is assumed during the design process and this assumption has to be confirmed for the proper operation of the final device, which will be done by means of our home-made mode matching program.

3.2.1. P&Z design method for rectangular waveguide

The general synthesis procedure presented in Section 2.2 for the design of microwave filters is valid for many waveguide technologies and transmission line implementations. In this section, the design process that was described in Figure 2.15 is particularized for rectangular waveguide technology, see Figure 3.4.

The proposed design technique starts with the approximation of the filter's specifications by a rational function of the form

$$S_{11}(s) = \frac{n(s)}{d(s)} = \frac{r_0 \cdot \prod_{n=1}^{M}(s - c_n)}{\prod_{n=1}^{N}(s - p_n)} \tag{3.4}$$

being c_n the zeros and p_n the poles of $S_{11}(s)$, M the number of zeros, and N the number of poles, where it is satisfied that $N \geq M + 1$ (to assure that $S_{11}(s = j\beta)$ is a band-limited function that tends to zero when frequency goes to infinity) and $\mathfrak{Re}\{p_n\} < 0$

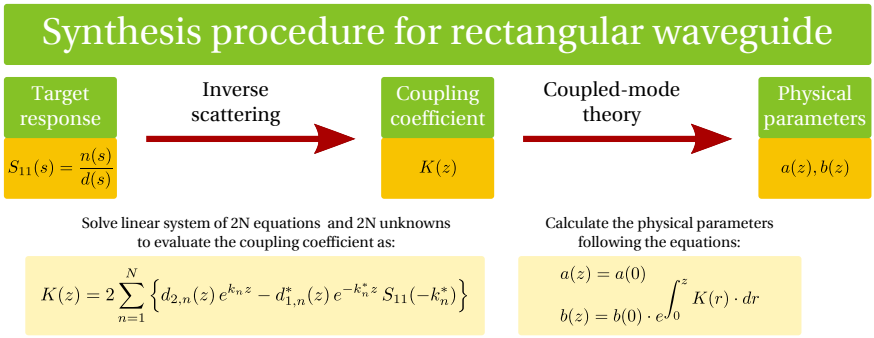

Figure 3.4: Diagram of the synthesis procedure for rectangular waveguide technology.

(all the poles must lie in the left-half of the s-plane to be a stable system). Finally, r_0 is a constant that must be adjusted to satisfy that $|S_{11}(s = j\beta)| < 1$, to have a passive system.

It is important to highlight that although the frequency response has been expressed in terms of the S_{11} parameter, the S_{21} parameter of the device arises univocally from it for our case of interest of reciprocal and lossless two-port networks [14]. Specifically, the magnitude can be calculated for each frequency (or equivalently β) as [15]:

$$|S_{21}(s = j\beta)|^2 = 1 - |S_{11}(s = j\beta)|^2 \tag{3.5}$$

Taking into account that $S_{11}(s)$ is a rational function as given in (3.4), it follows from (3.5):

$$|S_{21}(s = j\beta)|^2 = \frac{d(s)\cdot d^*(-s^*) - n(s)\cdot n^*(-s^*)}{d(s)\cdot d^*(-s^*)} = \frac{\Delta(s)}{d(s)\cdot d^*(-s^*)} \tag{3.6}$$

The phase of the $S_{21}(s)$ can be retrieved using the Hilbert Transform as explained in [11, 16], or it can be also obtained by directly deducing $S_{21}(s)$ from (3.6) taking only the zeros and poles with negative real part [17]:

$$S_{21}(s) = \frac{\prod_{n=1}^{N}(s - k_n)}{\prod_{n=1}^{N}(s - p_n)} \tag{3.7}$$

being k_n the zeros and p_n the poles of $S_{21}(s)$, where $\mathfrak{Re}\{k_n\} < 0$ (all the zeros are in the left-half s plane because $S_{21}(s)$ is a minimum-phase function) and $\mathfrak{Re}\{p_n\} < 0$ (all the poles must be in the left-half s plane to be a stable system). It is interesting to note that $S_{21}(s)$ has the same poles as $S_{11}(s)$, but different zeros [17].

The analytical closed-form expression obtained for the synthesis problem in section 2.2.2

$$K(z) = 2\sum_{n=1}^{N}\left\{d_{2,n}(z)\, e^{k_n z} - d^*_{1,n}(z)\, e^{-k^*_n z}\, S_{11}(-k^*_n)\right\} \tag{3.8}$$

allows us to calculate the necessary coupling coefficient for a device featuring the target frequency response, $S_{11}(s)$, with very low computational cost, after solving a linear system of $2N$ equations and $2N$ unknowns, $d^*_{1,n}(z)$, $d_{2,n}(z)$. The linear system is built by applying (2.110) (rewritten here for completeness)

$$\sum_{n=1}^{N}\left\{\frac{1}{S_{11}(k_n)}\cdot\frac{e^{-k_n z}}{p_i - k_n}\cdot\begin{bmatrix}d_{1,n}(z)\\ d_{2,n}(z)\end{bmatrix} - \frac{e^{k^*_n z}}{p_i + k^*_n}\cdot\begin{bmatrix}d^*_{2,n}(z)\\ d^*_{1,n}(z)\end{bmatrix}\right\} = \begin{bmatrix}0\\ 1\end{bmatrix} \tag{3.9}$$

for each of the N poles, $p_1, p_2, \ldots, p_N$. Algorithm 2.2 provides a detailed step-by-step procedure to perform this part of the design process.

After the calculation of the coupling coefficient, a link to the physical parameters has to be obtained which will obviously depend on the chosen technology. In Section 2.2.3 this relation has been derived for the most common technologies. Specifically, for rectangular waveguide technology the relation

$$K(z) = \frac{-1}{2b(z)}\cdot\frac{db(z)}{dz} + \frac{\pi^2}{2a(z)^3\beta^2}\cdot\frac{da(z)}{dz} \tag{3.10}$$

was attained. This expression for $K(z)$ depends also on β and therefore on frequency. To make it independent of frequency, as required by the synthesis method, only the height of the rectangular waveguide, b, will be varied along the device, while the width will be kept constant, $a(z) = a(0) = a_0$, giving rise to the following final expression for the coupling coefficient:

$$K(z) = \frac{-1}{2b(z)}\cdot\frac{db(z)}{dz}. \tag{3.11}$$

This expression can be solved for the height of the rectangular waveguide, b as

$$b(z) = b(0)\cdot e^{-2\int_0^z K(r)dr} \tag{3.12}$$

to achieve a device with the given frequency response, where it is assumed that the device begins at $z = 0$.

The phase constant can be easily calculated for the fundamental TE_{10} mode in rectangular waveguide technology, using the well-known expression [15]

$$\beta = \sqrt{\varepsilon_r\left(\frac{2\pi f}{c}\right)^2 - \left(\frac{\pi}{a_0}\right)^2} \tag{3.13}$$

where ε_r is the relative dielectric constant of the homogeneous medium that fills the waveguide and c is the speed of light in vacuum. As it can be seen the obtained β does not depend on z, as it was assumed in our synthesis method due to the proper election of constant waveguide width.

Finally, in order to guarantee single-mode operation, as required in the synthesis method, the coupling to higher-order modes must be avoided. It is important to notice that since it is assumed that the filter is excited by the fundamental TE_{10} mode, then the synthesized structure does not need to reject the higher-order modes. It suffices to guarantee that no coupling to those modes occurs within the structure. Using the general expression for the coupling coefficient between modes (2.69) given in section 2.2.1.1, and assuming that our waveguide device featuring variations just in the b parameter is excited by the fundamental TE_{10} mode, it can be deduced that only the TE_{1q} and TM_{1q} modes with $q = 1, 2, 3, 4, \ldots$ can be excited within the device. This set of modes can be significantly reduced if the variation of the height, b, of the rectangular waveguide is symmetrical with respect to a fixed axis in the propagation direction, z. In that case, only the TE_{1q} and TM_{1q} modes with $q = 2, 4, 6, 8, \ldots$ can be excited within the structure [18]. It is important to highlight that the use of symmetrical variations for the height of the waveguide, b, prevents the coupling to the higher-order modes with lowest cut-off frequency, TE_{11}, TM_{11}, making easier to ensure single-mode operation in the synthesized device. Actually, the cut-off frequency for a TE_{mq} and TM_{mq} mode in rectangular waveguide technology can be easily calculated by using the well-known expression [15]

$$f_c = \frac{c}{2\pi\sqrt{\varepsilon_r}}\sqrt{\left(\frac{m\pi}{a}\right)^2 + \left(\frac{q\pi}{b}\right)^2} \tag{3.14}$$

and the physical dimensions of the synthesized waveguide device should be chosen in such a way that the set of higher-order modes that can be excited remains cut-off throughout the device for the frequency range of interest, to make the coupling of energy to them negligible.

3.2.2. Multi-band Cauer filter implementation

In order to verify this novel synthesis method, in this section a multi-band filter featuring a Cauer (Elliptic) frequency response will be designed in rectangular waveguide technology. We are going to implement a filter in rectangular waveguide technology with two passbands and two rejected bands for the fundamental TE_{10} mode. The first rejected band will extend up to the cut-off frequency of the operation mode, TE_{10}. Standard WR-90 ports will be used, with dimensions $a_0 = 22.86$ mm and $b_0 = 10.6$ mm. As it was explained in the previous subsection, the width of the rectangular waveguide

will be kept constant along the device, $a(z) = a_0$, and a symmetric perturbation for the height, $b(z)$, will be applied. No dielectric material will fill the waveguide, and hence $\varepsilon_r = 1$. Thus, the cut-off frequency of the TE_{10} mode will be $f_c = 6.56$ GHz, see (3.14). This value fixes the end of the first stop band. The rest of the frequency requirements are: a pass band from 8 GHz to 11.4 GHz with return losses better than 20 dB, a rejected band from 13 GHz to 16.3 GHz with attenuation better than 60 dB, and a second pass band from 18.9 GHz up to 22.5 GHz with return losses better than 20 dB. The specification mask for the frequency response is detailed in Table 3.1 and sketched in Figure 3.5.

TABLE 3.1
ANALOG SPECIFICATIONS FOR A MULTIBAND FILTER.

Passbands	8 to 11.4 GHz 18.9 to 22.5 GHz	Return loss > 20 dB
Stopbands	DC to 6.56 GHz 13 to 16.3 GHz	Rejection > 60 dB

Once the frequency specifications are established they must be approximated by a rational function. For this purpose, a bandpass frequency response following a Cauer (Elliptic) approximation [19, 20] will be used for the S_{11} parameter (a bandstop frequency response will result for the S_{21} parameter). The order necessary for the approximation will be 14, and the passband will go from 13.1 GHz up to 16.2 GHz, with a passband ripple of 10^{-9} dB and a rejected band ripple of 25 dB. From the magnitude of the S_{11} parameter, the magnitude of the S_{21} can be immediately obtained by using (3.5), and a bandstop frequency response results for the S_{21} parameter, with rejected band attenuation of 67 dB. The selected frequency response for the S_{11} and S_{21} parameters, based on a rational function of the Cauer type as stated above, is depicted in Figure 3.5. As it can be seen, it satisfies the required specification mask with an added security margin. The poles, p_n, and zeros, c_n, of the selected $S_{11}(s)$ transfer function are given in Table 3.2). There are $N = 14$ poles and $M = 13$ zeros in our case. The r_0 constant, see (3.4), is fixed to $r_0 = 63.637$, to provide a maximum value for the S_{11} parameter of $|S_{11}(s = j\beta)|_{\max} = 0.9999999$, satisfying the requirement for our passive microwave devices, $|S_{11}(s = j\beta)| < 1$. It is important to note that in the actual transfer functions used in the synthesis method the phase constant, β, plays the role of the frequency. Regarding the $S_{21}(s)$ transfer function, it has the same poles, p_n , and order, $N = 14$, as $S_{11}(s)$, see (3.7), and its zeros, k_n, can be easily calculated by using (3.6) and (3.7). Their values are also given in Table 3.2. Finally, all the poles and zeros

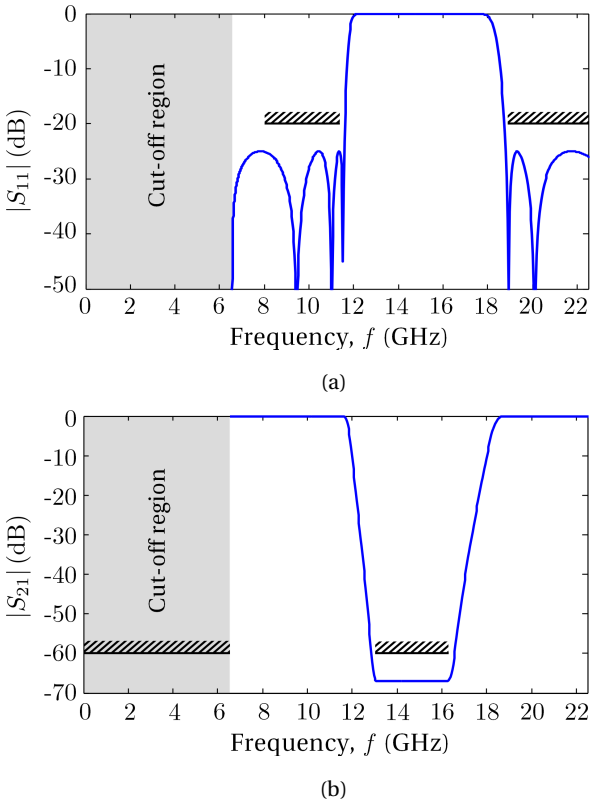

Figure 3.5: (a) S_{11} and (b) S_{21} parameters for the selected frequency response based on a 14 order rational function of the Cauer type. The specification mask for the frequency response is also given.

of $S_{11}(s)$ and $S_{21}(s)$ are depicted in Figure 3.6, in a pole-zero diagram. By inspecting the diagram it is easy to verify that all the assumptions for the poles and zeros in the synthesis method, summarized in section 2.2.2.3, are indeed satisfied.

The last step necessary to calculate the coupling coefficient required to implement the target frequency response is to get the value for $d_{1,n}(z)$, $d_{2,n}(z)$ with $n = 1, 2, 3, \ldots, N$. To do it, a linear system of $2N$ equations is built by applying (3.9) for each of the N poles, $p_1, p_2, \ldots, p_i, \ldots, p_N$. The solution for the linear system (with $N = 28$ equations and unknowns in our example) can be easily obtained with very low computational cost by using well-known numerical methods like Gaussian elimination with partial pivoting [21]. The solutions obtained for the $2N$ unknowns $d_{1,n}(z)$, $d_{2,n}(z)$, allow us to finally calculate the coupling coefficient, $K(z)$, by using the analytical closed-form expression (3.8). The result is depicted in Figure 3.7, with thin solid

TABLE 3.2
POLES AND ZEROS FOR THE SELECTED $S_{11}(s)$ AND $S_{21}(s)$ TRANSFER FUNCTIONS.

n	p_n	c_n	k_n
$1, 2$	$-105.26 \pm 360.70 \cdot j$	$\pm 518.05 \cdot j$	$-4.90 \pm 315.34 \cdot j$
$3, 4$	$-37.05 \pm 366.36 \cdot j$	$\pm 398.16 \cdot j$	$-14.46 \pm 307.43 \cdot j$
$5, 6$	$-9.25 \pm 358.91 \cdot j$	$\pm 371.90 \cdot j$	$-21.96 \pm 291.48 \cdot j$
$7, 8$	$-149.43 \pm 226.83 \cdot j$	$\pm 198.38 \cdot j$	$-23.74 \pm 270.59 \cdot j$
$9, 10$	$-55.01 \pm 188.49 \cdot j$	$\pm 185.30 \cdot j$	$-18.97 \pm 251.69 \cdot j$
$11, 12$	$-5.29 \pm 205.43 \cdot j$	$\pm 142.42 \cdot j$	$-11.27 \pm 239.46 \cdot j$
$13, 14$	$-20.16 \pm 199.35 \cdot j$	0	$-3.63 \pm 233.91 \cdot j$

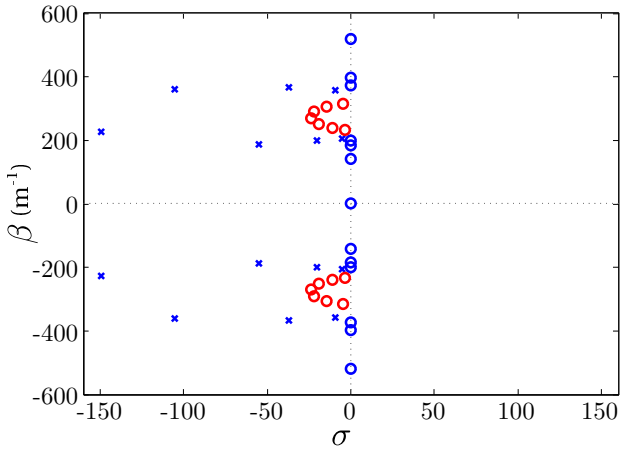

Figure 3.6: Pole-zero diagram. The poles of $S_{11}(s)$ and $S_{21}(s)$, p_n, are depicted as "x", the zeros of $S_{11}(s)$, c_n, are depicted as "o" with blue line, and the zeros of $S_{21}(s)$, k_n, are depicted as "o" with red line.

red line.

In order to implement the synthesized coupling coefficient in rectangular waveguide technology, the physical parameters of the waveguide will be calculated. Specifically, the width of the rectangular waveguide will be kept constant along the device, $a(z) = a_0$, and a symmetric perturbation for the height, $b(z)$, will be applied for convenience. Following these considerations, the evaluation of the waveguide height, $b(z)$, is obtained using (3.12). In our example, since standard WR-90 ports are used, the port dimensions are fixed to $a(0) = a_0 = 22.86$ mm and $b(0) = b_0 = 10.6$ mm. Hence, the profile for the resulting synthesized waveguide device is given in Figure 3.8, with thin

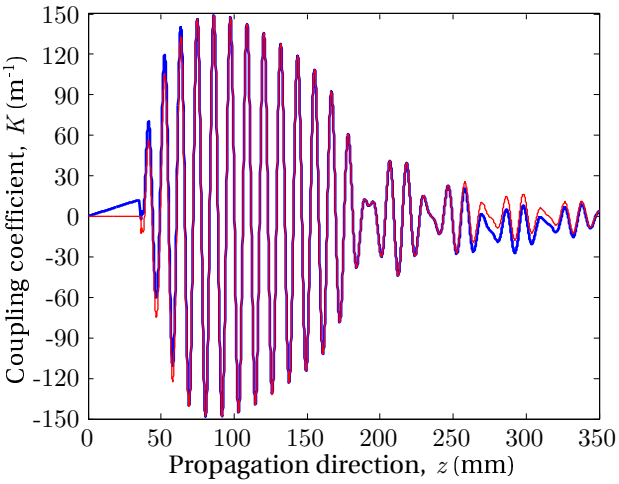

Figure 3.7: Coupling coefficient, $K(z)$, calculated by the synthesis method (thin red line) and actual value obtained after the tapering process (thick blue line). To ease the comparison, the first $K(z)$ is shifted 35 mm to the right due to the uniform waveguide section that is added at the beginning of the device during the tapering process.

solid line.

As it has been discussed in the previous subsection, the synthesis method assumes single-mode operation along the device. Hence higher order modes that can be excited (TE_{1q} and TM_{1q} with $q = 2, 4, 6, 8, \ldots$) must remain cut-off along the waveguide for our frequency range of interest. By inspecting the expression for the cut-off frequency in rectangular waveguide technology (3.14) given in the previous subsection, it can be concluded that the cut-off frequency of those modes is reduced if the height of the waveguide increases. Checking the synthesized waveguide profile in Figure 3.8, it can be seen that the maximum height for the device is $b_{\max} = 17.41$ mm, and applying (3.14) it can be obtained that the cut-off frequency for the higher-order modes with lowest cut-off frequency that can be excited, TE_{12}, TM_{12}, is $f_{c,\mathrm{TE/TM}_{12}} = 18.43$ GHz, clearly within the frequency range of interest. Therefore it is clear that the initial waveguide device proposed will not satisfy the single-mode operation condition.

This is confirmed by the analysis that has been performed using the home-made mode-matching program described in Section 3.1. The frequency response of the filter for the fundamental mode is depicted in Figure 3.9 together with the target response and the result of the simulation using CST Microwave Studio that also provides similar results. $P(z, f)$, as defined in Section 3.1, has been depicted for the fundamental

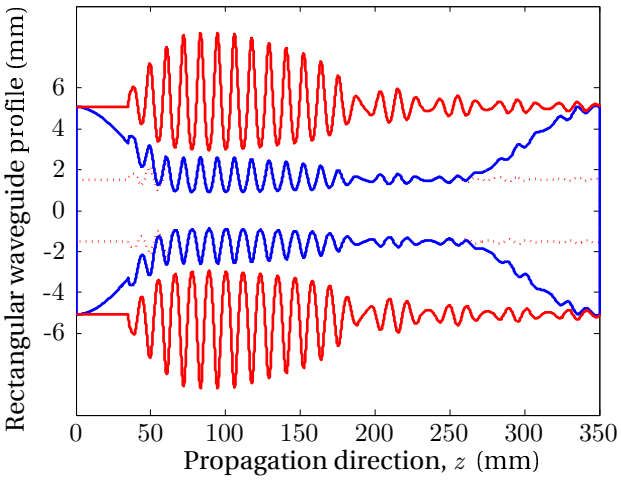

Figure 3.8: Initial rectangular waveguide profile (thin red line), intermediate profile obtained by multiplying the height by 0.3 (dotted red line), and final profile obtained after the tapering process (thick blue line). To ease the comparison between the different profiles, a uniform section with length 35 mm is added at the beginning of the initial and intermediate profiles.

mode, TE_{10}, and the interfering high-order modes, TE_{12} and TM_{12}, in Figure 3.10, assuming an injection power of 1 W in the fundamental TE_{10} mode at the input port of the waveguide. The cut-off frequency of TE_{12} and TM_{12} which varies along the device

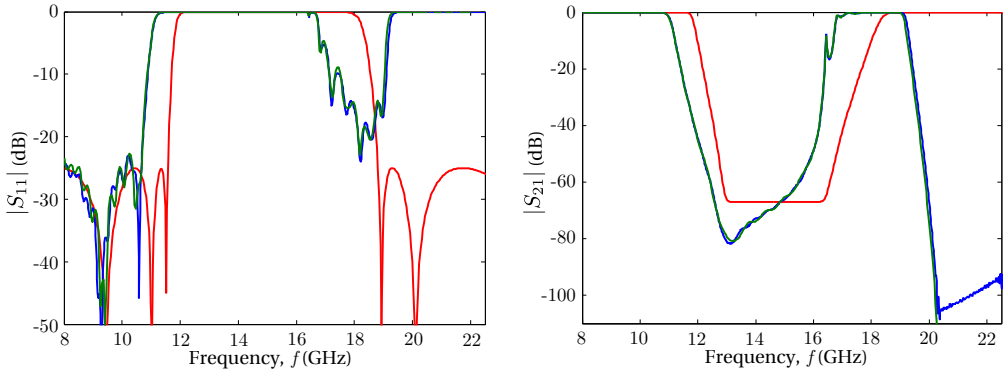

Figure 3.9: (a)$|S_{11}|$ and (b) $|S_{21}|$-parameters of the initially proposed rectangular waveguide filter simulated using the home-made mode matching program (green line) and using CST Microwave Studio (blue line) together with the target response (red line).

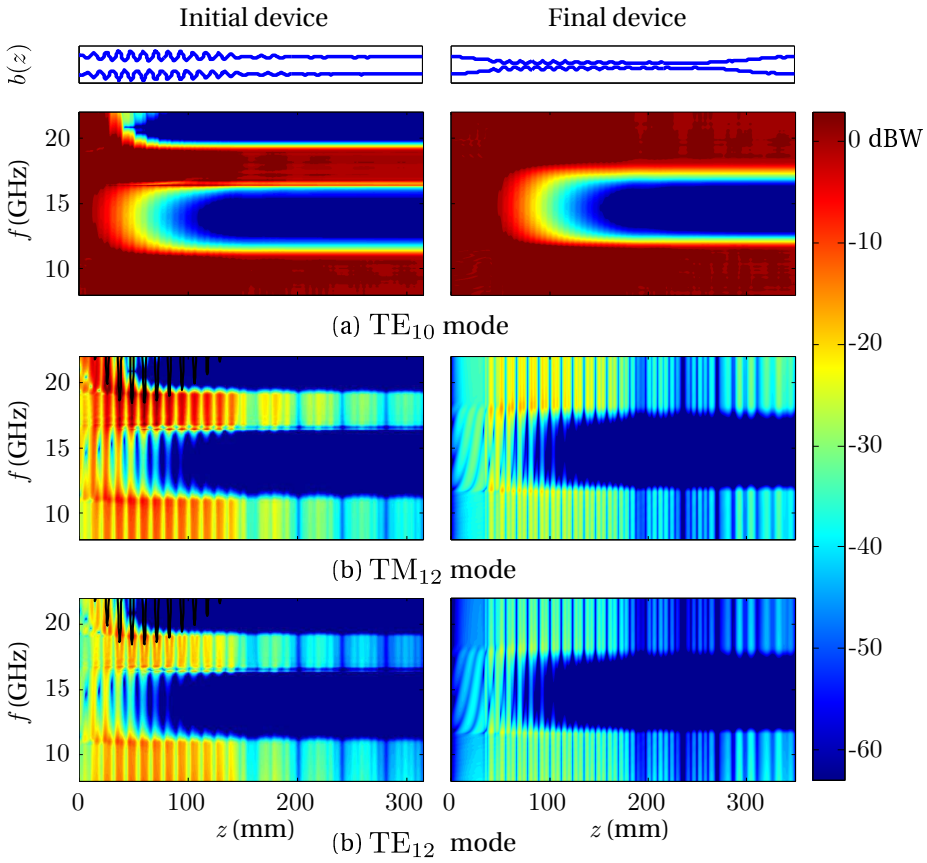

Figure 3.10: $P(z, f)$ for the (a) TE_{10} mode, (b) TM_{12} mode, and (c) TE_{12} mode in the initially proposed device and the final device. The cut-off frequency of TM_{12} and TE_{12} is included in black line whenever it gets within the frequencies of interest.

depending on the dimensions of the cross-section, has been also plotted in the figures. As it is observed in Figure 3.10(a) the response of the fundamental mode changes drastically with respect to the expected response, showing a stopband for frequencies above 19 GHz. In Figure 3.10(b) and 3.10(c), it can be clearly seen that the excitation level of high-order modes is important inside the device, even in evanescent mode for frequencies below cut-off.

This problem can be solved by applying a useful property of the relationship between the height of the rectangular waveguide, $b(z)$, and the coupling coefficient, $K(z)$. Specifically, as it can be easily demonstrated using (3.11) and (3.12), if $b(z)$ is multiplied by a constant, $K(z)$ remains identical. In our example, the height of the synthesized

waveguide is multiplied by a factor equal to 0.3, keeping the coupling coefficient unaltered but shifting the cut-off frequency of the potentially troublesome modes well beyond the frequency range of interest, and therefore guaranteeing single-mode operation. The resulting waveguide profile is depicted in Figure 3.8, with dotted red line.

If non-standard ports can be used in the designed waveguide filter, then the synthesis process is successfully finished with the last waveguide profile. However, in several occasions, a specific standard port is required for the waveguide filter (WR-90 in our design example). In those cases, a last step is necessary to complete the design. In order to employ the required standard ports, other useful property for the relationship between the height of the rectangular waveguide, $b(z)$, and the coupling coefficient, $K(z)$, will be exploited. In particular, if $b(z)$ is multiplied by a tapering function, $T(z)$, then $K(z)$ is altered just by adding the term $\frac{-1}{2T(z)} \cdot \frac{dT(z)}{dz}$. This property can be readily demonstrated using (3.11) and (3.12), and allows us to taper the beginning and the end of the profile to achieve the standard port dimensions. If the tapering function, $T(z)$, is smooth enough so that $\frac{dT(z)}{dz} \approx 0$, then its effect on $K(z)$ is negligible and the frequency response of the synthesized waveguide filter remains almost unaltered.

To ease the tapering process and to keep the desired single-mode operation obtained for the dotted line structure of Figure 3.8 (i.e. to maintain the maximum height of the structure small enough so as to keep the potentially troublesome modes cut-off in the frequency range of interest), in our design example a uniform section of rectangular waveguide with length 35 mm has been added at the beginning of the synthesized filter, prior to multiplying by the tapering function. Using the property of "space shifting" for the relationship between $K(z)$ and $S_{11}(\beta)$ reported in [11] it can be seen that the only effect of this modification is to include a linear phase term of the form $e^{-j2\beta z_0}$ in the $S_{11}(\beta)$ parameter, where $z_0 = 35$ mm in our example. For other designs different extra lengths (usually small) could be required. As it can be seen, a compromise between the total length of the device and the effect of the tapering over the coupling coefficient, $K(z)$, the single-mode operation of the device and finally over the frequency response, appears. A Hanning window has been employed in our design to generate the smooth tapering function:

$$T(z) = (T_{\max} - 1) \cdot \cos^2\left(\frac{\pi}{2} \cdot \frac{z}{L_{\text{taper}}}\right) + 1 \tag{3.15}$$

and it has been applied over the first 70 mm (with $T_{\max} = \frac{1}{0.3}$, $L_{\text{taper}} = 70$ mm) and the last 100 mm ($T(-z + L_{\text{taper}})$, with $T_{\max} = \frac{1}{0.3}$, $L_{\text{taper}} = 100$ mm) of the filter profile. The waveguide filter obtained after the tapering process is depicted in Figure 3.8, with thick solid blue line, and it features the required standard ports (WR-90 in our

Figure 3.11: Photograph of the fabricated filter prototype in rectangular waveguide technology. Standard WR90 ports are used.

example).

In spite of the important difference between the tapered and non-tapered filter profiles, the coupling coefficient suffers very small variations due the tapering process, provided that the tapering function is chosen smooth enough. This fact can be clearly seen in Figure 3.7, where the coupling coefficient for the final device with tapered profile is given in thick solid blue line.

Multi-mode analysis has been also performed for the final device. $P(z, f)$ has been depicted again in Figure 3.10 showing the expected results for the fundamental mode. In Figure 3.10(b) and 3.10(c) the slight excitation of high-order modes is under control being purely evanescent and without interfering the fundamental mode. It is interesting to note that their cut-off frequency is now out of the frequencies of interest, and hence it does not appear depicted in the representations. The frequency response has been also calculated and it is shown together with the results of the full-wave electromagnetic simulator CST Microwave Studio in Figure 3.12. The target frequency response (based on a 14-order rational function of the Cauer type as explained above) is also given. A very good agreement is achieved between the simulated and target frequency responses. The small discrepancies found can be attributed to the tapering process, to the truncation of the coupling coefficient in the implemented filter (ideally $K(z)$ extends along the full z-axis, although with vanishingly small values), and to the slight excitation of higher order modes in evanescent mode.

The designed waveguide filter has been fabricated in copper by electroforming. A picture of the prototype is presented in Figure 3.11. The measurements have been carried out by means of an Agilent 8722 Vector Network Analyzer, employing proper coaxial-to-waveguide transitions and calibration kits. Non-linear tapers have been used to avoid the mismatch between the higher frequency coaxial-to-waveguide transitions (WR-62, WR-42) and the filter ports (WR-90), in order to ensure excitation with the fundamental TE_{10} mode, as intended. The measurement results are shown in Figure 3.12.

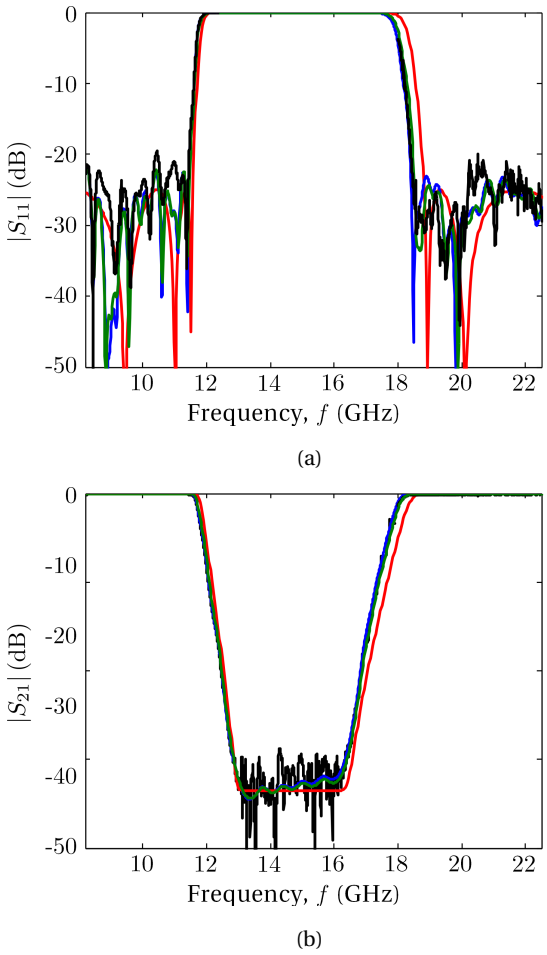

Figure 3.12: (a) $|S_{11}|$ and (b) $|S_{21}|$ of the final device. The target (red line), simulated with CST Microwave Studio (blue line), simulated with the home-made mode-matching program (green line) and measured (black line) frequency responses are given.

Again, a very good agreement is achieved between the measured and the simulated results. The small differences found can be attributed to the fabrication tolerances, the losses and the slight excitation of higher order modes, which can be slightly excited, although in evanescent form, for the highest frequencies in the regions of the waveguide filter with larger heights.

3.3. High power low-pass filter with spurious suppression based on the Bragg phenomenon

In Chapter 2, a general technique to synthesize microwave filters by inverse scattering has been explained. The synthesis method is exact for all the frequency range of interest, preventing the degradation of the frequency response that can be troublesome for wideband applications or to satisfy the out-of-band requirements of the filter. The resulting synthesized filters are, in general, nonuniform transmission lines or waveguides that feature a continuously varying smooth profile, avoiding the presence of sharp discontinuities and their detrimental effects. To demonstrate the potential of the proposed synthesis technique, a multiband microwave filter, fulfilling stringent specifications has been designed in rectangular waveguide technology in Section 3.2. As it has been mentioned, it can be necessary to multiply the synthesized profile of the waveguide by a factor less than 1 to assure single-mode operation. This leads to devices with minimum mechanical gaps, which is not desirable for high-power handling applications due to the fact that multipactor effect is more likely to occur.

Therefore, in this chapter a design method for high-power low-pass filters with wide rejection band is proposed for rectangular waveguide technology [22]. The new filters consist of a classical high-power E-plane corrugated low-pass filter that is cascaded with a quasi-periodic structure based on the Bragg reflection phenomenon and tuned to reject its undesired intrinsic spurious pass bands. The new design technique does not impose any limitations on the gap aperture of the original E-plane corrugated filter. This allows the minimum gap of the corrugated filter to be kept wide which, along with the smoothness and the large gap of the quasi-periodic structure itself, enables high-power TE_{10} mode operation in the whole structure as the spurious pass bands are suppressed.

3.3.1. High-power filter design based on the Bragg phenomenon

Bragg phenomenon

A periodic perturbation of the cross-section of a waveguide produces a periodic coupling between the modes supported by the structure [18]. If β_i and β_j are the phase constants of the i- and j-modes of the waveguide, respectively, a continuous transfer of energy is observed between the two modes when the difference of their phase constants, $\Delta\beta$, satisfies:

$$\Delta\beta = \beta_i - \beta_j = \frac{2\pi}{\lambda_B} \tag{3.16}$$

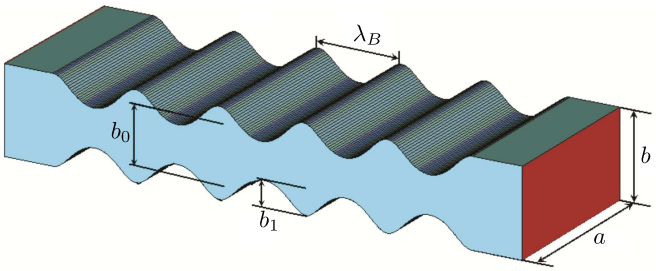

Figure 3.13: Sketch of a generic sinusoidally perturbed rectangular waveguide with its relevant parameters.

where λ_B is the so-called beat wavelength of the two modes, i.e. the period of the cross-section perturbation along the waveguide propagation axis. Equation (3.16) is also known as coherence relationship or Kovalev condition [23].

On the other hand, for the case of a weak periodic perturbation of a waveguide, the corresponding reflection coefficient can be approximately given by the Fourier transform of the geometrical perturbation [11, 24]. Hence, a sinusoidal perturbation may provide approximately a single rejected frequency band which, properly designed, may be tuned in our case to the harmonic to be suppressed in the filter.

Therefore, let's assume a $\sin\left(\frac{2\pi}{\Lambda}z\right)$-type perturbation of the cross-section of the waveguide (being z the propagation axis), which leads to mode-coupling between modes i and j, if the period of the sine function, Λ, satisfies equation (3.16), i.e. $\Lambda = \lambda_B$. In Figure 3.13, the cross-section of a generic waveguide has been perturbed following this sinusoidal law satisfying the following equation:

$$b(z) = b_0 + b_1 \sin\left(\frac{2\pi}{\lambda_B}z + \phi\right) \tag{3.17}$$

being $b(z)$ the height of the waveguide cross-section along the propagation axis, b_0 the mean value of the cross-section height, and b_1 and ϕ the amplitude and phase design parameters, respectively.

In the particular case where the two interacting modes are the same, the coupling occurs between the forward and backward traveling waves of the mode, whose phase constants are anti-parallel:

$$\beta_i = -\beta_{-i} \tag{3.18}$$

Hence, the coherence relationship given in equation (3.16) can be simplified to be

$$\Delta\beta = 2\beta_i = \frac{2\pi}{\lambda_B} \tag{3.19}$$

or, equivalently,

$$\lambda_B = \frac{\pi}{\beta_i} \tag{3.20}$$

which is also known as Bragg condition [25] for the reflection of the i-mode and it has been a subject of great interest in the last years for the microwave community [26–30].

Design method

The first step to design a high-power low-pass filter with spurious passband suppression consists in the implementation of a conventional E-plane corrugated low-pass filter with the desired passband specifications and out-of-band rejection [4, 31]. Spurious harmonic suppression is not considered during this first step and, therefore, the minimum gap of the corrugated filter will not impede high-power operation.

In the second step, a smooth quasi-periodic structure will be cascaded with the conventional filter. The quasi-periodic structure consists of different sections of sinusoidally perturbed waveguides, each one to achieve reflection at the central frequencies of the spurious harmonics to be rejected at the output of the corrugated filter. The smoothness and even larger minimum gap of the quasi-periodic structure will not reduce the high-power handling capabilities of the corrugated filter and, therefore, of the whole structure.

Assuming that the fundamental TE_{10}-mode propagates along a rectangular waveguide, the perturbation period, λ_B, of the cross-section of the waveguide to achieve a single rejected band at the undesired spurious frequency, f_0, can be calculated from (3.20) as

$$\lambda_B = \frac{\pi}{\beta_{\mathrm{TE}_{10}}(f_0)} \tag{3.21}$$

where $\beta_{\mathrm{TE}_{10}}$ is the phase-constant of the TE_{10}-mode at f_0, which is given for a rectangular waveguide by [15]

$$\beta_{\mathrm{TE}_{10}}(f_0) = \sqrt{\left(\frac{2\pi f_0}{c}\right)^2 - \left(\frac{\pi}{a}\right)^2} \tag{3.22}$$

where a is the constant width of the waveguide and c the speed of light in vacuum.

Introducing (3.22) in (3.21), the perturbation period, λ_B, can be calculated as:

$$\lambda_B = \frac{1}{\sqrt{\left(\frac{2f_0}{c}\right)^2 - \left(\frac{1}{a}\right)^2}} \tag{3.23}$$

Therefore, (3.23) is used to calculate the perturbation periods of each sub-section in the quasi-periodic structure to reject the TE_{10} mode at the undesired frequencies of the harmonics present at the output of the conventional corrugated filter.

3.3.2. Low-pass filter with high-power capability for spurious removal at the output of a Ku-band satellite OMUX

Following the design procedure proposed in the previous section, we will now design a filter aimed for the output of a satellite's Output Multiplexer (OMUX) that combines more than 18 channels in actual communication systems [32]. The power per channel is typically in the order of 150-250 W in Ku-band. As the number of channels increases, this also imposes a higher demand in power-handling capability for the filter that is required to suppers the intrinsic spurious harmonics of the non-linear operation of the amplifiers.

A stringent frequency behavior is required for the fundamental TE_{10} mode of the aimed filter. Specifically, the filter will feature a passband between 10.7 and 12.7 GHz with insertion losses better than $\mathrm{IL} < 0.15$ dB and return losses better than $\mathrm{RL} > 25$ dB. Moreover, a rejection level better than 60 dB for frequencies over 13.75 GHz and up to the third harmonic (around 40 GHz) is required.

As it has been explained before, the first step of the design process consists in the implementation of the classical high-power E-plane corrugated low-pass filter, which fulfils all frequency specifications except for the requirement of spurious harmonic-free behavior in the rejected band. This results in the device sketched in Figure 3.14, where two stepped H-plane tapers have been added to match standard WR-75 ports ($a = 19.05$ mm, $b = 9.525$ mm). The corrugated filter has been simulated using the 3D electromagnetic simulator CST Microwave Studio™ and the results for the $|S_{11}|$ and $|S_{21}|$ parameters are shown in Figure 3.15. This high-power filter has a minimum gap between E-planes equal to 4.75 mm which guarantees the use of a transmission power around several kilowatts [33].

The second and final step of the design process consists in the calculation of the quasi-periodic structure that will be cascaded with the classical corrugated low-pass filter, in order to reject its spurious passbands centered around $f_{0a} = 23$ GHz, $f_{0b} = 29$ GHz, and $f_{0c} = 35$ GHz. Therefore, the quasi-periodic structure will consist of three

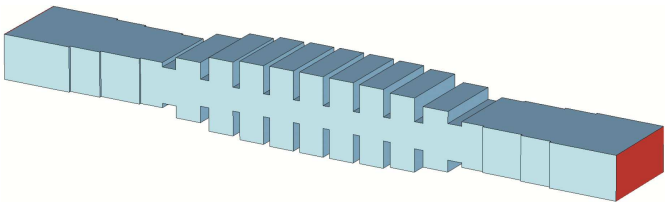

Figure 3.14: Sketch of the classical E-plane corrugated Ku-band low-pass filter.

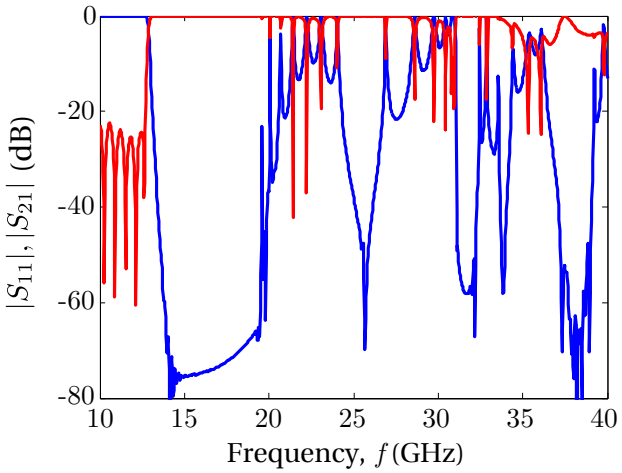

Figure 3.15: Simulated $|S_{21}|$ (blue line) and $|S_{11}|$ (red line) parameters obtained with CST Microwave Studio for the E-plane corrugated low-pass filter shown in Figure 3.14.

different sections of rectangular waveguide, whose cross-section height, $b(z)$, will follow a sinusoidal perturbation as depicted in Figure 3.13 and given mathematically in (3.17). Using the methodology proposed in the previous section, equation (3.23) can be used to determine the perturbation periods λ_{Ba}, λ_{Bb}, and λ_{Bc}, so that each of these three sections rejects one of the three spurious bands, resulting in $\lambda_{Ba} = 7$ mm, $\lambda_{Bb} = 5.3$ mm, and $\lambda_{Bc} = 4.4$ mm. Additionally, in equation (3.17), we will take as mean value for all the three sections $b_{0a} = b_{0b} = b_{0c} = b$. By geometrical considerations, this election implies that $\phi_{a,b,c} = n\,\pi$ with $n \in \mathrm{N}$. The rest of the parameters, i.e. b_{1a}, b_{1b}, b_{1c}, and the length of each section (an entire number of periods) are carefully adjusted taking into account the requirements for in-band insertion and return losses, and out-of-band rejection level. In particular, longer sections in the quasi-periodic structure lead to a deeper rejection at the corresponding spurious passband. Moreover, tapering techniques are applied to the sections to keep the return losses present at the corrugated low-pass filter. Finally, the increase of b_1 leads to deeper rejections and also to the appearance of multimode effects within the section, which in our example will be used to our benefit as it will be explained.

Using our mode-matching code, the excitation level of high order modes has been analyzed in the two quasi-periodic sections devoted to reject the first and second harmonic bands, around 23 GHz and 29 GHz. In Figure 3.16, $P(z, f)$ (as defined in Section 3.1) is depicted in dBW for the TE_{10}, TE_{12}, and TM_{12}-modes, assuming an injection power of 1 W in the fundamental TE_{10} mode at the input port of the waveguide. As

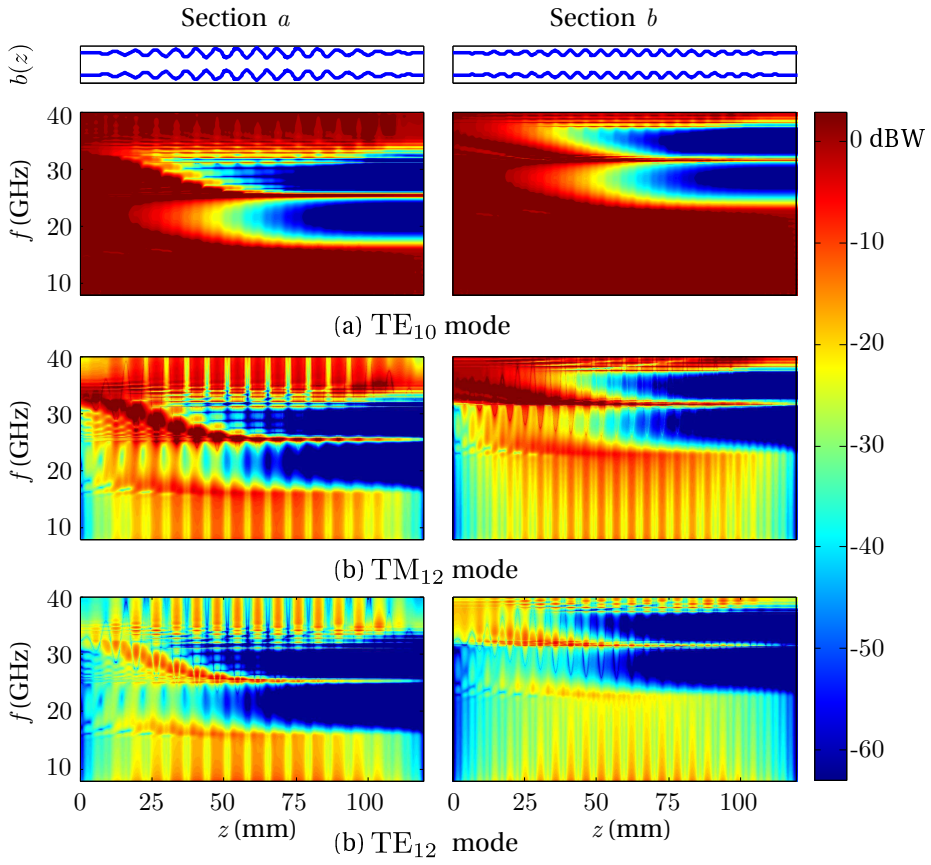

Figure 3.16: $P(z, f)$ for the (a) TE_{10} mode, (b) TM_{12} mode, and (c) TE_{12} mode in each section of the quasi-periodic structure in colored scale.

it can be seen in Figure 3.16(a), each section has a rejection band tuned at the Bragg frequency for which they were designed (23 GHz and 29 GHz respectively). Moreover, an additional rejection band is observed at higher frequencies in each section due to the excitation of high-order modes inside the device at these frequencies, as it can be seen in the Figure 3.16(b) and 3.16(c) (TM_{12} and TE_{12}-modes, respectively). As it was previously said, this multimode effect appears when the perturbation amplitude, b_1, in equation (3.17), is increased. In our case, the structure tuned to reject around 29 GHz also rejects the band centered at 35 GHz which avoids the use of a section especially devoted to the rejection of the third spurious band. The advantage of this solution is that we obtain a shorter quasi-periodic structure consisting only of the two first sections, with the physical parameters given in Table 3.3.

TABLE 3.3
PHYSICAL PARAMETERS OF THE QUASI-PERIODIC STRUCTURE.

	Section *a*	Section *b*
λ_B	7.0	5.3
b_1	8.3	5.2
b_0	9.525	9.525
ϕ (rad)	π	π
Length (mm)	119.0	116.6
Tapering function	cosine	cosine

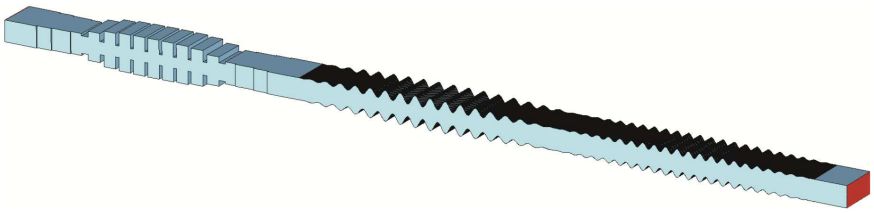

Figure 3.17: Sketch of the Ku-band low-pass filter with stringent requirements: frequency spurious-free behavior and high-power handling capability.

The final device, which has a total port-to-port distance of 393 mm including the corrugated filter and the quasi-periodic structure, is finally shown in Figure 3.17. The minimum gap in the whole structure is that of the corrugated filter, 4.75 mm (minimum gap in the quasi-periodic structure equal to 5.56 mm).

As it was shown in Figure 3.15, the classical high-power corrugated low-pass filter meets the requirements of the in-band specifications ($\mathrm{IL} < 0.15$ dB, $\mathrm{RL} > 25$ dB), but the out-of-band specifications (at least 60 dB of rejection) are only fulfilled up to near 20 GHz.

The whole device including the corrugated low-pass filter and the designed quasi-periodic structures has been also simulated and the results are given in Figure 3.18. In this case, a deep rejection of the out-of-band spurious passbands present in the conventional filter has been achieved up to the third harmonic (around 40 GHz) for the fundamental TE_{10} mode, as required. Simultaneously, the in-band insertion losses are kept around $\mathrm{IL} \approx 0.15$ dB and the obtained return losses are better than $\mathrm{RL} > 25$ dB as required (70% of silver conductivity is used for the results depicted in both Figure 3.15 and Figure 3.18).

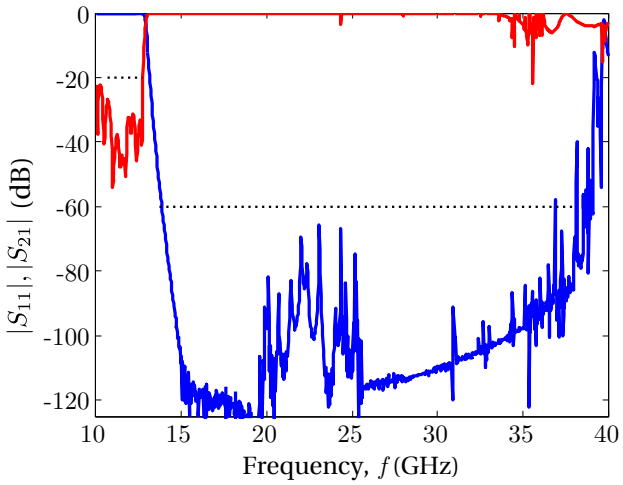

Figure 3.18: Simulated $|S_{21}|$ (blue line) and $|S_{11}|$ (red line) parameters obtained with CST Microwave Studio for the Ku-band low-pass filter with stringent requirements shown in Figure 3.17. Frequency specifications for $|S_{11}|$ and $|S_{21}|$ are also given in dotted line.

Another relevant feature of the designed prototype is its high-power handling capability. The novel structure cascaded to the classical high-power corrugated low-pass filter does not produce any decreasing of the operation power level due to its bigger gap and smooth profile [34]. Therefore, the final filter has the same power handling capability than the corrugated low-pass filter which, as it was said before, is around several kilowatts. This is a definitive advantage of this design method over other competing technologies like waffle iron waveguide low-pass filters, that are limited to lower power levels.

A photograph of the fabricated prototype is given in Figure 3.19. The filter has been manufactured in copper by electroforming and the inner prototype has been silver-plated to improve its conductivity. The measurements have been performed by means of an Agilent™ 8722 Vector Network Analyzer and proper waveguide to coaxial transitions. A Maury™ 7005E calibration kit for WR-75 has been used to perform the measurements over the standard frequency band (10-15 GHz) of operation of the

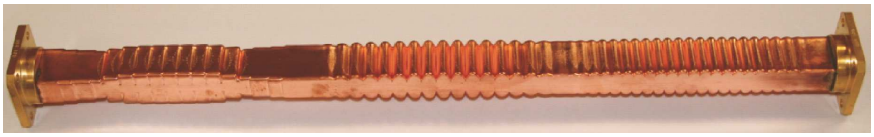

Figure 3.19: Prototype of the filter fabricated by electroforming in copper.

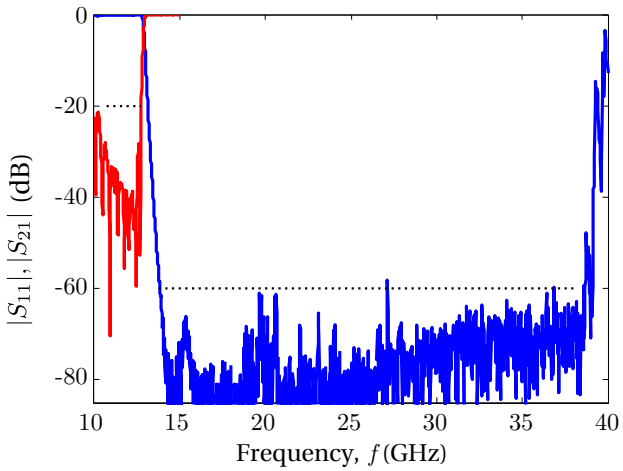

Figure 3.20: Measured $|S_{21}|$ (blue line) and $|S_{11}|$ (red line) parameters for the high-power low-pass filter prototype shown in Figure 3.19. Frequency specifications for $|S_{11}|$ and $|S_{21}|$ are also given in dotted line.

WR-75 device ports. For higher frequency bands, other calibration kits and transitions have been employed with standardized port dimensions (WR-62, WR-42, and WR-28) to ensure single mode (TE_{10}) excitation. In order to avoid the mismatch between the higher frequency coaxial-to-waveguide transitions and our filter, non-linear tapers have been used to impede the excitation of higher-order modes at the input of the filter so that the measurements can be performed over the TE_{10} mode only, as required.

The measurement results, see Figure 3.20, confirm the expectations from the simulations. An excellent level of spurious rejection is achieved (around 60 dB), while the in-band insertion and return losses are maintained better than $\mathrm{IL} < 0.15$ dB and $\mathrm{RL} > 25$ dB respectively, as intended.

3.4. Compact high-power low-pass waveguide filters with spurious suppression

In Section 3.3, a method to design high-power filters with wide spurious-free frequency response has been described. In order to achieve this goal, a high-power non-wide rejection band E-plane corrugated filter is cascaded with several quasi-periodic E-plane sinusoidally-shaped waveguide sections, the former being responsible for the minimum mechanical gap in the whole structure, which determines the maximum

power handled by the total device [34], and the latter achieving the spurious rejection through an appropriate tuning of the sinusoidal perturbation periods (Bragg reflection). In this section, an integrated design methodology of compact high-power low-pass filters for the suppression of the fundamental TE_{10} mode over a wide band is used [35]. The resulting filters consist of multiple E-plane bandstop elements of a sinusoidal profile, constituting a quasi-periodic structure, where the tuning of the rejected frequencies is this time achieved through the height of the bandstop elements and not through the period of the structure. Unlike [22, 36], no corrugated filter is required with this novel methodology. A windowing of the quasi-periodic structure height allows the implementation of low-pass filters with deep levels of out-of-band rejection in a broad band as intended, and also with good in-band return loss. Moreover, the same operation principle is used to provide also higher-order mode rejection by means of a width reduction [37, 38].

3.4.1. Design method for compact high-power low-pass filters

The low-pass filters designed following the method described in this section consist of three different sections of bandstop elements distributed along the rectangular waveguide propagation z-axis as shown in Figure 3.21(a). In Figure 3.21, the central section, L_2, mainly determines the rejected band of the filter while the initial and final sections, L_1 and L_3, mainly determine the in-band return loss.

The design process begins by setting the minimum E-plane mechanical gap, $g_{\min}$, that must be wide enough to handle the power level required [39]. Then, we fix the heights of the highest ($h_{\max}$) and shortest ($h_{\min}$) E-plane bandstop elements in section L_2 to reject the lowest ($f_{\min}$) and the highest ($f_{\max}$) frequency of the intended rejected band, respectively (Figure 3.21(b)). The height of the bandstop element is around $\lambda_g/4$, being λ_g the guided wavelength of the fundamental TE_{10} mode at the frequency to be rejected. Between $h_{\max}$ and $h_{\min}$, several bandstop elements with intermediate heights are used to reject the intermediate frequencies. A sinusoidal function is chosen as the bandstop element profile, although other profiles for the bandstop elements, as classical rectangular stubs, may be also used [40, 41]. Moreover, a symmetric (like in this case) or asymmetric distribution of E-plane bandstop elements at both sides of the z-axis can be used.

Sections L_1 and L_3 let us achieve the height, b_0, of the standard ports used. Moreover, they are mainly responsible for the filter return loss. In the design process, first we add some bandstop elements equal to the highest one (section L_3) and some more equal to the shortest one (section L_1), see Figure 3.21(c). Then, sections L_1 and L_3 are windowed in the following way: (*i*) subtract $b_0/2$ (Figure 3.21(d)); (*ii*) multiply sections

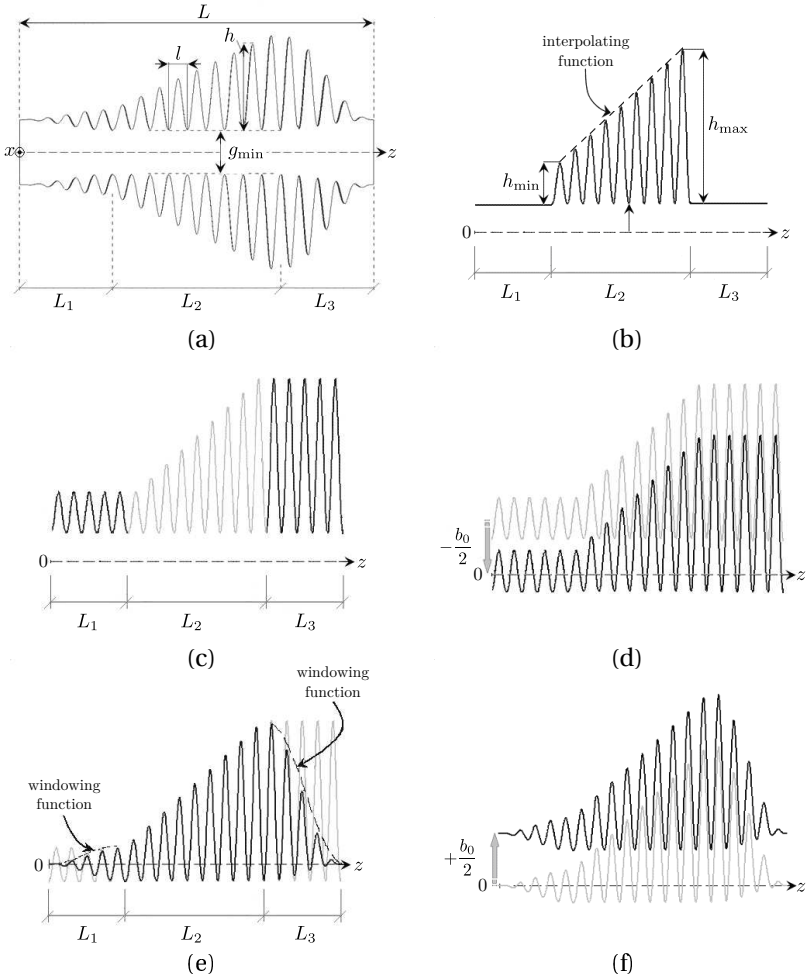

Figure 3.21: Schematics showing the novel design process: (a) sketch showing the final filter profile and its physical parameters, (b) shaping of section L_2 ($g_{\min}$, $h_{\min}$ and $h_{\max}$), (c) new bandstop elements added to define sections L_1 and L_3, (d), (e), and (f) windowing applied to sections L_1 and L_3.

L_1 and L_3 by an appropriate windowing function [42] (Figure 3.21(e)); (*iii*) add $b_0/2$ (Figure 3.21(f)). Making the resulting profile symmetric in the E-plane leads to the final device (Figure 3.21(a)).

It is interesting to note that as the number of bandstop elements in section L_2 between the highest and the shortest increases (and, hence, the total filter length, L, also

increases), the attenuation in the rejected band can be made higher. Moreover, if several additional bandstop elements with the largest height are included in section L_2, the slope between the pass- and the rejected band can be made steeper, since these additional elements reinforce the suppression of the lowest frequencies in the rejected band. On the other hand, if the number of bandstop elements in section L_1 and L_3 is increased, the filter is better matched (higher in-band return loss).

The influence of the bandstop element length, l, is weak: wider elements provide slightly better in-band return loss since the filter profile is smoother, while narrower elements provide a more uniform rejection level, since they allow a more distributed frequency rejection in the same filter length.

Variations of the filter dimensions in a final application due to fabrication tolerances or thermal expansion, for example, barely modifies the return loss and it induces a slight frequency drift that can be taken into account in the design process through safety margins around the specifications.

3.4.2. Compact high-power low-pass filter for spurious removal in Ku-band

Following the procedure described above, a compact high-power spurious-free low-pass rectangular waveguide filter that has the same stringent frequency behavior for the fundamental TE_{10} mode as the filter obtained in Section 3.3.2 will be designed. Specifically, the filter must feature a pass band between 10.7 and 12.7 GHz with return loss better than 20 dB. Moreover, a rejection level around 60 dB has to be also satisfied for frequencies over 13.75 GHz and up to the third harmonic (around 40 GHz).

In this example, WR75 input and output waveguide ports are used. As it has been just explained, the filter consists of three different sections. Section L_2 has the minimum E-plane gap of the filter, which in this case is fixed to be $g_{\min} = 6$ mm. The height of the largest and shortest E-plane bandstop elements in section L_2 are $h_{\max} = 8.6$ mm and $h_{\min} = 1.6$ mm, in order to reject the lowest and highest frequencies in the rejected band ($f_{\min} = 13.75$ GHz and $f_{\max} = 40$ GHz), respectively (the filter width is kept always constant and equal to the WR75 input/output port width, a_0, along the z axis). After obtaining the initial filter dimensions, the remaining dimensions are selected guided by the discussion in Section 3.4.1 during an optimization process. Specifically, the shorter the device, the more difficult it is to achieve the required frequency specifications. The final filter dimensions are given in Table 3.4.

The final device has been simulated using CST Microwave Studio, and its frequency response is shown in Figure 3.22 together with the simulated response of the solution proposed in Section 3.3. As it can be seen, return loss is better than 20 dB in the pass

band while the attenuation in the rejected band is higher than 60 dB for both filters, fulfilling the initial requirements (also included in the figure). The minimum mechanical gap of 6 mm is even larger in this case than in the Bragg reflector-based solution, where the minimum gap was of 4.75 mm. This fact, along with the smooth profile of both designs, leads to a much higher power-handling capability compared to the classical E-plane corrugated filters [34, 35]. Moreover, the new device is notably more compact than the solution based on cascading low-pass and bandstop filters. The total length of 218 mm of this solution versus the total length of 393 mm of the previous one, implies a length reduction of 45 %.

The multi-mode analysis tool has been used to show the operation basis of the device. The function $P(z, f)$, as defined in Section 3.1, is represented in Figure 3.23 for the TE_{10} mode, assuming an injection power of 1 W at the input port of the waveguide. As it is observed in Figure 3.23, the bandstop elements at the beginning of the device, the shortest ones, reject the high frequencies of the operation band. As the height of the bandstop elements increases gradually, lower frequencies are rejected until the cut-off frequency of the low-pass filter is reached.

The filter has been manufactured in copper by electroforming with dimension tolerances within $\pm 5\ \mu\mathrm{m}$ (see Figure 3.24). Measurements have been performed by means of an Agilent 8722 VNA and using proper waveguide to coaxial transitions and calibration kits. Non-linear tapers have been used to avoid the mismatch between the higher frequency coaxial-to-waveguide transitions and the filter ports in order to minimize the excitation of higher-order modes at the filter input. The measurement results shown in Figure 3.25 confirm that an excellent level of spurious rejection around 60 dB up to the third harmonic is achieved, while the return loss is better than 20 dB in the pass band. The in-band insertion loss is kept below 0.3 dB in this fabrication. It is important to note that no further tuning of the filter is necessary after it is fabricated.

The performance of the designed filter is very satisfactory for the fundamental

TABLE 3.4
FINAL DIMENSIONS OF THE COMPACT HIGH POWER SPURIOUS-FREE LOW-PASS WAVEGUIDE FILTER (WR75 PORTS: $a_0 = 19.05$ mm, $b_0 = 9.525$ mm).

Section L_1	no. of elements: 8 ; window: Hanning
Section L_2	$g_{\min} = 6$ mm; $h_{\max} = 8.6$ mm ; $h_{\min} = 1.6$ mm no. of elements: 45 (no. of elements with $h_{\max}$: 4)
Section L_3	no. of elements: 4 ; window: Hanning

Length of each element, l : 3.825 mm and total filter length, L: 218 mm.

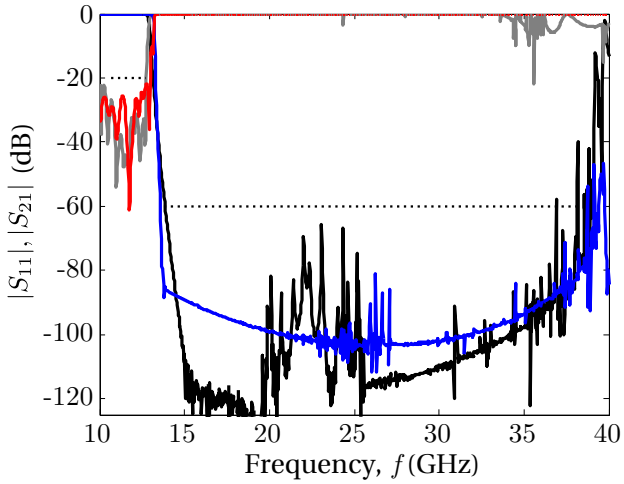

Figure 3.22: Simulated frequency response of the Bragg reflector-based solution ($|S_{11}|$ in gray line and $|S_{21}|$ in black line) and of the proposed filter ($|S_{11}|$ in red line and $|S_{21}|$ in blue line). Frequency specifications for $|S_{11}|$ and $|S_{21}|$ are also given in dotted line.

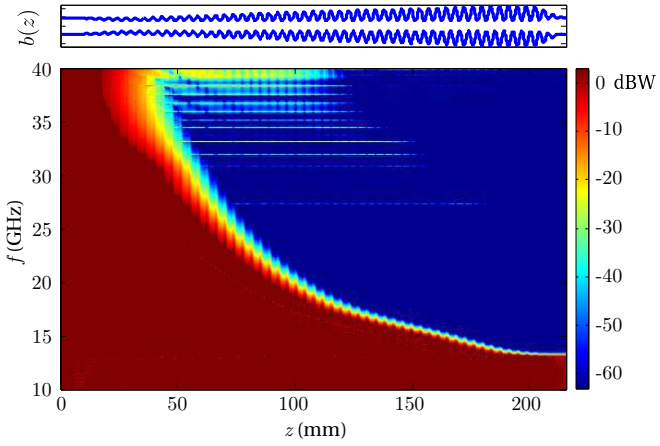

Figure 3.23: $P(z, f)$ in the final device for the TE_{10} mode in colored scale.

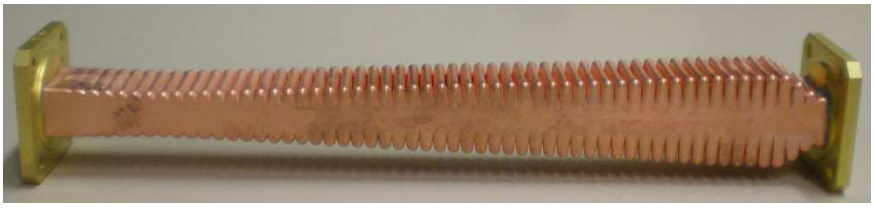

Figure 3.24: Photograph of the fabricated prototype.

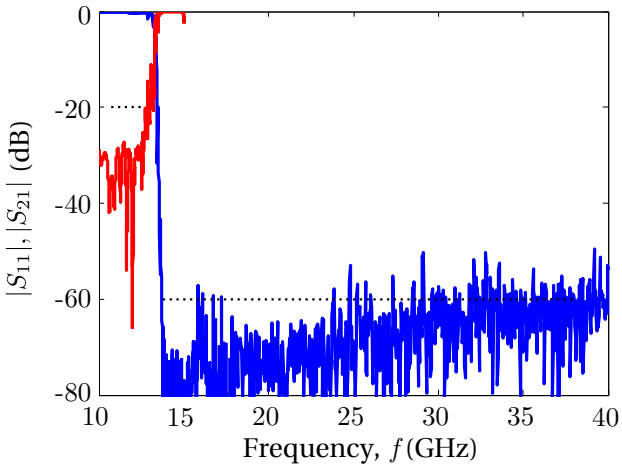

Figure 3.25: Measurements of the proposed filter: $|S_{11}|$ in red line and $|S_{21}|$ in blue line. Frequency specifications for $|S_{11}|$ and $|S_{21}|$ are also given in dotted line.

TE_{10} mode. However, higher order modes have not been considered in the design, and the filter will not suppress them. In the following Section, a design method for the suppression of higher order modes will be proposed for applications where this feature is required. The results of the higher order mode analysis of the filter designed here will be also included.

3.4.3. Modified design method for higher order mode suppression

Filters designed following the method described in subsection 3.4.1 provide wideband rejection removing up to the third harmonic of the fundamental mode. Moreover, apart from the wideband rejection high power capability is achieved due to the large minimum mechanical gap of this type of filters. Based on this design method and making slight changes, the suppression of higher order modes is also possible as it will be described below.

The design method described in subsection 3.4.1, uses bandstop elements of length $\lambda/2$ to get a wide stopband. Since the dimensions are obtained depending on the wavelength on the fundamental mode, they depend also on the phase constant of the mode, $\beta_{\mathrm{TE}_{10}}$. For increasing frequencies, the phase constant of higher order TE_{n0} modes, $\beta_{\mathrm{TE}_{n0}}$, will take the same values of the phase constant of the fundamental mode. The consequence is that TE_{n0} modes will present the same frequency response occurring at different frequency ranges. The relation between the frequency for the

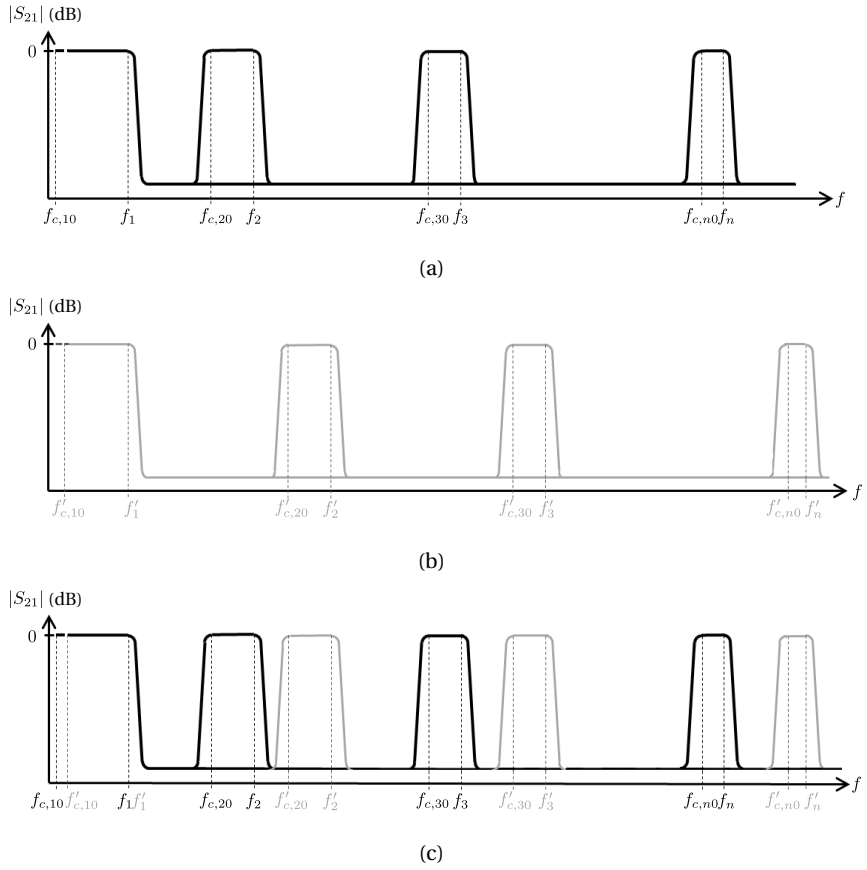

Figure 3.26: Higher-order TE_{n0}-mode behavior of the high-power filters presented in Section 3.4.1 (a) filter width equal to a_0 (waveguide-port width), (b) filter width a'_0, lower than a_0, and (c) two filters with different width (a_0 and a'_0, respectively) cascaded.

fundamental mode, $f_{\mathrm{TE}_{10}}$, and the frequency for the TE_{n0} mode, $f_{\mathrm{TE}_{n0}}$, where the response is replicated, can be easily deduced equaling both phase constant

$$\beta_{\mathrm{TE}_{n0}} = \beta_{\mathrm{TE}_{10}} \Longrightarrow \sqrt{\left(\frac{2\pi f_{\mathrm{TE}_{n0}}}{c}\right)^2 + \left(\frac{n\pi}{a}\right)^2} = \sqrt{\left(\frac{2\pi f_{\mathrm{TE}_{10}}}{c}\right)^2 + \left(\frac{\pi}{a}\right)^2}. \tag{3.24}$$

Solving for $f_{\mathrm{TE}_{n0}}$ the simple expression

$$f_{\mathrm{TE}_{n0}} = \sqrt{f^2_{\mathrm{TE}_{10}} + (n^2-1)f^2_{c,10}} \tag{3.25}$$

is obtained, where $f_{c,10}$ is the cutoff frequency of the TE_{10} mode. Using (3.25), the frequency ranges where spurious passbands or stopbands of high order TE_{n0} modes

can be calculated.

Considering an example of this kind of filters with constant width equal to the rectangular waveguide port, a_0, its frequency behavior is depicted in Figure 3.26(a). Pass bands are observed, for each TE_{n0} mode, between the cutoff frequency, $f_{c,n0}$, and the maximum frequency of the pass band, f_n. A filter with the same frequency response for the fundamental TE_{n0} mode and a constant width, a_0', lower than a_0 can be also designed. In this case, shown in Figure 3.26(b), the pass bands of the higher order TE_{n0} modes will be located at higher frequencies since the corresponding cutoff frequencies, $f_{c,n0}'$, and f_n' are higher.

Therefore, a device that rejects all the TE_{n0} higher-order modes can be achieved if two filters with different width, like the ones with the frequency response shown in Figure 3.26(a) and Figure 3.26(b), are cascaded. The use of at least two filters with a different width means that the pass bands of the higher-order TE_{n0} modes of one filter are forced to coincide with the frequencies where these modes are rejected by the other device (Figure 3.26(c)). The same idea can be implemented using only one filter if different widths are used along the same device. Now, the pass bands of the higher-order TE_{n0} modes are forced to coincide with the frequencies where these modes are rejected by sections of the filter with different widths. This concept was already used in [43] to design inhomogeneous stepped-impedance corrugated low-pass filters, not intended for high-power. Specifically, it extends the design of classical E-plane corrugated filters to the inhomogeneous structures and, although an improvement in the rejection of the higher-order TE_{n0} modes is achieved, the attenuation obtained for these modes is not high, much lower than the one achieved when the variation in the width is applied to the filters explained in Section 3.4.1.

In order to apply this idea to the high-power filters of Section 3.4.1, the next steps must be followed. First of all, a filter following the method proposed in Section 3.4.1 must be designed taking into account the frequency specifications for the fundamental TE_{10} mode. Therefore, the physical parameters: L_1, L_2, L_3, l, $g_{\min}$, $h_{\min}$, $h_{\max}$, will be determined (see Figure 3.27). Afterwards, the minimum width of the filter, $a_{\min}$, must be fixed to guarantee that $f_{c,n0}' > f_n$ is fulfilled (except for the fundamental TE_{10} mode). If a low value of the minimum width is chosen, it will be easily fulfilled but it is important to keep the cutoff frequency of the fundamental TE_{10} mode low enough to maintain the desired pass band for this mode. The length of the section with the minimum width, l_m, must be large enough to avoid that evanescent mode propagation may be significant. Once the minimum width is fixed, the transition between the standard waveguide ports, a_0, and the minimum width, $a_{\min}$, must be defined. In order to preserve the return loss of the filter, a slow variation of the width must be

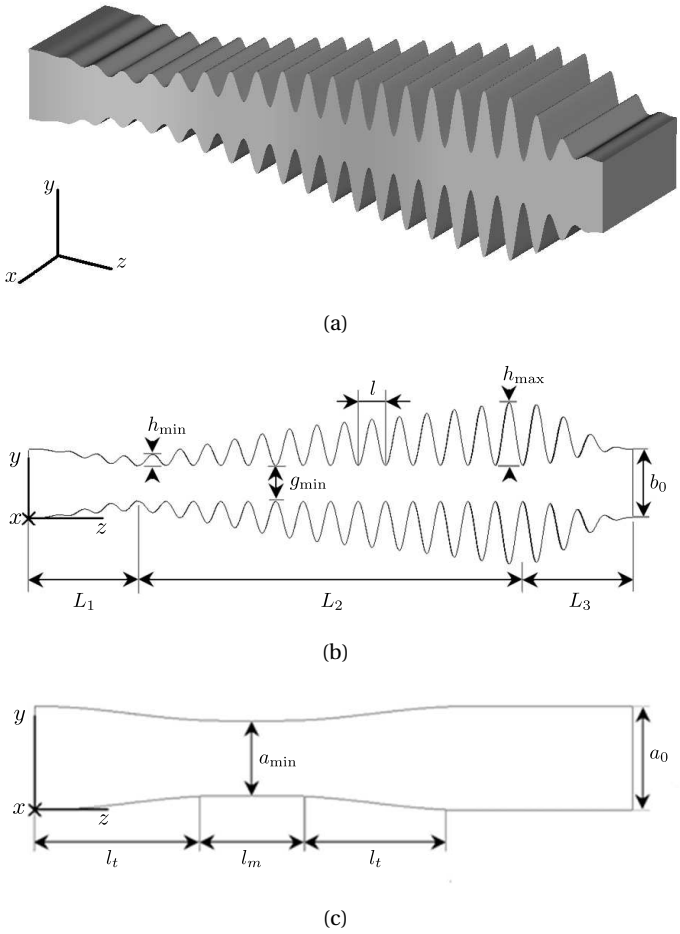

Figure 3.27: Schematics showing a high-power low-pass filter with width reduction and suppression of the high-order TE_{n0} modes: (a) 3D view, (b) side view, and (c) top view.

performed, for instance, by means of a Hanning window with length l_t. The longer the window used, the lower influence it has on the return loss of the designed filter. Finally, the height of the bandstop elements whose width values had been noticeably reduced may need to be tuned to larger values to fulfill the required rejected band of the fundamental TE_{10} mode. However, this tuning is slight as the bandstop element response is mainly determined by its height and not by its width [35].

If the rejection of the other higher (non-TE_{n0}) modes is desired, it must be ensured

during the design process that the cutoff frequency of the TE_{01} mode (the first non-TE_{n0} higher-order that can propagate) is larger than the highest frequency of the rejected band. This cutoff frequency will be determined by the sections of the structures with the minimum total height (which includes the minimum gap and the bandstop elements with the lowest heigth). Thus, by properly fixing the minimum gap of the filter, $g_{\min}$, and the minimum height of the bandstop elements, $h_{\min}$, the rejection of non-TE_{n0} higher-order modes can be achieved.

3.4.4. Low-pass filter in Ku-band featuring higher order mode suppression

Following the method described in the previous section a device is designed to have the same frequency specifications as in Section 3.4.2 and additionally suppresses higher order modes. The final dimensions are given in Table 3.5.

As it can be seen in Figure 3.28, the frequency specifications for the fundamental TE_{10} mode are perfectly fulfilled and the higher-order TE_{n0} modes clearly suppressed (see Figure 3.29).

Using the home-made mode-matching tool the device designed in Section 3.4.2 and the final device designed above have been analyzed. In Figure 3.30, $P(z, f)$, as it was defined in Section 3.1, has been represented for different modes and both devices. For each figure it is assumed a signal of 1 W of power of the considered mode at the input of the device. In Figure 3.30(a), it is clearly seen that both filters reject the fundamental mode gradually along the device, depending on the height of the bandstop elements, as it has been already said along the whole section. When considering higher-order modes, it is clear the different behavior of both devices for TE_{n0} modes.

TABLE 3.5
FINAL DIMENSIONS OF THE HIGH POWER LOW-PASS HARMONIC WAVEGUIDE FILTER WITH WIDTH REDUCTION AND SUPPRESSION OF ALL THE HIGHER-ORDER MODES (WR75 PORTS: $a_0 = 19.05$ mm, $b_0 = 9.525$ mm).

Section L_1	no. of elements: 12 ; window: Hanning
Section L_2	$g_{\min} = 3$ mm; $h_{\max} = 8.5$ mm ; $h_{\min} = 0.4$ mm no. of elements: 32 (no. of elements with $h_{\max}$: 5)
Section L_3	no. of elements: 13 ; window: Hanning
Width reduction	no. of windowed elements: 22; window: Hanning no. of elements with minimum width: 2; $a_{\min} = 15$ mm

Length of each element, l : 3.81 mm and total filter length, L: 218 mm.

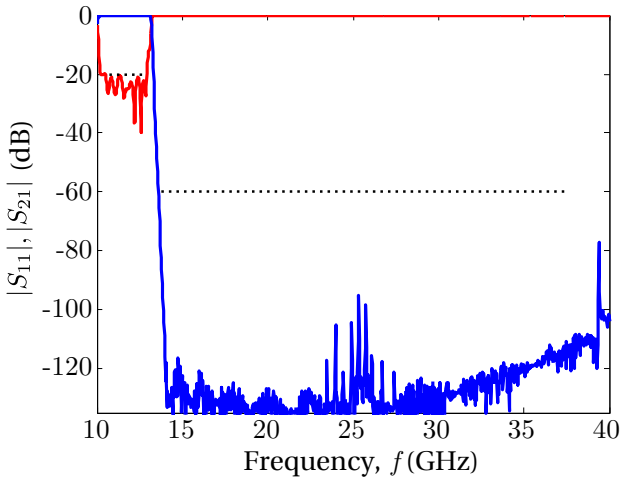

Figure 3.28: $|S_{11}|$ (red line) and $|S_{21}|$ (blue line) for the filter with width reduction and suppression of all the higher-order modes when it is excited with the TE_{10} mode.

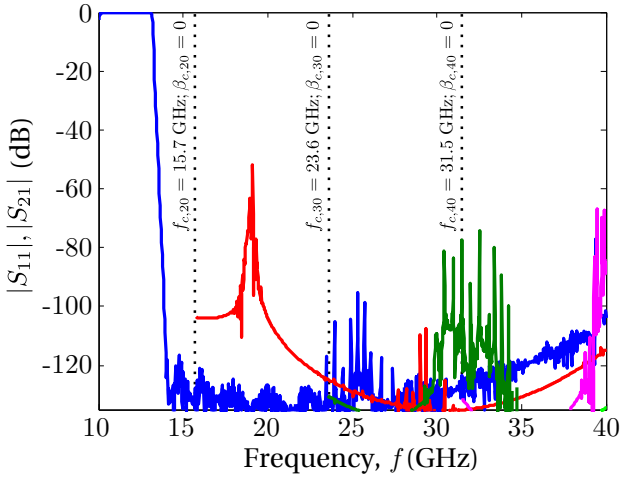

Figure 3.29: Simulated $|S_{21}|$ of the high-power filter with width reduction and suppression of all the higher-order modes: TE_{10} mode (blue line), TE_{20} mode (red line), TE_{30} mode (green line), and TE_{40} mode (magenta line).

The filter designed in the previous section does not reject TE_{n0} modes. A passband appears for each mode from the cut-off frequency of the mode (represented with a black line) up to the frequency where the highest bandstop elements correspond to $\lambda_g/4$ for the considered mode. Higher frequencies are also rejected by shorter perturbations of the device. However, in the section with reduced width of the second filter,

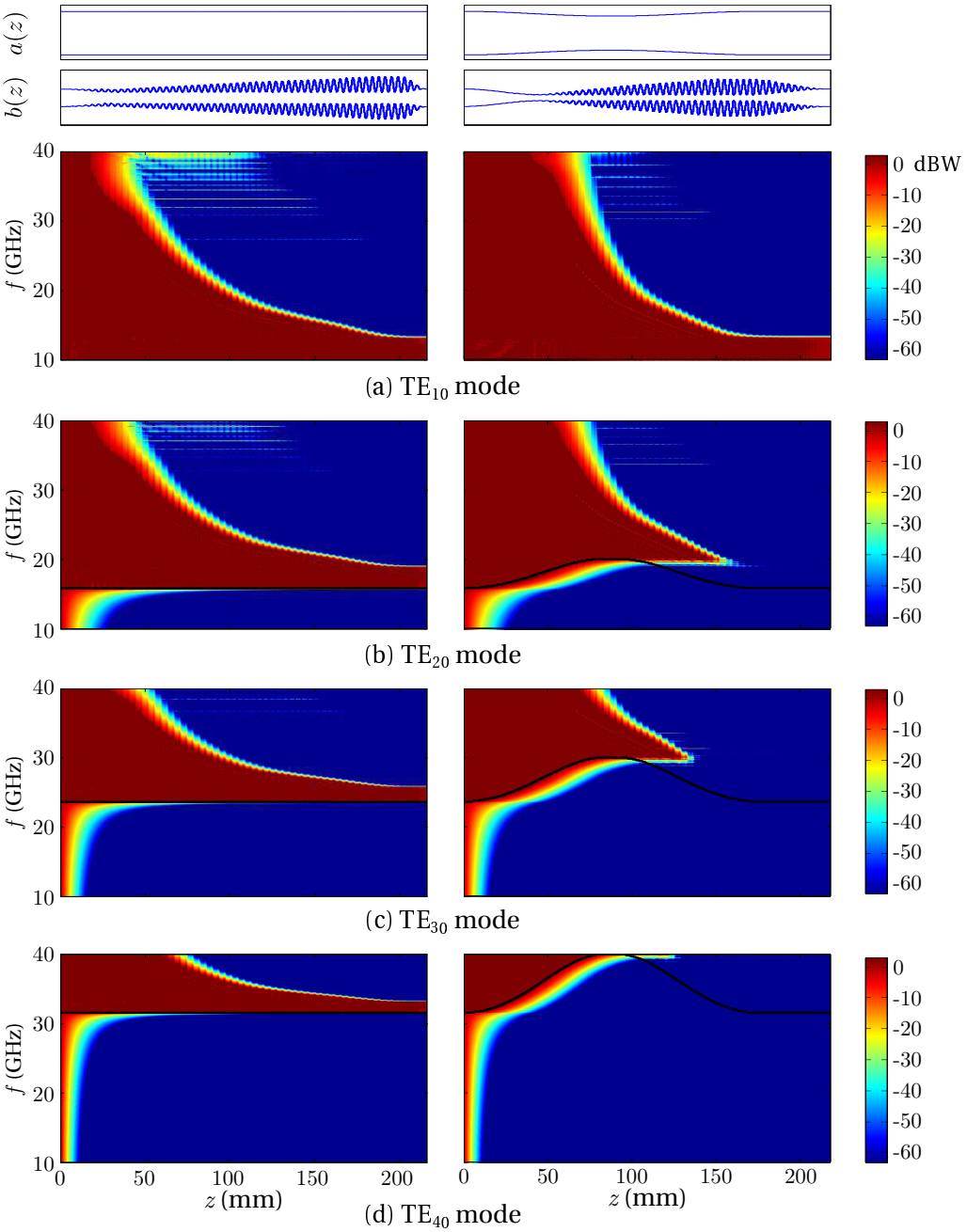

(a) TE_{10} mode

(b) TE_{20} mode

(c) TE_{30} mode

(d) TE_{40} mode

Figure 3.30: $P(z, f)$ in the device designed in Section 3.4.2 and the device designed with width reduction for (a) TE_{10} mode, (b) TE_{20} mode, (c) TE_{30} mode, and (d) TE_{40} mode in colored scale. Device profiles have been added on the top for both filters, and the cut-off frequency of each mode is included in black line.

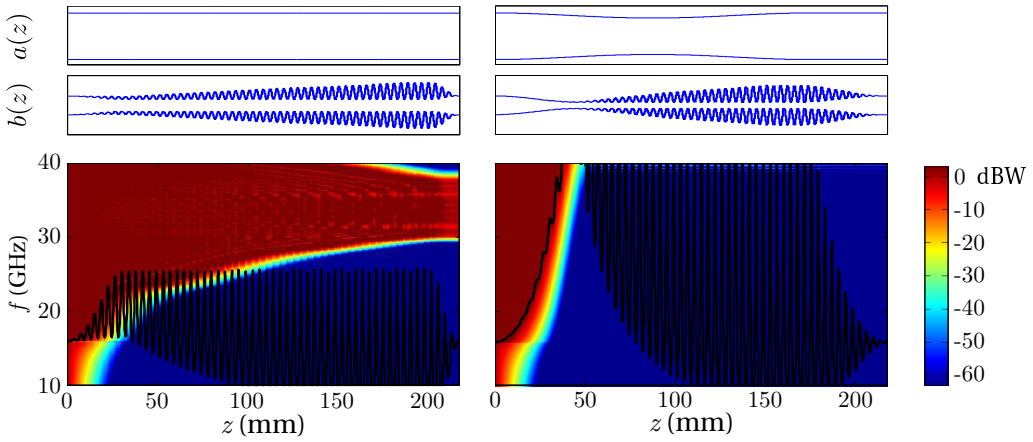

Figure 3.31: $P(z, f)$ in the device for the TE_{01} mode. The variation of the cut-off frequency along the devices is also depicted using black solid line.

Figure 3.32: Photograph of the high-power filter with width reduction, minimum gap equal to 3 mm and suppression of the higher-order modes. Prototype fabricated by electroforming.

the cut-off frequency of the modes is increased to surpass the highest frequency of their passband and to achieve in that way the passband elimination.

Moreover, the section with the minimum height makes possible the suppression of all the other (non-TE_{n0}) higher-order modes. $P(z, f)$ is represented in Figure 3.31 for the TE_{01} mode, the non-TE_{n0} mode with the lowest cut-off frequency. It can be seen in the figure how the reduction of the height in the device causes the mode to be in cut-off in a section which is long enough to eliminate its propagation in the rest of the device. Assuring that this mode is rejected, we can say that all other high-order non-TE_{n0} modes will be also rejected in the device.

The photograph of a prototype, fabricated using electroforming, is shown in Figure 3.32. Measurements have been performed with an Agilent 8722 VNA, proper waveguide to coaxial transitions and calibration kits. Non-linear tapers have been used to avoid the mismatch between the higher frequency coaxial-to-waveguide transitions and the filter ports for a correct characterization of the filter TE_{10}-mode behavior. In Figure 3.33, the measured TE_{10}-mode frequency response of the filter is shown along

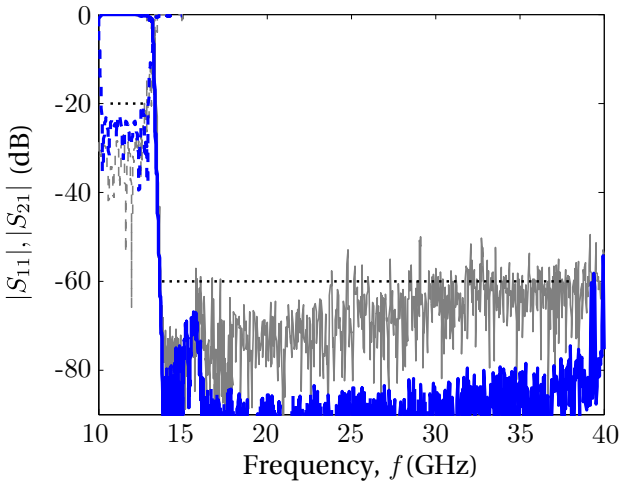

Figure 3.33: Measured frequency response for the TE_{10} mode of the filter with width reduction ans suppression of higher order modes (blue line) and the high-power filter in Section 3.4.2 (grey line): $|S_{11}|$ is given in dashed line and $|S_{21}|$ in solid line. Frequency specifications for $|S_{11}|$ and $|S_{21}|$ are also given in dotted line.

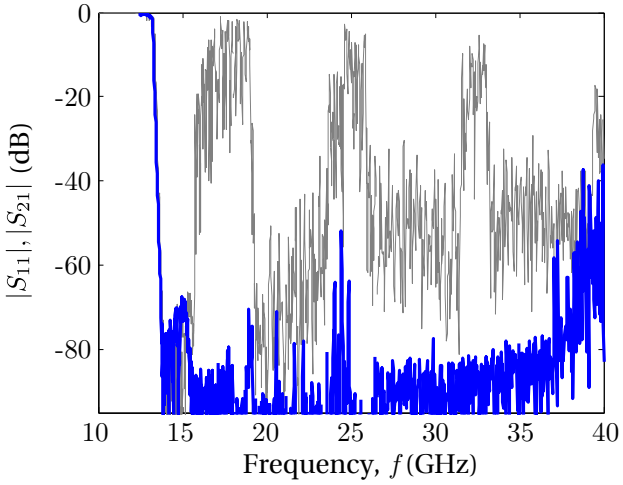

Figure 3.34: Measured $|S_{21}|$ frequency response for the TE_{10} mode (obtained with the 90º H-plane bends in the measurement set-up) of the novel filter with width reduction and suppression of the higher-order modes (blue line) and the high-power filter in Section 3.4.2 (grey line).

with the measured TE_{10}-mode frequency response of the solution given in Section 3.4.2. As it can be seen, both filters fulfill the TE_{10}-mode specifications. Specifically, the filter with width reduction has an excellent rejection level over 60 dB up to the third harmonic, while the in band insertion and return losses are better than 0.32 dB and 20 dB, respectively. Moreover, in order to validate with measurements the suppression of the higher order TE_{n0} modes, the set-up proposed in [44] that makes use of 90º H-plane bends has been used. The measurement results (see Figure 3.34) show the high attenuation of the peaks due to the suppression of the TE_{n0} modes demonstrating an excellent performance of the designed filter.

3.5. Conclusions

This Chapter focuses on the design and analysis of rectangular waveguide filters featuring smooth profiles. During the analysis special emphasis is made on multi-mode effects which are likely to occur, since the presented techniques deal with wide frequency bands. To analyze multi-mode operation of the presented filters, the mode-matching technique has been used and implemented using Matlab. A brief explanation of the well-known mode-matching technique that is behind the home-made software is presented as an introduction.

The synthesis method based on pole and zero decomposition (P&Z), presented in Chapter 2, has been particularized for rectangular waveguide technology. A multi-band Cauer filter has been designed using the P&Z synthesis method. Single-mode operation is assumed during design and it can be necessary to multiply the synthesized profile of the waveguide by a factor less than 1 to assure it. The home-made mode-matching program is used to confirm single-mode operation.

Reducing the synthesized profile can lead to minimum gaps that reduce the power capability of the filters. For high-power filters with very wide rejection band, a design method based on the Bragg phenomenon is presented. A classical high-power E-plane corrugated low-pass filter is cascaded with a quasi-periodic structure that performs sinusoidal perturbations with a period tuned to reject each of the harmonics. In this case, multi-mode effects provide an additional rejected frequency band coinciding with the third harmonic which avoids the need to use a periodic section specifically devoted to this frequency band and reduces the total length of the filter.

Lastly, an integrated design methodology of compact high-power low-pass filters is presented to reject the fundamental mode and its harmonics in a wide frequency band. The resulting filters consist of multiple E-plane bandstop elements of a sinusoidal profile, constituting a quasi-periodic structure, where the tuning of the rejected

frequencies is this time achieved through the height of the bandstop elements. A filter that satisfies the same specifications as the Bragg reflector-based solution has been designed following this method. To obtain also the rejection of higher order modes the design method has been modified by introducing a width reduction of some sections of the filter. Another design example is given for the same operation range showing excellent performance. The performance of both examples in response to high order modes is compared using the home-made mode-matching program and providing at the same time a better understanding of the operation basis of this type of filters.

References

[1] C. Ernst and L. Rigaudeau, "ESA-CNES keynote presentation," in *International Workshop on Microwave Filters (IWMF 2009)*, Toulouse, France, November 2009.

[2] V. E. Boria, P. Soto, and S. Cogollos, "Distributed models for filter synthesis," *Microwave Magazine*, vol. 12, no. 6, pp. 87–100, October 2011.

[3] S. B. Cohn, "Direct-coupled-resonator filters," *Proc. IRE*, vol. 45, no. 2, pp. 187–196, February 1957.

[4] G. Matthaei, L. Young, and E. M. T. Jones, *Microwave filters, impedance-matching networks, and coupling structures*. Artech House, Inc., 1980.

[5] R. J. Cameron, C. M. Kudsia, and R. R. Mansour, *Filters for Communications Systems: Fundamentals, Design, and Applications*. Hoboken, NJ: John Wiley & Sons, 2007.

[6] A. Garcia-Lamperez, S. Llorente-Romano, M. Salazar-Palma, and T. K. Sarkar, "Efficient electromagnetic optimization of microwave filters and multiplexers using rational models," *IEEE Transactions on Microwave Theory & Techniques*, vol. 52, no. 2, pp. 508–521, February 2004.

[7] J. V. Morro, P. Soto, H. Esteban, V. E. Boria, C. Bachiller, M. Taromcher, S. Cogollos, and B. Gimeno, "Fast automated design of waveguide filters using aggressive space mapping with a new segmentation strategy and a hybrid optimization algorithm," *IEEE Transactions on Microwave Theory & Techniques*, vol. 53, no. 4, pp. 1130–1142, April 2005.

[8] W. C. Hahn, "A new method for the calculation of cavity resonators," *Journal of Applied Physics*, vol. 12, no. 1, pp. 62–68, January 1941.

[9] J. Whinnery and H. W. Jamieson, "Equivalent circuits for discontinuities in transmission lines," *Proc. IRE*, vol. 32, no. 2, pp. 98–114, February 1941.

[10] A. Wexler, "Solution of waveguide discontinuities by modal analysis," *IEEE Transactions on Microwave Theory & Techniques*, vol. 15, no. 9, pp. 508–517, September 1999.

[11] I. Arnedo, M. A. G. Laso, F. Falcone, D. Benito, and T. Lopetegi, "A series solution for the single-mode synthesis problem based on the coupled mode theory," *IEEE Transactions on Microwave Theory & Techniques*, vol. 56, no. 2, pp. 457–466, February 2008.

[12] M. Muriel, A. Carballar, and J. Azaña, "Field distributions inside fiber gratings," *IEEE Transactions on Microwave Theory & Techniques*, vol. 35, pp. 548–558, 1999.

[13] I. Arnedo, I. Arregui, A. Lujambio, M. Chudzik, M. A. Laso, and T. Lopetegi, "Synthesis of microwave filters by inverse scattering using a closed-form expression valid for rational frequency responses," *IEEE Transactions on Microwave Theory & Techniques*, vol. 60, no. 5, pp. 1244–1257, May 2012.

[14] D. S. Heim and C. B. Sharpe, "The synthesis of nonuniform lines of finite length – part I," *IEEE Transactions on Circuit Theory*, vol. CT-14, pp. 393–403, 1967.

[15] R. E. Collin, *Foundations for microwave engineering*, 2nd ed. New York, NY: McGraw Hill, 1992.

[16] M. J. Erro, I. Arnedo, M. A. G. Laso, T. Lopetegi, and M. A. Muriel, "Phase-reconstruction in photonic crystals from S-parameter magnitude in microstrip technology," *Optical Quantum Electronics*, vol. 39, no. 4–6, pp. 321–331, Jun. 2007.

[17] I. Kay, "The inverse scattering problem when the refection coefficient is a rational function," *Communications on Pure and Applied Mathematics*, vol. 13, no. 3, pp. 371–393, 1960.

[18] B. Z. Katsenelenbaum, L. Mercader, M. Pereyaslavets, M. Sorolla, and M. Thumm, *Theory of nonuniform waveguides – The cross-section method*. London, UK: IEE Electromagnetic Waves Series, 1998, vol. 44.

[19] W.-K. Chen, *The circuits and filters handbook*. CRC Press, 1995.

[20] R. Schaumann and M. E. V. Valkenburg, *Design of analog filters*. New York, NY: Oxford University Press, 2001.

[21] G. H. Golub and C. F. V. Loan, *Matrix Computations*, 3rd ed. Baltimore, MD: The Johns Hopkins University Press, 1996.

[22] I. Arregui, I. Arnedo, A. Lujambio, M. Chudzik, M. A. G. Laso, T. Lopetegi, and M. Sorolla, "Design method for satellite output multiplexer low-pass filters exhibiting spurious-free frequency behavior and high-power operation," *Microwave and Optical Technology Letters*, vol. 52, no. 8, pp. 1724–1728, August 2010.

[23] N. F. Kovalev, I. M. Orlova, and M. I. Petelin, "Wave transformation in a multimode waveguide with corrugated walls," *Radiophysics and Quantum Electronics*, vol. 11, no. 5, pp. 449–450, 1986.

[24] E. F. Bolinder, "The relationship of physical applications of Fourier transforms in various fields of wave theory and circuitry," *IRE Trans. on Microwave Theory and Techniques*, vol. 6, no. 5, pp. 153–158, April 1957.

[25] C. K. Chong, D. B. McDermott, M. M. Razeghi, N. C. Luhmann, Jr., J. Pretterebner, D. Wagner, M. Thumm, M. Caplan, and B. Kulke, "Bragg reflectors," *IEEE Transactions on Plasma Science*, vol. 20, no. 3, pp. 393–402, June 1992.

[26] Y. Qian, V. Radisic, and T. Itoh, "Simulation and experiment of photonic band-gap structures for microstrip circuits," in *Proceedings Asia-Pacific Microwave Conference (APMC 1997)*, Hong Kong, 1997, pp. 585–588.

[27] I. Rumsey, M. Picket-May, , and P. K. Kelly, "Photonic bandgap structure used as filter in microstrip circuits," *IEEE Microwave and Guided Wave Letters*, vol. 10, no. 6, pp. 336–338, October 1998.

[28] F. Falcone, T. Lopetegi, and M. Sorolla, "1-D and 2D photonic band gap microstrip structures," *Microwave and Optical Technology Letters*, vol. 22, no. 6, pp. 411–412, September 1999.

[29] D. Nesic and A. Nesic, "Bandstop microstrip PBG filter with sinusoidal variation of the characteristic impedance and without etching in the ground plane," *Microwave and Optical Technology Letters*, vol. 29, no. 6, pp. 418–420, June 2001.

[30] M. A. G. Laso, T. Lopetegi, M. J. Erro, D. Benito, M. J. Garde, and M. Sorolla, "Multiple-frequency-tuned photonic bandgap microstrip structures," *IEEE Microwave and Guided Wave Letters*, vol. 10, no. 6, pp. 220–222, June 2000.

[31] J. Uher, J. Bornemann, and U. Rosenberg, *Waveguide Components for Antenna Feed Systems: Theory and CAD*. Artech House, 1993.

[32] P. Fortescue and J. Stark, *Spacecraft system engineering*. Chichester, UK: Wiley, 1995.

[33] M. Sorolla, D. Schmitt, M. Guglielmi, J. Gil, and N. Ortiz, "Microwave bandstop filter for an output multiplexer," US Patent 7 468 641, December 23, 2008.

[34] I. Arregui, S. Anza, I. Arnedo, C. Vicente, A. Lujambio, J. Gil, M. Chudzik, B. Gimeno, T. Lopetegi, M. A. G. Laso, and V. E. Boria, "Multipactor prediction in novel high-power low-pass filters with wide rejection band," in *Proceedings European Microwave Conference (EuMC 2009)*, Rome, Italy, September 2009, pp. 675–678.

[35] I. Arregui, I. Arnedo, A. Lujambio, M. Chudzik, D. Benito, R. Jost, T. L. F. J. Görtz, and M. A. G. Laso, "A compact design of high-power spurious free low-pass waveguide filters," *IEEE Microwave and Wireless Components Letters*, vol. 20, no. 11, pp. 595–597, November 2010.

[36] I. Arnedo, J. Gil, N. Ortiz, T. Lopetegi, M. Laso, M. Sorolla, M. Thumm, D. Schmitt, and M. Guglielmi, "Ku-band high-power lowpass filter with spurious rejection," *Electronics Letters*, vol. 42, no. 25, pp. 1460–1461, December 2006.

[37] I. Arregui, F. Teberio, I. Arnedo, A. Lujambio, M. Chudzik, D. Benito, T. Lopetegi, R. Jost, F. J. Görtz, J. Gil, C. Vicente, B. Gimeno, V. Boria-Esbert, D. Raboso, and M. A. G. Laso, "Multipactor-resistant low-pass harmonic filters with wide-band higher-order mode suppression," in *Proc. of International Microwave Symposium (IMS2013)*, Seattle, June 2013.

[38] I. Arregui, F. Teberio, I. Arnedo, A. Lujambio, M. Chudzik, D. Benito, T. Lopetegi, R. Jost, F. J. Görtz, J. Gil, C. Vicente, B. Gimeno, V. E. Boria, D. Raboso, and M. A. G. Laso, "High-power low-pass harmonic filters with higher-order TE_{n0} and non-TE_{n0} mode suppression: Design method and multipactor characterization," *IEEE Transactions on Microwave Theory & Techniques*, vol. 61, no. 12, pp. 4376–4386, December 2013.

[39] P. Sarasa, A. González, H. Esteban, P. Mader, K. Tossou, and P. Lepeltier, "Comparative study of the power handling capability of space broadband antenna filters in Ku-band," in *Proceedings 5th ESA International Workshop on Multipactor, Corona and Passive Intermodulation in Space RF Hardware*, Noordwijk, September 2005.

[40] I. Arregui, I. Arnedo, M. A. G. Laso, T. Lopetegi, and A. Marcotegui, "Lowpass filter for electromagnetic signals," US Patent 2010/0 308 938, January 21, 2008.

[41] ——, "Lowpass filter for electromagnetic signals," European Patent 2 244 330, January 21, 2008.

[42] M. A. G. Laso, M. J. Erro, T. Lopetegi, D. Benito, M. J. Garde, and M. Sorolla, "Optimization of tapered bragg reflectors in microstrip technology," *International Journal of Infrared and Millimeter Waves*, vol. 21, no. 2, pp. 231–245, February 2000.

[43] R.Levy, "Inhomogeneous stepped-impedance corrugated waveguide low-pass filters," in *Proceedings IEEE MTT-S Digest*, Long Beach, 2005, pp. 123–126.

[44] K. L. Wu and G. McDonald, "Coping with hidden spurious harmonic modes in the design of low pass corrugated waveguide filters," *Microwave Journal*, vol. 44, no. 11, pp. 180–183, November 2001.

Chapter 4

Dispersive delay lines

Actual communication systems require wide bandwidths in order to allow high data-rates. Both the wide bandwidth and high data-rates, suppose an important challenge for the design and analysis of system components. The extensive use of digital signal processing (DSP) devices due to their small size, low cost and reliability in low frequency applications, encounters several drawbacks at high frequencies. Their performance limitations, the cost of ultrafast A/D and D/A converters, and their power consumption make necessary to find an alternative to digital processors.

In these circumstances, microwave analog signal processing (ASP) is presented as a very appealing approach that has attracted the interest of the microwave community in recent years [1, 2]. By this concept many different systems are described, all of them aimed to process signals in their pristine analog form and in real time. The principal property of those systems is that they don't focus on a specific magnitude response, but in their phase response, leading to a new concept defined as phase engineering or also dispersion engineering.

Table 4.1 contains a summary of different applications depending on the required phase characteristic. The constant and linear phase responses correspond to a non-dispersive device. However, to obtain a quadratic phase response a dispersive behavior is required. For this reason, this type of devices is usually called dispersive delay line (DDL) emphasizing their dispersive behavior. They are also named after phasers, dispersive delay structures (DDS) or all-pass networks in literature. Thus, an ideal DDL is characterized by having uniform insertion losses and a linear group-delay response (or equivalently a quadratic phase response).

This chapter begins with a review of the state of the art on the design of DDLs.

TABLE 4.1
ANALOG SIGNAL PROCESSING APPLICATIONS FOR DIFFERENT PHASE SPECIFICATIONS.

Constant phase	Linear phase	Quadratic phase
Multi-band components	Tunable delay line	Real-time Fourier transformer (RTFT)
Bandwidth enhancement	True time delayer	Dispersion compensator
Coupling enhancement	Pulse position modulator	Real-time spectrum analyzer (RTSA)
Flexible combiner/divider	Tunable pulse generator	Frequency discriminator
Direction of Arrival (DoA)	...	Convolvers and correlators
...		...

In the next section, a new method for the design of DDLs in coupled-lines producing effective transmission-type DDLs will be presented. Finally, the last section of this chapter provides examples of applications of the proposed DDLs in analog signal processing schemes.

4.1. State of the art

The design of Dispersive Delay Lines (DDLs) has recently experienced a boost because of the great interest of wideband communication systems and other high frequency applications. However, many different DDL technologies were reported long before. The interest on DDLs arose mainly due to the requirements of military applications. In 1960, a technique to provide long range and high resolution for radar applications was devised [3], named as *chirp radars*. Soon, the surface acoustic wave (SAW) DDLs were developed. They were demonstrated to be well-suited for this application, since they are able to both generate the required swept-frequency waveform and function as an ideal receiver (matched filter). SAW DDLs are readily implemented by chirped interdigital transducers (IDT) [4], and their performance can be improved using Reflective Array Compressors (RACs) [5, 6]. Due to their slow-wave characteristic, SAW devices provide large delays and high time-bandwidth products. In addition,

the designed devices are very compact in size, and their design allows amplitude control. However, they are restricted to narrow-band and low-frequency applications.

An alternative to SAW technology in order to increase the operation frequency is based on magnetostatic wave (MSW) technology [7]. The inherently dispersive MSWs can propagate in ferrimagnetic films. Using different orientation for the bias magnetic field, different magnetostatic propagation modes can be excited, and many applications can be found for them. The interesting case for us is that of a linear DDL. Different methods, described in [7], can be used to modify the originally non-linear dispersive propagation characteristics of MSWs and linearize the group delay. In this manner, large delays for relatively high frequencies and bandwidths are achieved. However, they suffer from several drawbacks such as their complex fabrication, having high losses and requiring a magnet.

Also in the 1980s, a method consisting of multi-section couplers was proposed [8]. Each section of the designed device is a $\lambda/4$ backward-wave coupler, tuned to a frequency within the passband of the DDL. Cascading many couplers, each of them designed for a different frequency, the desired linear group-delay is achieved. The amplitude can be also controlled while obtaining large delays for arbitrary operation frequencies. Moreover, wide bandwidths can be achieved, depending the size of the device on the bandwidth characteristic. Thus, wide bandwidths require very long devices which drastically increases the losses. In order to solve this problem, superconducting materials are employed, initially low-temperature superconductors, but nowadays also high temperature superconductors are used [9].

In 2001, chirped delay lines (CDL) in microstrip technology were proposed [10]. They are obtained implementing a quasi-sinusoidal perturbation of the characteristic impedance that varies linearly its period. In such a way, each frequency is reflected back at different points of the device and the linear group-delay characteristic is obtained. As opposed to the previous technologies, they operate in reflection, requiring a circulator to separate the input and output signals. As main advantages, we should point out that large delays can be achieved for wide bandwidths and at arbitrary frequencies. Moreover, they are fabricated in planar technology and there is control of the amplitude during design. Since firstly reported, many practical applications have been proposed using CDLs [11–16]. Based on the same operation principle, a design method for substrate integrated waveguide (SIW) technology has been recently presented [17]. Finally, to avoid the need of using a circulator of the CDLs, they were adapted to coupled-line technology during this thesis [18].

As mentioned above, in the last decade the interest on the DDLs has increased, producing a high number of publications regarding the topic. Specifically, Caloz and

Transmission operation

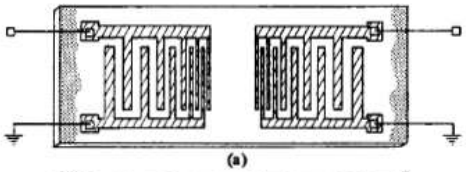

SAW

Advantages	Disadvantages
Large delay High TB product Amplitude control Compact size	Low f_0 Narrow-band

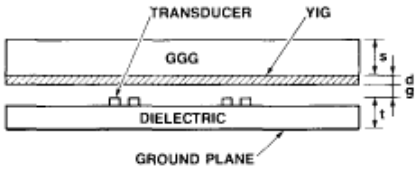

MSW

Advantages	Disadvantages
Relatively high f_0 Relatively wide-band Large delay High TB product	High loss Requires magnet Complex fabrication

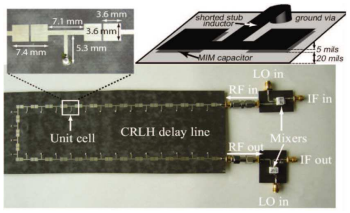

CRLH

Advantages	Disadvantages
Arbitrary f_0 Wide-band Size-BW independence Planar fabrication	Requires shielding No amplitude control

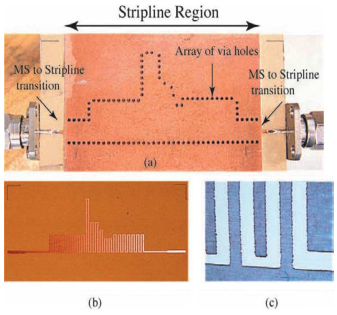

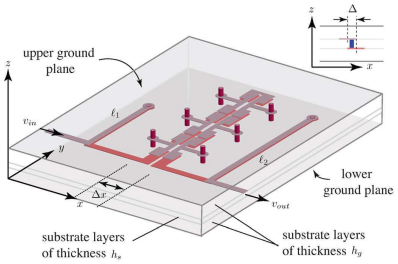

CRLH-CRLH C-section

Advantages	Disadvantages
Arbitrary f_0 Wide-band Planar fabrication Compacct size High TB product	Requires shielding (stripline) No-closed form synthesis Complex design

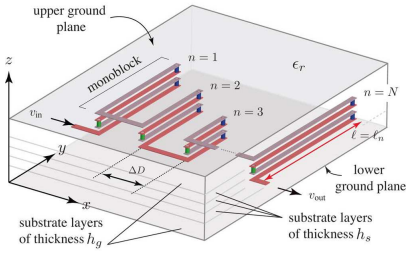

C-section

Advantages	Disadvantages
Arbitrary f_0 Wide-band Planar fabrication Analytical models	Large size Requires shielding Small TB product

Figure 4.1: Overview of the principal transmission-type DDL technologies with a summary of their properties.

(a) Effective transmission operation

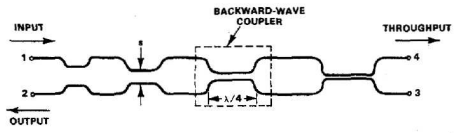

Multi-section coupler

Advantages	Disadvantages
Arbitrary f_0 Wide-band Large delay High TB product Amplitude control	Size-BW dependence HTS and cryogenics Complex fabrication

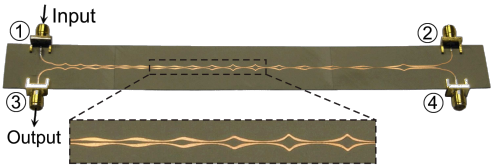

Coupled-line CDL

Advantages	Disadvantages
Arbitrary f_0 Wide-band Amplitude control Planar fabrication	Size-BW dependence

(b) Reflection operation

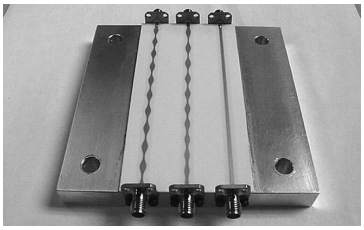

CDL

Advantages	Disadvantages
Arbitrary f_0 Wide-band Amplitude control Planar fabrication	Size-BW dependence Requires circulator

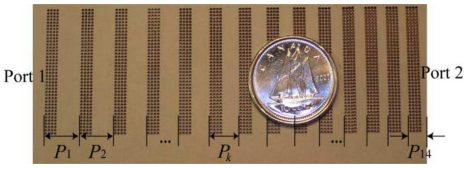

ADS

Advantages	Disadvantages
Arbitrary f_0 Wide-band Planar fabrication	Size-BW dependence Requires circulator Complex fabrication

Figure 4.2: Overview of the principal (a) effective transmission-type and (b) reflection-type DDL technologies with a summary of their properties.

his research group have produced many publications reporting different approaches focused on DDLs, the more general phase engineering concept and their application for analog signal processing. One of the proposed methods is based on the same principle as the CDLs. Instead of implementing the quasi-sinusoidal impedance variation by modifying the strip-width of a microstrip line, sections of conventional and an artificial dielectric substrate (ADS) microstrip are alternated with a linearly varying period [19]. Thus, the desired response is obtained in reflection.

Another approach is based on electromagnetic metamaterials. Several applications have been demonstrated to be feasible using composite right/left-handed (CRLH) transmission lines (TL) [20, 21]. A CRLH TL is an artificial transmission line constructed by unit cells, made of a composition of capacitors and inductors. The propagation constant of a CRLH TL is composed by a linear term and an hyperbolic term that account for their right-handed and left-handed contributions respectively. This results in a dispersive behavior that can be used for many different ASP applications requiring all-pass response in magnitude and different phase characteristics, as it is the case of DDLs. But it should be pointed out that they do not provide a linear group-delay. Their non-linearity has been compensated in practice by a proper use of the elements of the systems where they have been employed [22]. They can be designed at arbitrary frequencies and for wideband applications in planar technology. However, their amplitude response cannot be controlled and shielding is required to avoid radiation.

Focusing on the phase engineering concept and also in obtaining a properly linear group-delay response, a design technique was proposed based on the use of transmission-line C-sections [23]. A C-section is composed of two coupled-lines of length $\lambda/4$ short circuited at one end. They provide an all-pass response in magnitude and a group-delay that varies in frequency presenting a maximum at the design frequency and its odd multiples. By cascading C-sections of different lengths (noncommensurate C-sections) the desired group-delay can be obtained at arbitrary frequencies. A genetic algorithm is used to determine the length and coupling of the required C-sections. For wide bandwidths a high number of sections needs to be used obtaining large devices. Moreover, the group-delay swing depends on the coupling between the coupled-lines and it is limited to be quite low, which produces a small time-bandwidth product. In order to improve this property, several alternatives have been reported: using a loop system to increase the delay slope in several processing turns [24] or increasing the coupling of the C-sections by employing broadside-coupled C-sections [25], ferrimagnetic substrates [26] or CRLH-CRLH C-sections [27].

This very year, new closed-form synthesis methods to obtain arbitrary prescribed group-delays [28, 29] using the already described C-sections have been reported. In addition, similar synthesis methods have been used also for rectangular waveguide technology working in reflection [30] and in transmission [31].

To end this section, the principal DDL technologies are summarized in Figure 4.1 and Figure 4.2 where the advantages and disadvantages of each technology are also included.

4.2. Chirped delay lines in coupled lines

Chirped delay lines (CDLs) [10, 11] have been already introduced in the review of the actual state of the art. Their applicability has been demonstrated in practical applications such as real-time spectrum analysis [12], time magnification and compression of signals [13], continuously tunable delay lines [14], chromatic dispersion compensation for optical communication systems [15] or sub-wavelength antenna arrays using the time reversal technique [16]. The devices operate in reflection which implies that a circulator is required to separate the input and output signals. However, coupled-line technology can be used to avoid the use of a wideband circulator and increase the practical applicability of the CDLs.

This section will be devoted to present the CDLs in coupled lines. The first subsection will summarize the requirements of coupled lines in order to obtain a satisfactory design. It follows a description of the operation principle of CDLs and based on that, the design method for coupled lines. Finally, in order to demonstrate the validity of the proposed technique a design example will be presented aimed for UWB signal processing which has been characterized in frequency and time domain.

4.2.1. Requirements of coupled-line technology

Coupled-line technology has been presented already in Section 2.2.3.3, where the cross-section method of the coupled-mode theory was applied. When symmetrical edge-coupled transmission lines are considered (see Figure 4.3), even and odd mode decomposition can be applied. Hence, the equations resulting from the direct application of the coupled-mode theory can be greatly simplified.

The operations have been performed in Section 2.2.3.3, concluding that the equations modeling the performance of symmetrical edge-coupled transmission lines can be divided into two independent systems: one involving only the even mode, and another one involving only the odd mode. The set of equations for the two systems are

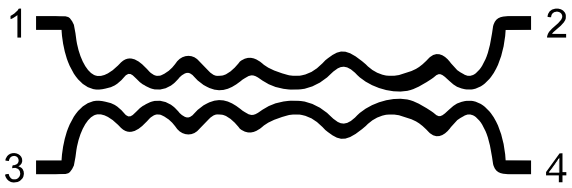

Figure 4.3: Sketch of symmetrical edge-coupled transmission lines. Port (#1) is the input port, port (#2) is the direct port, port (#3) is the coupled port and port (#4) is the isolated port.

rewritten here:

$$\begin{aligned} \frac{da_e^+}{dz} &= -j\beta_e a_e^+ + K_e a_e^- \\ \frac{da_e^-}{dz} &= K_e a_e^+ + j\beta_e a_e^- \end{aligned} \tag{4.1a}$$

$$\begin{aligned} \frac{da_o^+}{dz} &= -j\beta_o a_o^+ + K_o a_o^- \\ \frac{da_o^-}{dz} &= K_o a_o^+ + j\beta_o a_o^- \end{aligned} \tag{4.1b}$$

being a_e^+, a_e^- the complex amplitudes of the forward and backward waves of the even mode and a_o^+, a_o^- the complex amplitudes of the forward and backward waves of the odd mode; β_e and β_o are the propagation constants of the forward waves of the even and odd modes, respectively; K_e and K_o are the coupling coefficients between the forward and backward waves of the even and odd modes, respectively.

As it has been explained in detail in Section 2.2.3.3, K_e and K_o can be related to the even- and odd-mode characteristic impedances as:

$$K_e = \frac{-1}{2Z_{0e}(z)} \cdot \frac{dZ_{0e}(z)}{dz}. \tag{4.2a}$$

$$K_o = \frac{-1}{2Z_{0o}(z)} \cdot \frac{dZ_{0o}(z)}{dz}. \tag{4.2b}$$

Equations in (4.2) can be solved analytically for the even- and odd-mode characteristic impedances to obtain:

$$Z_{0e}(z) = Z_{0e}(0^+)\, e^{-2\int_0^z K_e(r)dr} \tag{4.3a}$$

$$Z_{0o}(z) = Z_{0o}(0^+)\, e^{-2\int_0^z K_o(r)dr} \tag{4.3b}$$

being $Z_{0e}(0^+)$ and $Z_{0o}(0^+)$ the limits from the right side of the even- and odd-mode characteristic impedances, respectively, at the beginning of the device ($z = 0$) and r an auxiliary variable over which the integral is carried out.

Moreover, taking advantage of the even and odd mode decomposition, the most meaningful S-parameters can be calculated as [32]:

$$S_{11} = \frac{\Gamma_e + \Gamma_o}{2} \tag{4.4a}$$

$$S_{21} = \frac{\mathrm{T}_e + \mathrm{T}_o}{2} \tag{4.4b}$$

$$S_{31} = \frac{\Gamma_e - \Gamma_o}{2} \tag{4.4c}$$

$$S_{41} = \frac{\mathrm{T}_e - \mathrm{T}_o}{2} \tag{4.4d}$$

where Γ_e, Γ_o are the reflection coefficients, and T_e, T_o are the transmission coefficients of the even and odd modes, respectively, where the port numbers follow the convention of Figure 4.3. Indeed, these coefficients can be linked with the variables defined in the systems (4.1), resulting in:

$$\Gamma_e = \left.\frac{a_e^-(z=0)}{a_e^+(z=0)}\right|_{a_e^-(z=L)=0} \tag{4.5a}$$

$$\Gamma_o = \left.\frac{a_o^-(z=0)}{a_o^+(z=0)}\right|_{a_o^-(z=L)=0} \tag{4.5b}$$

$$\mathrm{T}_e = \left.\frac{a_e^+(z=L)}{a_e^+(z=0)}\right|_{a_e^-(z=L)=0} \tag{4.5c}$$

$$\mathrm{T}_o = \left.\frac{a_o^+(z=L)}{a_o^+(z=0)}\right|_{a_o^-(z=L)=0} \tag{4.5d}$$

where it is also assumed that the normalization of the modes does not vary with z, or that all the involved ports are identical.

Considering (4.4a) and (4.4c), it is straightforward to show that if the design condition

$$\Gamma_e(f) = -\Gamma_o(f) \tag{4.6}$$

is satisfied, then

$$\begin{aligned} S_{11}(f) &= 0 \\ S_{31}(f) &= \Gamma_e(f) \end{aligned} \tag{4.7}$$

producing a device with the input port (#1) matched at all frequencies and with the reflected signal redirected to the coupled port (#3).

The requirement (4.6) is equivalent to

$$\Gamma_o(\beta_o) = -\Gamma_e(\beta_e) \tag{4.8}$$

where we can clearly distinguish two different possibilities: $\beta_o = \beta_e$, the case of the symmetrical edge-coupled stripline, and $\beta_o \neq \beta_e$, the case of the symmetrical edge-coupled microstrip.

Considering the equal propagation case, $\beta_o = \beta_e$, it has been demonstrated in Section 2.2.3.3 that this condition can be translated to the coupling coefficients as

$$K_o(z) = -K_e(z). \tag{4.9}$$

Substituting (4.9) in (4.3b) and multiplying the result with equation (4.3a), it can be shown that the relation in (4.9) can be rewritten as

$$Z_{0e}(z) \cdot Z_{0e}(z) = Z_{0e}(0^+) \cdot Z_{0e}(0^+) = Z_0^2 \tag{4.10}$$

where Z_0 is the characteristic impedance of the access lines that coincides with the one of the ports. It has been supposed that the ports are decoupled (independent ports), where obviously, $Z_{0e}(0^+) = Z_{0o}(0^+) = Z_0$.

Moreover, and due to the intrinsic behavior of symmetrical edge-coupled transmission lines, the relation

$$Z_{0e} \geq Z_{0o} \tag{4.11}$$

between the even- and odd-mode characteristic impedances is always hold, and the equality will be possible only in the limit, when the separation between the lines tends to infinity [32].

For the case of symmetrical edge-coupled microstrip, it can be stated that the following relationship between the effective relative permittivities of the even and odd modes will be always satisfied [32]:

$$\varepsilon_r > \varepsilon_{ee} > \varepsilon_{eo} \tag{4.12}$$

implying that the even and odd modes will propagate at different speeds, $\beta_o \neq \beta_e$. In this situation, directly satisfying condition (4.6) becomes troublesome, since the effective relative permittivities for the even and odd modes have a complicated dependence with the physical dimensions. Then, a new strategy has to be employed. The design strategy starts with the assumption of equal even- and odd-mode propagation constants (like in the stripline case). Thus, an auxiliary device with a total length of L_{aux} and relative permittivity of ε_{aux} is obtained. Afterwards, the Algorithm 2.4 described in Section 2.2.3.3 is applied, which takes into account in each step the phase constant of each mode along the device, modifying the spatial distribution of the even- and odd-mode characteristic impedances accordingly, in order to satisfy (4.6).

The effect of the algorithm can be explained intuitively as a spatial redistribution of the even- and odd-mode characteristic impedances calculated for the case where both modes propagate at the same speed. The auxiliary impedances are redistributed along the propagation direction, in such a way that the even and odd modes, propagating at different speeds, are affected at each time instant by the same pair of even- and odd-mode characteristic impedances as in the case of equal speed propagation. Due to the fact that (4.12) always holds, the process leads to a local compression for the even-mode characteristic impedance, and to a local expansion for the odd-mode characteristic impedance. For the same reason, it will be necessary to pad with enough

values equal to $Z_{0e}(L_{\text{aux}})$ the even characteristic impedance $Z_{0e}(z)$, in order to have both characteristic impedances with the same length at the output of the algorithm.

4.2.2. Operation principle and design method

In the last years, the area of periodic structures for electromagnetic waves has been a subject of great interest for the microwave community due to the introduction of the novel and fruitful concepts of Photonic Bandgap (PBG) and Electromagnetic Bandgap (EBG) structures [33–36]. These novel concepts gave rise to new design approaches that allow obtaining improved microwave devices.

Using coupled mode theory, the electromagnetic behavior of an EBG-type structure can be characterized through the coupling coefficient, $K(z)$, which provides a measure of the energy transfer between the forward and backward traveling waves [37]. If the structure is periodic along the propagation axis z with period a_0, then the coupling coefficient, $K(z)$, produced by the perturbation is also periodic and it can be expanded in a Fourier series. This means that the frequency response of the structure will present several stopbands corresponding to the fundamental frequency of the Fourier series expansion and its harmonics, as it is shown in Figure 4.4. The first stopband is centered at the frequency where the period of the perturbation corresponds to a half of the guided wavelength, $a_0 = \lambda_g/2$ (π-rad phase shift), satisfying the Bragg condition.

If only the first term of the Fourier series expansion of $K(z)$ is considered, the coupling coefficient will be purely sinusoidal and only the first band will be rejected (see

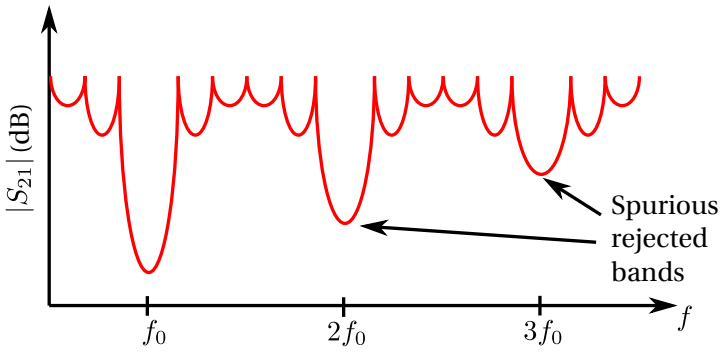

Figure 4.4: Sketch of the typical frequency response of a classical EBG structure.

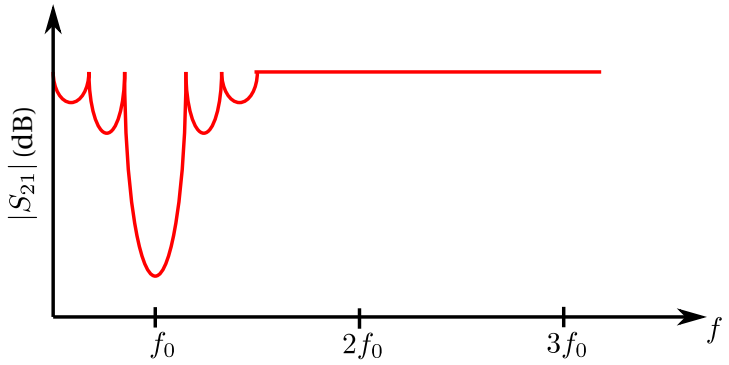

Figure 4.5: Sketch of the frequency response of the optimum EBG structure, free of spurious rejected bands.

Figure 4.5), obtaining a spurious-free frequency response [38–40]. For planar technology, where the operation mode is TEM or quasi-TEM, the relation between the coupling coefficient and the characteristic impedance is [1]:

$$K(z) = -\frac{1}{2Z_0(z)} \cdot \frac{dZ_0(z)}{dz} \leftrightarrow Z_0(z) = Z_0\left(0^+\right) e^{-2\int_0^z K(r)dr} \tag{4.13}$$

being $Z_0\left(0^+\right)$ the characteristic impedance at the beginning of the device, chosen to be the characteristic impedance of the port to provide a good matching. Thus, for the mentioned purely sinusoidal coupling coefficient, $K(z) = A\cos\left(\frac{2\pi}{a_0}z + \phi\right)$, we will have a characteristic impedance modulation of the form:

$$Z_0(z) = Z_0\left(0^+\right) e^{A\sin\left(\frac{2\pi}{a_0}z + \theta\right)} \tag{4.14}$$

where A is a nondimensional amplitude factor, and θ is properly selected to make sure that the characteristic impedance at the beginning and the end of the device is equal to $Z_0\left(0^+\right)$, which is selected to be the characteristic impedance of the ports.

Based on the same operation principle, the chirped delay lines proposed in our research group some years ago for microstrip technology [10, 11], correspond to a characteristic impedance of the same type which has been linearly frequency-modulated (chirped). This means that the frequency of the sinusoidal in (4.14) varies with the propagation direction following a linear variation of the form $\zeta(z) = \frac{2\pi}{a_0} + Cz$, being

[1] The derivation of this relationship is explained in detail in Section 2.2.3.2.

C the chirp coefficient that fixes the variation rate of the perturbation. Hence, the characteristic impedance results in

$$Z_0(z) = Z_0\left(0^+\right)\, e^{A\sin\left(\int \zeta(z)dz + \gamma\right)} \tag{4.15}$$

being γ an integration constant selected appropriately. It should be noted also that in this expression the propagation direction, z, takes values in $[-L/2, L/2]$ in order to vary the frequency around the center value $\dfrac{2\pi}{a_0}$ chosen adequately for the center frequency of operation. Moreover L, the total length of the device, has to be a multiple of a_0 so that an entire number of periods is included in the device.

In this case, the phase-matching condition for resonant Bragg coupling between the quasi-TEM microstrip mode and the same but counter-propagating mode is ideally satisfied at only one position for each spectral frequency. At this position the propagating wave will be back-reflected. Moreover, since the perturbation is linearly chirped then the mode-coupling location varies linearly in frequency. As a result, the reflection time is also a linear function of frequency. This is equivalent to say that the group-delay varies linearly with frequency. Thus, the typical response is that given in Figure 4.6(a). It is important to point out that the coupling coefficient will be obviously a linearly chirped sinusoidal.

The characteristic impedance finally implemented in [10, 11] followed the expression:

$$Z_0(z) = 50\, e^{A\,W(z)\,\sin\left(\frac{2\pi}{a_0}z + Cz^2 - CL^2/4\right)} \tag{4.16}$$

where the integration constant is fixed to $\gamma = -CL^2/4$ in order to match 50 Ω input and output ports, and $W(z)$ is a windowing function to smooth input and output impedance transitions to avoid partial reflections from the extremes of the structure that give rise to different long-path Fabry-Perot like resonances, which cause undesirable rapid ripple to appear around the mean values in the magnitude and group-delay versus frequency patterns degrading the performance of the device.

The major disadvantage of this structure is that it operates in reflection and hence, it requires a circulator that increases the losses and the complexity of the system where the device needs to be used. To avoid this inconvenience coupled-line technology can be used following the design conditions deduced in Section 4.2.1. According to (4.7), it is possible to achieve a device with an input port (#1) matched for all frequencies and the desired response in the coupled port (#3) (see Figure 4.6(b)). The resulting device will keep all the advantages of the previous two-port devices without the need of employing a circulator.

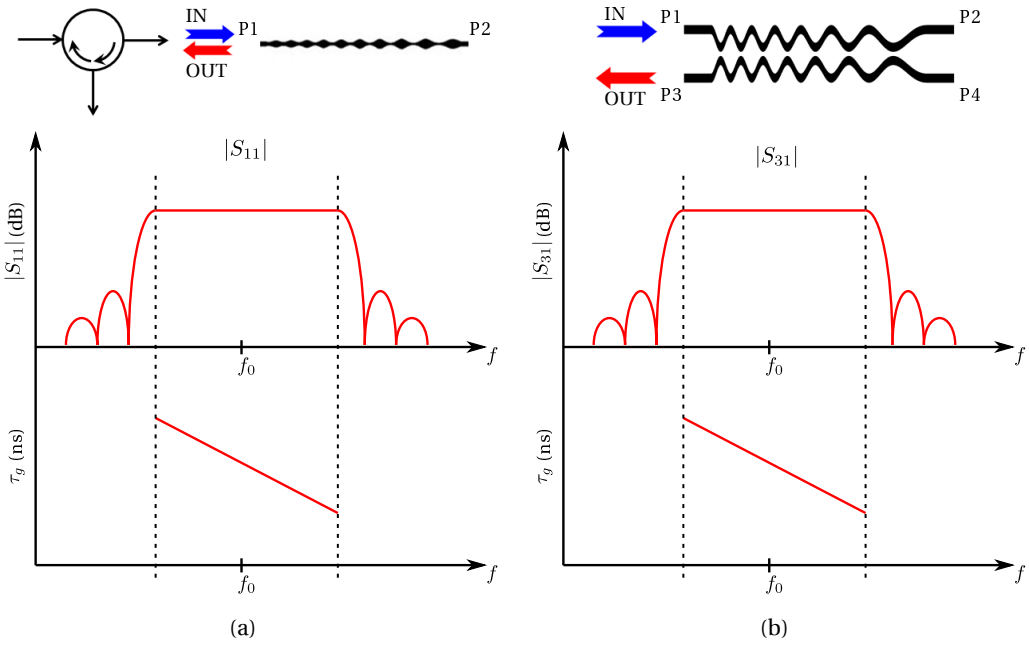

Figure 4.6: Sketch of the frequency response of a chirped EBG structure in (a) microstrip and (b) coupled-line technology.

We can define an expression, similar to (4.16), for the even-mode characteristic impedance of coupled-lines:

$$Z_{0e}(z) = Z_{0e,\text{init}}\, e^{A\,W(z)\left\{1+\sin\left[\left(\frac{2\pi}{a_0}-CL\right)z+Cz^2-\frac{\pi}{2}\right]\right\}} \tag{4.17}$$

Several changes have been introduced compared to (4.16). First, a variable change in z has been performed to take values in $[0, L]$ since this is more conventional. The value of Z_{0e} at the beginning and the end of the device is fixed to $Z_{0e,\text{init}}$. In order to guarantee a proper matching, this value will be ideally equal to the port impedance. Finally, the necessary constants have been introduced to satisfy the intrinsic limitation of coupled-lines in (4.11).

Following the condition in (4.9), the odd-mode characteristic impedance will be defined by simply changing the sign of the exponent in (4.17):

$$Z_{0o}(z) = Z_{0o,\text{init}}\, e^{-A\,W(z)\left\{1+\sin\left[\left(\frac{2\pi}{a_0}-CL\right)z+Cz^2-\frac{\pi}{2}\right]\right\}} \tag{4.18}$$

where $Z_{0o,\text{init}}$ is the value of Z_{0o} at the beginning and the end of the device.

The design parameters employed correspond to the same parameters defined for microstrip chirped delay lines. In order to summarize all the information, they will be described newly here. Moreover, their design equations will be given in order to calculate them to satisfy the requirements of bandwidth, Δf (Hz), central frequency, f_0 (Hz), and group-delay slope, ψ (s/Hz).

The design parameter a_0 is the mean period of the quasi-sinusoidal perturbation, that will correspond to the required perturbation period for the central frequency of operation. It can be calculated for a given substrate as:

$$a_0 = \frac{c}{2f_0\sqrt{\varepsilon_{\text{eff}}|_{Z_0}}} \tag{4.19}$$

being $\varepsilon_{\text{eff}}|_{Z_0}$ the substrate effective permittivity for the microstrip ports of characteristic impedance Z_0, and c is the speed of light in free space.

The variation rate of the perturbation is fixed by the chirp coefficient, C, which controls the slope of the group-delay. It is defined by:

$$C = \frac{4\pi\varepsilon_{\text{eff}}|_{Z_0}}{\psi c^2} \tag{4.20}$$

as a function of the slope of the group-delay, ψ, and the substrate.

In order to have the same impedance value at the beginning and the end of the device, the length of the device must contain an integer number of periods, N, and thus, it will be defined as $L = N\,a_0$. However, a minimum length is required to achieve the desired bandwidth, Δf, and the given group-delay slope, ψ, and this minimum can be calculated as:

$$L \geq \frac{c|\psi|\Delta f}{2\sqrt{\varepsilon_{\text{eff}}|_{Z_0}}}. \tag{4.21}$$

Another important parameter is the windowing function, $A\,W(z)$. The peak amplitude of the modulation, A, governs the amount of energy that will be coupled to the coupled port (#3). And a windowing function, $W(z)$, is employed to smooth out the impedance transitions between the accesses and the core of the structure, taking normalized values between 0 and 1 [10]. This function is used to reduce the ripple level of the response in the operation frequency band, although it also reduces the operation bandwidth [10]. This is compensated by increasing the peak amplitude of the modulation, A, and the length of the device, L, using a higher number of perturbation periods, N. A compromise between the ripple level and the device length has to be achieved to satisfy the application requirements. On the other hand, by using a proper windowing function, the frequency dependency of the losses can be compensated to get uniform insertion losses in the operation bandwidth: stronger coupling should be achieved at the regions where the frequencies more attenuated by the losses are coupled [10].

Finally, the values of even- and odd-mode characteristic impedances at the beginning and the end of the device, $Z_{0e,\text{init}}$ and $Z_{0o,\text{init}}$, need to be defined. Both parameters should be ideally chosen equal to the specified port impedance, Z_0. However, this would lead to infinitely separated strips [32], so in practice, they are chosen to be close to the ideal value and satisfying both (4.10) and (4.11).

The impedance pair is fully defined for the case of symmetrical edge-coupled stripline. For microstrip technology, the difference between the even- and odd-mode propagation constants has to be compensated at this point following the Algorithm 2.4 proposed in Section 2.2.3.3.

Finally, for each even- and odd-mode impedance pair, the width of the metal strips, W, and the separation between them, s, are calculated using classical references [32] or a design software, e.g. Agilent™ LineCalc.

4.2.3. Design example

The method proposed above has been used to design a linear DDL, also known as chirped delay lines (CDL), aimed for UWB signal processing. The requirements include working in a bandwidth of $\Delta f = 4$ GHz, centered at $f_0 = 6$ GHz, and with a group-delay slope of $\psi = -0.5$ ns/GHz in microstrip coupled-lines. For a Rogers RO3010 substrate (with $\varepsilon_r = 10.2$ and thickness $h = 0.635$ mm), the design parameters have been calculated using (4.19), (4.20) and (4.21) to obtain $a_0 = 9.59$ mm, $C = -1898\,\text{m}^2$, and $L \geq 115$ mm.

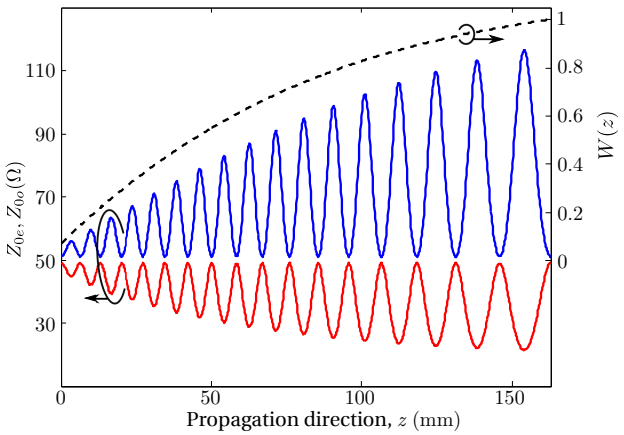

Figure 4.7: Characteristic impedances for the even mode, Z_{0e} (blue line), and the odd mode, Z_{0o} (red line), as a function of the propagation direction, z. The windowing function is included in black dashed line.

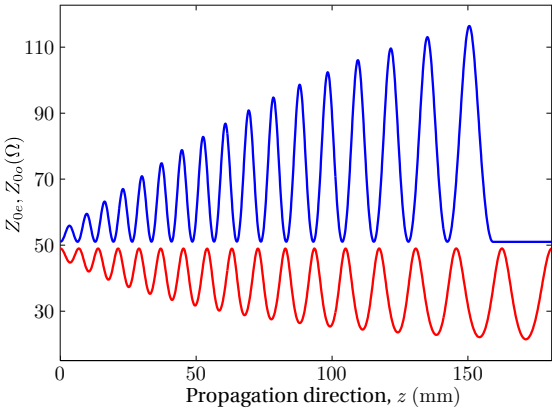

Figure 4.8: Characteristic impedances for the even mode, Z_{0e} (blue line), and the odd mode, Z_{0o} (red line), as a function of the propagation direction, z after compensating the difference between the propagation constant of the even and odd modes.

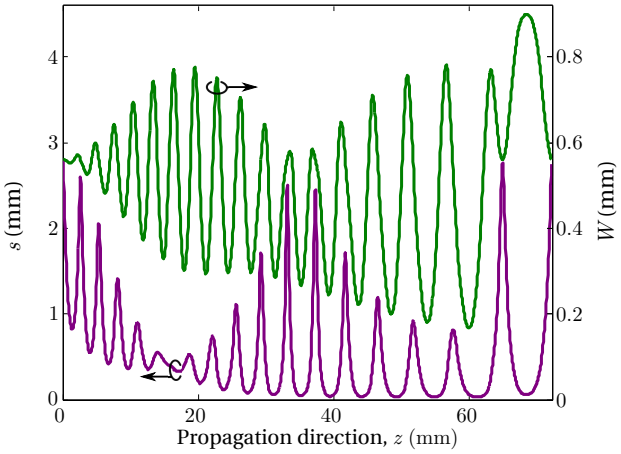

Figure 4.9: Separation (purple line) and width (green line) of the coupled-lines that correspond to the impedances given in Figure 4.8.

Then, a modified Kaiser window (depicted in Figure 4.7) is chosen with $A = 0.42$. The length of the device is increased to $N = 17$ periods to compensate for the bandwidth reduction due to the windowing function.

For the ports with characteristic impedance $Z_0 = 50\ \Omega$, $Z_{0e,\text{init}}$ has been fixed to $51\ \Omega$ and $Z_{0o,\text{init}} = 49.02\ \Omega$. The even- and odd-mode characteristic impedances are calculated using (4.17) and (4.18), which have been plotted in Figure 4.7 together

with the windowing function employed. Afterwards, the pair of characteristic impedances are redistributed applying Algorithm 2.4 (see Section 2.2.3.3). The compressed even-mode characteristic impedance and the expanded odd-mode characteristic impedance depicted in Figure 4.8 are obtained. The total device length reaches $L = 180.8$ mm.

Finally, the physical parameters corresponding to the depicted characteristic impedances are calculated by means of Agilent™ LineCalc, obtaining the separation and width of the coupled-lines shown in Figure 4.9.

4.2.3.1. Frequency domain characterization

The designed device has been simulated using Agilent™ ADS Momentum (including the effect of dielectric and conductor losses) and the fabricated prototype has been measured with an Agilent™ 8722 Vector Network Analyzer. The results are depicted in Figure 4.10 ($|S_{11}|$ and $|S_{31}|$), Figure 4.11 ($|S_{21}|$ and $|S_{41}|$) and Figure 4.12 (S_{31}-group delay). A photograph of the prototype is also shown in Figure 4.13 where the ports have been numbered indicating the input and output ports. Moreover, a more detailed view of the coupled-lines is shown by zooming an area of the device.

A good agreement can be observed between the measurements and the simulations for all the S-parameters. Although a small ripple level is present, the S_{31}-group delay of the device plotted in Figure 4.12 shows the desired slope of -0.5 ns/GHz from 4 to 8 GHz. Moreover, a flat response in $|S_{31}|$ has been achieved with insertion losses

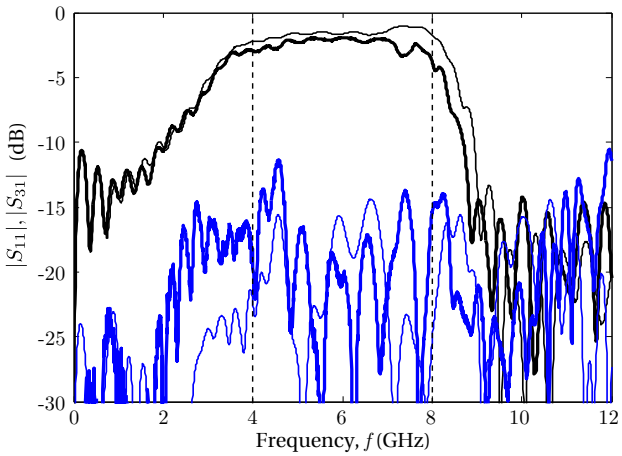

Figure 4.10: Simulations (thin line), and measurements (thick line) of $|S_{11}|$ (solid blue line) and $|S_{31}|$ (solid black line). The bandwidth of interest is delimited by two vertical dashed lines.

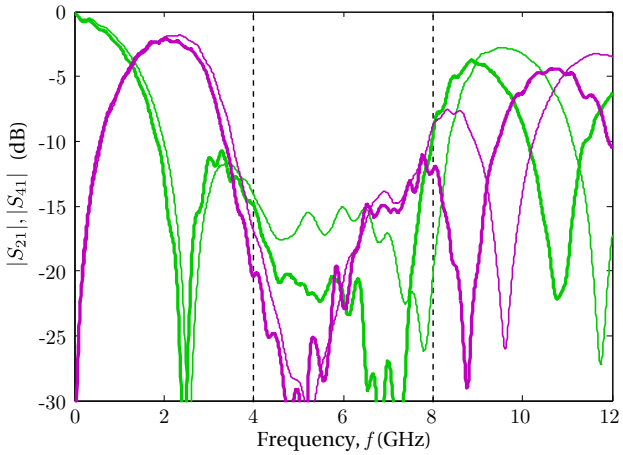

Figure 4.11: $|S_{21}|$ (green line) and $|S_{41}|$ (purple line), both in measurement (thick line) and simulation (thin line). The bandwidth of interest is delimited by two vertical dashed lines.

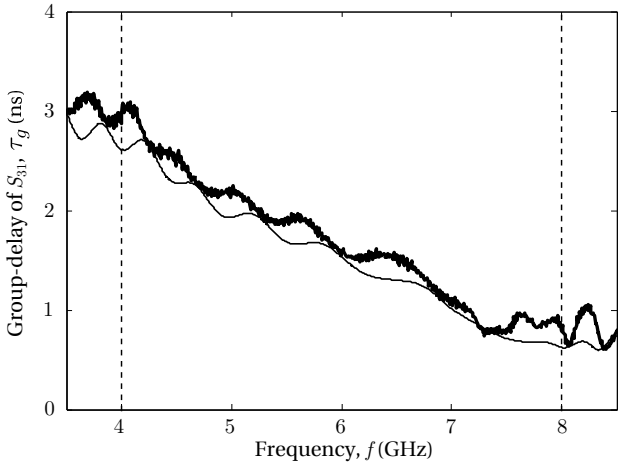

Figure 4.12: Group-delay of S_{31} in measurement (thick line) and simulation (thin line). The bandwidth of interest is delimited by two vertical dashed lines.

better than 4 dB for the operation bandwidth (better than 2.5 dB over most of the band, out of which 2 dB can be attributed to the losses) while good isolation is kept (see $|S_{41}|$ in Figure 4.11). In addition, very good matching for the input port is obtained for the entire frequency range (see $|S_{11}|$ in Figure 4.10).

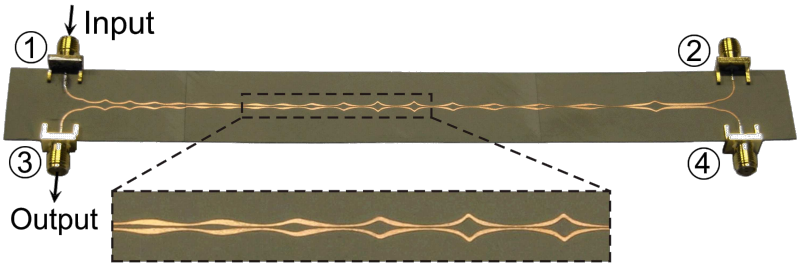

Figure 4.13: Photograph of the fabricated prototype where the ports are numbered, and the input and output ports marked. A zoomed view shows a detail of the coupled-lines.

4.2.3.2. Time domain characterization

In order to fully verify the features of the design, the temporal response of the device has been measured by means of a digital oscilloscope Agilent-86116C. The impulse response of a chirped delay line is basically a chirped cosine, i.e. a cosine signal with a linearly varying frequency. Its amplitude is ideally square-like shaped with rapid rise and fall times. The length of the impulse response is related with the group-delay slope and the bandwidth as $T_0 = \psi\,\Delta f$. In practice, the rise and fall times are not that sharp and longer impulse responses are obtained.

The impulse response of the device can be calculated applying the inverse Fourier

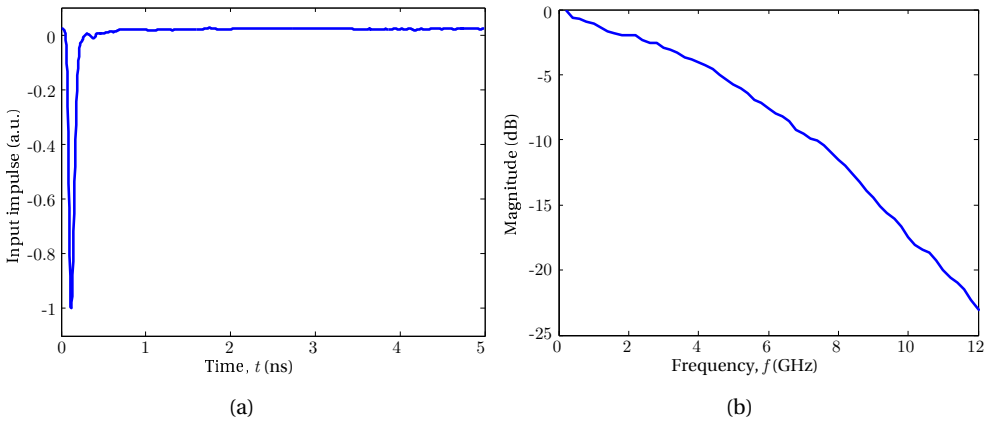

Figure 4.14: Characterization of the input impulse in (a) time and (b) frequency domains.

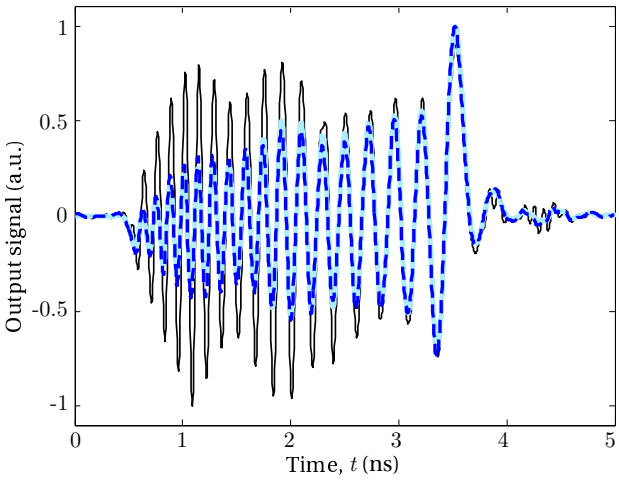

Figure 4.15: Measured (dashed dark blue line) and calculated (solid light blue line) time-domain response of the device to the impulse in Figure 4.14(a). The inverse Fourier transform of the measured frequency response of the device is also included (black thin line).

transform to the measured frequency response (plotted in Figure 4.10). To measure exactly the impulse response, an ideal impulse signal would be necessary, thus, in practice a wideband impulse generator is used. A Model 3600 impulse generator from Picosecond Pulse Labs has been used. It generates a negative impulse of approximately 70 ps of duration. This input signal has been measured and it is shown in Figure 4.14(a) after normalization. Its spectral content has been also depicted in Figure 4.14(b) calculating the Fourier transform of the measured temporal signal.

The time-domain response of the device for the measured input signal has been calculated by a convolution in the time domain using the inverse Fourier transform of the measured frequency response. The result is shown in Figure 4.15 together with the time-domain measurement of the output signal. A very good agreement can be observed between the measurement and the calculated output, while a quite important difference in amplitude is found compared to the inverse Fourier transform of the measured frequency response. This discrepancy is due to the non-uniform spectral content of the input signal, where a variation of approximately 8 dB is present between the lowest and highest frequencies inside the operation bandwidth of the device (4 GHz to 8 GHz). As a result, the amplitude of the highest frequencies of the response has been highly attenuated.

4.3. Applications

4.3.1. Compensation of chromatic dispersion in fiber optics communication systems

Chromatic dispersion is one of the most limiting factors for the improvement of the transmission rates of fiber optic systems already installed in metropolitan or regional networks. In particular, in systems based on standard single-mode fiber (SSMF) the maximum propagation distance is limited to approximately 80 km when a transmission rate of 10 Gb/s of a classical non-return-to-zero (NRZ) intensity modulation and direct demodulation (IM-DD) in the third window (1550 nm) is used.

For this reason, many strategies have been proposed to compensate chromatic dispersion. Those strategies can be grouped into optical and electrical methods. The optical techniques (fiber-based compensation systems or chirped fiber gratings) are usually expensive and not reconfigurable. The electrical techniques are usually cheaper than the optics and hence, they are more convenient for low-cost applications. For the compensation by electrical means, it is possible to use modulation techniques which are robust against the dispersion like duo-binary transmission [41], or alternatively, Electrical Dispersion Compensators (EDC) [42]. Recently, another method has been proposed, based on the coherent detection of the optical signal combined with the successive digital signal processing to eliminate the chromatic dispersion. Such a combination allows currently the propagation at very high transmission rates through thousands of kilometers of SSMF fiber [43]. However, this method requires the use of a local oscillator and an analogical/digital conversor (ADC) at the receptor capable of operating at very high sampling rates. Hence, this solution is appropriate for transport networks, but not for the metropolitan and regional networks.

A different approach has been tested recently taking advantage of DDLs operating

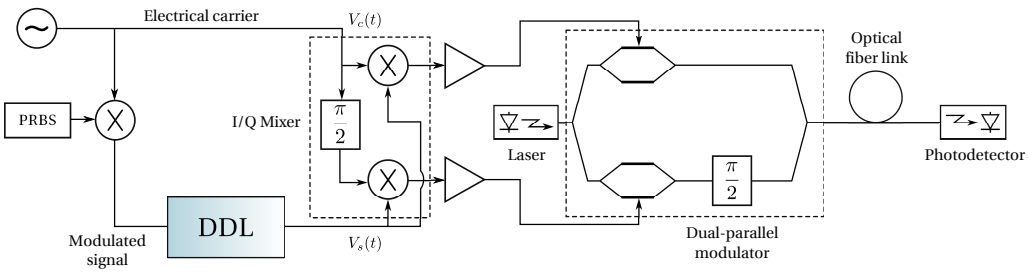

Figure 4.16: Schematic view of the communication system based on the predistorsion of the microwave signal.

at the microwave frequency regime. They are used to predistort the transmitted signal in order to precompensate for the dispersion that will be afterwards introduced in the optical fiber link. The proposed communication scheme is illustrated in Figure 4.16. The information signal, a pseudo-random binary sequence (PRBS) in this case, is modulated in an electrical carrier using a NRZ modulation. The modulated signal is then processed by a DDL to predistort it. Afterwards, the predistorted signal is converted into the optical domain by means of an In-Phase-Quadrature (I/Q) mixer followed by an electrooptical dual-parallel Mach-Zehnder modulator (DPMZM). This way, the amplitude and phase of the predistorted signal is transferred proportionally to the generated optical signal.

The proposed method has been demonstrated using different ways to obtain the required predistorsion. A simple uniform microstrip line that is long enough to introduce the required dispersion was used in [44], while a device composed by two reflection-type CDLs together with a $\pi/2$ 3-dB hybrid was also proposed [15]. Moreover, the possibility of adapting dynamically the dispersion has been proved [45]. The main advantages of these solutions are the low-cost and the simplicity of the design method. In the case of the uniform transmission lines, the design has been performed with the aid of commercial software, while the CDLs have been designed following the method described in [10, 11]. However, the designed devices are bulky and lossy. The simplest option based on the uniform microstrip line requires a length of several tens of centimeters to compensate the dispersion introduced by 100 km length SSMF. The solution based on CDLs, requires including a wideband circulator or other element to separate the input and output signals, increasing the complexity and losses of the design and of the complete system. Hence, further improvements can be done in the design of the dispersive element of the scheme to improve the performance and to obtain a better integration of the proposed solution.

In this section, several CDLs in coupled-lines will be presented, that can be used for the compensation of chromatic dispersion. The results presented here are the outcome of the work carried out in collaboration with Dr. Leonardo Ranzani from the University of Colorado at Boulder, Dr. Mario Martinelli and Dr. Pierpaolo Boffi from the Politecnico di Milano, and their respective research groups. The method described in Section 4.2 allows the design of compact devices that do not require any other additional element to provide the desired predistorsion. The longer the optical fiber link, the higher the chromatic dispersion introduced in the signal, and the harder to recover it. Hence, two different dispersion values will be considered, low dispersion and high dispersion, which result in different group-delay slope specifications.

4.3.1.1. Low dispersion

Following the design method described in Section 4.2, a device to compensate the dispersion of an optical link of 130 km of standard single-mode fiber (SSMF) with a data rate of 8.5 Gb/s will be designed. The required specifications for the CDL considering the properties of the optical link are: a bandwidth of $\Delta f = 14$ GHz at the central frequency $f_0 = 16.5$ GHz, and a group-delay slope of $\psi = -18$ ps/GHz.

Following the design method described in Section 4.2.2, the design parameters $a_0 = 3.4$ mm and $C = -55408.4\ \mathrm{m}^{-2}$ are obtained for an Arlon AD1000 substrate ($\varepsilon_r = 10$ and thickness $h = 0.508$ mm). The minimum length is $L \geq 14.1$ mm ($N = 5$ perturbation periods) but a higher length has to be used to compensate the bandwidth reduction produced by the windowing function. Hence, the selected length is $N = 8$, and the windowing function is a modified Kaiser window with a peak amplitude of $A = 0.455$. Since microstrip coupled lines will be used, the algorithm defined in Section 2.2.3.3 to compensate the difference between the even- and odd-mode propagation constants is applied to obtain the final even- and odd-mode characteristic impedances shown in Figure 4.17(a) with a final length of $L = 33.4$ mm. For this pair of even- and odd-mode characteristic impedances, the separation and the width of the microstrip coupled-lines are obtained using Agilent™ LineCalc and plotted in Figure 4.17(b).

The designed device has been simulated using Agilent™ ADS Momentum and the

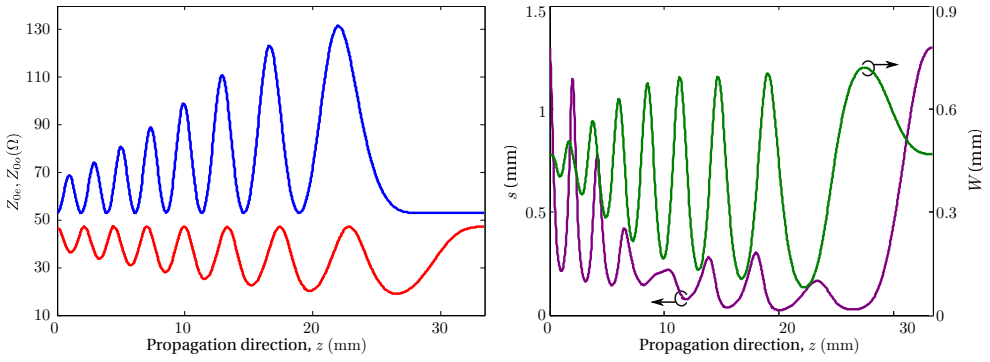

Figure 4.17: (a) Z_{0e} (blue line) and Z_{0o} (red line) of the designed device and (b) separation (purple line) and width (green line) of the coupled-lines that correspond to the given impedances.

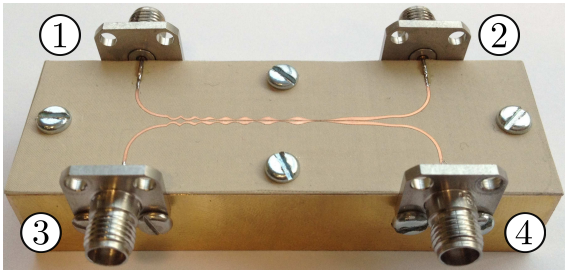

Figure 4.18: Photograph of the fabricated prototype.

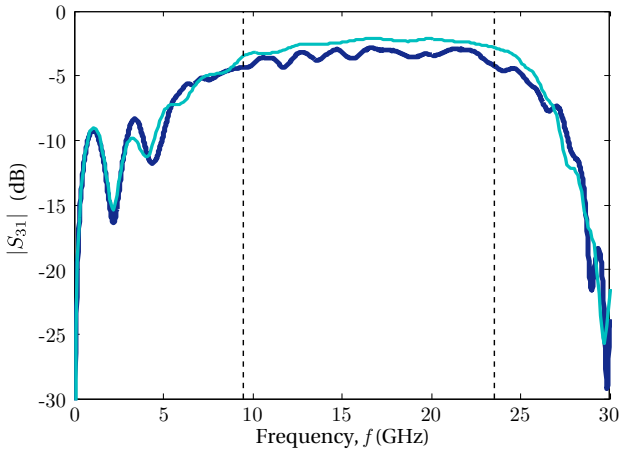

Figure 4.19: $|S_{31}|$ of the designed device: simulation (thin light blue line) and measurement (thick dark blue line). The design bandwidth is indicated by two vertical dashed lines.

fabricated prototype has been measured using an Agilent™ 8722 Vector Network Analyzer. A photograph of the prototype is shown in Figure 4.18. The results of the simulation and the measurements of the device are shown in Figure 4.19, Figure 4.20, and Figure 4.21, where a very good agreement has been achieved. In order to measure the response of the device, and also to use it into the experimental setup, ports (#2) and (#4) have been loaded with 50 Ω matched loads. The resulting device presents an operation bandwidth of $\Delta f = 14$ GHz centered at $f_0 = 16.5$ GHz as desired, with a ripple level of approximately 1.5 dB. The slope of the group-delay, calculated using linear fitting, is equal to $\psi = -18$ ps/GHz, both in simulation and measurement. This dispersion is enough to compensate for accumulated dispersion of approximately 130 km of SSMF at 8.5 Gb/s.

In order to fully verify the correct operation of the new fabricated DDL, it has been tested into the system shown in Figure 4.16. Specifically, in the experimental setup

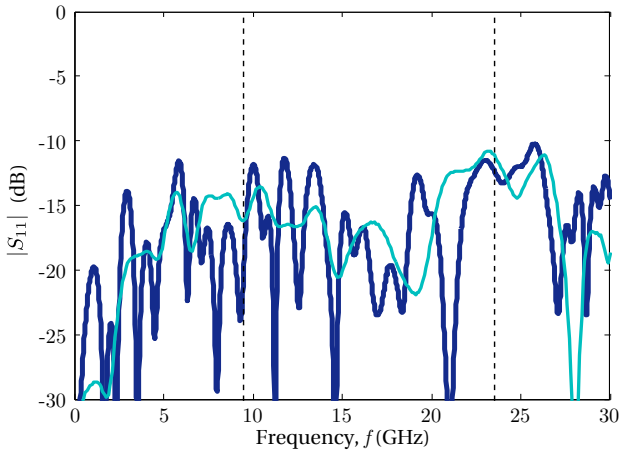

Figure 4.20: $|S_{11}|$ of the designed device: simulation (thin light blue line) and measurement (thick dark blue line). The design bandwidth is indicated by two vertical dashed lines.

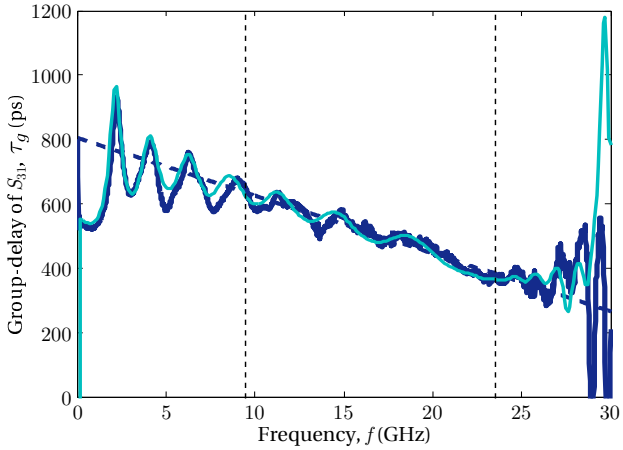

Figure 4.21: Group-delay of S_{31} of the designed device: simulation (thin light blue line), measurement (thick dark blue line) and linear fitting of measured data (dashed dark blue line). The design bandwidth is indicated by two vertical dashed lines.

mixers with very wide operation bandwidths have been used. The data signal has been modulated at 8.5 Gb/s with a carrier frequency of 16.5 GHz. The laser emits radiation at 1550 nm and the employed dual-parallel modulator has a bandwidth of 25 GHz. The signal is received using a photodiode after being propagated through the SSMF link.

Figure 4.22 shows the performance of the system in terms of the bit error rate (BER)

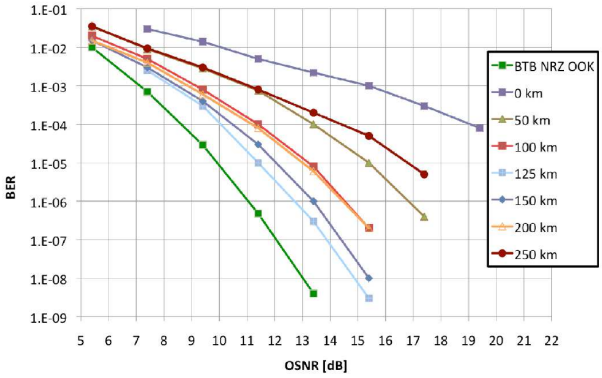

Figure 4.22: BER as a function of the OSNR at the receiver.

as a function of the signal-to-noise ratio of the optical signal (OSNR). The measurement has been performed in back-to-back conditions (without the DDL) and after the propagation through links of different lengths using the DDL in the transmission scheme. When the DDL is introduced into the system the performance is greatly penalized due to the introduced predistorsion. As the length of the propagation link is increased, the penalty is reduced until the optimal performance is obtained for 125 km of propagation. For the optimal operation distance of 125 km, the performance of the signal shows a penalty of approximately 1.5 dB compared to the back-to-back situation of the NRZ IM-DD signal. When the propagation distance goes over 125 km, part of the accumulated dispersion is not properly compensated and the obtained BER is again penalized. Between 100 and 200 km of propagation, the mean penalty compared to the back-to-back situation is less than 3 dB for BER values around 10^{-6}.

Finally, after performing the measurements of the frequency response of the DDL and the tests within the optical communication system, we can conclude that the designed DDL provides very satisfactory results and a very compact solution compared to previous alternatives.

4.3.1.2. High dispersion

In order to increase the length of the optical fiber link, in this section we aim to design a device for an optical link of approximately 300 km which requires a larger group-delay slope, approximately $\psi = -40$ ps/GHz. Moreover, to increase the data transmission rate to 10 Gb/s, a wider bandwidth of $\Delta f = 16$ GHz centered at $f_0 = 18$ GHz will be targeted.

Following the design method described in Section 4.2.2, the design parameters

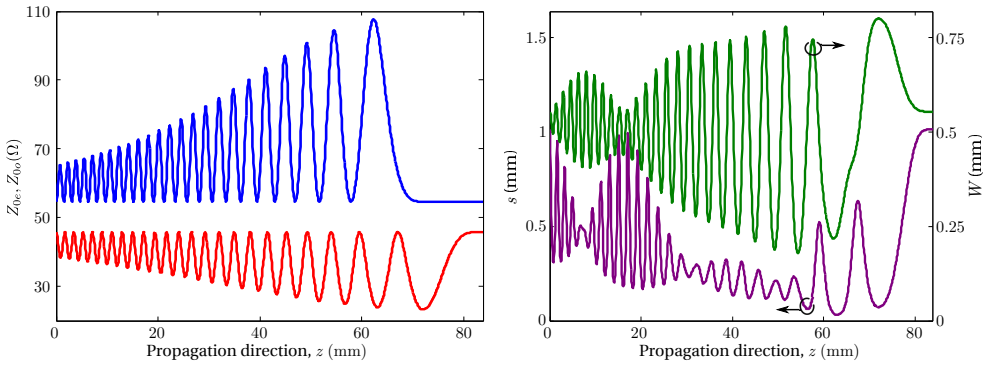

Figure 4.23: (a) Z_{0e} (blue line) and Z_{0o} (red line) of the designed device and (b) separation (purple line) and width (green line) of the coupled-lines that correspond to the given impedances.

$a_0 = 3.1$ mm and $C = -24933.8\ \mathrm{m}^{-2}$ are obtained for a Rogers RO3010 substrate ($\varepsilon_r = 10.2$ and thickness $h = 0.635$ mm). The minimum length is $L \geq 37$ mm ($N = 13$ perturbation periods) but a higher length has to be used to compensate the bandwidth reduction produced by the windowing function. Hence, the selected length is $N = 24$, and the windowing function is a modified Kaiser window with a peak amplitude of $A = 0.34$. Since microstrip coupled lines will be used, the algorithm defined in Section 2.2.3.3 to compensate the difference between the even- and odd-mode propagation constants is applied to obtain the final even- and odd-mode characteristic impedances shown in Figure 4.23(a) with a final length of $L = 83.8$ mm. For this pair of even- and odd-mode characteristic impedances, the separation and the width of the microstrip coupled-lines are obtained using Agilent™ LineCalc and plotted in Figure 4.23(b). The maximum and minimum separation and width required for this design have been summarized in Table 4.2. It should be pointed out that the minimum value for the separation between strips is a very challenging objective. Specifically, the most precise tool available to us is a laser milling machine with a laser spot diameter of 25 μm that can create such a narrow separation but with several drawbacks that will be analyzed later on.

TABLE 4.2
MINIMUM AND MAXIMUM DIMENSIONS OF THE DESIGNED DEVICE FOR HIGH DISPERSION SPECIFICATIONS.

$s_{\min}$ (mm)	$s_{\max}$ (mm)	$W_{\min}$ (mm)	$W_{\max}$ (mm)
0.031	1.01	0.178	0.8

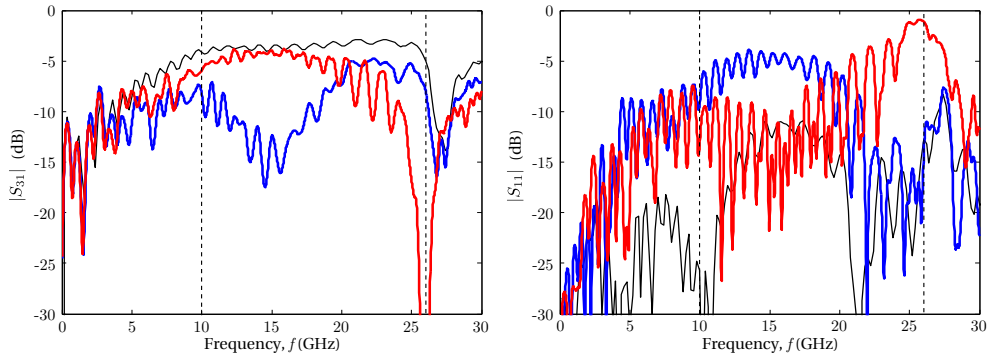

Figure 4.24: Measured (a) $|S_{31}|$ and (b) $|S_{11}|$ of the initial prototype, fabricated using a laser milling machine (blue thick line) and using photo etching (red thick line), together with the simulated results (black thin line). The design bandwidth is indicated with vertical dashed lines.

The device has been simulated using Agilent™ ADS Momentum and two prototypes were fabricated using two different fabrication methods: a laser milling machine and photo etching. The measurements of both devices are plotted in Figure 4.24 together with the simulation results. Unfortunately, the measurements do not agree with the simulation results and the reasons are related with two important aspects that we will consider in detail: the fabrication method and the substrate.

Fabrication method

The different fabrication methods employed to fabricate the prototypes of the high dispersion CDL designed above will be considered in detail here.

The laser milling machine is an automated milling machine that ablates selectively the conductor layer of a substrate. When the separation between conductors is very narrow, the conductor is usually overheated to make sure that all the conductor material will be properly removed. However, this implies that also part of the dielectric is burnt out producing grooves into the substrate, specially in the contour of the conductor strips and the narrowest areas between conductors. This is clearly seen in Figure 4.25, where images of the prototype obtained using an optical microscope are shown. The depth of the groove varies along the device, being deeper in the narrowest separation between the conductors since the laser spot can burn this point twice if the separation in lower than 50 μm. The depth of the deepest grooves was measured using the microscope and it was found that it can reach up to approximately 50 μm. However, it has to be pointed out that this measurement is an approximation. An accurate

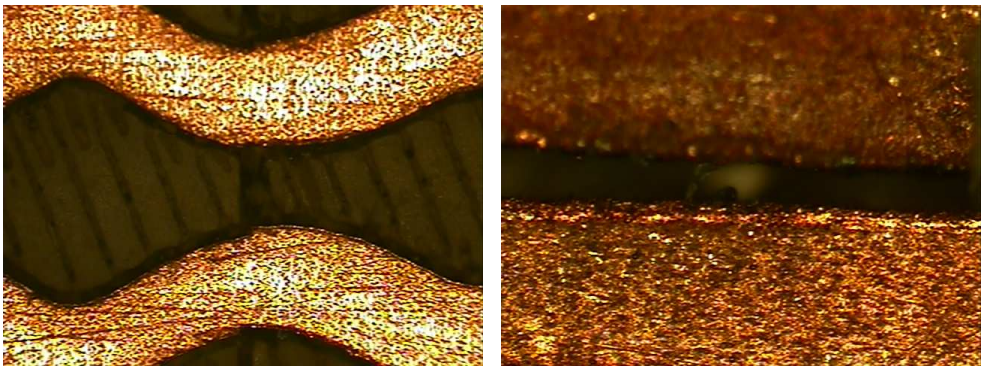

(a) (b)

Figure 4.25: Photographs of the device fabricated with the laser milling machine: (a) an area of wide separation using a 50x magnification and (b) the narrowest separation using a 200x magnification.

measurement is difficult to obtain because it requires a good illumination which is not possible in the narrow space between the two conductors (see Figure 4.25(b)).

The grooves produced by the fabrication modify the even- and odd-mode effective permittivities. The variation of the permittivity typically has an effect of frequency deviation. However, in this case, an accurate estimation of the effective permittivities is required to compensate the difference of velocities between the even and odd modes. If this estimation is not good enough the compensation is not properly done, and the design requirements are not satisfied anymore. In order to estimate how important is this deviation, CST Microwave Studio has been used. A 3D model of the ideal fabricated device has been simulated first to validate the previous simulation results, and afterwards, the grooves created during the fabrication have been included into the model. The results of both simulations have been compared with the measurements. In Figure 4.26, the critical effect of the grooves in the performance of the device is clearly noticeable.

On the other hand, the device fabricated using photo etching techniques follows better the simulation results, but the performance, specially at the edges of the band, is not good enough (see Figure 4.24). In this case, the dielectric of the substrate is not removed, but the metallization of the device is altered. Using the microscope, it can be seen that the conductors of the device present some holes (see Figure 4.27). Moreover, the dimensions of the separation and conductor widths are not very accurate. Both effects are due to the photoresist used in the fabrication. A thin photoresist of approximately 1.5 μm of thickness was used, overexposing the device and removing too much

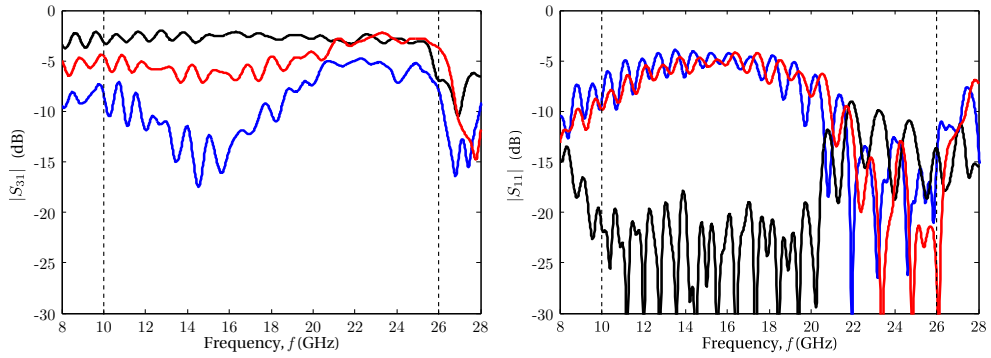

Figure 4.26: (a) $|S_{31}|$ and (b) $|S_{11}|$ of the CST Microwave Studio simulation results of the device with (red line) and without the grooves (black line), together with the measurements of the device fabricated using a laser milling machine (blue line). The design bandwidth is indicated using vertical dashed lines.

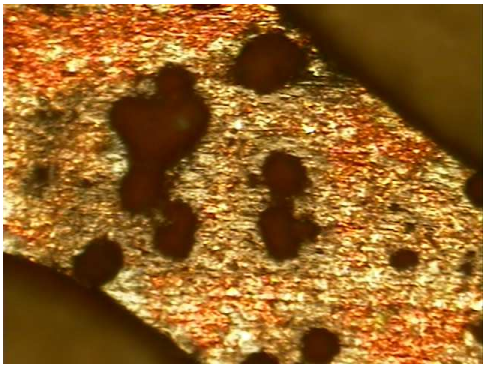

Figure 4.27: Photograph of the device fabricated by photo etching using a 200x magnification.

conductor material. A thicker photoresist can be used, but it requires to increase the minimum separation between the conductor strips to 63.5 μm.

As a conclusion, we can say that the fabrication by photo etching is a more reliable method for this type of device. However, the requirements have to be relaxed in order to fabricate the device properly. A higher minimum gap provides a lower coupling level which can be compensated in the optical system increasing the gain of the signal.

Substrate

We should point out that the selected substrate is electrically large for the target frequencies. As it was mentioned in Section 2.2.3.2, the quasi-TEM mode in a microstrip transmission line can be considered to be close to the TEM mode behavior if the separation between the ground plane and the conductor strip is very small in comparison with the wavelength. As a rule of thumb, the separation should be smaller than 1/20 of the wavelength in the medium. In our case, the substrate with 0.635 mm of thickness does not satisfy this condition and anomalous behavior can occur at high frequencies. In addition, other propagating modes, such as surface waves are more likely to propagate in an electrically large substrate and even radiation could occur.

The first designs obtained after relaxing the requirements and forcing the minimum gap to be higher than 63.5 μm had frequency responses that showed this anomalous behavior. The simulation results of a design with a minimum gap of 67 μm are shown in Figure 4.28(a). It is clear that above 18 GHz, the response of the device does not correspond to the expected behavior. The energy balance of the lossless simulation (see Figure 4.28(b)) makes clear that other modes or even radiation are interfering with the fundamental mode and taking away great part of the energy.

A thinner substrate would be more adequate for the given frequency specifications. As an example, the same even- and odd-mode characteristic impedances as for the previous design were implemented into a thinner substrate with the same dielectric permittivity, $\varepsilon_r = 10.2$, and thickness $h = 0.254$ mm. The simulation results, depicted

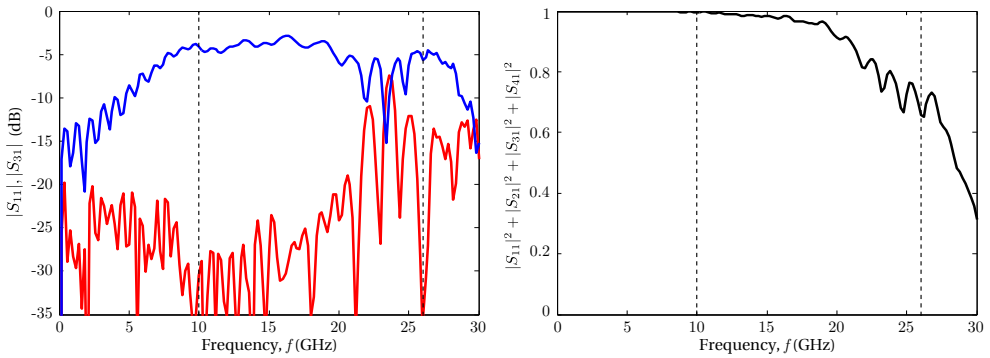

Figure 4.28: Simulated (a) $|S_{31}|$ (blue line) and $|S_{11}|$ (red line) and (b) energy balance, $|S_{11}|^2 + |S_{21}|^2 + |S_{31}|^2 + |S_{41}|^2$, of the device with a minimum gap of 67 μm implemented in a substrate of 0.635 mm thickness. The design bandwidth is indicated with vertical dashed lines.

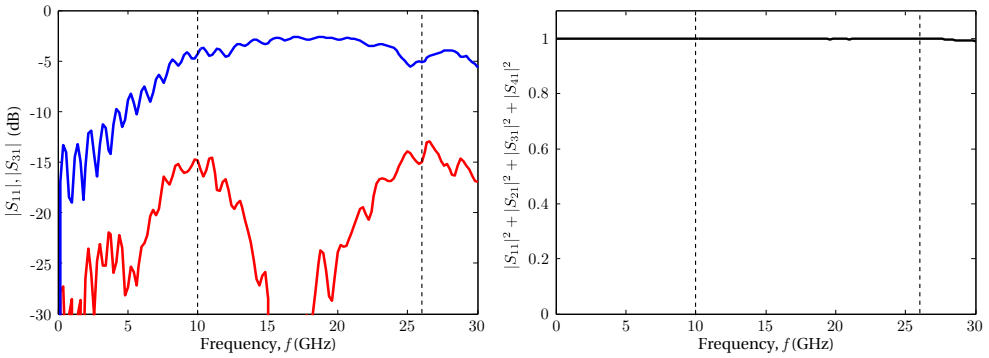

(a) (b)

Figure 4.29: Simulated (a) $|S_{31}|$ (blue line) and $|S_{11}|$ (red line) and (b) energy balance, $|S_{11}|^2 + |S_{21}|^2 + |S_{31}|^2 + |S_{41}|^2$, of the same design as in Figure 4.28 but in a substrate of 0.254 mm thickness. The design bandwidth is indicated with vertical dashed lines.

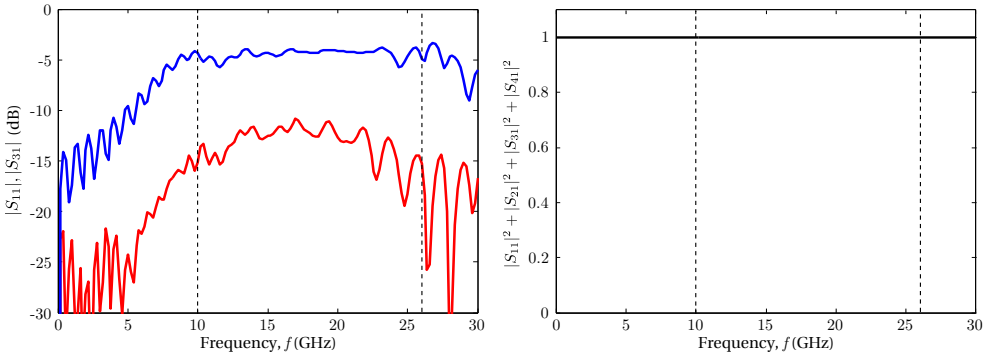

(a) (b)

Figure 4.30: Simulated (a) $|S_{31}|$ (blue line) and $|S_{11}|$ (red line) and (b) energy balance, $|S_{11}|^2 + |S_{21}|^2 + |S_{31}|^2 + |S_{41}|^2$, of the same design as in Figure 4.28 but in symmetrical edge-coupled stripline technology using a substrate of 1.27 mm thickness. The design bandwidth is indicated with vertical dashed lines.

in Figure 4.29(a), provide the expected response with a proper energy balance for a lossless substrate as shown in Figure 4.29(b).

Another alternative would be avoiding radiation and the inhomogeneous microstrip medium, and using stripline technology instead of microstrip. This alternative has been also tested with a substrate of relative permittivity $\varepsilon_r = 10.2$ and thickness $h = 1.27$ mm. The lossless simulation results depicted in Figure 4.30 are again satisfactory.

TABLE 4.3
MINIMUM AND MAXIMUM DIMENSIONS OF THE SAME IMPEDANCE PAIR FOR DIFFERENT SUBSTRATE THICKNESS (h) AND TECHNOLOGIES WITH THE SAME RELATIVE PERMITTIVITY ($\varepsilon_r = 10.2$).

Technology	h (mm)	$s_{\min}$ (mm)	$s_{\max}$ (mm)	$W_{\min}$ (mm)	$W_{\max}$ (mm)
Microstrip	0.635	0.067	1.13	0.286	0.787
Microstrip	0.254	0.039	0.479	0.097	0.302
Stripline	1.27	0.077	0.814	0.061	0.151

However, both alternatives imply more stringent fabrication requirements that we can not achieve using the photo etching fabrication method, see Table 4.3. Specifically, the thinner substrate requires to implement a minimum strip width of 0.097 mm and a minimum separation between strips of 0.039 mm. The design in stripline coupled-lines required a minimum strip width of 0.061 mm and a minimum separation between strips of 0.077 mm. In addition, a reliable fabrication for stripline technology was not available to us, so this alternative was not considered for fabrication. For these reasons, we had to cope with the problems that imply the given substrate. And we had to find the optimal election of design parameters in order to have a good performance (with respect to bandwidth, group-delay slope, coupling and ripple level) and satisfying the restrictions of our fabrication capabilities.

Finally, using a thinner substrate can be a good alternative to avoid spurious effects. For this reason, and also because the design requirements were already relaxed in order to fabricate the device using the photo etching method, we have designed a device in a thinner substrate. It can not be fabricated using photo etching, but it can be fabricated using the laser milling machine easier than the first prototypes.

Final results

Taking into consideration the analysis presented above, two final devices have been obtained, for two different substrates, and fabricated using two different methods. The design specifications are $\psi = -40$ ps/GHz, $\Delta f = 16$ GHz and $f_0 = 18$ GHz.

The first device has been implemented using a Rogers RO3010 substrate ($\varepsilon_r = 10.2$ and thickness $h = 0.635$ mm) with a copper metallization with gold coating. Applying the method presented in Section 4.2.2, the main design parameters are obtained: $a_0 = 3.1$ mm, $C = -24933.8\ \mathrm{m}^{-2}$, $N = 24$, $A = 0.28$ and a modified gaussian windowing function. After using the algorithm to compensate the difference between the even- and odd-mode propagation constants the design is $L = 83$ mm length, and the impedances and dimensions of the coupled-lines shown in Figure 4.31 are

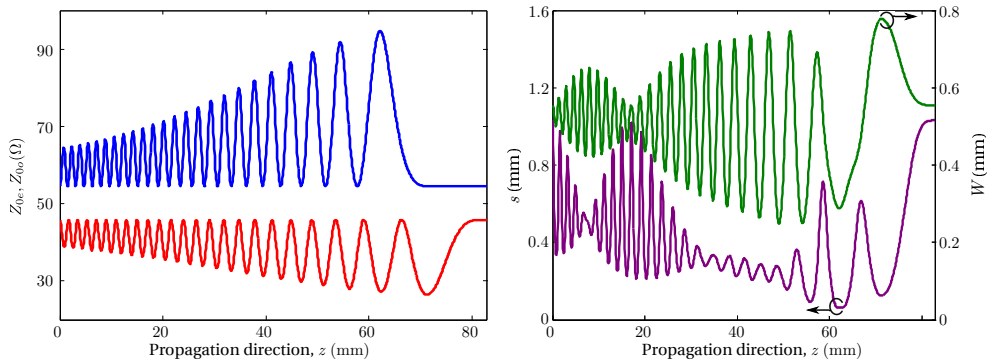

Figure 4.31: (a) Z_{0e} (blue line) and Z_{0o} (red line) of the device in RO3010 substrate and (b) separation (purple line) and width (green line) of the coupled-lines that correspond to the given impedances.

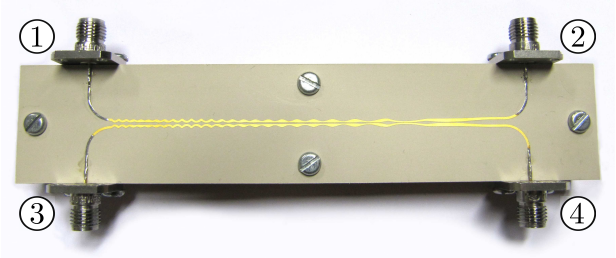

Figure 4.32: Photograph of the final device fabricated by photo etching using RO3010 substrate.

achieved. The designed device has been simulated using Agilent™ ADS Momentum. The prototype has been fabricated using the photo etching method and is shown in Figure 4.32. It has been measured using an Agilent™ 8722 Vector Network Analyzer. The results of the simulations and measurements are shown in Figure 4.33, Figure 4.34, and Figure 4.35. A good matching is obtained for the input port (#1) of the device in all the design frequency band. The measured coupling of the device $|S_{31}|$ has low ripple level, although it is not very uniform, specially at high frequencies. Regarding the group-delay, the desired linear frequency response is obtained with a difference of a constant delay term that appears in the measurements due to the transitions (2.4 mm to 3.5 mm) used to measure the response. Both the simulation and measurement data have been linearly fitted in the design frequency band, obtaining a slope of $\psi = -40.114$ ps/GHz for the simulation and $\psi = -45.132$ ps/GHz for the measurements. This difference can be the result of the higher ripple of the group-delay at high

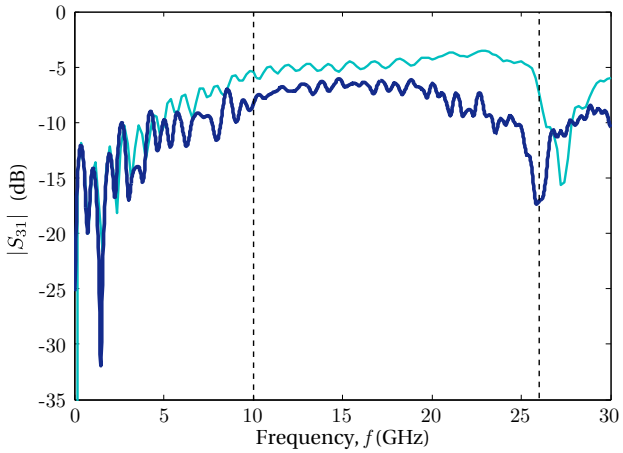

Figure 4.33: $|S_{31}|$ of the final device fabricated by photo etching using RO3010 substrate: simulation (thin light blue line) and measurement (thick dark blue line). The design bandwidth is indicated by vertical dashed lines.

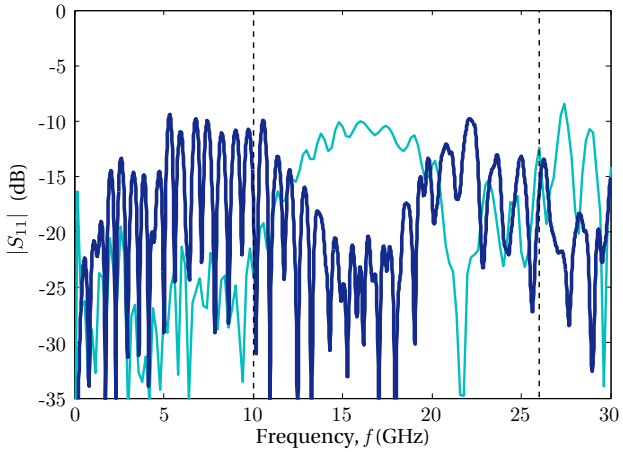

Figure 4.34: $|S_{11}|$ of the final device fabricated by photo etching using RO3010 substrate: simulation (thin light blue line) and measurement (thick dark blue line). The design bandwidth is indicated by vertical dashed lines.

frequencies in the measured data due to a considerably attenuated signal.

A second device has been designed for a thinner substrate, and has been fabricated using a laser milling machine since it requires a smaller separation between the coupled-lines, which is not feasible by photo etching. The chosen substrate is a high permittivity substrate, specifically AD1000 with $\varepsilon_r = 9.3$ and thickness $h = 0.254$ mm.

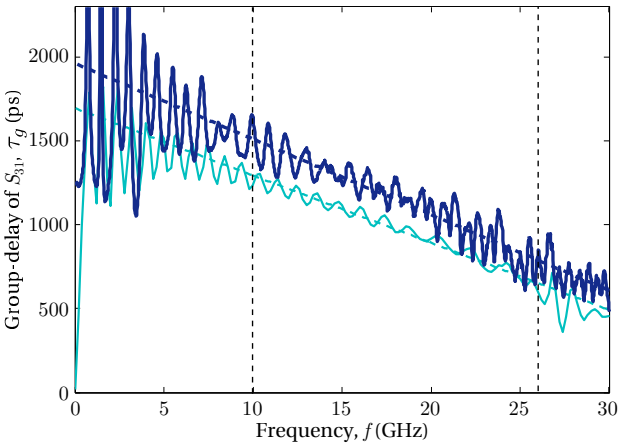

Figure 4.35: Group-delay of S_{31} of the final device fabricated by photo etching using RO3010 substrate: simulation (thin light blue line) and measurement (thick dark blue line). The linear fitting of both curves is shown in dashed line. The design bandwidth is indicated by vertical dashed lines.

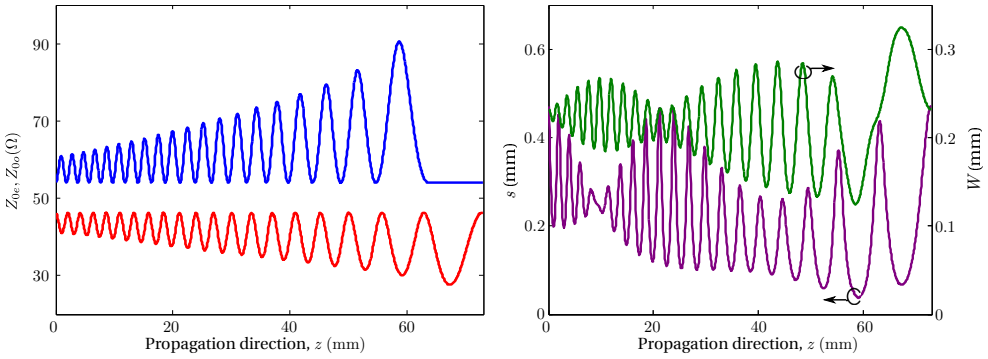

Figure 4.36: (a) Z_{0e} (blue line) and Z_{0o} (red line) of the device in AD1000 substrate and (b) separation (purple line) and width (green line) of the coupled-lines that correspond to the given impedances.

Applying the method presented in Section 4.2.2, the main design parameters are obtained: $a_0 = 3.4$ mm, $C = -20922.8\,\mathrm{m}^{-2}$, $N = 20$, $A = 0.38$ and a modified gaussian windowing function. After using the algorithm to compensate the difference between the even- and odd-mode propagation constants the design is $L = 73$ mm length. The even- and odd-mode characteristic impedances and the corresponding dimensions

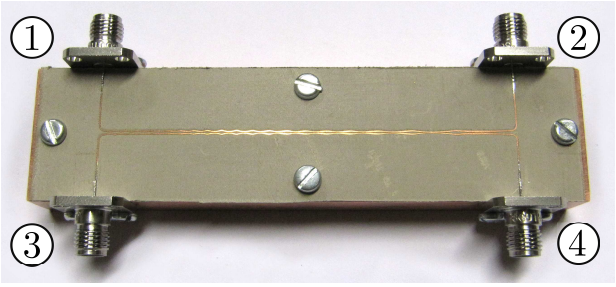

Figure 4.37: Photograph of the final device fabricated using the laser milling machine in AD1000 substrate.

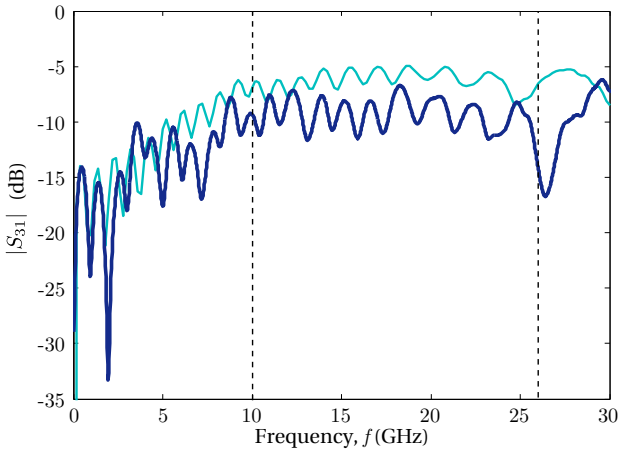

Figure 4.38: $|S_{31}|$ of the final device fabricated using the laser milling machine in AD1000 substrate: simulation (thin light blue line) and measurement (thick dark blue line). The design bandwidth is indicated by vertical dashed lines.

of the coupled-lines are shown in Figure 4.36. A photograph of the fabricated prototype is shown in Figure 4.37. The designed device has been simulated using Agilent™ ADS Momentum and the fabricated prototype has been measured using an Agilent™ 8722 Vector Network Analyzer. The results of the simulations and measurements are shown in Figure 4.38, Figure 4.39, and Figure 4.40. Due to the shorter length of the device, a higher ripple is present already in the simulation results, as it is clearly seen in the S_{31} response, both in the magnitude and the group-delay. This ripple has been increased in the measured results due to the fabrication method employed. However, in this case the uniformity of the coupling level, $|S_{31}|$, is better than that obtained in

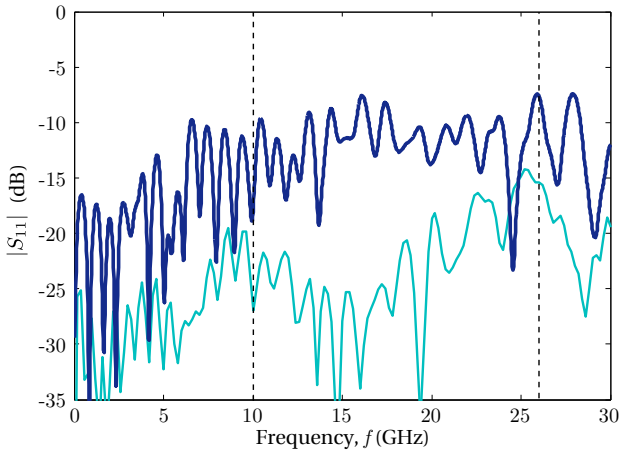

Figure 4.39: $|S_{11}|$ of the final device fabricated using the laser milling machine in AD1000 substrate: simulation (thin light blue line) and measurement (thick dark blue line). The design bandwidth is indicated by vertical dashed lines.

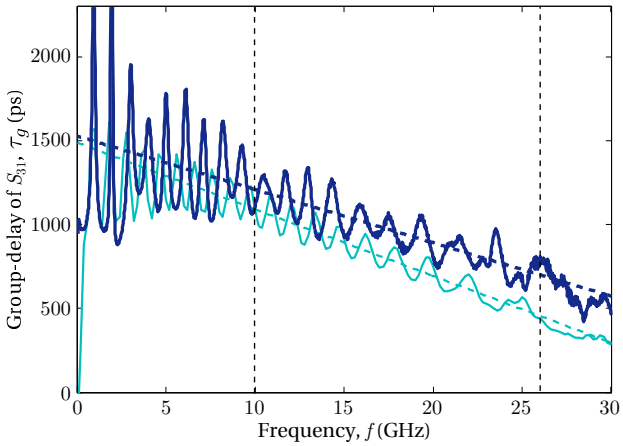

Figure 4.40: Group-delay of S_{31} of the final device fabricated using the laser milling machine in AD1000 substrate: simulation (thin light blue line) and measurement (thick dark blue line). The design bandwidth is indicated by vertical dashed lines.

the thicker substrate. The effect of the grooves produced by the laser spot in the fabricated prototype is also evident in the return loss parameter, $|S_{11}|$, which is clearly worse than expected in the simulation. Finally, the group-delay response has been linearly fitted in the design bandwidth to obtain the approximated slope, which is

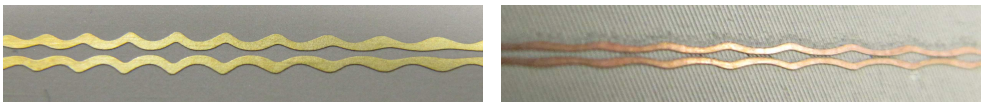

(a) (b)

Figure 4.41: Detailed photograph of both final devices, fabricated using (a) photo etching and (b) the laser milling machine.

$\psi = -39.785$ ps/GHz for the simulation, and $\psi = -31.807$ ps/GHz for the measurement. The slope of the measurement is clearly lower which can be produced by the higher ripple present in the measurements and the reduction of the effective permittivity produced by the grooves.

Finally, the two photographs shown in Figure 4.41 confirm the previously mentioned considerations about the fabrication method. A clear and well defined finish is obtained using photo etching, but unfortunately the attainable dimensions limit the use of a thin substrate to avoid spurious effects at high frequencies. The laser milling machine allows to fabricate much stringent dimensions, but a better control of the fabrication process, specially of the grooves created by the laser spot on the substrate, would be necessary to obtain fully satisfactory results.

4.4. Conclusions

The crescent interest on analog signal processing systems has boosted the development of dispersive delay lines, the basic building block of this type of systems. A review of the different technologies and design techniques has been done to begin this chapter.

A new method to design chirped delay lines in coupled-line technology has been proposed. The design technique benefits from all the advantages of previously reported microstrip chirped delay lines. Additionally, the use of coupled-lines provides an effective transmission-type operation, avoiding the circulator required in the previous two-port counterparts. The proposed technique has been validated with the design of a device intended for UWB signal processing. A prototype has been fabricated and fully verified with measurements both in frequency and time domains.

Finally, several devices have been designed for the compensation of the chromatic dispersion in fiber optics communication systems. A device to compensate the dispersion of a relatively short optical link (130 km with a bit rate of 8.5 Gb/s) has been designed. Its applicability has been proved with measurements of the bit-error-rate

(BER) of the optical communication system, obtaining very good results. The design of devices with higher dispersion for longer optical links (300 km with a data rate of 10 Gb/s) has encountered practical limitations due to the fabrication techniques. A compromise between the fabricability and the frequency requirements has been achieved to obtain two devices that are being tested into the optical communication system.

References

[1] M. Lewis, "SAW and optical signal processing," in *IEEE Proc. Ultrason. Symp.*, Rotterdam, The Netherlands, September 2005, pp. 800–809.

[2] C. Caloz, S. Gupta, Q. Zhang, and B. Nikfal, "Analog signal processing: A possible alternative or complement to dominantly digital radio schemes," *Microwave Magazine*, vol. 14, no. 6, pp. 87–103, Sept.-Oct. 2013.

[3] J. R. Klauder, A. C. Price, S. Darlington, and W. J. Albersheim, "The theory and design of chirp radars," *Bell Syst. Tech. J.*, vol. 39, no. 4, pp. 745–808, July 1960.

[4] R. H. Tancrell, M. B. Schulz, H. H. Barret, L. D. Jr., and M. G. Hollan, "Dispersive delay lines using ultrasonic surface waves," *Proc. IEEE*, vol. 57, no. 6, pp. 1211–1213, June 1969.

[5] V. S. Dolat and R. C. Williamson, "A continuously variable delay-line system," in *Proc. IEEE Ultrason. Symp.*, Annapolis, MD, Sep. 1976, pp. 419–423.

[6] M. A. Jack, P. M. Grant, and J. H. Collins, "The theory, design, and applications of surface acoustic wave Fourier-transform processors," *Proc. IEEE*, vol. 68, no. 4, pp. 450–468, April 1980.

[7] W. Ishak, "Magnetostatic wave technology: A review," *Proceedings of IEEE*, vol. 76, no. 2, pp. 171–178, Sept. 1988.

[8] R. S. Withers, A. C. Anderson, P. V. Wright, and S. A. Reible, "Superconductive tapped delay lines for microwave analog signal processing," *IEEE Transactions on Magnetics*, vol. 19, no. 3, pp. 480–484, May 1983.

[9] M. J. Lancaster, *Passive microwave device applications of high-temperature superconductors*, 1st ed. Cambridge, U.K: Cambridge Univ. Press, 2006.

[10] M. A. G. Laso, T. Lopetegi, M. J. Erro, D. Benito, M. J. Garde, M. A. Muriel, M. Sorolla, and M. Guglielmi, "Chirped delay lines in microstrip technology," *IEEE Microwave and Wireless Components Letters*, vol. 11, no. 12, pp. 486–488, Dec. 2001.

[11] ——, "Real-time spectrum analysis in microstrip technology," *IEEE Transactions on Microwave Theory & Techniques*, vol. 51, no. 3, pp. 705–717, March 2003.

[12] J. D. Schwartz, J. Azaña, and D. V. Plant, "Experimental demonstration of real-time spectrum analysis using dispersive microstrip," *IEEE Microwave and Wireless Components Letters*, vol. 16, no. 4, pp. 215–217, April 2006.

[13] ——, "A fully electronic system for the time magnification of ultra-wideband signals," *IEEE Transactions on Microwave Theory & Techniques*, vol. 55, no. 2, pp. 327–334, Feb. 2007.

[14] J. D. Schwartz, I. Arnedo, M. A. G. Laso, T. Lopetegi, J. Azaña, and D. V. Plant, "An electronic UWB continuously tunable time-delay system with nanosecond delays," *IEEE Microwave and Wireless Components Letters*, vol. 18, no. 2, pp. 103–105, Feb. 2008.

[15] L. Ranzani, P. Boffi, R. Siano, S. Rondineau, Z. Popovic, and M. Martinelli, "Microwave-domain analog predistortion based on chirped delay lines for dispersion compensation fo 10-Gb/s optical communication signals," *Journal Lightwave Technol.*, vol. 26, no. 15, pp. 2641–2646, August 2008.

[16] S. Ding, B.-Z. Wang, G. Ge, and D. Zhao, "Sub-wavelength array with embedded chirped delay lines based on time reversal technique," *IEEE Transactions on Microwave Theory & Techniques*, vol. 61, no. 5, pp. 2868–2873, May 2013.

[17] J. D. Schwartz, R. Abhari, D. V. Plant, and J. Azaña, "Design and analysis of 1-D uniform and chirped electromagnetic bandgap structures in substrate-integrated waveguides," *IEEE Transactions on Microwave Theory & Techniques*, vol. 8, no. 7, pp. 1858–1866, July 2010.

[18] A. Lujambio, I. Arnedo, M. Chudzik, I. Arregui, T. Lopetegi, and M. A. G. Laso, "Dispersive delay line with effective transmission-type operation in coupled-line technology," *IEEE Microwave and Wireless Components Letters*, vol. 21, no. 9, pp. 459–461, September 2011.

[19] M. Coulombe and C. Caloz, "Reflection-type artificial dielectric substrate microstrip dispersive delay line (DDL) for analog signal processing," *IEEE Transactions on Microwave Theory & Techniques*, vol. 57, no. 7, pp. 1714–1723, July 2009.

[20] S. Gupta and C. Caloz, "Analog signal processing in transmission line metamaterial structures," *Radioengineering*, vol. 18, no. 62, pp. 155–167, June 2009.

[21] C. Caloz, "Metamaterial dispersion engineering concepts and applications," *Proc. IEEE*, vol. 99, no. 10, pp. 1711–1719, October 2011.

[22] S. Abielmona, S. Gupta, and C. Caloz, "Compressive receiver using a CRLH-based dispersive delay line for analog signal processing," *IEEE Transactions on Microwave Theory & Techniques*, vol. 57, no. 11, pp. 2617–2626, Nov. 2009.

[23] S. Gupta, A. Parsa, E. Perret, R. V. Snyder, R. J. Wenzel, and C. Caloz, "Group-delay engineered noncommensurate transmission line all-pass network for analog signal processing," *IEEE Transactions on Microwave Theory & Techniques*, vol. 58, no. 9, pp. 2392–2407, September 2010.

[24] B. Nikfal, S. Gupta, and C. Caloz, "Increased group-delay slope loop system for enhanced-resolution analog signal processing," *IEEE Microwave and Wireless Components Letters*, vol. 59, no. 6, pp. 1622–1628, June 2011.

[25] Y. Horii, S. Gupta, B. Nikfal, and C. Caloz, "Multilayer broadside-coupled dispersive delay structures for analog signal processing," *IEEE Microwave and Wireless Components Letters*, vol. 22, no. 1, pp. 1–3, January 2012.

[26] S. Gupta, L.-P. Carignan, and C. Caloz, "Group delay swing enhancement in transmission-line all-pass networks using coupling and dispersion boosting ferrimagnetic substrate," *Microwave and Optical Technology Letters*, vol. 54, no. 3, pp. 589–593, March 2012.

[27] S. Gupta, D. L. Sounas, H. V. Nguyen, Q. Zhang, and C. Caloz, "CRLH-CRLH C-section dispersive delay structures with enhanced group-delay swing for higher analog signal processing resolution," *IEEE Transactions on Microwave Theory & Techniques*, vol. 60, no. 12, pp. 3939–3949, December 2012.

[28] S. Gupta, D. L. Sounas, Q. Zhang, and C. Caloz, "All-pass dispersion synthesis using microwave C-sections," *Int. J. Circ. Theor. Appl.*, 2013.

[29] Q. Zhang, S. Gupta, and C. Caloz, "Synthesis of broadband dispersive delay structures by commensurate C- and D-sections," *Int. J. RF and Microwave Comp. Aid. Eng.*, 2013.

[30] ——, "Synthesis of narrowband reflection-type phasers with arbitrary prescribed group delay," *IEEE Transactions on Microwave Theory & Techniques*, vol. 60, no. 8, pp. 2394–2402, August 2012.

[31] Q. Zhang, D. L. Sounas, and C. Caloz, "Synthesis of cross-coupled reduced-order dispersive delay structures (DDSs) with arbitrary group delay and controlled magnitude," *IEEE Transactions on Microwave Theory & Techniques*, vol. 61, no. 3, pp. 1043–1052, March 2013.

[32] R. Mongia, I. Bahl, and P. Bhartia, *RF and microwave couple-line circuits*, 1st ed. London: Artech House, 1999.

[33] Y. Qian, V. Radisic, and T. Itoh, "Simulation and experiment of photonic band-gap structures for microstrip circuits," in *Proceedings Asia-Pacific Microwave Conference (APMC 1997)*, Hong Kong, 1997, pp. 585–588.

[34] I. Rumsey, M. Picket-May, , and P. K. Kelly, "Photonic bandgap structure used as filter in microstrip circuits," *IEEE Microwave and Guided Wave Letters*, vol. 10, no. 6, pp. 336–338, October 1998.

[35] F. Falcone, T. Lopetegi, and M. Sorolla, "1-D and 2D photonic band gap microstrip structures," *Microwave and Optical Technology Letters*, vol. 22, no. 6, pp. 411–412, September 1999.

[36] D. Nesic and A. Nesic, "Bandstop microstrip PBG filter with sinusoidal variation of the characteristic impedance and without etching in the ground plane," *Microwave and Optical Technology Letters*, vol. 29, no. 6, pp. 418–420, June 2001.

[37] T. Lopetegi, M. A. G. Laso, M. J. Erro, M. Sorolla, and M. Thumm, "Analysis and design of periodic structures for microstrip lines by using the coupled mode theory," *IEEE Microwave and Wireless Components Letters*, vol. 12, no. 11, pp. 441–443, November 2002.

[38] I. Arnedo, M. Chudzik, J. D. Schwartz, I. Arregui, A. Lujambio, F. Teberio, D. Benito, M. A. G. Laso, D. V. Plant, J. Azaña, and T. Lopetegi, "Analytical solution for the design of planar electromagnetic bandgap structures with spurious-free frequency response," *Microwave and Optical Technology Letters*, vol. 54, no. 4, pp. 956–960, April 2012.

[39] M. Chudzik, I. Arnedo, A. Lujambio, I. Arregui, F. Teberio, M. Laso, and T. Lopetegi, "Microstrip coupled-line directional coupler with enhanced coupling based on EBG concept," *Electronics Letters*, vol. 47, no. 23, pp. 1284–1286, November 2011.

[40] ——, "Microstrip coupled-line directional coupler with enhanced coupling based on EBG concept: Errata," *Electronics Letters*, vol. 48, no. 7, p. 411, March 2012.

[41] D. Penninncks, M. Chbat, L. Pierre, and J.-P. Thiery, "The phase-shape binary transmission (PSBT): A new technique to transmit far beyond the chromatic dispersion limit," *IEEE Photon. Technol. Lett.*, vol. 9, no. 2, pp. 259–261, February 1997.

[42] H. Bulow, "Electronic equalization of transmission impairments," in *OFC 2000*, Anheim, CA, 2002, pp. 24–25.

[43] J. Renaudier, G. Charlet, M. Salsi, O. B. Pardo, H. Mardoyan, P. Tran, and S. Bigo, "Linear fiber impairments mitigation of 40-Gbit/s polarization multiplexed QPSK by digital processing in a coherent receiver," *Journal Lightwave Technol.*, vol. 26, no. 1, pp. 36–42, January 2008.

[44] L. Ranzani, P. Boffi, R. Siano, and M. Martinelli, "Transmitter-side microwave domain dispersion compensation using direct detection for 10-Gb/s signals," *IEEE Photon. Technol. Lett.*, vol. 19, no. 22, pp. 1849–1851, November 2007.

[45] L. Ranzani, J. G. Serrano, P. Boffi, and M. Martinelli, "Microwave tunable dispersion compensator for optical fiber systems," *Applied Optics*, vol. 50, no. 12, pp. 1786–1791, April 2011.

upna

Universidad Pública de Navarra
Nafarroako Unibertsitate Publikoa

Chapter 5

Conclusions and future work

In this thesis the main goal of providing flexibility to the microwave filter design techniques has been achieved. A new approach has been proposed to solve the two problems in which the filter design is typically divided: the approximation problem and the synthesis problem.

A new approximation procedure has been proposed using the well-established and readily available techniques for the design of digital filters, in order to obtain a frequency response that satisfies the given specifications. The proposed methodology relies on the proper translation of the analog target specifications to the digital domain that allows the microwave designer to take advantage of the sophisticated and continuously developing digital filter design techniques without requiring a deep understanding of the complex mathematics involved. The resulting digital filter is then translated back into the analog domain obtaining the desired response.

Three methods have been presented to transform the specifications and the designed filters from the analog domain to the digital domain and vice versa: the invariant impulse response method, the bilinear transformation and the matched-z transformation. The bilinear transformation has been selected to design two multiband filters along the document.

The main characteristics of digital filters and their design techniques have been summarized to give a brief introduction to the topic. One of the many design techniques available in the literature has been chosen to satisfy the specifications of the two multiband filters presented here.

A different approach for the synthesis problem is also presented. The coupling coefficient is an intermediate parameter of this approach that can be related to the

physical parameters of a device using the coupled-mode theory. Analytical expressions for this relation are given for rectangular waveguide and various planar transmission lines. To complete the synthesis, a direct synthesis method based on inverse scattering has been presented. It permits to calculate the coupling coefficient needed for the filter by means of a closed-form expression, that requires just to solve a linear system of equations. The method is exact for all the frequency range of interest and valid when the target frequency response can be expressed as a rational function. The resulting microwave filters feature a continuously varying smooth profile, avoiding the presence of sharp discontinuities and their detrimental effects. The flexibility of the synthesis method is specially exploited when combined with the approximation procedure based on digital filter design techniques. The validity of this combination has been proved by the design, fabrication and measurement of a multiband filter. In order to improve the integration of the designed filter, a compaction process using Low Temperature Cofired Ceramics (LTCC) multilayer technology has been employed.

The filters designed to prove the validity of the proposed novel procedures satisfy specifications which are difficult to achieve using classical filter design techniques, and are found to be interesting applications for the newly proposed design scheme. Additionally, specific solutions have been provided for two demanding applications, which are rectangular waveguide filters for space communication systems and dispersive delay lines.

The design and analysis of rectangular waveguide filters featuring smooth profiles are included in a chapter devoted to this specific application. The target specifications include wide rejection bands, high power capability and higher order mode suppression, typical characteristics in rectangular waveguide filters for space communication systems. During the analysis special emphasis is made on multi-mode effects which are likely to occur, since the presented techniques deal with wide frequency bands. To analyze multi-mode operation of the presented filters, the mode-matching technique has been used and implemented using Matlab. The main advantage of this analysis tool is that the evolution of the modes and the coupling between modes along the structure can be obtained, which is not possible with other commercial software. A brief explanation of the well-known mode-matching technique that is behind the home-made software is presented first and then it has been used for the analysis of various designed filters described later on.

The proposed direct synthesis method based on pole and zero decomposition (P&Z) has been particularized for rectangular waveguide technology, and a multi-band Cauer filter has been designed. Single-mode operation is assumed during design and it can be necessary to multiply the synthesized profile of the waveguide by a factor less than

1 to assure it. The home-made mode-matching program is used to confirm single-mode operation.

Reducing the synthesized profile can lead to minimum gaps that reduce the power capability of the filters. For high-power filters with very wide rejection band, a design method based on the Bragg phenomenon is presented. A classical high-power E-plane corrugated low-pass filter is cascaded with a quasi-periodic structure that performs sinusoidal perturbations with a period tuned to reject each of the harmonics. In this case, multi-mode effects provide an additional rejected frequency band coinciding with the third harmonic which avoids the need to use a periodic section specifically devoted to this frequency band and reduces the total length of the filter.

To finish the chapter focused on rectangular waveguide filters, an integrated design methodology of compact high-power low-pass filters is presented to reject the fundamental mode and its harmonics in a wide frequency band. The resulting filters consist of multiple E-plane bandstop elements of a sinusoidal profile, constituting a quasi-periodic structure, where the tuning of the rejected frequencies is this time achieved through the height of the bandstop elements. A filter that satisfies the same specifications as the Bragg reflector-based solution has been designed following this method. To obtain also the rejection of higher order modes the design method has been modified by introducing a width reduction of some sections of the filter. Another design example is given for the same operation range showing excellent performance. The performance of both examples in response to high order modes is compared using the home-made mode-matching program and providing at the same time a better understanding of the operation basis of this type of filters.

Dispersive delay lines (DDLs) have been considered in detail in this thesis. The crescent interest on analog signal processing systems has boosted the development of DDLs, the basic building block of this type of systems. A review of the different technologies and design techniques has been done to provide a up-to-date state of the art.

A new method to design chirped delay lines (CDLs) in coupled-line technology has been proposed. The design technique benefits from all the advantages of previously reported microstrip chirped delay lines. Additionally, the use of coupled-lines provides an effective transmission-type operation, avoiding the circulator required in the previous two-port counterparts. The proposed technique has been validated with the design of a device intended for UWB signal processing. A prototype has been fabricated and fully verified with measurements both in frequency and time domains.

Finally, several devices have been designed for the compensation of the chromatic

dispersion in fiber optics communication systems. A device to compensate the dispersion of a relatively short optical link (130 km with a bit rate of 8.5 Gb/s) has been designed. Its applicability has been proved with measurements of the bit-error-rate (BER) of the optical communication system, obtaining very good results. The design of devices with higher dispersion for longer optical links (300 km with a data rate of 10 Gb/s) has encountered practical limitations due to the fabrication techniques. A compromise between the fabricability and the frequency requirements has been achieved to obtain two devices that are being tested into the optical communication system.

Although many topics have been analyzed along this thesis, there are still several pending issues and new ideas that require further investigation:

- The fabrication and measurements of the compact multiband filter designed in LTCC technology are planned to be done in the near future. The results of the first approach to LTCC can confirm the possibility of employing multilayer technology with the proposed synthesis method which opens a new work line focused on the optimization of the adaptation of the designs to multilayer technology.

- The designed high dispersion CDLs are being tested in the optical communications systems and measurement results are expected to be obtained soon.

- Avoiding the use of inhomogeneous microstrip technology was envisaged as a solution to surpass the limitations encountered in the fabrication of CDLs. Alternative transmission lines, such as stripline coupled-lines or broadside coupled-lines in LTCC could be used. Coplanar waveguide coupled-lines are also a good candidate to minimize the effect of different even- and odd-mode propagation constants.

- CDLs in coupled-lines can be employed in other analog signal processing systems. For instance, the generation of linear-frequency-modulated waveforms for chirp radars can be easily achieved with the effective transmission-type CDLs and an impulse generator. At the reception of the radar, a CDL with a group-delay slope of opposite sign can be used as a matched filter.

- Further research can be done on other transformation methods and different digital design techniques to optimize the obtained frequency responses in order to obtain more compact results or other desired characteristics. Specially interesting would be using phase response specifications to design dispersive delay lines for analog signal processing systems.

- Improvements can be done in the mode-matching code to optimize its computational costs. Moreover, it can be combined with the tools presented here for the approximation and synthesis methods to integrate a flexible design and analysis tool for rectangular waveguide filters.
- New applications where classical design techniques find difficulties can take advantage of the flexibility of the presented approximation and synthesis procedures, such as Ultra Wideband filters or differential filters.

Conclusiones

En esta tesis, el objetivo de conseguir flexibilidad en el diseño de filtros de microondas ha sido satisfecho. Se han propuesto nuevas opciones para resolver los dos problemas en los que se divide típicamente el diseño de filtros: el problema de aproximación y el problema de síntesis.

Se ha propuesto un nuevo prodecimiento de aproximación basado en las técnicas de diseño de filtros digitales, que son fácilmente accesibles, para obtener una respuesta en frecuencia que satisfaga las especificaciones de diseño. La metodología propuesta depende de una correcta transformación de las especificaciones analógicas iniciales al dominio analógico de modo se puede sacar provecho de las sofisticadas técnicas de diseño de filtros digitales que se encuentran en constante evolución sin necesidad de conocer en detalle toda la complejidad matemática que implican. El filtro digital resultante se transforma finalmente al dominio analógico para obtener la respuesta en frecuencia deseada. Varios métodos de transformación han sido presentados. Ademas, se ha realizado una breve introducción a los filtros digitales y sus técnicas de diseño. El procedimiento propuesto ha sido validado mediante el diseño de filtros multibanda.

Además, un nuevo método de síntesis basado en técnicas de scattering inverso ha sido propuesto. Este método permite obtener el coeficiente de acoplo requerido para una determinada respuesta, de manera directa mediante expresiones cerradas que requieren simplemente la resolución de un sistema de ecuaciones lineales. Además, es un método exacto en todo el ancho de banda de interés y es válido para cualquier respuesta en frequencia que pueda expresarse como una función racional. Los filtros diseñados siguiendo este método se caracterizan por tener perfiles continuos que varían suavemente, evitando así las discontinuidades abruptas y sus efectos perjudiciales. La flexibilidad de esta técnica de síntesis se potencia especialmente cuando se utiliza en combinación con el procedimiento de aproximación basado en técnicas de diseño de filtros digitales. La validez de dicha combinación ha sido probada mediante

el diseño, fabricación y medida de un filtro multibanda. Con el objetivo de mejorar la integración de dicho diseño, se ha seguido un proceso de compatación utilizando la tecnología multicapa Low Temperature Cofired Ceramics (LTCC).

Los filtros diseñados para probar la validez de los procedimientos propuestos satisfacen especificaciones que son difíciles de obtener utilizando las técnicas clásicas de diseño de filtros, y se consideran aplicaciones interesantes para los métodos de diseño propuestos. Asimismo, se ha trabajado en obtener soluciones concretas para dos aplicaciones especialmente exigentes, que son los filtros en guía de onda rectangular para sistemas de comunicaciones espaciales y las líneas de retardo dispersivas.

El diseño y análisis de filtros en guía rectangular con perfiles suaves ha sido incluido en un capítulo especialmente dedicado a dicha aplicación. Las especificaciones requeridas para dicho tipo de filtros incluyen gran anchos de banda de rechazo, capacidad de manejo de alta potencia y rechazo de modos de alto orden, especificaciones típicas para los filtros en guía rectangular para aplicaciones espaciales. Durante el análisis de los filtros propuestos se ha hecho especial hincapié en los efectos multi-modo ya que es muy probable que ocurran en anchos de banda tan grandes. Para analizar la operación multi-modo de los filtros presentados se ha utilizado la conocida técnica de mode-matching que ha sido implementada utilizando Matlab. La mayor ventaja del uso de la herramienta de diseño desarrollada es que permite obtener la evolución de los modos y el acoplo entre los mismo a lo largo de la estructura, lo cual no es posible mediante otras herramientas comerciales. Una breve explicación de la técnica de mode-matching que esta tras el programa desarrollado es presentado primero y después ha sido utilizado para analizar los diversos diseños que se han propuesto.

Las líneas de retardo dispersivas han sido también consideradas en detalle en esta tesis. El interés creciente en los sistemas de procesado analógico de señales ha incrementado el desarrollo de nuevas líneas de retardo dispersivas, que es el elemento básico que conforma dichos systemas. Se ha relizado un revisión de las diferentes tecnologías y técnicas de diseño que proporcionan un resumen actualizado del estado del arte.

A continuación, se ha propuesto un nuevo método de diseño de líneas de retardo chirpeadas en tecnología de líneas acopladas. Dicha técnica se beneficia de todas las ventajas de las líneas de retardo chirpeadas en dos puertos. Además, el uso de líneas acopladas proporciona una operación en transmisión efectiva, que elimina la necesidad de utilizar un circulador. La técnica propuesta ha sido validada mediante el diseño de un dispositivo para el proceso de señales Ultra Wideband. Un prototipo ha sido fabricado y verificado con medidas tanto en el dominio frecuencial como en el temporal.

Finalmente, se han diseñado varios dispositivos para la compensación de la dispersión cromática en sistemas de comunicaciones de fibra óptica. Se ha diseñado un dispositivo para compensar la dispersión de un enlace de fibra óptica relativametne corto (130 km y una velocidad de transmisión de 8.5 Gb/s), que ha sido probado en el sistema de comunicaciones ópticas obteniendo resultados muy satisfactorios. El diseño de dispositivos que permitan compensar enlaces de fibra óptica de mayor longitud (300 km y una velocidad de transmisión de 10 Gb/s) se ha enfrentado a limitaciones prácticas debidas a los métodos de fabricación. Se ha llegado a un compromiso entre la capacidad de fabricación y los requerimientos en frecuencia para obtener dos dispositivos que estan siendo probados en el sistema de comunicaciones ópticas.

upna

Universidad Pública de Navarra
Nafarroako Unibertsitate Publikoa

RESEARCH MERITS OF THE AUTHOR

Journal Papers: 13

1. I. Arregui, F. Teberio, I. Arnedo, A. Lujambio, M. Chudzik, D. Benito, T. Lopetegi, R. Jost, F. -J. Görtz, J. Gil, C. Vicente, B. Gimeno, V. E. Boria, D. Raboso, and M. A. G. Laso, "Multipactor characterization of high-power low-pass harmonic filters with higher-Order TE_{n0} and non-TE_{n0} mode suppression", *IEEE Transactions on Microwave Theory and Techniques*, vol. 61, no. 12, pp. 4376–4386, December 2013

2. I. Arnedo, I. Arregui, M. Chudzik, F. Teberio, A. Lujambio, D. Benito, T. Lopetegi, and M. A. G. Laso, "Passive microwave component design using inverse scattering: theory and applications," *International Journal of Antennas and Propagation, Special Issue on "Inverse Scattering and Microwave Tomography in Safety, Security, and Health"*, vol. 2013, Article ID 761278, pp. 1-10.

3. A. Santorelli, M. Chudzik, E. Kirshin, E. Porter, A. Lujambio, I. Arnedo, M. Popovic, and J. D. Schwartz, "Experimental demonstration of pulse shaping for time domain microwave breast imaging," *Progress In Electromagnetics Research*,vol. 133, pp. 309?-329, 2013.

4. M. Chudzik, I. Arnedo, A. Lujambio, I. Arregui, I. Gardeta, F. Teberio, J. Azaña, D. Benito, M. A. G. Laso, and T. Lopetegi, "Design of transmission-type N^{th}-order differentiators in planar microwave technology," *IEEE Transactions on Microwave Theory and Techniques*, vol. 60, no. 11, pp. 3384–3394, November 2012.

5. I. Arregui, F. Teberio, I. Arnedo, A. Lujambio, M. Chudzik, D. Benito, R. Jost, F. -J. Görtz, T. Lopetegi, and M. A. G. Laso, "High-power low-pass harmonic waveguide filter with TE_{n0}-mode suppression," *IEEE Microwave and Wireless Components Letters*, vol. 22, no. 7, pp. 339–341, July 2012.

6. I. Arnedo, I. Arregui, A. Lujambio, M. Chudzik, M. A. G. Laso, and T. Lopetegi, "Synthesis of microwave filters by inverse scattering using a closed-form expression valid for rational frequency responses," *IEEE Transactions on Microwave Theory and Techniques*, vol. 60, no. 5, pp. 1244–1257, May 2012.

7. I. Arnedo, M. Chudzik, J. D. Schwartz, I. Arregui, A. Lujambio, F. Teberio, D. Benito, M. A. G. Laso, D. V. Plant, J. Azaña, and T. Lopetegi, "Analytical solution for

the design of planar electromagnetic bandgap structures with spurious-free frequency response," *Microwave and Optical Technology Letters*, vol. 54, no 4, pp 956–960, April 2012.

8. M. Chudzik, I. Arnedo, A. Lujambio, I. Arregui, F. Teberio, M. A. G. Laso, and T. Lopetegi, "Microstrip coupled-line directional coupler with enhanced coupling based on EBG concept," *Electronics Letters*, vol. 47, no 23, pp 1284–1286, November 2011.

9. A. Lujambio, I. Arnedo, M. Chudzik, I. Arregui, T. Lopetegi, and M. A. G. Laso, "Dispersive delay line with effective transmission-type operation in coupled-line technology," *IEEE Microwave and Wireless Components Letters*, vol. 21, no 9, pp 459–461, September 2011.

10. M. Chudzik, I. Arnedo, I. Arregui, A. Lujambio, M. A. G. Laso, D. Benito, and T. Lopetegi, "Novel synthesis technique for microwave circuits based on inverse scattering: efficient algorithm implementation and application," *International Journal of RF and Microwave Computer-Aided Engineering*, vol. 21, no. 2, pp. 164–173, March 2011.

11. I. Arregui, I. Arnedo, A. Lujambio, M. Chudzik, D. Benito, R. Jost, F.-J. Görtz, T. Lopetegi, and M. A. G. Laso, "A compact design of high-power spurious-free low-pass waveguide filter," *IEEE Microwave and Wireless Components Letters*, vol. 20, pp. 595–597, November 2010.

12. I. Arregui, I. Arnedo, A. Lujambio, M. Chudzik, M. A. G. Laso, T. Lopetegi, and M. Sorolla, "Design method for satellite output multiplexer low-pass filters exhibiting spurious-free frequency behavior and high-power operation," *Microwave and Optical Technology Letters*, vol. 52, no. 8, pp. 1724–1728, August 2010.

13. I. Arnedo, A. Lujambio, T. Lopetegi, and M.A.G. Laso, "Design of Microwave Filters with Arbitrary Frequency Response Based on Digital Methods," *IEEE Microwave Wireless Components Letters*, vol. 17, no. 9, pp. 634–636, September 2007.

International Conferences: 13 + 2

1. J. Munoz-Ferreras, I. Arnedo, A. Lujambio, M. Chudzik, M. A. Laso, R. Gomez-Garcia, "Chirped Impulse-Radio Ultra-Wideband (IR-UWB) Radar Concept," *International Microwave Symposium, IMS 2014. Submitted.*

2. M. Chudzik, A. Ghaddar, I. Arnedo, A. Chahadih, I. Arregui, F. Teberio, A. Lujambio, G. Ducournau, J. F. Lampin, T. Lopetegi, M. A. Laso, T. Akalin, "Pulse shaping for millimeter-wave and terahertz applications in coplanar technology," *International Microwave Symposium, IMS 2014. Submitted.*

3. A. Chahadih, M. Chudzik, I. Arnedo, A. Ghaddar, I. Arregui, F. Teberio, A. Lujambio, M. A. G. Laso, T. Lopetegi, and T. Akalin, "Low loss microstrip transmission-lines using Cyclic Olefin Copolymer COC substrate for sub-THz and THz applications", *International Infrared, Millimeter and Terahertz Waves IRMMW-THz.* Mainz on the Rhine, Germany, September 2013.

4. I. Arregui, F. Teberio, I. Arnedo, A. Lujambio, M. Chudzik, D. Benito, T. Lopetegi, R. Jost, F. J. Görtz, J. Gil, C. Vicente, B. Gimeno, V. E. Boria, D. Raboso, and M. A. G. Laso, "Multipactor-resistant low-pass harmonic filters with wide-band higher-order mode suppression," *International Microwave Symposium, IMS 2013.* Seattle, USA, June 2013.

5. I. Arnedo, I. Arregui, M. Chudzik, F. Teberio, A. Lujambio, D. Benito, T. Lopetegi, and M. A. G. Laso, "Novel synthesis techniques of passive microwave components: theory and applications," *International 9th Iberian Meeting on Computational Electromagnetics.* Dénia, Spain, May 2013.

6. M. Chudzik, A. Chahadih, I. Arnedo, A. Ghaddar, A. Lujambio, F. Teberio, I. Arregui, G. Ducournau, J.-F. Lampin, D. Benito, T. Lopetegi, M. A. G. Laso, and T. Akalin, "Synthesis of passive terahertz devices in coplanar Technology," *International Workshop on Terahertz Science and Technology, OTST 2013.* Kyoto, Japan, April 2013.

7. M. Chudzik, A Ghaddar, I. Arnedo, A. Lujambio, I. Arregui, F. Teberio, M. A. G. Laso, T. Lopetegi, and T. Akalin, "Microstrip EBG structures for millimeter-wave range with a broadband coplanar waveguide to microstrip transition," *International Symposium on Frontiers in Terahertz Technologies 2012 (FTT2012).* Nara, Japan, November 2012.

8. I. Arnedo, M. Chudzik, A Ghaddar, A. Lujambio, F. Teberio, I. Arregui, G. Ducournau, J.-F. Lampin, T. Lopetegi, M. A. G. Laso, and T. Akalin, "Pulse shaper for THz wireless communication," *International Symposium on Frontiers in Terahertz Technologies 2012 (FTT2012).* Nara, Japan, November 2012.

9. F. Teberio, I. Arregui, I. Arnedo, A. Lujambio, M. Chudzik, D. Benito, R. Jost, F. -J. Görtz, T. Lopetegi, and M. A. G. Laso, "High-power alternative to the design of

wide-band spurious-free waffle-iron filters and prediction of multipacting breakdown," *International Workshop on Microwave Filters (IWMF 2012)*. Toulouse, France, October 2012.

10. M. Chudzik, I. Arnedo, A. Lujambio, I. Arregui, F. Teberio, D. Benito, T. Lopetegi, and M. A. G. Laso. "Design of EBG microstrip directional coupler with high directivity and coupling," *European Microwave Conference (EuMC 2012)*. Amsterdam, The Netherlands, October 2012.

11. I. Arregui , S. Anza, F. Teberio, C. Vicente, I. Arnedo, J. Gil, A. Lujambio, M. Chudzik, R. Jost, F. J. Görtz , B. Gimeno, D. Benito, T. Lopetegi, M. A. G. Laso, D. Raboso, and V. E. Boria, "Multipactor prediction in novel high-power low-pass filters with wide rejection band," *7th International Workshop on Multipactor, Corona and Passive Intermodulation in Space RF Hardware (MULCOPIM 2011)*. Valencia, Spain, September 2011.

12. I. Arnedo, I. Arregui, M. Chudzik, A. Lujambio, J. D. Schwartz, D. V. Plant, J. Azaña, T. Lopetegi, and M. A. G. Laso, "Customized pulses for UWB applications," in *Proceedings European Microwave Conference (EuMC 2010)*. Paris, France, September 2010, pp. 320–323.

13. I. Arregui, S. Anza, I. Arnedo, C. Vicente, A. Lujambio, J. Gil, M. Chudzik, B. Gimeno, T. Lopetegi, M. A. G. Laso, and V. E. Boria, "Multipactor Prediction in Novel High-Power Low-Pass Filters with Wide Rejection Band," *International Workshop on Microwave Filters (IWMF 2009)*. Toulouse, France, November 2009.

14. I. Arregui, S. Anza, I. Arnedo, C. Vicente, A. Lujambio, J. Gil, M. Chudzik, B. Gimeno, T. Lopetegi, M. A. G. Laso, and V. E. Boria, "Multipactor prediction in novel high-power low-pass filters with wide rejection band," in *Proceedings European Microwave Conference (EuMC 2009)*. Rome, Italy, September 2009, pp. 675–678.

15. I. Arnedo, I. Arregui, M. Chudzik, A. Lujambio, M. A. G. Laso, T. Lopetegi, J. Schwartz, J. Azaña, and D. Plant, "Arbitrary UWB pulse generation and optimum matched-filter reception," in *Proceedings IEEE International Conference on Ultra-Wideband (ICUWB 2009)*. Vancouver, Canada, September 2009, pp. 43–48.

National Conferences: 8

1. M. Chudzik, V. Urrea, A. Lujambio, I. Arnedo, I. Arregui, F. Teberio, T. Lopetegi, and M. Á. Gómez Laso, "Medidas en el dominio temporal de circuitos derivadores

para el procesado de señales analógicas UWB," *XXVIII Simposium Nacional de la Unión Científica Internacional de Radio (URSI 2013)*. Santiago de Compostela, Spain, September 2013.

2. I. Arregui, F.Teberio, I. Arnedo, A. Lujambio, M. Chudzik, D. Benito, T. Lopetegi, R. Jost, F. -J.Görtz, J. Gil, C. Vicente, B. Gimeno, V. E. Boria, D. Raboso, and M. A. G. Laso, "Medida del multipactor en filtro paso bajo de alta potencia con supresión de modos de alto orden en gran ancho de banda," *XXVIII Simposium Nacional de la Unión Científica Internacional de Radio (URSI 2013)*. Santiago de Compostela, Spain, September 2013.

3. A. Lujambio, M. Chudzik, I. Arregui, F. Teberio, I. Arnedo, P. Boffi, M. Ferrario, A. Gatto, M. Martinelli, L. Ranzani, T. Lopetegi, and M. A. G. Laso, "Línea de retardo dispersiva en líneas acopladas para la compensación de la dispersión cromática en fibra mediante la predistorsion analógica en microondas", *XXVII Simposium Nacional de la Unión Científica Internacional de Radio (URSI 2012)*. Elche, Spain, September 2012.

4. I. Arnedo, M. Chudzik, A. Lujambio, I. Arregui, F. Teberio, D. Benito, T. Lopetegi, and M. A. G. Laso, "Acoplador direccional en lineas microstrip acopladas con factor de acoplo mejorado mediante estructura EBG", *XXVII Simposium Nacional de la Unión Científica Internacional de Radio (URSI 2012)*. Elche, Spain, September 2012.

5. F. Teberio, I. Arregui, I. Arnedo, A. Lujambio, M. Chudzik, D. Benito, R. Jost, F. -J. Görtz, T. Lopetegi y M. A. G. Laso, "Filtros paso-bajo compactos de alta potencia con eliminación de espurios y esquinas redondeadas", *XXVI Simposium Nacional de la Unión Científica Internacional de Radio (URSI 2011)*. Leganes, Spain, September 2011.

6. A. Lujambio, I. Arregui, J. D. Schwartz, M. Chudzik, T. Egozcue, D. V. Plant, J. Azaña, T. Lopetegi, I. Arnedo, and M. A. G. Laso, "Dispositivos con retardo de grupo lineal para UWB con líneas acopladas en stripline", *XXIV Simposium Nacional de la Unión Científica Internacional de Radio (URSI 2009)*. Santander, Spain, September 2009.

7. I. Arregui, A. Lujambio, J. D. Schwartz, M. Chudzik, I. Gardeta, D. V. Plant, J. Azaña, M. A. G. Laso, I. Arnedo, and T. Lopetegi, "Derivador de orden N en líneas acopladas microstrip para UWB", *XXIV Simposium Nacional de la Unión Científica Internacional de Radio (URSI 2009)*. Santander, Spain, September 2009.

8. A. Lujambio, I. Arnedo, T. Lopetegi, D. Benito, F. J. Falcone, and M. A. G. Laso, "Síntesis de filtros de microondas con respuesta arbitraria", *XXI Simposium Nacional de la Unión Científica Internacional de Radio (URSI 2006)*. Oviedo, Spain, September 2006.